Measuring Sound-Induced Motions of the Alligator Lizard Cochlea

by

Alexander James Aranyosi

Submitted to the Harvard–Massachusetts Institute of Technology
Division of Health Sciences and Technology
in partial fulfillment of the requirements for the degree of

Doctor of Philosophy

at the

MASSACHUSETTS INSTITUTE OF TECHNOLOGY

June 2002

Author .....
Harvard–Massachusetts Institute of Technology Division of Health Sciences and Technology
March 21, 2002

Certified by .....
Dennis M. Freeman
Associate Professor of Electrical Engineering
Thesis Supervisor

Accepted by .....
Martha Gray
Chair, Departmental Committee on Graduate Students

Measuring Sound-Induced Motions of the Alligator Lizard Cochlea

by

Alexander James Aranyosi

Submitted to the Harvard–Massachusetts Institute of Technology Division of Health Sciences and Technology
on March 21, 2002, in partial fulfillment of the requirements for the degree of Doctor of Philosophy

Abstract

The sensitivity and frequency selectivity of the hearing sense are determined primarily by mechanical properties of the cochlea. These mechanical properties are poorly understood in any species. This thesis contributes to our understanding of cochlear mechanics by presenting measurements of sound-induced motion of the alligator lizard cochlea. Novel methods were developed to maintain the cochlea *in vitro* for the time required to measure three-dimensional motions. Three-dimensional images of cochlear motion were taken by illuminating the cochlea with a light-emitting diode stroboscopically at predetermined phases of the acoustic stimulus. The resulting images were analyzed using computer vision algorithms to extract three-dimensional motions of all visible structures with nanometer precision. The sound-induced motion of the entire basilar papilla and of individual hair bundles of hair cells were simultaneously measured. The basilar papilla, in which the hair cells reside, moved as a rigid body, exhibiting simultaneous translational and rotational modes of motion. Both modes apply shearing forces to hair bundles. A simple mechanical model of the basilar papilla, based on these measurements, provides a physical basis for a mechanical low-pass filter hypothesized in previous models. In the tectorial region of the cochlea, motion of the tips of hair bundles and of the tectorial membrane (TM) were in phase with motion of the basilar papilla. None of the motions had significant frequency dependence, suggesting that this region does not exhibit appreciable mechanical frequency selectivity. In the free-standing region, which has no TM, hair bundle deflection depended on stimulus frequency and hair bundle height. At high frequencies, hair bundle deflection was proportional to basilar papilla displacement. At low frequencies, hair bundle deflection was proportional to a linear combination of basilar papilla velocity and acceleration. Measured hair bundle deflections were well fit by a simple hydrodynamic model (Freeman and Weiss, 1990) of this region of the cochlea. The measurements in this study provide the first characterization of the three-dimensional motion of all structures in a vertebrate cochlea.

Thesis Supervisor: Dennis M. Freeman
Title: Associate Professor of Electrical Engineering

Acknowledgments

Although completing a PhD thesis may seem to be the pinnacle of individual academic achievement, it is simply not possible without the help and guidance of a large number of people. Although their names appear only in this section, their ideas, hard work, and words of encouragement permeate the entire thesis. First and foremost, I want to thank my advisor, Denny Freeman, for more things than I can list, but mostly for teaching me how to do research. Everything I know about conducting experiments, collecting data, analyzing it, interpreting the results, and writing it up I learned from Denny. Everything I don't know yet is my own fault. Over the years Denny has also become a great friend, and I look forward to continuing our personal and professional relationships in the future. My other committee members, David Mountain and David Corey, have provided insightful questions and comments throughout the course of my thesis research. Tom Weiss has been an invaluable resource throughout my time as a graduate student, and in particular has done a wonderful job in catching my mistakes (the ones that remain are there through no fault of his). John Rosowski and Bill Peake have both helped me along by politely hinting that after eight years, I should start to think about finishing up. Joe Adams and Ed Mroz convinced me (with considerable effort!) that understanding the mechanical properties of a biological tissue was impossible without taking into account the physiological properties of the tissue. I've had the good fortune of working with a wonderful, constantly changing crew of graduate students in the micromechanics group, most of whom have long since graduated and left me behind. I got a lot of help early on from Quentin Davis, who built the first lizard experiment chamber and did some of the first experiments, and has since moved on to bigger and better salaries. Cameron Abnet always cheered me up by telling me how life could be worse, and Zoher Karu helped me focus on the practical aspects of research (like where the money is!). Janet Slifka was the first person to convince me to start writing my thesis, and proved definitively that research and modern dance are not mutually exclusive career options. Michael Mermelstein has been a great inspiration to me in a number of ways, not the least of which has

been reminding me that I shouldn't spend all of my time maintaining the computer network. Werner Hemmert provided a uniquely inscrutable German perspective on my research, and has almost convinced me that mammalian hearing is interesting enough to study. Mike Gordon was a great officemate, partly because he was willing to listen to me rant about the latest "cool" thing I'd discovered, only to find out five minutes later that I was totally wrong. Kinu Masaki and Betty Tsai provided me with all the snack food I could eat, and helped renew my interest in the tectorial membrane and viscoelasticity. Amy Englehart has kept me happy and smiling during the laborious process of writing, and has a unique talent for asking great questions. Janice Balzer, the power behind the throne, has done a hero's duty keeping the machinery of the lab running, and taking care of all the things that I have no clue how to do. Several students working in other labs have also been helpful. Domenica Karavitaki has been a valuable colleague and a wonderful friend; informal discussions with her have often given me insights that I would never have found in journal articles. I would never have known about FM1-43 uptake by hair cells or the use of PPADS to block P2X channels if not for Rick MacDonald, so without his help chapter 2 of this thesis would be far less interesting. Finally, I want to thank some people who are not associated with the research community. My friend and erstwhile housemate, Séan McSherry, has always been there to help me out, even when it made his life more difficult. The whole McSherry clan has been a surrogate family to me during my time in graduate school. Of course, my true family cannot be forgotten. Mom, Dad (I wish you could be here to see me finish), Margaret, Floyd, Joe — I love you all, and thank you for everything you've done for me. Without you, I wouldn't even be close to where I am today.

Contents

List of Figures

Chapter 1

Introduction

1.1 Why study cochlear mechanics?

Two old friends meet after not seeing each other for several years. The first says, "Remember how I was almost deaf? I got a new hearing aid, and it's wonderful. I can hear the leaves falling from the trees, and the flapping wings of the birds as they fly." The other says, "That's wonderful! What kind is it?" The first looks at his watch and says, "4:15."

From the deepest bass to the highest piccolo, the softest whisper to the loudest scream, we have an amazing ability to hear and distinguish a wide variety of sounds. This ability has its basis in the remarkable mechanical properties of the cochlea, an organ which contains auditory receptor cells called hair cells. The cochlea is a structure with more than a million moving parts (Hudspeth, 1985) working together to convert acoustic signals into neural impulses which are sent to the central nervous system. Understanding the mechanical properties of the cochlea is vital for the clinical treatment of hearing loss, fascinating from an engineering standpoint, and necessary for the improvement of models of cochlear function. This thesis contributes to an understanding of cochlear function by describing the motion of structures of the alligator lizard cochlea in response to sound stimulation.

Understanding cochlear mechanics will provide better tools for treating hearing loss. As the quote introducing this chapter illustrates, hearing loss not only raises the threshold of audibility, but can dramatically alter our perception of audible sounds. This alteration is particularly tragic when it affects a person's ability to communicate with others. For more than 28 million people in the United States alone — 10% of the population — with some form of hearing impairment*, this loss of contact can lead to feelings of frustration, isolation, and depression, and may hamper their ability to function. Improving techniques to compensate for hearing loss will have a large effect on the quality of life for a vast number of people.

Hearing impairment is typically measured in terms of loss of sensitivity. The simplest approach to compensate for this loss is to amplify the sound signals presented to the ear. However, this simple approach often fails in practice. The primary reason for this failure is that the mechanical properties of the ear appear to change following damage. This change is believed to be at least partly due to the loss of outer hair cells, which undergo length changes in response to changes in transmembrane potential (Brownell et al., 1985) or mechanical stimulation (Zenner, 1986), and may act as mechanical amplifiers in the cochlea. To understand how the loss of this amplification affects the cochlea, we need to understand not only the amplifiers themselves but also the passive mechanical properties of the cochlea. Improved understanding of cochlear mechanics is necessary for significant improvements in the treatment of hearing loss.

Measuring cochlear mechanics will provide insight into the cochlea's remarkable properties. The sensitivity of the cochlea is remarkable from an engineering standpoint. At the threshold of hearing we can detect sounds that cause air molecules to vibrate by mere picometers, and the same structures continue to work for sounds a trillion times more intense. Only recently have microphones with an equivalent sensitivity and dynamic range (ER-10Bplus, Etymōtic Research) been manufactured.

The cochlea is also a remarkable frequency analyzer. Humans can detect an 0.2%

*Data from the NIDCD web site at http://www.nidcd.nih.gov/health/hb.htm.

change in the frequency of a tone. This resolution provides about 3500 distinct frequencies over the hearing range, roughly comparable to the number of mechanosensory inner hair cells. In addition, the cochlea has a time resolution to rival that of any other biological system. Timing information is maintained so precisely that we can detect differences of $5 - 10$ μsec in the arrival times of a sound at our two ears. Both the sensitivity and frequency selectivity of the cochlea are determined primarily by the cochlea's mechanical properties. By studying cochlear mechanics, we hope to better understand these remarkable biological engineering feats.

Measurements of cochlear mechanics can be used to improve cochlear models. To date, complete three-dimensional mechanical models of the cochlea have proven to be intractably complex. The variety of simplifications chosen by different modelers have led to a bewildering array of mutually contradictory models. Many of these models attribute highly anisotropic material properties to different structures; for example, most models assume individual cochlear structures move as rigid bodies in radial cross-section, but are completely uncoupled longitudinally. Nonetheless, no single model has been able to account for all of the observed mechanical properties of the cochlea while using physically plausible parameters. By providing measurements of the motion of individual cochlear structures, we can validate or refute the underlying assumptions of various cochlear models.

1.2 Macro- and micro-mechanics

Descriptions of the mechanical properties of the cochlea are divided, somewhat arbitrarily, into macromechanics and micromechanics (Patuzzi, 1996). *Macromechanics* refers to the motion of the basilar membrane and the cochlear partition as a whole, while *micromechanics* refers to the relative motion of hair bundles and of structures at the level of the reticular lamina and tectorial membrane. Studies of macromechanics were pioneered by von Békésy (von Békésy, 1960), who first described a broadly-tuned travelling wave of motion in human cadaver cochleae in response to sound. After con-

siderable investigation, it has now been established (Rhode, 1971; Rhode, 1973; Page and Johnstone, 1980; Sellick et al., 1982; Robles et al., 1991; Ruggero and Rich, 1991) that the motion of the basilar membrane is nonlinear, sharply tuned in frequency, and that this sharp tuning is labile: in response to loud sounds, or in dead or damaged cochleae, the mechanical properties become linear and the sharpness of tuning decreases to values similar to those observed by von Békésy. However, even in the best preparations the responses measured differ from those recorded at the level of the auditory nerve. The differences between the broad tuning of dead cochleae and the sharp tuning of auditory nerve fibers are believed to be due to both active and passive micromechanical processes within the cochlea. Two recent reviews of cochlear macromechanics provide an excellent introduction to this topic (Patuzzi, 1996; Ruggero et al., 2000).

In recent years, the focus of auditory mechanics has increasingly shifted to the micromechanical properties of the cochlea. Micromechanical studies have proven to be more difficult than macromechanical ones, and only within the last 20 years have successful results been reported. The first measurements, in 1983, demonstrate frequency-dependent motion of individual hair bundles in the alligator lizard cochlea (Frishkopf and DeRosier, 1983; Holton and Hudspeth, 1983). These results will be discussed further in section 1.3.3. The first measurements in mammal were made using an isolated guinea pig cochlea (ITER, 1989). The sound-induced motions of structures in this preparation are essentially linear, with Q_{10dB} values of 0.5–1, significantly lower than the values of 2–5 measured in auditory nerve fibers innervating this region (Kiang et al., 1965).

Most models of cochlear micromechanics assume that the cochlea has multiple modes of motion. To evaluate the number and nature of modes, it is necessary to make 2D, and preferably 3D, measurements of cochlear motions as a function of frequency and location. Although measurements in the ITER study were primarily in the transverse direction, one two-dimensional measurement showed piston-like motion of a Hensen's cell. Measurements of tectorial membrane velocity in a similar preparation (Gummer et al., 1996; Hemmert et al., 2000) show frequency-dependent

elliptical motion, demonstrating two modes of motion of the TM. Elliptical motions of the basilar membrane and a Hensen's cell were also seen, but the variance in phase measurements was too large to conclude that these structures had multiple modes of motion. In response to 4 Hz mechanical stimulation, structures in a hemicochlea preparation move elliptically (Hu et al., 1999), demonstrating the presence of two out-of-phase components of motion which may be two separate modes. Measurements of electrically-evoked motion of the cochlea (Karavitaki and Mountain, 1997; Karavitaki and Mountain, 2002) show differential motion of the first and third rows of outer hair cells. With the exception of the ITER study, all of these studies provide some evidence that the mammalian cochlea has multiple modes of motion. However, there is currently no consensus on the number of modes present, nor on the contribution of the various modes to cochlear function.

Many aspects of the mammalian cochlea make micromechanical studies difficult. First, the macromechanical properties of the mammalian cochlea vary with distance along the cochlea, with stimulus frequency, with stimulus intensity, and with the physiological condition of the cochlea. In addition, the cochlea is encased in the hardest bone in the body, making access difficult. Obtaining visual access to cochlear structures usually requires disrupting the normal separation of fluids necessary to keep cochlear tissues healthy, and often requires disrupting the normal sound conduction pathways (ITER, 1989).

In contrast, the macromechanical properties of the alligator lizard *Gerrhonotus multicarinatus* cochlea do not depend strongly on frequency, intensity, or location (Peake and Ling, 1980; but see chapter 4). The alligator lizard cochlea can be isolated easily, and can be maintained in a near-normal fluid environment for several hours under the right conditions (see chapter 2). These properties make the alligator lizard cochlea easier to study, yet our understanding of this cochlea may still provide insight into the functioning of the mammalian cochlea. The next section provides a brief review of the anatomy and physiology of the alligator lizard cochlea.

1.3 The alligator lizard sense of hearing

The Southern alligator lizard (figure 1-1) is a member of the family Anguidae residing primarily in the southwestern United States. It feeds largely on small insects and suburban trash. Like most lizards, the alligator lizard does not make vocalizations, and thus its sense of hearing is not likely to be used for communcation. Rather, acoustic stimuli are probably used to detect prey and evade predators. However, it has proven notoriously difficult to elicit behavioral responses from lizards (Manley, 2000b), and thus it is not clear to what extent lizards attend to sounds. Although lizards have not been an advantageous choice for psychophysical studies, many aspects of the mechanical and electrical responses to sound in the alligator lizard have been measured; some of the relevant studies are described here.

FIG. 10-1. The alligator lizard *Gerrhonotus multicarinatus*. Drawing by Anne Cox.

Figure 1-1: The alligator lizard *Gerrhonotus multicarinatus*. The alligator lizard, shown in this drawing, is a typical member of the Anguid family of lizards. The lizards are typically brownish-green in color, with bodies 10-12 cm long. The tail length varies, but is often longer than the rest of the body. The external ear of this lizard consists of a short ear canal, located roughly midway between the eye and the foreleg. Figure reproduced from *The Reptile Ear* (Wever, 1978).

Terminology. Although *basilar papilla* is the proper term for the inner-ear hearing organ of lizards, the term *cochlea* has come into common usage based on homology

with the mammalian organ (Wever, 1974; Manley, 2000b). This convention will be used throughout the thesis; however, when the properties of the basilar papilla itself are being discussed (such as in chapter 4), the proper term will be used. The terms *apical* and *basal* are used to describe the axis connecting the low- and high-CF ends of the cochlea (Wever, 1974; Mulroy, 1974). These ends correspond to the tectorial and free-standing regions of the cochlea, respectively, although each region itself has an apical and basal end. Unfortunately, the terms *apical* and *basal* are also used to refer respectively to the endolymphatic and synaptic poles of individual hair cells. Any confusion resulting from this overlapping terminology should be resolved by the context of usage; the former meaning is used primarily in chapters 4, the latter is used primarily in chapter 2.

1.3.1 Anatomy

The anatomy of the alligator lizard cochlea has been described thoroughly elsewhere (Miller, 1966; Miller, 1973; Mulroy, 1968; Mulroy, 1974; Wever, 1965). We provide a brief review here. The alligator lizard cochlea (figure 1-2) is a planar structure 500 μm in diameter. The hair cells are contained within the basilar papilla, which is roughly cylindrical and rests on the basilar membrane (Mulroy, 1974). The basilar papilla sits between the neural limbus (the taller ridge) and the triangular limbus, which both sit above the edge of a bony ring outlining the basilar membrane. The endolymphatic surface of the cochlea (the surface visible in figure 1-2) forms a tight seal separating two fluid spaces. The endolymphatic fluid space contains endolymph, a fluid high in potassium and very low in calcium ions (Peterson et al., 1978). The perilymphatic fluid space (below the visible surface in figure 1-2) contains perilymph, a fluid with a composition that is more typical of extracellular fluids. The vestibular membrane (not shown in the drawing) extends from the triangular limbus beyond the neural limbus, and completes the enclosure of endolymphatic space. The footplate of the columella (homologous to the mammalian stapes) sits above the vestibular membrane facing the cochlea.

The basilar papilla itself is divided into two regions based on morphology (figure 1-

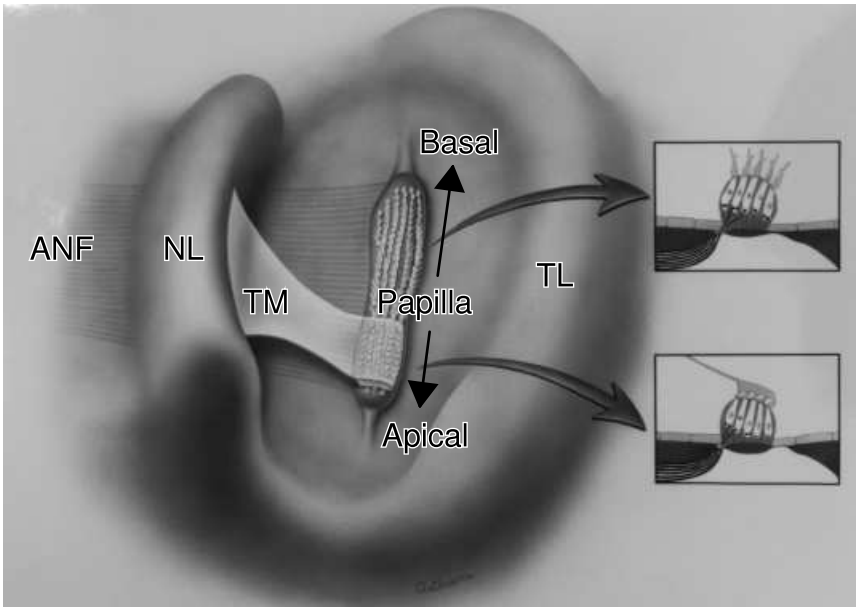

Figure 1-2: The alligator lizard cochlea. The papilla, which contains the hair cells, rests on the basilar membrane which extends between the neural limbus (NL) and triangular limbus (TL). In the basal, free-standing region of the cochlea (upper 2/3 of drawing), the hair bundles project freely into endolymph; bundle height is inversely correlated with the frequency to which the cells are most sensitive, which varies from 1 kHz for the most apical cells to 4 kHz for the most basal cells. In the apical, tectorial region (lower 1/3 of drawing), the bundles are covered with a tectorial membrane (TM), which attaches to the neural limbus on the left. The best frequencies of hair cells in this region are between 200 and 800 Hz. Auditory nerve fibers (ANF) project to the left. The triangular limbus borders the cochlea on the right. Insets show cross-sections of the cochlea in the apical free-standing (top) and basal tectorial (bottom) regions. This cochlea is simpler in cross-section than the mammalian cochlea, but shares many of the same basic features. Drawing by Anne Greene.

3). The apical, tectorial region, which makes up the apical 1/3 of the cochlea, contains hair cells whose bundles project into an overlying tectorial membrane (TM). The veil of the TM extends to the neural limbus. Our images show that the TM forms "cups" around each hair bundle, but it is not clear whether the hair bundles are attached to the TM. The hair bundles of hair cells in this region are about 8 μm in length. The hair cells in this region form gap junctions with supporting cells and other hair cells (Nadol et al., 1976). These hair cells receive projections from both afferent and efferent neurons.

In cross-section (figure 1-4), the basilar papilla is nearly circular. The basilar papilla rests off-center on a thin region of the basilar membrane. The portion of the

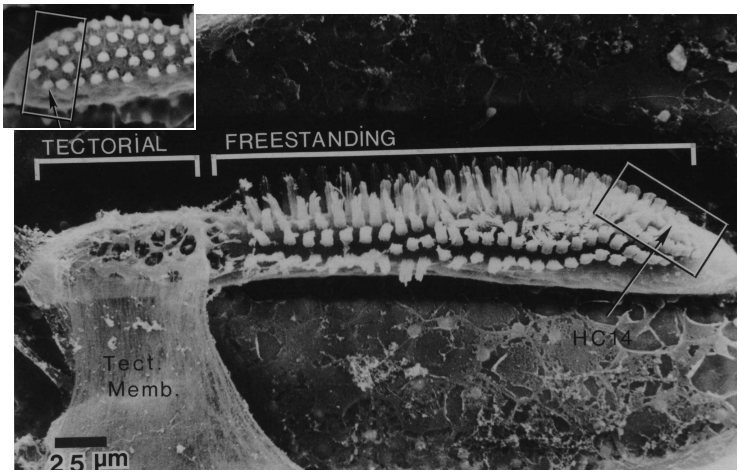

Figure 1-3: SEM Image of the alligator lizard cochlea. The tectorial and free-standing regions are labeled. In the tectorial region (shown with the TM removed in the inset), hair cells are covered by a gelatinous tectorial membrane. This TM attaches through a thin 'veil' to the neural limbus (below bottom of image). Fewer than 50 hair bundles are in this region, with bundles that are about 8 μm tall. In the free-standing region, no gelatinous overlying structure is present. Hair bundles range from over 30 μm in the most apical region to about 12 μm in the most basal region. Four or five hair cells can be seen at each longitudinal position, for a total of about 150 hair cells with free-standing bundles. SEM from Mulroy (1986), figure 1.

basilar membrane underneath the basilar papilla is stained blue by iron hematoxylin and aniline blue (IHAB), which has an affinity for collagen. This blue stain does not extend to the region beneath the epithelial cells on either side of the basilar papilla. On the neural side of the basilar papilla, the auditory nerve fibers run beneath a thickened region called the neural limbus. On the abneural side, the tissue thickens and is attached to bone. Hair bundles project from the endolymphatic surface of the papilla.

The free-standing region, which makes up the basal 2/3 of the cochlea, contains hair cells whose bundles project freely into endolymph. The hair bundles of cells in this region are longer than in the tectorial region. The longest bundles, 30–34 μm, are at the apical end adjacent to the TM. The bundles get progressively shorter in the basal direction, so the basalmost cells have hair bundles that are about 12 μm in

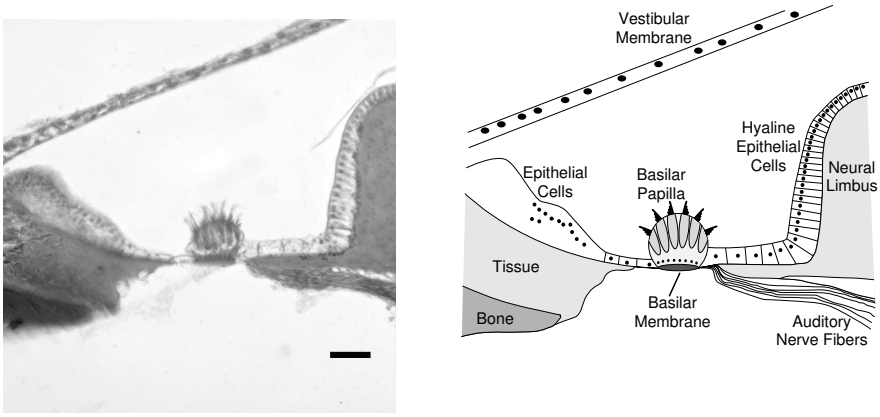

Figure 1-4: Histological cross-section of the alligator lizard basilar papilla. The left-hand figure shows a light microscope image of a thin slice of a fixed alligator lizard cochlea stained with IHAB. The right-hand figure schematizes this anatomy and provides labels. This slice comes from the apical end of the free-standing region. Several hair bundles project from the apical surface of the basilar papilla. The nuclei of hair cells are visible as dark circles near the center of the basilar papilla, and those of supporting cells are visible just above the basilar membrane. The auditory nerve fibers extend in the neural direction (right) beneath the neural limbus. Hyaline epithelial cells extend from both sides of the basilar papilla; the cells immediately to the neural side of the basilar papilla are much thicker than those immediately to the abneural side. The basilar membrane does not appear to contact the darkened tissue regions on either the neural or abneural side of the basilar papilla. Scale bar = 50 μm. Fixed tissue courtesy Michael Mulroy.

length. Hair cells in the free-standing region are innervated only by afferent neurons. Thus the alligator lizard cochlea, similar to those of other lizards, contains two types of hair cells (Mulroy, 1968; Mulroy, 1974; Wever, 1974). However, unlike in mammalian and avian cochleae, the two types of hair cells are confined to different frequency regions, and both types appear to be primarily sensors rather than effectors (Manley, 2000b; Manley, 2000a)[†].

[†]Manley notes that both types of hair cells may also provide electromechanical feedback in the form of bundle motility.

Direction conventions

Throughout this thesis, the following naming and sign conventions, based on a right-handed coordinate system[‡], will be used for various directions of structures and motion.

lateral: the neural/abneural axis, extending from the neural limbus to the triangular limbus. This axis is homologous to the radial direction in the mammalian cochlea. Positive directions are towards the neural axis. The lateral axis will also be referred to as the x axis.

longitudinal: the direction along the long axis of the papilla, extending from the basal to the apical end. This axis is homologous to the longitudinal direction in the mammalian cochlea. Positive directions are towards the apical end. The longitudinal axis will also be referred to as the y axis.

transverse: the direction normal to the basilar membrane surface. This axis is homologous to the transverse direction in the mammalian cochlea. Positive directions are towards endolymphatic space. The transverse axis will also be referred to as the z axis.

rotation: rotation of the basilar papilla is positive in the direction which causes the abneural edge to move in the positive z direction. Although this direction is opposite that of a right-handed system, it allows positive static displacements of the basilar membrane in the z direction to induce positive rotations.

In general, the microscope/camera system was oriented so that the first three axes above correspond to the x, y, and z axes in the microscope coordinate system. To reduce confusion between angles of rotation and angles of phase, rotational displacements of structures such as the basilar papilla or hair bundles will be reported in either degrees or radians, while phase angles of stimuli or of motions will be reported in cycles.

[‡]The direction conventions follow a right-handed system for the lizard's left ear, which was used in the majority of experiments. The right ear is mirror-symmetric.

1.3.2 Physiology

Hair cell electrical responses to sound

The auditory nerve fibers that innervate the tectorial region of the cochlea have best frequencies ranging from 200 to 800 Hz (Weiss et al., 1976). The sharpness of tuning (Q_{10dB}) of these fibers ranges from about 1 to 4, which is roughly comparable to those of mammalian auditory nerve fibers with the same best frequencies. The responses of neurons innervating this region of the cochlea can be supressed by the presentation of another tone, a phenomenon called two-tone suppression (Holton and Weiss, 1978).

The auditory nerve fibers that innervate the free-standing region of the cochlea have best frequencies ranging from 1 kHz at the apical end to 4 kHz at the basal end (Weiss et al., 1976). The receptor potentials of hair cells in this region have best frequencies that match those of the neural responses (Holton and Weiss, 1983a), with Q_{10dB} values of 0.5–3. These neurons and hair cells are not as sharply tuned as either the hair cells in the tectorial region or mammalian hair cells with similar best frequencies.

Macromechanical responses to sound

The alligator lizard outer ear consists of a short ear canal leading to the tympanic membrane. The middle ear contains one bone, the columella, attached to the tympanic membrane by the cartilaginous extracolumella (Wever, 1978; Rosowski et al., 1985). The footplate of the columella creates a pressure difference across the cochlea, causing the basilar membrane to move in the transverse direction (towards/away from the stapes). As it does for other species, the middle ear of alligator lizard serves to couple airborne sound vibrations to fluid vibrations in the cochlea. At the same time, it provides a certain amount of pressure gain. The pressure gain of the middle ear of alligator lizard has not been measured directly. However, Rosowski *et al* (1985) have measured the macromechanical transfer function relating velocity of the basilar membrane to pressure at the tympanic membrane. In addition, the same authors present estimates of the acoustic impedance and effective area of the basilar

membrane as

$$\begin{aligned} Z_{BM} &= 290 + \tfrac{1260}{1+j\omega 7.182\times 10^{-4}}\ \mathrm{Pa\cdot s\cdot mm^{-3}}, \\ A_{BM} &= 0.07\ \mathrm{mm^3}. \end{aligned} \tag{1.1}$$

From these values we can estimate the pressure gain of the alligator lizard middle ear, as shown in figure 1-5. This pressure gain is roughly comparable to that of the mammalian outer and middle ear complex (Rosowski et al., 1985; Rosowski, 1996). However, the response threshold of auditory-nerve fibers is about 20 dB higher (Weiss et al., 1976), suggesting that the inner ear of alligator lizard is less sensitive than those of mammals.

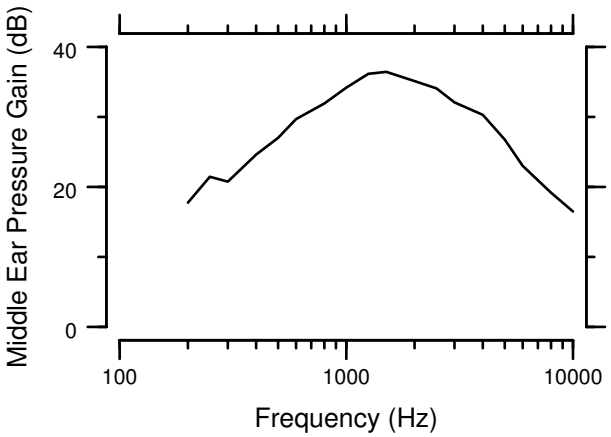

Figure 1-5: The estimated pressure gain of the alligator lizard middle ear. The pressure gain is between 20 and 40 dB over the range of frequencies to which the alligator lizard is sensitive. This curve was derived from a measured macromechanical transfer function (Rosowski et al., 1985, figure 9) plotting the ratio of basilar membrane velocity to tympanic membrane pressure.

In response to acoustic stimulation, the basilar membrane moves in phase along its length (Peake and Ling, 1980), with a frequency response similar to that of the middle ear. This motion causes the papilla to rock about its longitudinal axis (Frishkopf and DeRosier, 1983; Holton and Hudspeth, 1983; see also chapter 4). Both middle-ear and basilar membrane responses to sound are linear.

1.3.3 Previous studies of micromechanics in the cochlea of the alligator lizard

The first measurements of sound-induced motion of hair bundles were performed in the free-standing region of the alligator lizard cochlea (Frishkopf and DeRosier, 1983; Holton and Hudspeth, 1983). Both studies demonstrate two features of free-standing hair bundles:

1. the motion of hair bundles depends on frequency;

2. this frequency dependence varies with hair bundle height.

In addition, both studies report that the predominant motion of the basilar papilla is rocking about the longitudinal axis, and that the motion of the basal (high-frequency) end of the papilla increases for frequencies above 3 kHz.

These studies lend some support to hypotheses (Weiss, Peake, Ling and Holton, 1978) that the frequency of maximum hair bundle rotation is inversely dependent on hair bundle height. However, neither study provides sufficient information to characterize this dependence quantitatively. Frishkopf and DeRosier report only the relative phase of motion of the tip and base of the bundle. Figure 1-6 shows the data measured in their study. These measurements clearly demonstrate that hair bundle motion varies with frequency and bundle height. Without information about the relative amplitudes of motion, however, the relative phase is an ambiguous measure. For example, if the tip moves in phase with the base but with a magnitude 1.01 times as large, then rotation of the bundle is in phase with displacement of the base. If the magnitude of tip displacement is 0.99 times that of the base, however, rotation of the bundle is out of phase with displacement of the base, even though the tip and base still move in phase. Consequently, the phase of hair bundle deflection cannot be determined from their measurements. Although these phase measurements can be predicted by a model (Freeman and Weiss, 1990a), the measurements themselves are not sufficient to validate or refute the model predictions.

The study by Holton and Hudspeth provides measurements of both the magnitude and phase of hair bundle motion (figure 1-7). However, their paper presents

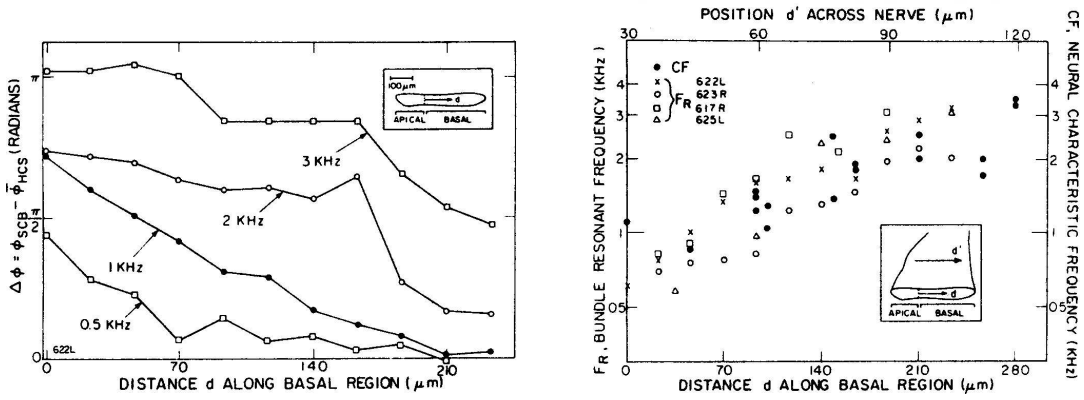

Figure 1-6: Measurements presented by Frishkopf and DeRosier, 1983. The left panel shows the measured phase of motion of the tips of several hair bundles relative to their respective bases at four frequencies. No measurements of the amplitude of motion were reported. The right panel shows the 'resonant frequency' of 33 hair bundles as a function of location; resonant frequency is estimated as the frequency at which the tip of the hair bundle lags the base by 1/4 cycle.

measurements of only two hair bundles at two frequencies. The measurements confirm that longer hair bundles are deflected more at lower frequencies, while shorter hair bundles are deflected more at higher frequencies. However, from the sparse data it is impossible to estimate a resonant frequency, much less to compare the sharpness of tuning to neural or intracellular recordings.

Studies in the turtle cochlea (Crawford and Fettiplace, 1985) demonstrate the presence of spontaneous mechanical oscillations of hair bundles. The frequency of oscillation is correlated to the acoustic frequency to which the hair cell is most sensitive. Frequency selectivity in the turtle cochlea is based on an electrical resonance between Ca^{+2} and K^{+} channels (Fettiplace and Fuchs, 1999). Since the frequency of spontaneous oscillation of hair bundles depends on Ca^{+2} concentration, which in turn varies with hair bundle deflection, the electrical and mechanical resonances are correlated. The term "bidirectional transduction" has been coined to describe such a relation (Weiss, 1982).

Although there is little direct evidence of electrical tuning in lizard cochlear hair cells, there is a significant amount of anecdotal evidence to suggest that hair cells in the tectorial region are electrically tuned (Manley, 2000b; Manley, 2000a). Lizards and

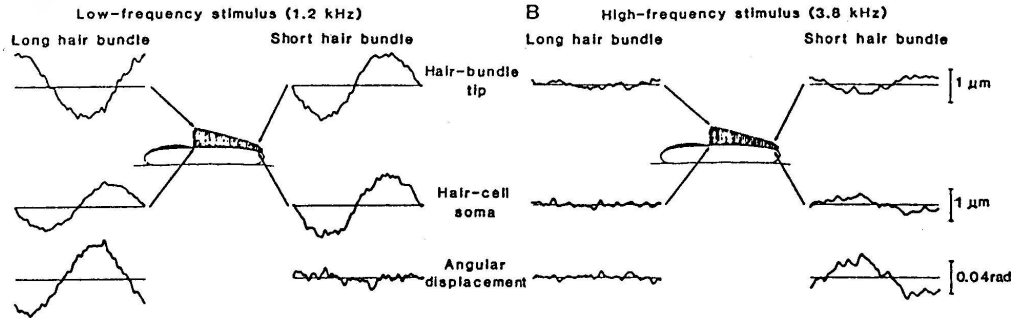

Figure 1-7: Measurements presented by Holton and Hudspeth, 1983. The left panel shows the motion of both the base and tip of one short and one tall hair bundle in response to a 1.2 kHz tone. For the tall hair bundle, the tip moves more than the base, and lags the motion of the base by about 1/4 cycle, resulting in an angular deflection of the hair bundle. For the short hair bundle, the tip and base displacements are similar in magnitude and phase, and the hair bundle is not detectably deflected. The right panel shows the motion of the same bundles in response to a 3.8 kHz tone. Motion of the tall hair bundle is obscured by noise. The tip and base of the short hair bundle move with a similar magnitude but opposite phase, resulting in an angular deflection of the hair bundle.

turtles are closely related phylogenetically, and the apical[§] regions of lizard cochleae are anatomically similar to turtle cochleae, suggesting that they function similarly. Second, auditory nerve fibers innervating the apical regions of lizard cochleae are sharply frequency selective, consistent with the sharp electrical tuning of both hair cells and auditory nerve fibers of the turtle cochlea. This sharp tuning is inconsistent with the broad tuning of hair cells and auditory nerve fibers of the basal regions of lizard cochleae, which are believed to be mechanically tuned. Third, isolated hair cells from basal regions of the alligator lizard cochlea are electrically resonant with best frequencies below 1 kHz (Eatock et al., 1993). These best frequencies are too low to explain frequency selectivity in the basal region; however, this result demonstrates that hair cells can be electrically tuned at the best frequencies of hair cells in the apical region. Thus the alligator lizard cochlea appears to have two mechanisms of frequency selectivity — electrical resonance of hair cells in the tectorial region for frequencies

[§]In many lizards, all hair cells are covered by a tectorial structure, so we cannot refer to this region as the "tectorial" region.

below 1 kHz, and mechanical resonance of hair bundles in the free-standing region for frequencies above 1 kHz.

1.3.4 Previous models of alligator lizard micromechanics

The literature on models of mammalian micromechanics is extensive, and once again we refer the reader to recent reviews (Hubbard and Mountain, 1996; deBoer, 1996). The micromechanical properties of the alligator lizard cochlea were first modeled quantitatively by Weiss and Leong, as part of an effort to model the entire peripheral auditory pathway of alligator lizard (Weiss et al., 1985; Rosowski et al., 1985; Weiss and Leong, 1985a; Weiss and Leong, 1985b). In this model, the rotational stiffness of a hair bundle interacts with the viscosity and inertia of the surrounding fluid to form a resonant rotational system. This model provides good fits to tuning curves measured from hair cells and auditory nerve fibers, but only with the addition of a first-order low-pass filter to the model. The authors were careful to point out that this low-pass filter occurs before the transduction nonlinearity, since it affects the DC receptor potentials of hair cells, and thus is of mechanical origin. However, they were unable to pinpoint the origin of this filter. Freeman and Weiss (1990a-d) extended the free-standing hair bundle model to two dimensions, incorporating more accurate models of the mechanical properties of the fluid. These improvements give more accurate fits to electrical responses, but the additional low-pass filter is still necessary. A three-dimensional model (Shatz, 1996) shows that for a given height, the resonant frequency of a hair bundle depends in a complex manner upon the shape of the bundle. However, this model lacks a closed-form solution, so detailed comparisons of the model to measured hair cell electrical responses have not been reported. Although all models make similar predictions about the nature of hair bundle motion, at arbitrarily low frequencies the Shatz model predicts that hair bundle sensitivity is proportional to the cube of bundle height, as opposed to the square of bundle height in the Freeman and Weiss model. The experimental support for these models is limited to the results of the Frishkopf/DeRosier and Holton/Hudspeth studies. One goal of this thesis project was to provide quantitative data to test these models more thoroughly.

1.4 Organization of this document

Each chapter of this thesis has been written as draft of a paper for publication, and thus is intended to stand alone[¶]. For this reason there is some overlap of information in the methods sections. Where there is overlap, one chapter provides detailed information while the others provide brief descriptions. Chapter 2 describes the isolated cochlea preparation, and presents the results of attempts to reduce the 'blebbing' of hair cells in this preparation. Chapter 3 describes the computer microvision system for measuring motions of cochlear structures in three dimensions. Chapter 4 demonstrates the presence of two modes of motion of the basilar papilla, and describes how two-mode motion contributes to the sensitivity of the cochlea. Chapter 5 shows that the hair bundles and the TM in the tectorial region exhibit no micromechanical frequency selectivity. Chapter 6 presents the frequency dependence of motion of free-standing hair bundles, and compares these measurements to the predictions of the Freeman and Weiss model. Taken together, these chapters provide the most complete characterization of cochlear mechanics — both macro- and micro-mechanics — in any vertebrate species to date.

[¶]In retrospect, some of these chapters might be better off as multiple publications.

Chapter 2

Manipulations Affecting the Physiological State of an *in vitro* Cochlea Preparation

Abstract

We have developed a preparation of the isolated alligator lizard cochlea for studying cochlear mechanics. This preparation provides high-resolution visualization of the tissue and control over the fluid environment. These same features allow us to study the coordinated anatomical and physiological changes induced by the mechanical trauma of isolating the cochlea, and to investigate mechanisms by which these changes occur. The first visible response to isolation of the organ was the formation of blebs, evaginations of the cell membrane, on hair cells of the tectorial region. When the cochlea was bathed in a perilymph-like solution (AP), the blebs grew quickly with time. When the cochlea was bathed with an endolymph-like solution (AE) apically with AP basally, blebs grew more slowly and often shrank. During bleb growth, hair cells maintained a constant pH as judged by BCECF fluorescence in response to an acid load/unload challenge. Blebbing hair cells initially took up FM1-43 perfused apically, but later did not. Bleb growth was stopped by perfusion of media with im-

permeant cations or anions. Perfusion of cytochalasin D or addition of 1 mM Gd^{+3} to the apical bath also stopped blebbing, although blocking transduction channels with gentamicin or removal of Ca^{+2} did not. However, removal of Ca^{+2} during dissection prevented blebbing, even after subsequent addition of Ca^{+2} to the bath. Addition of 100 μM PPADS, a selective blocker of P2 receptor channels, to the apical bath dramatically slowed the rate of blebbing. These results are consistent with the hypothesis that mechanical overstimulation causes excess ion entry through transduction channels, initiating hair cell damage. Damaged or dead hair cells presumably release ATP, which opens endolymphatic P2X receptors that allow cations to flow into hair cells. The resulting net solute influx causes a volume increase, which leads to blebbing.

Key words: Hearing, cochlea, basilar papilla, hair cell, acoustic trauma, hearing loss, bleb, alligator lizard.

2.1 Introduction

Studies of hair cell function often require the isolation of hair cells or hair cell organs. Because hair cells are remarkably sensitive to mechanical stimuli, they are easily damaged by the isolation process. This damage leads to both anatomical and physiological changes, similar to those seen in noise-induced hearing loss (Saunders et al., 1985; Schmiedt, 1984). To maintain an isolated hair cell organ *in vitro* for extended periods of time, it is important to minimize the extent of trauma caused by isolation.

One common visible symptom of trauma is the formation of blebs on the apical surfaces of hair cells (Robertson et al., 1980; Tilney et al., 1982; Thorne et al., 1986; Liberman, 1994). Blebbing is a component of the response to traumatic stimuli causing both temporary and permanent shifts in hearing threshold, and is commonly seen *in vitro*. Under certain conditions, the blebs that form in response to trauma can shrink so that hair cells recover their normal appearance (Tilney et al., 1982). However, the mechanisms underlying this recovery are unknown. We have developed

an *in vitro* preparation which develops blebs on some hair cells upon isolation. By measuring the rate at which blebs grow and shrink in various fluid environments, we hope to develop a better understanding of the process of blebbing, which is a component of hair cell trauma under many different conditions.

The preparation is based on the cochlea of alligator lizard (*Gerrhonotus multicarinatus*). This cochlea is planar and easily accessible, so it can be isolated and observed *in vitro* while maintaining the epithelial separation of fluids that is critical for cochlear function. Isolating the cochlea induced trauma, presumably due to the large mechanical forces involved. In this paper, we provide quantitative measurements of anatomical and physiological changes to hair cells in response to isolation-induced trauma. We show that blebbing, which is induced by trauma, is associated with ion entry through apical P2X channels. We also demonstrate the recovery of hair cells from blebbing, and show that this recovery is critically dependent on the composition of the apical fluid. A preliminary analysis of some of these results was presented previously (Aranyosi and Freeman, 1999).

2.2 Methods

2.2.1 *In vitro* preparation

Adult alligator lizards were sacrificed by decapitation and pithing. The tissue over the dorsal surface of the skull was removed. A scalpel blade was used to penetrate the posterior semicircular canal and remove the thin bone covering the saccule. The head was submerged in the initial bathing medium to be used, typically artificial perilymph (AP). The membranes covering the saccular otoconia were peeled away with fine forceps, and the otoconia were removed by gentle suction. The eighth nerve was cut with a razor blade shard. The cochlear duct was then lifted out by the nerve with a pair of hydraulically-actuated forceps mounted on a 4-axis micromanipulator. A small cup was positioned under the duct to keep the tissue surrounded by fluid as it was transferred to the experiment chamber. The duct was clamped in the

experiment chamber so the basilar membrane sat over a hole separating two fluid spaces. Clamping the duct occasionally caused otoconia to squirt from the lagena onto the cochlear duct. Cutting a small hole into the vestibular membrane above the lagena before clamping eliminated this problem. Except in experiments involving NMDG or gluconate, both fluid spaces in the experiment chamber initially contained AP. Before removing the vestibular membrane, artificial endolymph (AE) was perfused into the apical fluid space. The vestibular memebrane was then removed with fine forceps. The entire process took roughly 30 minutes.

2.2.2 Experiment chamber

The experiment chamber (figure 4-1, described in more detail in chapter 4) contained two fluid spaces separated by a small hole. The cochlear duct was clamped over the hole by a plastic ring. This ring encircled the neural and triangular limbi to avoid direct contact with the mechanically sensitive cochlear structures. The apical fluid space was typically perfused with AE, and the basal fluid space was typically perfused with AP. In some experiments the media were perfused continuously. In experiments in which motion measurements were made, the media were perfused between measurements, typically every 5–10 minutes. The chamber was designed to allow acoustic stimulation, microscopic observation, and measurement of electrical activity using voltage- or current-clamp techniques.

2.2.3 Bathing media

For most experiments, the media used were an artificial perilymph (AP) as the basal fluid and an artificial endolymph (AE) as the apical fluid. Artificial perilymph contained (in mM): Na^{+}, 168; K^{+}, 3; Ca^{+2}, 2; Mg^{+2}, 1.2; Cl^{-}, 174.9; SO_4^{-2}, 2; $H_2PO_4^{-}$, 0.5; D-glucose, 5; Hepes, 5. Artificial endolymph contained (in mM): Na^{+}, 2; K^{+}, 174; Ca^{+2}, 0.02; Cl^{-}, 171.5; SO_4^{-2}, 2; $H_2PO_4^{-}$, 0.5; D-glucose, 5; Hepes, 5. Both solutions contained MEM essential and non-essential amino acids, and were oxygenated immediately before use. The solutions were adjusted to a pH of 7.30 and an osmo-

lality of 342±8 mmol/kg. In some experiments Liebowitz' L-15 was used in place of AP. The standard AP recipe was modified for some experiments. These modifications will be discussed in the relevant sections. All chemicals were purchased from Sigma Chemical Company (St. Louis, MO), except for FM1-43 and BCECF from Molecular Probes (Eugene, OR).

2.2.4 Video microscopy

The cochlea was imaged through a 63x, 0.9 NA water-immersion objective (Zeiss, Oberkochen, Germany) using transmitted light Köhler illumination. Köhler illumination minimizes the depth of focus of the microscope system, allowing us to take optical sections by changing the focus of the microscope. Images were collected using a scientific grade 12-bit CCD camera (CA-D7-1024A, Dalsa, Waterloo, Ontario) with 1024×1024 pixels and stored on an IBM-PC compatible computer running custom software written for the Linux operating system. In early experiments a 40x, 0.75 NA water-immersion objective and a 384×576 pixel camera (200 Series, Photometrics Inc., Tucson, AZ) were used. The microscope focus was adjusted with a piezoelectric focusing device (PIFoc P-721, Physik Instrumente, Waldbronn, Germany). For brightfield images, the light source was a green light-emitting diode (Nichia, Tokushima, Japan). For fluorescence images, the light source was a tungsten bulb used with a fluorescein filter set.

2.2.5 pH measurement

In some experiments we measured the pH of hair cells as they were subjected to an acid load and washout. The cochlea was bathed in AP, and hair cells were loaded with BCECF-AM, a pH-sensitive fluorescent dye. The ratio of BCECF fluorescence emission in response to 450 and 490 nm excitation varies with intracellular pH (Paradiso et al., 1984). Light from a tungsten bulb was passed through one of two narrowband filters and reflected off a dichroic mirror to illuminate the cochlea. A computer-controlled filter wheel (Ludl Electronic Products, Hawthorne, NY) was used to switch

between narrowband filters centered at 450 and 490 nm wavelengths. Fluorescence emmisions passed through the dichroic mirror and a long-pass filter (520 nm cutoff) to the camera. The acid load was applied by adding Na^+-proprionate to the extracellular medium. Proprionate$^-$ associates weakly with H^+, and in its uncharged form can enter the cell. After entering the cell it tends to dissociate, releasing H^+ to acidify the cell. Washing out the extracellular proprionate reverses this process, raising the intracellular pH.

At the end of the experiment, the cochlea was bathed in a high-K^+ medium containing the K^+/H^+ exchanger nigericin. If the K^+ concentration is the same in the cells and the bath, then nigericin equilibrates the H^+ concentration; that is, nigericin clamps the intracellular pH to that of the bath. Imaging BCECF fluorescence at known pH values provides calibration points for determining pH from the fluorescence images. The pH of the high-K^+ medium was adjusted sequentially to 6.6, 6.9, 7.2, 7.5, and 7.8 to provide five calibration points for relating the fluorescence emission ratio to intracellular pH. This calibration method assumes that the high-K^+ medium zeroes the transmembrane potential. Because the hair cells most likely had a high intracellular Na^+ concentration during these experiments (see discussion), the pH calibrations were probably inaccurate.

2.3 Results

2.3.1 Initial extent of damage

The alligator lizard cochlea has two regions: a tectorial (TM) region, in which hair bundles are less than 10 μm tall and covered by a tectorial membrane, and a free-standing (FS) region in which hair bundles range from 12–30 μm and have no overlying tectorial structure. Upon isolation of the cochlea, all hair cells of the TM region typically had blebs, but hair cells of the FS region did not. Cells lining the basilar membrane had a pillow-like appearance, thicker than their appearance in fixed tissue slices. In the best preparations, the blebs were barely visible, and the hair bundles of

the FS region were fully intact and organized. In the worst preparations, the blebs were larger than hair bundles, and the hair bundles of the FS region were mostly missing or disarrayed.

Figure 2-1 shows the typical appearance of blebs in the alligator lizard cochlea tectorial region. Blebs were roughly spherical, and emerged from the apical surface of the hair cell near the kinociliary rootlet. Typically each cell developed a single bleb, although we have seen multiple blebs on a single cell in some preparations that had severely deteriorated. In the preparation shown in figure 2-1, blebs were roughly the size of hair bundles, and were present only in the tectorial region. Figure 2-2 shows the same cochlea after having AP perfused across both basal and apical surfaces for three hours. After this time the blebs were much larger and were visible in the free-standing region as well as the tectorial region. In addition, the tissue as a whole was more swollen.

Blebs usually remained attached to their hair cells; we have seen only one case of a bleb detaching (figure 2-9) when the cells were bathed in a high-K^+ medium for calibrating pH. Although blebs often grew to be quite large, they did not rupture even in severely degraded preparations.

2.3.2 Progression of trauma

AP apically

When the apical fluid space contained artificial perilymph (AP), blebs formed quickly and grew with time. Blebs were initially smaller than adjacent hair bundles, but grew over time to reach a maximum size. The blebs often became larger than the rest of the cell; blebs from adjacent cells typically contacted one another. Larger blebs often caused static deflections of hair bundles in the inhibitory direction. Figure 2-3 shows the growth of six blebs with time, measured as the maximum cross-sectional diameter, for one cochlea bathed in AP. When bleb growth was fit with an exponential curve of the form $A(1 - e^{-\frac{t}{\tau}})$, the time constant for the increase in diameter was 6.2 ± 4 min (n=6 blebs). These measurements were from one preparation in which bleb

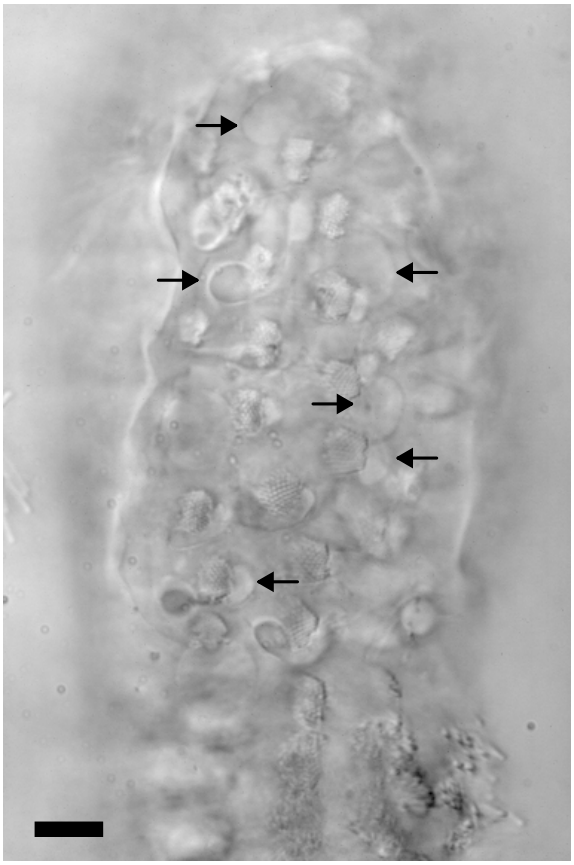

Figure 2-1: Appearance of blebs in the alligator lizard cochlea tectorial region. Blebs are visible as circles on the kinociliary side of each hair bundle. Arrows point to some of the blebs. In this image, the blebs are roughly the same size as the hair bundles. No blebs are visible in the free-standing region at the bottom of the image. This image was taken immediately following surgical dissection of the cochlea.

growth was initially inhibited by NMDG-Cl. *N*-methyl-D-glucamine (NMDG) is a large (molecular weight 195.2) weak acid which in its charged form can act as a cell-impermeant replacement for Na^+. Bleb growth was observed in more than twenty preparations in which the cochlea was bathed in AP. The rate of growth and final size of blebs in these preparations were similar to those shown in figure 2-3.

AE apically

Cochlear hair cells normally have their apical surfaces exposed to an endolymphatic solution. In 6 of 14 preparations, perfusion of AE apically caused existing blebs to shrink (figure 2-4, left side). The diameter of blebs decreased linearly with time, at

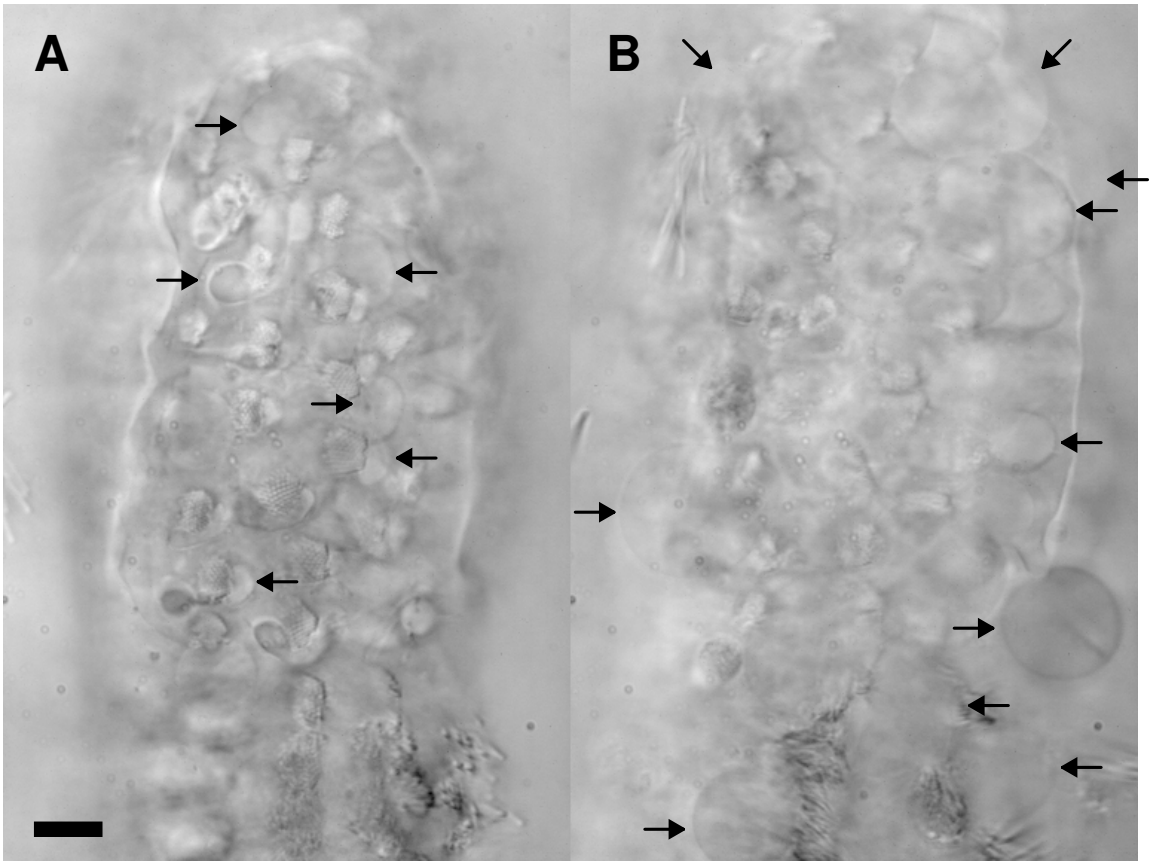

Figure 2-2: Images of bleb growth. (A) The image from figure 2-1. (B) An image of the same tissue, after three hours in an AP medium. The blebs have grown larger, and the tissue as a whole is more swollen. Blebs have also appeared in the free-standing region at the bottom of the image.

a rate of 4.8 ± 1.2 μm/hr (n=9). These preparations were subsequently maintained bleb-free for more than an hour. In 7 of 14 preparations in which AE was perfused apically, blebs grew with time (figure 2-4, right side). The growth rate with AE apically was much slower than with AP apically, with a time constant of 41 ± 36 min (n=18). The maximum bleb size was similar to that in AP. In one preparation with AE apically, no blebs formed.

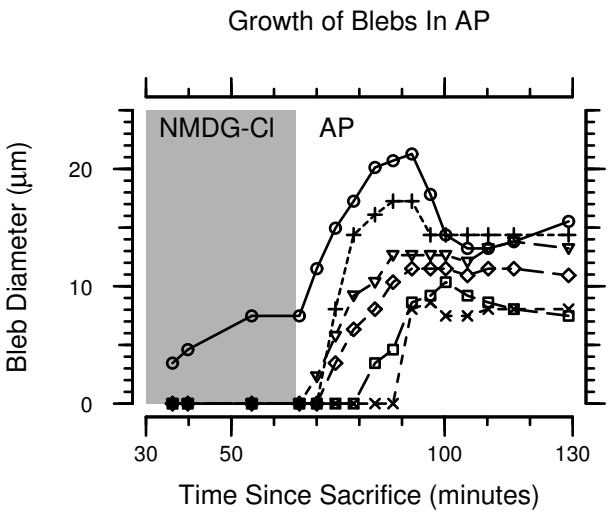

Figure 2-3: Bleb size vs. time in AP. Different symbols represent different blebs from the same preparation. Bleb size was measured as the maximum diameter of the bleb at a single focal plane. Because the blebs grew in the axial direction of the microscope, the focal plane in which the bleb diameter was largest changed over time. Note that bleb growth was largely monotonic, except for the two largest blebs, and that blebs reached a maximum size. These measurements were from one preparation in which bleb growth was initially inhibited by NMDG-Cl (section 2.3.3). Bleb growth in other preparations was similar.

2.3.3 Manipulations affecting the progression of trauma

Removing permeant ions stopped bleb growth

N-methyl-D-glucamine ($NMDG^+$) is an ion to which hair cells are at most weakly permeant (Housley and Ashmore, 1992; Mroz and Lechene, 1993). Replacement of Na^+ with $NMDG^+$ in AP thus makes the dominant cation in the medium impermeant. Such replacement prevented bleb growth in six preparations (see the beginning of figure 2-3). However, after about an hour in this medium the tissue somtimes took on a mushy appearance and lost its integrity. Replacing Cl^- with gluconate blocked blebs in one preparation, but impaired the function of our Ag/AgCl electrodes. Subsequently NMDG or gluconate lymph with AP led to the continued growth of blebs (figure 2-3). Tamoxifen, a blocker of the CLC-3 chloride channel (Duan et al., 1997; Yamazaki et al., 1998) which prevents cell swelling in the isolated mammalian cochlea (Zeddies et al., 2000; Siegel et al., 2001), did not prevent blebbing in this preparation.

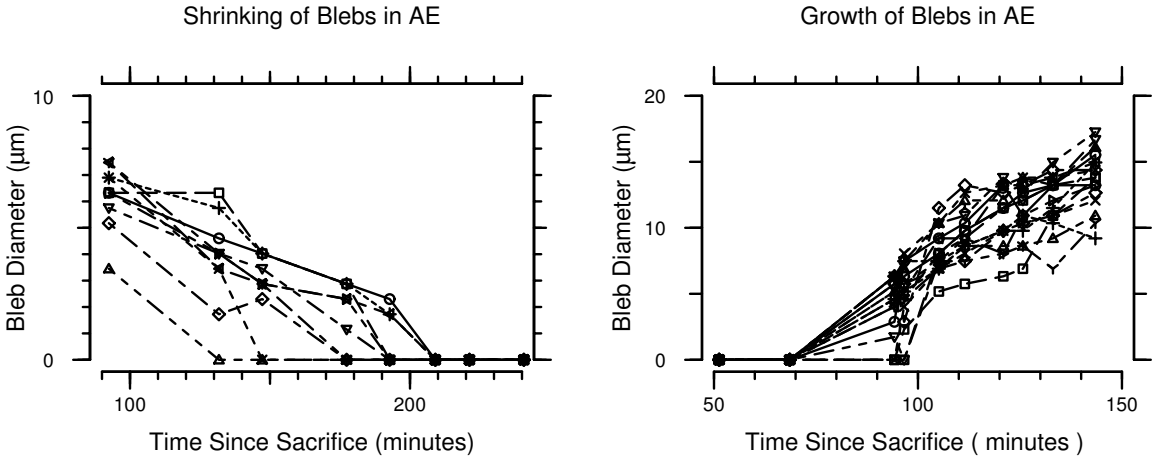

Figure 2-4: Bleb size vs. time with AE apically. On the left, nine blebs that were initially present shrank when AE was perfused apically, and ultimately could no longer be seen. The blebs shrank at an average rate of 4.8 μm/hr. On the right, a preparation that was initially bleb-free developed blebs with AE apically. Bleb growth for the 18 blebs shown had an average time constant of 41 min.

Gd^{+3} apically blocked bleb growth

Gd^{+3} blocks a variety of stretch-sensitive channels (Yang and Sachs, 1989; Franco and Lansman, 1990; Zhou et al., 1991; Ruknudin et al., 1993), including the hair cell transduction channel (Kimitsuki et al., 1996), and also blocks ATP-gated channels such as the P2X receptor (Nakazawa et al., 1997). The addition of 1 mM Gd^{+3} to the apical medium in five preparations blocked bleb growth, and caused existing blebs to disappear. However, Gd^{+3} also destroyed the tectorial membrane (figure 2-5; Wei and Freeman, unpublished obesrvations). Washing out the Gd^{+3} medium allowed blebs to grow again (figure 2-6). In contrast, addition to AP of 760 μM gentamicin, which blocks transduction channels (Kroese et al., 1989), had no effect on bleb growth.

PPADS greatly slowed bleb growth

Pyridoxal phosphate-6-azophenyl-2',4'-disulfonic acid (PPADS) is a selective P2 receptor channel blocker (Lambrecht et al., 1992) which blocks ATP-gated currents in hair cells (Chen et al., 1998; Housley et al., 1998). After dissection in AP, one cochlea was bathed with AP basally and AE plus 100 μM PPADS apically. Figure 2-7 (A) shows an image of the tectorial region of this cochlea after having AE+PPADS

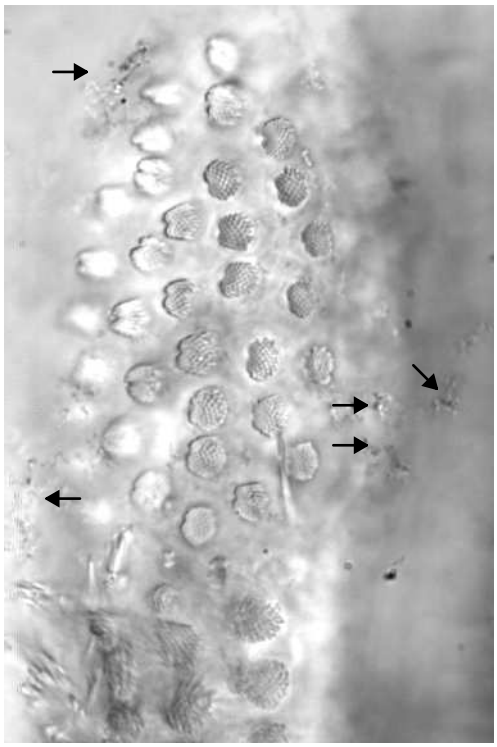

Figure 2-5: A cochlea dissected in AP supplemented with 1 mM Gd^{+3}. No blebs developed in this cochlea. This image is of the tectorial region; the Gd^{+3} had the additional effect of dissolving the TM into stringy material (arrows).

apically for about 25 minutes. Because brightness variations due to out-of-focus structures obscure some details of this image, figure 2-7 (B) shows the same image with a local normalization applied*. Small blebs, roughly 8 μm in diameter, were present on each hair cell. Images (C) and (D) were normalized using the same procedure. The image in (C) was taken after the papilla was bathed with AE+PPADS apically for an additional five hours. The blebs were about 50% larger, and the cell bodies appeared slightly swollen. Five minutes after image (C) was taken, the apical AE+PPADS bath was replaced with AE. Image (D) was taken 15 minutes after this replacement. Blebs in image (D) were significantly larger than in image (C). Although not readily apparent in this plane of focus, the cell bodies were also more swollen in (D). The increase in bleb size during the 15 minutes between images (C) and (D) was nearly as large as the increase in bleb size during the 5 hours between images (B) and (C).

*Normalization was applied by dividing the grey value of each pixel in the image by the average grey value of a 50×50 pixel region centered on the pixel.

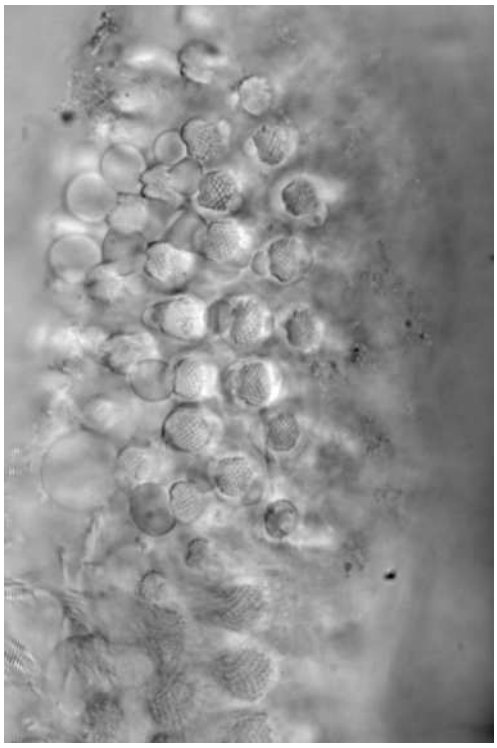

Figure 2-6: The same cochlea as in figure 2-5, 30 minutes after Gd^{+3} had been removed. Blebs are clearly visible on all hair cells of the tectorial region.

Removal of Ca^{+2} or addition of cytochalasin D during surgery prevented bleb formation

Dissection in a Ca^{+2}-free medium with 10 mM EGTA prevented the growth of blebs in two of six preparations, even if Ca^{+2} was subsequently added. However, removal of Ca^{+2} after dissection in $NMDG^{+}$ medium containing Ca^{+2} did not prevent bleb growth. Perfusion of AP with 100 μM rather than 2 mM Ca^{+2} did not prevent bleb growth. Addition of 1.3 μM cytochalasin D, an actin-depolymerizing agent, to the bathing medium during dissection in one preparation also prevented the formation of blebs, even after subsequent removal of cytochalasin D.

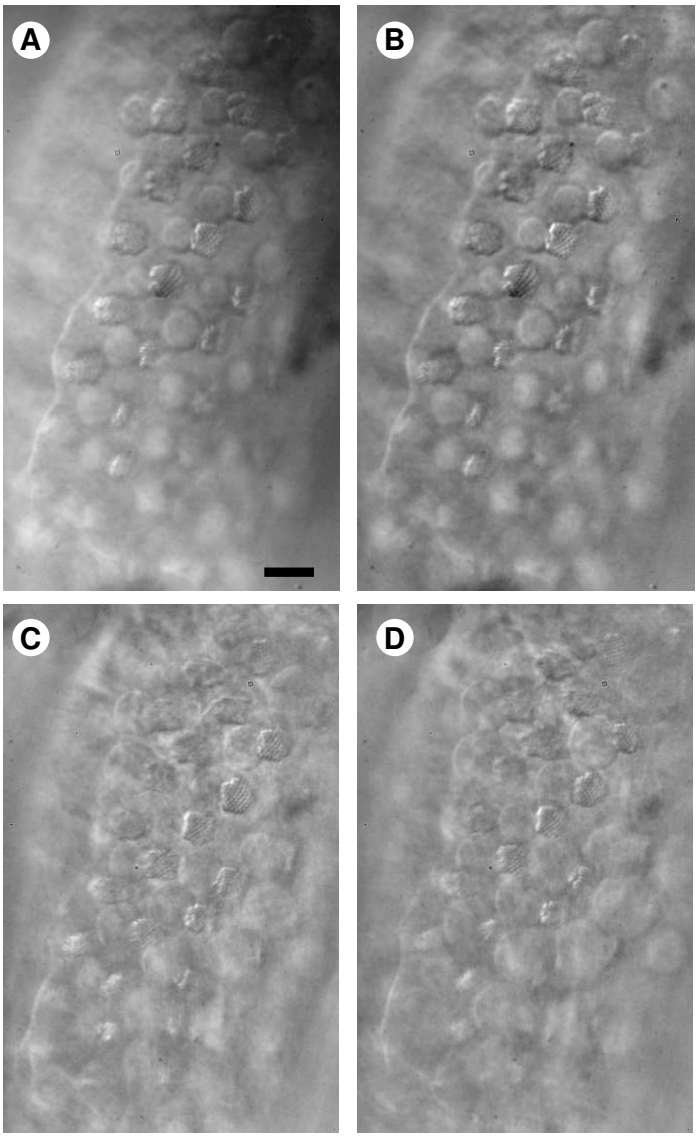

Figure 2-7: A cochlea in a PPADS-containing medium. (A) An image of the cochlea shortly after dissection. The cochlea has been bathed with AE+PPADS (100 μM) apically and AP basally for about 25 minutes. Small blebs are visible on all hair cells. (B) The same image as in (A), with a local normalization applied. (C) An image at roughly the same focal plane, taken after an additional five hours with AE+PPADS apically. Bleb diameter has increased by about 50%. (D) An image taken 20 minutes later, 15 minutes after washout of PPADS. Bleb diameter has increased by about 25% as compared to (C). Scale bar = 10 μm.

Summary of manipulations that affect bleb growth

Manipulation	*Effect on Blebbing*
Perfuse AP apically and basally	Blebs grow
Perfuse AE apically, AP basally	Blebs shrink or grow more slowly
Perfuse NMDG lymph apically and basally	Bleb growth stops
Replace NMDG lymph with AP	Bleb growth resumes
Add 1 mM Gd^{+3} to apical AE	Bleb growth stops, blebs disappear
Remove Gd^{+3} from apical AE	Bleb growth resumes
Add 100 μM PPADS to apical AE	Bleb growth nearly stops
Remove PPADS	Bleb growth resumes
Add 1.3 μM Cytochalasin D during dissection	No blebs formed

2.3.4 Physiological measures of hair cell function

Cochlear microphonic potential

No electrical response to acoustic stimulation was detected when the epithelium was voltage-clamped. Attempts to measure intracellular responses to acoustic stimulation were made in four preparations[†]. No responses to acoustic stimulation were detected in 25 cells that were successfully penetrated. In three of the four preparations, the median resting potential of cells in the basilar papilla was −71 mV. In the fourth preparation, the median resting potential was −15 mV.

FM1-43 uptake

FM1-43 is a small fluorescent dye that is selectively taken up by hair cells when perfused over the apical surfaces of hair cells (Nishikawa and Sasaki, 1996; Gale et al., 2000). Adding FM1-43 to the apical bathing medium of the alligator lizard cochlea in two experiments caused the hair cells of the free-standing region to rapidly take up the dye. In one experiment, hair cells of the tectorial region did not take up the dye (figure 2-8, A and B). In this experiment, blebs on the tectorial hair cells were smaller than hair bundles before perfusing the dye, and were comparable in size to those of figure 2-2 after perfusing the dye and taking fluorescence pictures. In a second experiment, hair cells of the tectorial region took up the dye (figure 2-8, C and D). In this experiment, blebs on the tectorial hair cells were slightly larger than hair bundles before perfusing the dye and taking fluorescence images, and roughly the same size after.

Live/Dead assay

The dye BCECF-AM does not fluoresce until the AM group is cleaved by cellular esterase enzymes (Haugland, 1996). Therefore a significant increase in fluorescence after application of the dye is a sign of functional enzymatic activity. In addition, the ability of the cells to hold the dye indicates that cell membrane integrity is maintained.

[†]These measurements were done with the assistance of Quentin Davis and Pankaj Oberoi.

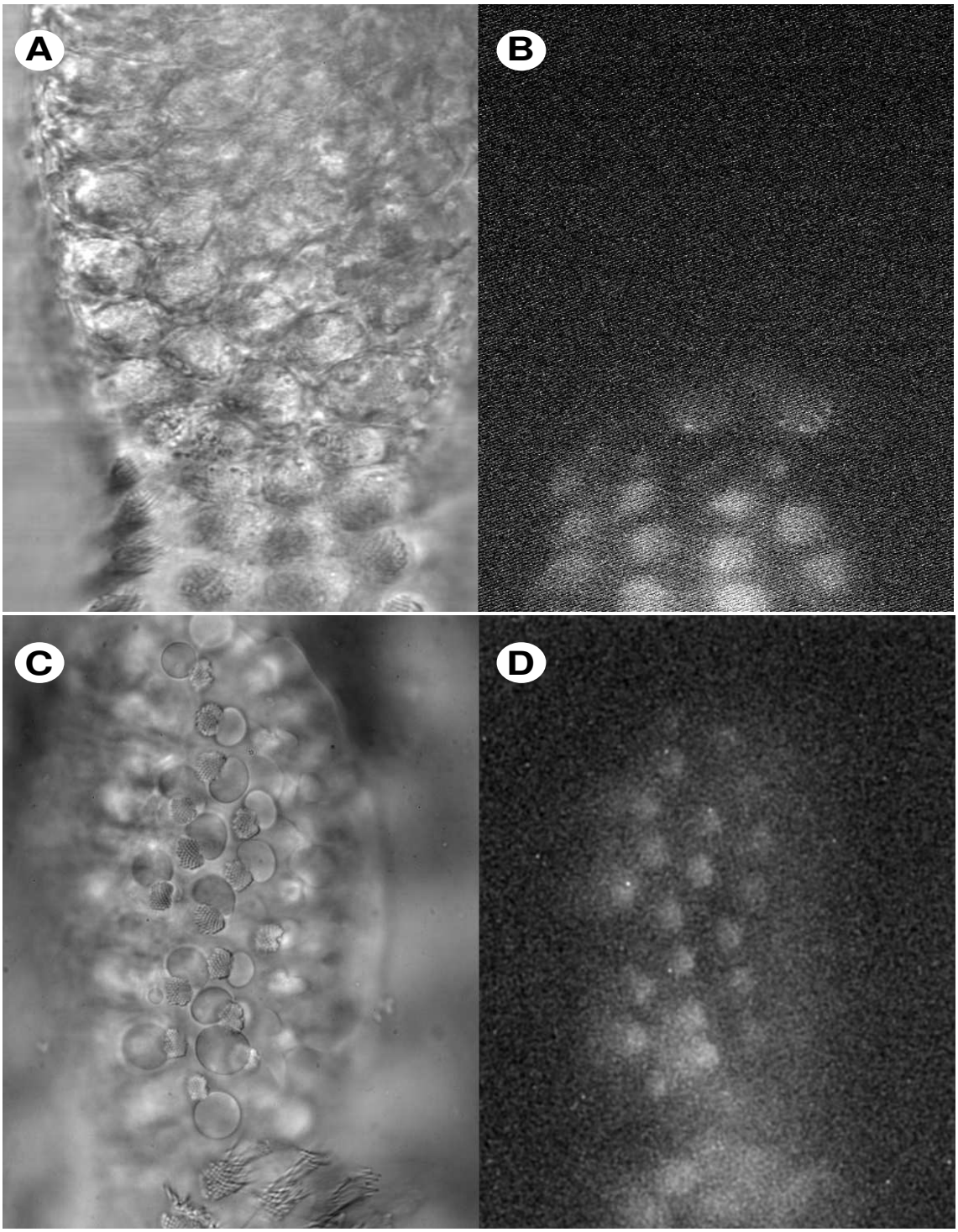

Figure 2-8: Uptake of FM1-43 by hair cells. A. Brightfield image of the cochlea. Although not visible in this plane, blebs were present on hair cells of the tectorial region, but not those of the free-standing region. B. Fluorescence image of the cochlea in A, after application of 5 μM FM1-43 for 1 minute. Free-standing hair cells fluoresced, but tectorial hair cells did not. C. Another cochlea, shortly after dissection. Bundle-sized blebs are visible in the tectorial region. D. Fluorescence image of the cochlea in C, after application of 5 μM FM1-43 for 1 minute. Both free-standing and tectorial hair cells fluoresced.

Figure 2-9 shows an image of an isolated alligator lizard cochlea loaded with BCECF-AM. All of the cells fluoresced, indicating the presence both of functioning enzymes and of an intact cell membrane. When the cells were loaded with fluorescent dye, the blebs fluoresced as well. The brightness of fluorescence, which varies with the concentration of dye, was comparable for apical and basal hair cells. Cells were able to maintain dye for several hours after loading.

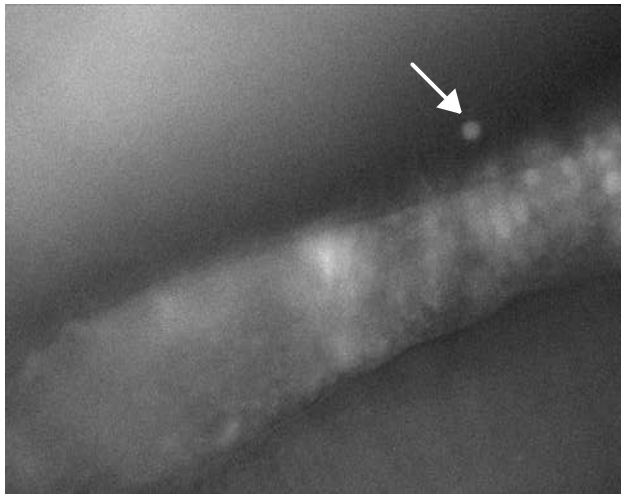

Figure 2-9: Fluorescence image of hair cells loaded with the AM ester of the fluorescent dye BCECF. The brightness of blebs was comparable to the brightness of their associated hair cell. However, the brightness of different hair cells varied significantly, depending on how much dye got into a particular cell. The arrow shows one bleb which had detached from its hair cell. This picture was taken at the end of a pH experiment, when the cochlea was bathed in a high-K^+ medium.

pH regulation

The presence of blebs suggests that the homeostatic mechanisms of the cells have been compromised. To determine whether these cells had suffered a general failure of homeostasis, we measured pH homeostasis in response to an acid load/unload challenge[‡]. Figure 2-10 shows the estimated pH of hair cells in the tectorial and free-standing regions in response to the addition and subsequent washout of 20 mM

[‡]These measurements were done in collaboration with Ed Mroz of the Eaton-Peabody Laboratory of Auditory Physiology.

proprionic acid. Addition of the acid caused a rapid drop in pH followed by a slow recovery. Washout caused a similar rise and recovery. Throughout the experiment the estimated pH of the tectorial hair cells was lower than that of the free-standing hair cells.

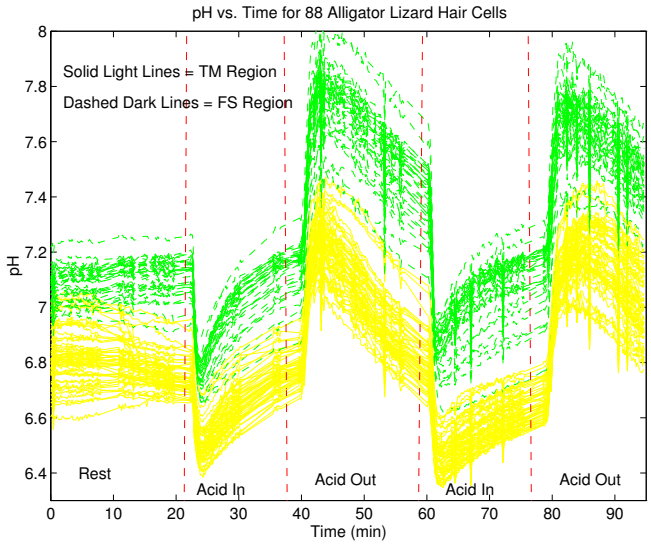

Figure 2-10: pH vs. time in response to an acid load/unload challenge. Lines show pH estimated from changes in BCECF fluorescence ratio for 88 hair cells in one preparation. Solid light grey lines are for hair cells in the tectorial region, dashed dark grey lines are for hair cells in the free-standing region. The extracellular medium contained 20 mM proprionate during the times labeled "acid in", and was removed during the times labeled "acid out". For both hair cell types, addition of proprionate causes a rapid decrease in pH followed by a slow recovery. Subsequent removal of proprionate causes a rapid increase followed by a slow recovery. This process was repeated with similar results. Throughout the experiment, the estimated pH of the tectorial hair cells was lower than that of the free-standing hair cells.

2.4 Discussion

2.4.1 Statistical significance

Because the main goal of this thesis was to study cochlear mechanics rather than to investigate blebbing, many of these experiments were performed only one or two times. Consequently, many of the results reported here are not statistically significant. However, we have dissected more than 100 alligator lizard cochleae over the years,

and seen blebs in the free-standing region in nearly every one; the exceptions occurred when we manipulated the bath, as described in the results section. For this reason, we suspect that the reductions or eliminations of blebbing reported in this chapter were the result of the manipulations we made, rather than being due to random variability. Despite the lack of statistical significance of some experiments, the results presented here allow us to draw several conclusions about the nature of blebbing, and to hypothesize a model for blebbing that is consistent with these measurements.

2.4.2 Hair cell blebbing is a reversible process

Based on *in vivo* studies, it has been surmised that hair cells that develop blebs eventually recover their normal appearance. However, the process by which the bleb disappears was unknown. By observing individual hair cells over time, we have shown that this process involves the shrinking of the bleb back into the cell. This shrinking often occurred when AE was perfused apically, but the presence of AE itself was not sufficient to cause shrinking of blebs. In a given preparation, the process was all-or-none: either all of the blebs shrank, or all of them continued to grow. Our experience suggests that the preparations which suffered the least amount of trauma during extraction were the most likely to recover, but because we could not quantify the extent of trauma, we can only make such a statement anecdotally.

Hair cells *in vivo* form part of an epithelium separating endolymph from perilymph. Maintaining a similar separation of fluids *in vitro*, with AE apically and AP basally, was necessary but not sufficient for reversal of blebbing. Endolymph and perilymph differ in both Na^+/K^+ content and in Ca^{+2} concentration. Manipulating Ca^{+2} concentration alone had no effect on blebbing. Thus the substitution of K^+ for Na^+ apically is most likely the critical factor that led to bleb reversal in these experiments. It has previously been suggested that the leakage of endolymph into the perilymphatic space around hair cells plays a role in hair cell damage due to acoustic trauma (Bohne, 1971; Bohne, 1976; Bohne and Rabbitt, 1983). Our results suggest that leakage of perilymph into the endolymphatic space may also play a role.

2.4.3 Ion entry through the apical surface is necessary for bleb growth

Several methods of blocking ion entry through the apical surfaces of hair cells prevented or reversed the growth of blebs. Replacement of either Na^+ or Cl^- with impermeant ions in the bathing medium stopped the growth of blebs. Addition of 1 mM Gd^{+3}, a blocker of many cation channels (including the transduction channel and P2X channels), to the apical medium stopped and reversed bleb growth. Blocking P2X receptors specifically by using PPADS in the apical bath slowed the rate of bleb growth; subsequently removing PPADS led to rapid bleb growth. However, blocking the transduction channel by adding gentamicin or removing Ca^{+2} had no effect on blebbing. These results show that entry of cations from the apical bath is necessary for bleb growth. The entry of cations most likely occurs in part through apical P2X receptors. These results did not reveal the pathway for anion entry.

P2X receptors are nonselective cation channels known to be on the apical surfaces of hair cells (Housley et al., 1995; Brändle et al., 1995; Housley et al., 1996). The channels are gated by extracellular ATP. Housley *et al* (1998) showed that the channels can provide a conductance of ∼20–25 nS across the apical membrane, roughly ten times larger than the conductance of the transduction apparatus. They proposed that the channels might be used to modulate the driving force for transduction, and thus affect the sensitivity of the cochlea.

Opening such a high-conductance cation channel can lead to equilibration of the intracellular medium with the apical bath. If both the intracellular space and the apical bath are high in K^+, equilibration will likely be rapid. However, if the two media are substantially different in ionic content, equilibration may involve an increase in cell volume. A volume increase can lead to an increase in membrane tension, which promotes exocytosis over endocytosis (Dai and Sheetz, 1995). Blebs then form near the kinociliary bulb, where endo- and exocytosis occur. Formation of blebs can allow such volume increases to occur without causing large changes in the shape or structure of the hair cell.

In our preparation, removing PPADS from the apical bath five hours after surgical dissection caused an increase in the rate of bleb growth. This result suggests that P2X channels were still open at this time. Since P2X channels are gated by ATP, it is likely that ATP was present in the fluid near the apical surface beneath the TM. No ATP was added to the fluid being perfused, so any ATP present must have come from the tissue. Due to the nature of the preparation, a large number of cells near the cochlea were damaged or lysed during dissection (e.g., the auditory nerve was cut, the vestibular membrane was torn open, several supporting cells outside the clamping ring were exposed to endolymph on all surfaces). In response to this damage, these cells most likely released ATP into the extracellular medium.

2.4.4 Blebbing hair cells have intact cell membranes and functioning enzymes

Commercially available cell-viability assays test for intact cell membranes (e.g. by adding an impermeant DNA-binding dye to the extracellular medium) and functional enzymatic activity (e.g. by adding a cell-permeant dye that fluoresces after an ester group is cleaved). By these criteria the hair cells in this preparation are viable. The cells cleaved the AM ester group from BCECF, making it fluorescent. In addition, the cells maintained the dye for several hours, indicating that the cell membrane was intact.

The hair cells in this study exhibited two other signs of viability. First, they were able to maintain their pH in the face of repeated acidification and alkalinization challenges. Second, under appropriate conditions they were able to recover from blebbing. However, the hair cells typically had blebs, and showed no measureable electrical response to sound stimulation. Thus although the cells exhibted some normal behavior, they were not completely normal.

Although both apical and basal hair cells regulated their pH, the measured resting pH values were so unphysiologically low that they are unlikely to be accurate. These low values are most likely artefactual due to excess intracellular Na^+. The pH

experiments were done with AP bathing both the apical and basal surfaces, so Na^+ entry through the apical surface was probably large. The pH calibration technique is based on the assumption that the intracellular medium is high in K^+. 'If the cells contain significant Na^+, the cells will have a positive resting potential when bathed in K^+ lymph for calibration. This positive potential will repel H^+ ions, causing the calibration curve to be shifted towards lower pH values. The lower measured pH for apical hair cells suggests that these cells may have contained more Na^+ than basal hair cells.

FM1-43 normally enters the hair cell either through endocytosis or through the transduction channel (MacDonald and Corey, 2001). Recent evidence suggests that the P2X receptors of hair cells also pass FM1-43 (Corey and MacDonald, unpublished). FM1-43 in the apical bath was taken up by tectorial hair cells in one experiment, but was not taken up in a second experiment. Given the number of pathways by which FM1-43 has been suggested to enter the cells, it is difficult to interpret these experiments in terms of a molecular mechanism. Nonetheless, FM1-43 uptake occurs normally in many other hair cell preparations. The inhibition of this uptake, which may be correlated with periods of bleb growth, is another indication of pathology.

With two notable exceptions (Fettiplace and Crawford, 1978; Russell et al., 1986), *in vitro* cochlear preparations have typically not exhibited electrical responses to sound[§]. In our preparation, no electrical response to sound could be detected, either in whole-organ voltage clamp or single-cell electrical recordings. However, the transmembrane potentials measured with intracellular electrodes were within the range of potentials measured *in vivo* (Weiss, Altmann and Mulroy, 1978). The mean potential of -71 mV is comparable to that of hair cells *in vivo*, -74 mV, and slightly depolarized compared to that of supporting cells, -97 mV. Assuming that at least some of these measurements came from hair cells, the resting potentials provide sufficient drive to allow ion entry through transduction channels. Thus it is likely that the transduction apparatus has been disrupted. It has been suggested that P2X channels

[§]Fettiplace and Crawford merely expose rather than isolate the cochlea of a turtle; Russell *et al* isolate neonatal mouse cochleae before the hair cells become mechanically sensitive.

may serve to modulate the transduction process (Housley et al., 1998). If so, then the opening of P2X channels in this preparation may directly cause the lack of electrical response.

2.4.5 A hypothetical model of blebbing

The results presented in this study suggest a simple model to describe the process by which blebbing occurs. In this model, the initial insult is chemical rather than mechanical; since removing Ca^{+2} during surgery prevented blebbing, the chemical process may be an influx of Ca^{+2}. This insult leads to the release of ATP, possibly as part of an apoptotic pathway. The ATP then activates P2X receptors on hair cells, opening the channels and allowing cation entry. Since P2X is a nonselective cation channel, the rate of ion entry depends on both the intracellular and extracellular fluid compositions. In hair cells with predominantly K^+ intracellularly (which is presumably the normal physiological state), ion entry through P2X channels will be faster with AP apically than with AE apically. Electroneutrality requires the entry of anions to roughly balance the entry of cations, so a path for Cl^- entry is also necessary; this is evident from the fact that removing extracellular Cl^- stops bleb growth. Net ion entry causes the osmotic flow of water into the cell, leading to a volume increase. This volume increase causes an increase in membrane tension, which promotes exocytosis over endocytosis (Dai and Sheetz, 1995). Exocytosis in the kinociliary region of the hair cell leads to bleb formation. This hypothesis is consistent with the observations reported in this study. However, the hypothesis is based on limited experimental data, and many other scenarios are plausible. Nonetheless, this model provides a basis for further investigation.

2.4.6 Confinement of blebbing to the tectorial region

In the excised alligator lizard cochlea, blebs form primarily in the tectorial region. Blebs do not typically appear in the free-standing region for several hours after dissection. Several differences between these two regions may contribute to the difference

in blebbing. First, the tectorial region is more sensitive to low-frequency stimuli, and dissection (particularly by hand) is more likely to cause low-frequency vibrations. Second, hair cells in the tectorial region are capped by a tectorial membrane (TM). Relative motion of the basilar papilla and the neural limbus (to which the other end of the TM is attached) may increase mechanical trauma. Third, hair cells in the tectorial region may be electrically resonant (see chapter 5). Electrical resonance mechanisms typically involve Ca^{+2} influx, and excess intracellular Ca^{+2} is cytotoxic. Finally, hair cells in the tectorial region have efferent as well as afferent innervation. Severing the auditory nerve during dissection may cause efferent nerve fibers to release neurotransmitters which selectively affect tectorial hair cells.

Ultimately, the initial insult leading to blebbing in this preparation is unknown. However, the results presented here provide more insight into the process by which blebbing progresses, and by which, in some cases, hair cells can recover from blebbing.

Chapter 3

An Image-based Technique For Measuring Sound-Induced Motions of Cochlear Structures with Six Degrees of Freedom

Abstract

A method, Computer Microvision, for measuring three-dimensional motions of cochlear structures is described. The cochlea of an alligator lizard was isolated and imaged with a microscope. Sinusoidal acoustic stimuli drove cochlear motions, while stroboscopic illumination was used to image these motions with a CCD camera. This process was repeated at several focal planes to gather a 3D data set. The resulting images were viewed to observe qualitative features of motion. Computer vision algorithms were used to extract quantitative estimates of motion. The system has a noise floor of 2 nanometers in the microscope plane of focus, and 40 nanometers in the orthogonal direction. The system has been used to measure the motion of the entire cochlea, of the hair bundles of hair cells, and of individual stereocilia of hair bundles, all from the same data set. Although the computer microvision system is

slower than techniques such as laser Doppler velocimetry or the Mössbauer method, it provides measurements of three-dimensional motions of all visible structures in the cochlea, making it a valuable tool for studying cochlear mechanics.

Key words: Hearing, cochlea, basilar papilla, microscopy, computer vision, alligator lizard.

3.1 Introduction

Our sense of hearing is governed by the microscopic motions of structures in the cochlea in response to sound stimulation. These motions determine the remarkable sensitivity and frequency selectivity of the cochlea (chapter 1). Cochlear function involves the interaction of many structures with independent modes of motion. At the threshold of hearing, these motions are sub-nanometer. Experimental studies of micromechanics seek to measure the coordinated microscopic movements of cell bodies, hair cell stereocilia, and the tectorial membrane in response to sound. In this paper we describe a system, Computer Microvision (CMV), that allows us to measure periodic motions of cochlear structures with nanometer sensitivity and accuracy. The system has several useful properties for studying cochlear mechanics:

- There is no mechanical contact with the moving tissue
- Motions are measured in three dimensions
- Motion of all visible structures can be measured simultaneously
- Use of low-intensity visible light minimizes light-induced tissue damage
- Periodic motions over the entire frequency range of hearing can be measured
- Both quantitative estimates of motion of specific targets and qualitative observations of the three-dimensional motion of the whole organ are possible; comparison of these two can help to interpret the motion of specific targets

As early as 1928, stroboscopic illumination was used to study the mechanical properties of the cochlea (von Békésy, 1960). By adjusting the phase of the strobed light relative to the acoustic stimulus, von Békésy quantified the passive traveling-wave motion of the cochlea. This technique was later applied to studying the phase of hair bundle rotation as a function of frequency in the alligator lizard cochlea (Frishkopf and DeRosier, 1983). These studies required unphysiologically intense sounds to generate motions large enough to be visible, and the measurements were not automated.

The use of a photodiode pair to measure changes in light intensity due to motion allowed automated sensitive measurements of both the magnitude and phase of hair bundle motion (Crawford and Fettiplace, 1985; Howard and Hudspeth, 1988). However, this technique was limited to measuring the motion of a single hair bundle in a single direction at a time. Consequently, few measurements were possible on a single preparation.

The CMV system combines some of the best features of these techniques. Stroboscopic illumination is used to stop the apparent motion of structures, so images at multiple phases of motion can be taken with a CCD camera. Computer vision algorithms estimate motion from changes in light intensity between images; this method is analogous to measuring the voltage difference in a photodiode pair. By taking images at multiple focal planes we can apply the same algorithms to estimate motion in the direction of the microscope axis. Rotation about each of three orthogonal axes can be estimated by measuring the displacement of multiple points on the body of the rotating object (Gordon, 1999). Using these techniques we can make quantitative measurements of the translation and rotation of all visible structures with six degrees of freedom.

Several groups have used video techniques to measure the motion of cochlear structures (Holton and Hudspeth, 1983; Assad et al., 1989; Karavitaki and Mountain, 1996; Hu et al., 1996; Yamauchi et al., 2002), employing measurement methods that range from image subtraction to finite-element modeling. In addition, several groups use similar techniques to study the motion of artificial structures such as microelectromechanical systems, or MEMS (Freeman et al., 1998; Muhlstein et al., 2001).

Some of these techniques dramatically increase the computational cost of the measurement without providing significant gains in accuracy (Cai et al., 2002). To facilitate the evaluation and comparison of different video techniques, we provide here a detailed description of our measurement system, along with an evaluation of its performance limitations.

3.2 Methods

3.2.1 3D imaging

Fundamental to the design of the CMV system are techniques for obtaining 3D images of an object. We obtain such images with a light microscope using transmitted-light microscopy for nearly transparent targets such as tissue, and reflected-light microscopy for opaque targets such as micro-electromechanical systems (MEMS). The transmitted-light system uses a 63x, 0.9 NA objective on an Axioplan microscope (Zeiss, Oberkochen, Germany). The light source is a green LED (Nichia, Tokushima, Japan), projected through a condenser with an NA of 0.8. The resolution of this system in the focal plane is nominally 376 nm. A 12-bit CCD camera (CAD7-1024A, Dalsa, Ontario, Canada) is attached to the camera port. The sampling resolution at the specimen plane is 188 nm/pixel as measured with a calibrated Ronchi rule (Inoué, 1986); thus the imaging system satisfies the Nyquist sampling criterion. Figure 3-1 shows a typical image of an alligator lizard cochlea collected by our system. Individual stereocilia of the cochlear hair bundles are clearly resolved.

The microscope is configured for brightfield imaging using Köhler illumination. Köhler illumination minimizes the depth of field of the focal plane (Inoué, 1986), as long as care is taken to keep the light path free of intervening objects. The light path passes from the condenser through air, a coverslip, fluid, the cochlea, and more fluid before reaching the objective. Our resulting depth of focus is estimated to be ~ 750 nm.

To obtain 3-dimensional images, we collect images such as in figure 3-1 at 80

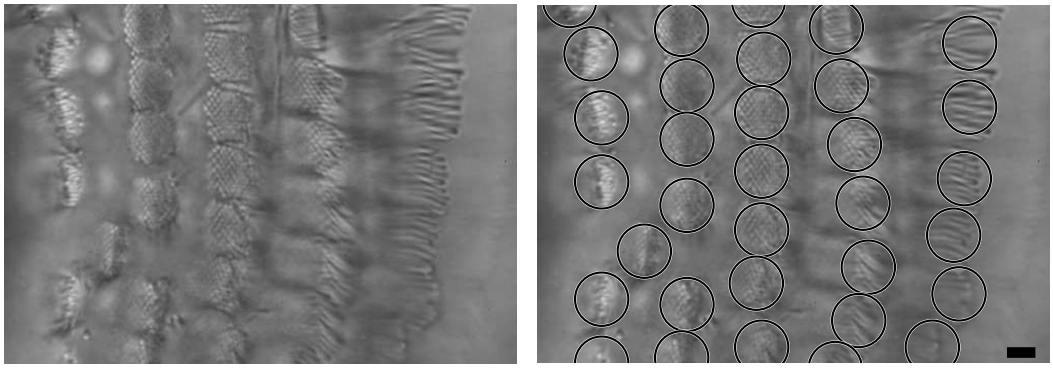

Figure 3-1: Image of the alligator lizard basilar papilla. Left: five columns of hair bundles are visible. In the second and third columns, the bases of hair bundles are visible; in the first and fifth columns, the tips of hair bundles can be seen. The dots and/or lines within each bundle are the individual stereocilia. Right: the same image repeated, with circles highlighting the position of each hair bundle. Scale bar = 5 μm.

focal planes spaced 1 μm apart*. The focus is changed by moving the objective with a piezoelectric device (P-721.10, Physik Instrumente, Waldbronn, Germany). The resulting images can be stacked to form a 3D image, in which the voxels have dimensions of $0.19 \times 0.19 \times 1.0$ μm.

From the resulting 3D data set we can create 2D images along any desired plane†. The simplest recreated image is an xz slice, as shown in the left side of figure 3-2. This image is created by taking a single row of pixels from each of several images taken at different focal planes. The resulting image is then interpolated to have the same scale factor in both dimensions. This cross-sectional view of the alligator lizard cochlea shows the body of the basilar papilla and the stereocilia of several hair bundles (compare to a schematic cross-sectional drawing in figure 1-2). Because the depth of field of this image is roughly equal to the in-plane resolution of 376 nm, this image is not directly analagous to a direct lateral view of the cochlea, as obtained in the gerbil hemicochlea preparation (Edge et al., 1998; Richter, Evans, Edge and Dallos, 1998).

*Because this spacing is larger than our depth of focus, our images are slightly undersampled in the axial direction. This undersampling causes a stair-stepping effect in our cross-sectional images. The 1 μm spacing was chosen as a compromise between resolution of the measurement system and speed of acquisition.

†Hardware specifications, software source code, and animated versions of selected images in this paper are available at http://umech.mit.edu/umech/index.html.

Rather, this image is more like transmission EM images in that, for example, only a portion of each stereocilium is visible. In addition, blurring increases towards the bottom of the image, since light passing through the plane of focus is subsequently scattered by overlying structures.

Sometimes it is useful to view images sliced along an arbitrary plane; for example, to view individual sterocilia. We can make such images by interpolating from the original 3D data set. For each pixel in the output image, the corresponding location in the input volume is computed with subpixel resolution. The nearest pixel to that location is chosen as the center of a $3\times3\times3$ array of pixels, and a bilinear interpolation of the intensities of those pixels is used to determine the value of the output pixel. This interpolation method was qualitatively judged to give the best image quality, as compared to zero-order hold, linear interpolation, and bilinear interpolation of a $5 \times 5 \times 5$ region. The right side of figure 3-2 shows an image created by rotating the focal plane by 90° about the x axis, 2° about the y axis, and 2° about the z axis (the microscope focus is in the xy plane). The resolution of this image is slightly degraded, as can be seen by comparing the lowest hair bundle on the right side in the two images. However, rotating the image makes some structures more visible, such as the hair bundles just to the right of center in the images.

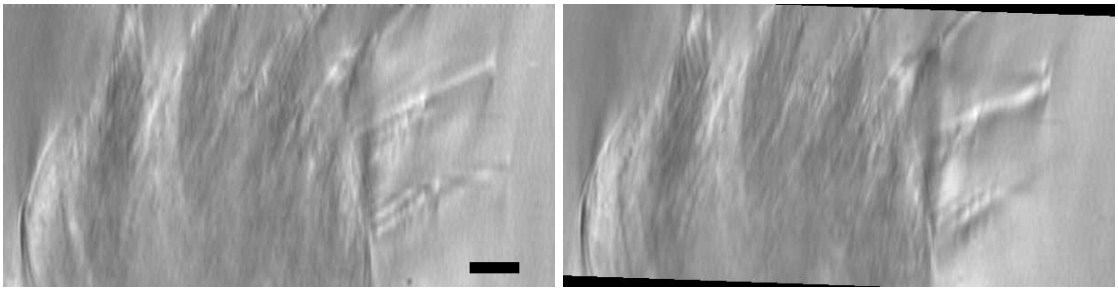

Figure 3-2: Cross-sectional views of the alligator lizard basilar papilla. The image on the left is an xz section through a 3D volumetric image of the cochlea. The resulting image shows the body of the basilar papilla and the stereociliary bundles of several hair cells. The image on the right is of the same region, with the 3D image sliced along an arbitrary plane. The plane of view is defined by rotating the image (xy) plane by 90° about the x axis, 2° about the y axis, and 2° about the z axis. The black regions in the lower-left and upper-right fall outside the original 3D image. Scale bar = 10 μm.

3.2.2 Data acquisition

The motions of cochlear structures occur at audio frequencies, which are too fast for conventional imaging systems to capture. For this reason we use stroboscopic illumination to freeze the apparent motion of the cochlea at each of several stimulus phases. Figure 3-3 provides an overview of the measurement system for collecting these images. A control box generates a periodic stimulus waveform and an illumination waveform. The stimulus waveform is typically sinusoidal, but can be any periodic waveform that can be described by 65,536 12-bit samples. The illumination waveform consists of rectangular pulses centered on a particular phase of the stimulus; the phase, pulse width, and pulse intensity are adjustable. The stimulus waveform drives the piezoelectric disk in the experiment chamber, while the illumination waveform drives an LED connected to the microscope. A CCD camera attached to the microscope is continuously exposed while these waveforms are played. The resulting image on the CCD camera shows the position of all visible structures at a specific phase of the stimulus waveform. This image is then read out and stored on a computer. This process is repeated with the illumination pulses centered on a different phase of the stimulus. Once images at a number of phases (typically 8) are collected, the focus is changed under computer control and the process is repeated to collect a 4D data set (3D images at multiple stimulus phases). Collecting such images requires precise coordination of the stimulus, the strobe signal, and the camera timing signals. This coordination is provided by a custom-built board, the XPOZ system.

The XPOZ system (figure 3-4) was designed by Prof. Dennis M. Freeman, Stan Hong, and Tim Dunn, with firmware written by Prof. Freeman and modified by the author. A field programmable gate array (FPGA, XC4010E, Xilinx, San Jose, CA) provides programmable real-time control of the system. The waveform to be generated is stored as 65,536 12-bit samples in SRAM. The current phase is stored as a 32-bit value, the highest 16 bits of which are used to select an address in SRAM whose contents are fed to the DAC. The frequency of the stimulus is controlled by setting the 32-bit value by which the phase is incremented on each clock cycle. The

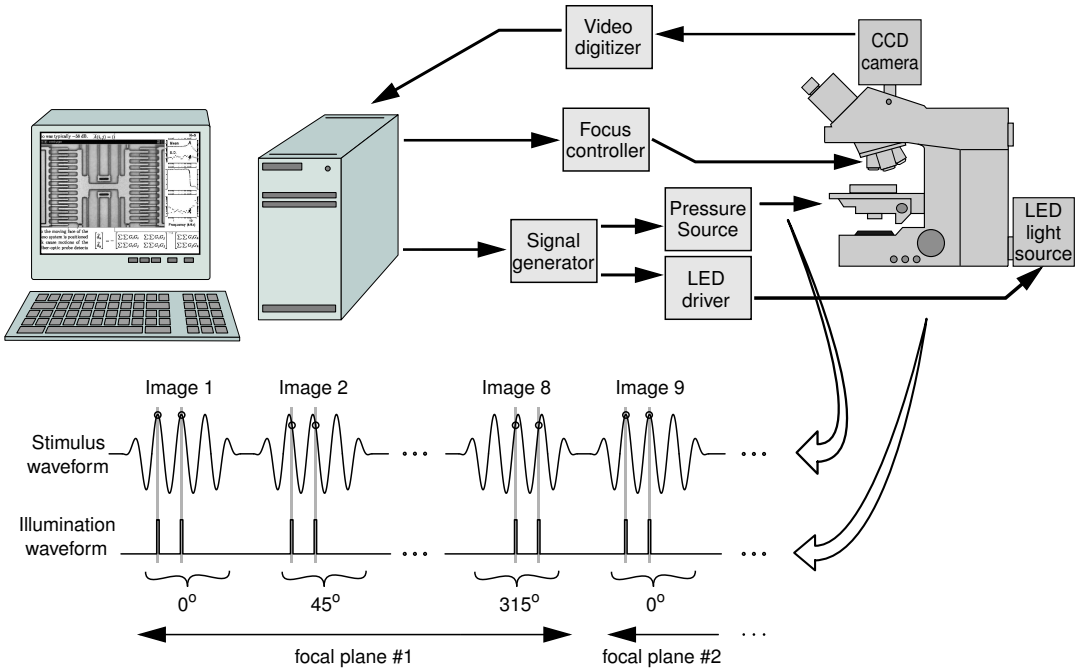

Figure 3-3: Computer microvision measurement system. The object to be studied is placed on the stage of the microscope (right). A Pentium-class computer controls a signal generator that provides two synchronized waveforms: one to drive the voltage stimulus and one to strobe the light source. Typical waveforms are shown. Motions are driven with sinusoidal voltage stimuli. The first image is acquired when light from the LED samples the image at times corresponding to peaks in the stimulus waveform. Successive images are acquired at different stimulus phases. This process is then repeated for different focal planes selected by a computer-controlled focus adjustment.

resulting system can generate arbitrary periodic waveforms at frequencies ranging from 0.002328 Hz to 1.25 MHz with 0.002328 Hz resolution, using a 10 MHz clock crystal. The LED is switched with a TTL signal, allowing illumination to be controlled with 100 nanosecond time resolution. The total exposure time is controlled by a separate counter which decrements only when the LED is on. LED brightness is controlled by a separate DAC.

Images are typically collected at each of 8 evenly-spaced stimulus phases. The LED is turned on with a 1/8 duty cycle centered on the stimulus phase being collected. The total exposure time is set so that the brightest pixel in the image is slightly below saturation. The imaging system is degraded by shot noise, so maximizing the image brightness maximizes our SNR. In addition, longer exposure times reduce the effect of unintended vibrations on the measurement (Davis and Freeman, 1998b).

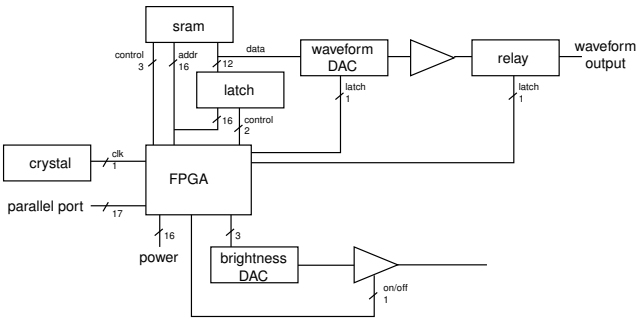

Figure 3-4: The XPOZ stimulus generation system. Boxes denote integrated circuits and other devices, lines denote interconnections. The number next to each line is the width of the bus, in bits. System timing is provided by the 10 MHz crystal. The FPGA executes digital logic configured by a PC via the parallel port. SRAM stores digital samples of the waveform to be written to the waveform D/A converter (DAC). The latch stores waveform values being written to SRAM. The brightness DAC controls the voltage of the LED driving signal. A digital signal from the FPGA controls a normally-open relay which disconnects the waveform DAC from the output until the FPGA is properly programmed. A second digital signal toggles the LED output, allowing the LED to be pulsed at frequencies up to 5 MHz.

The microscope is placed on a vibration-isolation table to reduce external vibrations. The stage and camera are both rigidly coupled to the microscope body to minimize relative motion. With this configuration we have reduced the unintended vibrations during the collection of a 2D data set to less than 2 nanometers (section 3.3.1). Drift of the setup due to thermal fluctuations and settling of viscously coupled parts (such as gears in the focus controller) can also affect the measurements, as can unintended motions of the target (such as slow changes in biological preparations).

To determine the amount of drift in our system, we took repeated images of the bottom of the experiment chamber over an extended time period. The amount of drift in the plane of focus was determined using computer vision algorithms with a noise floor of about 1 nanometer (section 3.2.3). At the end of the experiment, a set of images was taken at different focal planes. Images taken at different times were manually compared with this set to estimate the amount of axial drift. This method has a resolution of 0.1 μm.

The chamber drifted in the y direction for about an hour (figure 3-5), for a total drift of 0.4 μm. Drift in the z direction had a similar time course. However, drift in the

x direction continued for several hours at a rate of 0.8 nm/min. Thus while collecting images at a single focal plane, the chamber may drifts by about 0.2 nanometers. The source of this drift is unknown.

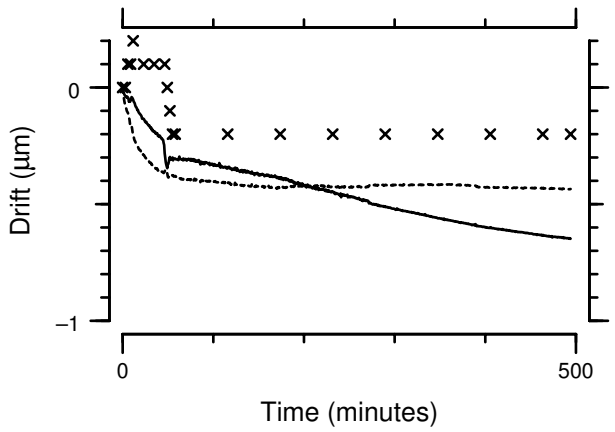

Figure 3-5: Drift of the experimental setup over time. Motions in x and y are measured using computer vision algorithms, and motions in z are estimated from changes in focus. The solid line shows the x component of drift, corresponding to the left-right axis of the microscope. The dashed line shows the y component, corresponding to the front-back axis. The y component stops drifting after about an hour, but the x component has a steady-state drift of about 0.8 nm/min. $\times$ symbols show estimates of the z component of drift, which is comparable in magnitude and time course to the y component.

3.2.3 Quantitative analysis

Images collected using the computer microvision system can be animated in sequence to allow a qualitative assessment of motion. In addition to viewing the images, we can quantitatively measure the motion in three dimensions of any structure in the images. In this paper, we focus on the measurement of small motions for three reasons.

1. Large motions can be measured by counting pixels of displacement.

2. Large motions can be converted into small motions by either downsampling images or shifting them to subtract estimates of displacement.

3. Many biologically interesting problems involve the measurement of small motions.

Motion is detected using gradient-based algorithms from the field of computer vision. These algorithms, based on ones developed by Horn (Horn, 1986; Horn and Weldon Jr., 1988) and described in detail elsewhere (Davis and Freeman, 1998a; Davis and Freeman, 1998b; Timoner and Freeman, 2001), can estimate motion with an accuracy of up to 1/1000 pixel. Figure 3-8 demonstrates how motions smaller than a pixel can be detected in the images.

The algorithms are based on the assumption that the brightness of an object does not change when the object moves. That is, if the brightness at a point is represented by $\mathrm{E}(x, y, z, \theta)$ (where we now treat the set of 3D images at multiple stimulus phases as a single four-dimensional image), and that point moves by (Δx,Δy,Δz) while the phase changes by $\Delta\theta$, then

$$\mathrm{E}(x, y, z, \theta) = \mathrm{E}(x + \Delta x, y + \Delta y, z + \Delta z, \theta + \Delta\theta) \tag{3.1}$$

If we take a Taylor series expansion of the right side and ignore higher-order terms, we get

$$\frac{\partial E}{\partial x}\Delta x + \frac{\partial E}{\partial y}\Delta y + \frac{\partial E}{\partial z}\Delta z + \frac{\partial E}{\partial \theta}\Delta\theta = 0. \tag{3.2}$$

The least-squares solution of equation 3.2 over the voxels in a region of interest provides an estimate of the motion of that region.

The gradients in equation 3.2 must be estimated from quantized images. In addition, these estimates must be interpolated to co-localize the various gradients (Davis, 1997; Timoner, 1999). Using a first-difference estimator with a linear interpolator introduces significant bias; however, this bias can be reduced by simple techniques (Davis and Freeman, 1998a). Using more sophisticated estimators and interpolators significantly reduces bias and improves measurement accuracy (Timoner, 1999; Timoner and Freeman, 2001), at the expense of computational time. With identical estimators and interpolators, gradient-based methods are equivalent to block-matching and correlation methods for sub-pixel motions (Davis et al., 1995). Because of their closed-form solution, however, gradient-based methods are significantly faster.

Two-point flat fielding technique

The gain and offset of each camera pixel are affected by spatial variations of sensitivity of the CCD array and by imperfections in the optics (Janesick et al., 1987). As a result, the intensity $I(x, y)$ measured at each pixel is related to the brightness function $E(x, y)$ by

$$I(x, y) = \alpha(x, y)E(x, y) + D(x, y) \tag{3.3}$$

where $\alpha(x, y)$ is a pixel-by-pixel variation in sensitivity due to CCD imperfections and dust on optical components, and $D(x, y)$ is the so-called "dark current", the intensity read from the camera when the illumination source is turned off. To reconstruct $E(x, y)$, we use a two-point flat fielding technique (Hiraoka et al., 1987; Healey and Kondepudy, 1994). The offset for each pixel is estimated by taking a picture with the light source disconnected (the dark picture D). The gain for each pixel is estimated by taking a picture with the light on and the specimen removed, to provide a constant $\mathrm{E}(x, y) = \mathrm{E}_0$ across the field (the bright picture B). For each image I of the specimen, a new image P is created by applying the following formula at each pixel (x, y):

$$P(x, y) = \frac{I(x, y) - D(x, y)}{B(x, y) - D(x, y)}. \tag{3.4}$$

The resulting image is a more accurate representation of the brightness function. Since each image contains noise, this two-point correction process increases the noise in our images. By creating bright and dark images from averages of fifty individual images, we limit the increase to an additional 2%[‡]. Since the gain and offset can both change between experiments, it is important to collect the bright and dark images under the same conditions used to collect the images of the specimen.

[‡]Analysis is available at http://umech.mit.edu/umech/poissonratio.pdf.

3.3 Results

3.3.1 Calibration

The CMV system was calibrated by measuring the motion of a target simultaneously with computer microvision and a laser Doppler velocimeter (OFV 511, Polytec, Waldbronn, Germany). The results, shown in figure 3-6, demonstrate that computer microvision can measure sinusoidal motions accurately for peak displacements as small as 2 nanometers. These displacements correspond to less than 0.02 pixels in the images. At larger displacements, CMV underestimates motion as determined by laser Doppler velocimetry by about 5–10%.

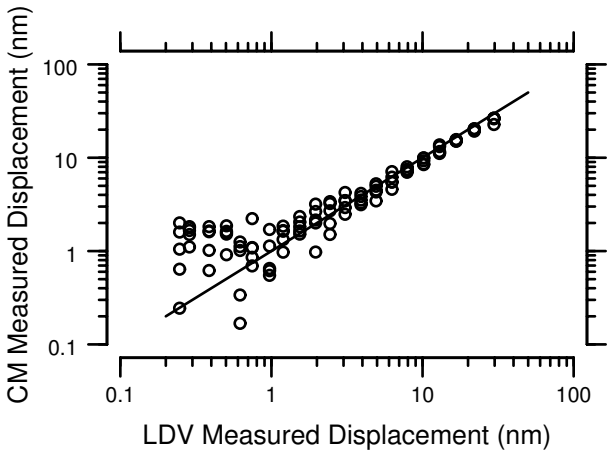

Figure 3-6: Calibration of the system against a laser Doppler velocimeter (LDV) in the plane of microscope focus. The target was a piece of plexiglass glued to the end of a piezoelectric crystal. The microscope was focused on the center of the plexiglass while the LDV was aimed at a piece of retroreflective tape on the end of the plexiglass. Circles show five independent measurements of motion at each of 20 stimulus intensities. The straight line has a slope of one and passes through the origin. The two estimates are linearly related above ∼2 nm displacement. For larger displacements, the CMV measurement is consistently 5–10% smaller than the LDV measurement.

Axial motion was calibrated from images of the alligator lizard cochlea. We collected a series of images of the cochlea at 0.1 μm spacing. These images were split into ten evenly-spaced volumes with 1.0 μm spacing, each shifted by 0.1 μm relative to the last. We then estimated the motion of 6425 regions of 4 μm^3 between each pair of volumes. Figure 3-7 shows the mean and standard deviation of the estimate for each

shift. The mean estimate for each displacement was within one standard deviation of the imposed displacement. The overall standard deviation of the estimates is 40 nm, or 0.04 pixel.

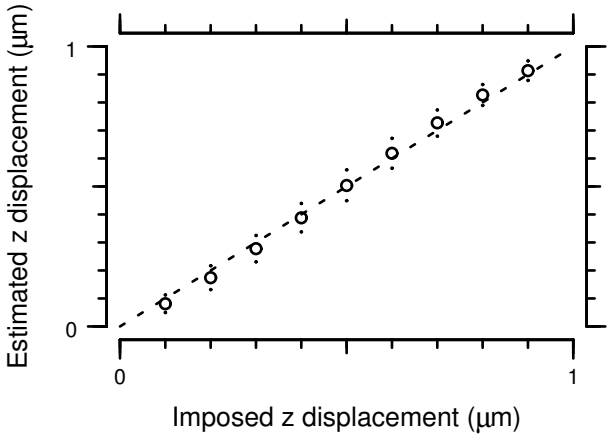

Figure 3-7: Calibration of CMV in the axial direction against the focus control system. Circles indicate mean estimated displacement; dots indicate ±1 standard deviation of the estimate. Dashed line has a slope of 1. The means are all within one standard deviation of the imposed displacement.

3.4 Measurements of the motion of a hair bundle

Figure 3-8 shows the motion of the base and tip of a single hair bundle in response to a 3.75 kHz tone with a sound pressure of 120 dB SPL in fluid. This bundle was oriented at about 45° from vertical, so images of the bundle were first rotated to orient the bundle vertically. Regions of the rotated images were cropped and stacked together using the kymographic technique (Gall et al., 1971; Tigges et al., 1999) to create the images in figure 3-8. The resulting images (repeated four times for clarity) show the motion of the tip (left) and base (center) of the hair bundle as a function of stimulus phase. The plot on the right shows the motion of the same hair bundle as measured using the CMV system[§]. The motions were measured perpendicular

[§]Quantitative measurements were made from the original images rather than the rotated ones.

to the bundle axis; that is, in the direction in which hair bundles are mechanically sensitive (Shotwell et al., 1981). The base moved by 0.49 μm peak. The tip moved by 0.24 μm peak, with a phase lag of 0.11 cycles relative to the base. Motion of the base is almost perfectly sinusoidal, but motion of the tip contains some higher harmonic components; the second harmonic is 10 dB smaller than the fundamental. The peak-to-peak motion of the bundle tip spans 2.5 camera pixels, so the motion between each phase and the next was typically less than a pixel. Nonetheless, these subpixel motions are clearly visible in the kymograms.

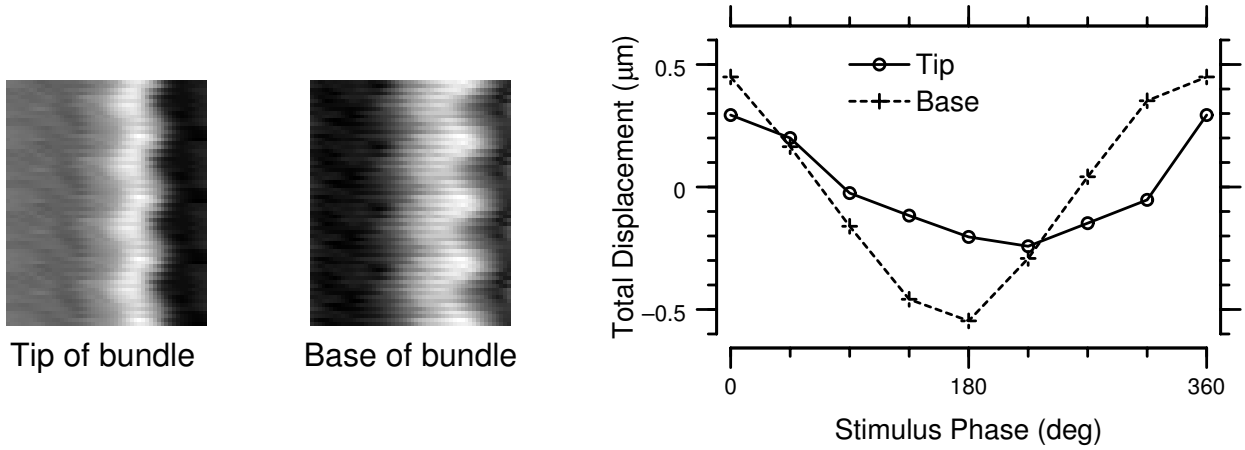

Figure 3-8: Motion of the base and tip of a hair bundle. This hair bundle was oriented so that the principal direction of hair bundle motion was in the xz plane at an angle of 117 degrees from the positive x axis. The kymograms on the left were created by cropping a small region of each image perpendicular to the axis of hair bundle motion, then stacking these regions in sequence vertically. Each sequence is repeated four times for clarity. The plot on the right shows the measured motion of the tip and base as a function of stimulus phase.

The relevant stimulus for excitation of a hair cell is the rotation of its bundle about the base. From the measurements in figure 3-8, we can compute this rotation. In addition, we can shift our images to subtract the motion of the base of the bundle in order to view this relative motion directly. Figure 3-9 shows kymograms made from these shifted images, along with the relative deflection of the tip of the hair bundle. The bundle is deflected by 0.33 μm peak, and lags deflection of the base by 0.43 cycles. The measured deflection is largely sinusoidal; the second harmonic is 12

dB smaller than the fundamental, and higher harmonics are smaller still.

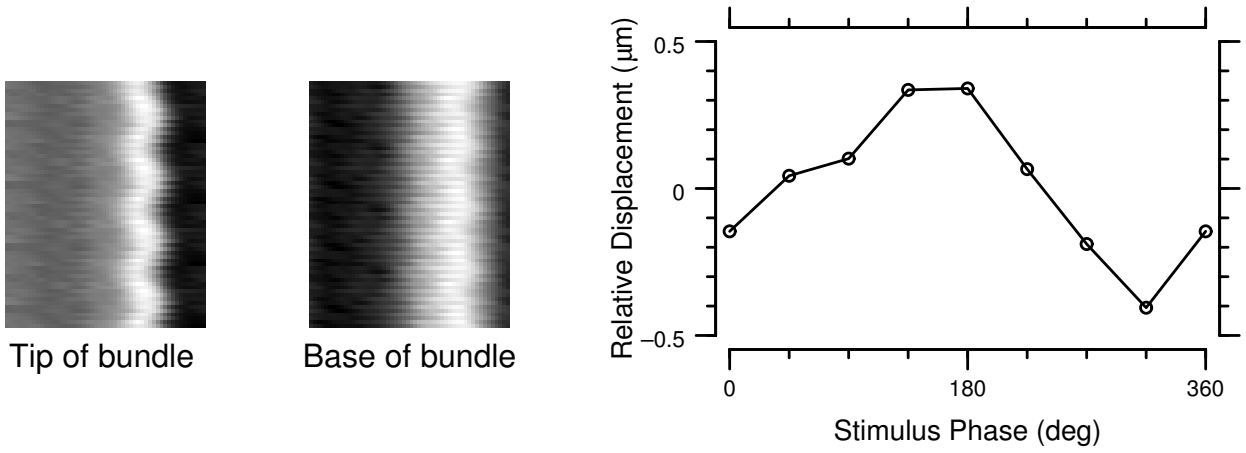

Figure 3-9: The left and center figures show kymograms of the relative motion of the tip and base of a hair bundle, respectively. These kymograms were made from images that were shifted to subtract the measured motion of the hair bundle base. The plot on the right shows the deflection of the tip of the hair bundle relative to its base. The deflection is nearly sinusoidal.

3.5 Discussion

3.5.1 Accuracy of computer microvision

The CMV system can track the motion of a target with peak sinusoidal displacements as small as 2 nanometers under ideal conditions. Displacement estimates are accurate to within 10% as compared to measurements made with a laser-Doppler velocimeter. For displacements in the range of 10–100 nm, the fundamental components of motion as measured by CMV were consistently 5–10% lower than those measured with the LDV. This difference is not simply due to misalignment of the LDV and/or target relative to the microscope, since an alignment error of more than 18° would be necessary to produce a 5% decrease in the CMV estimate. This error is most likely due to uncompensated bias in the algorithms. Using algorithms with no bias compensation gave a 20–25% difference between CMV and LDV. Although the linear bias

compensation method reduces this bias, it does not eliminate bias completely. The remaining bias causes small displacements to be underestimated, resulting in CMV measurements smaller than those measured by the LDV.

The noise floor of the CMV system is limited in practice by low-frequency vibrations, which are not well damped by the vibration-isolation table. These vibrations are coupled into our measurements due to the fact that the aquisition of a single image often requires a large fraction of a second. Thus low-frequency vibrations are aliased to the stimulus frequency and its harmonics. The noise floor of measurements in the axial direction is more than an order of magnitude higher than for in-plane measurements. In units of pixels, however, the noise floor was only twice as large in the axial direction. Several factors contribute to the higher noise floor in the axial direction. The point-spread function of the optical system is larger in the axial direction, and axial blurring is nonlinear for targets such as hair bundles which have diameters close to the center wavelength of the LED output. The specimen was sampled at 0.12 μm/pixel in-plane, but at 1.0 μm/pixel in the axial direction. Finally, axial motion estimates are made from images taken over much longer time scales, so the contribution of drift and ambient noise is greater. Since the point-spread function is determined by the microscope objective, and the axial spacing and acquisition time are inversely correlated, none of these factors can be easily adjusted to improve axial resolution.

Measurements of hair bundle motion appear to have a drift component separate from that of the chamber. This drift component is due to physiological changes in the tissue over time (chapter 2). The drift component is larger than the noise floor of the CMV system, and is often larger than the periodic motions being observed. For example, motions of the hair bundle tip in figure 3-8, and of bundle deflection in figure 3-9, contain harmonic components that are most likely due to drift of the specimen. Observing motions of the specimen in the microscope before collecting data allows one to judge whether the motions measured by CMV are corrupted by drift.

3.5.2 Comparison of computer microvision to other metrology systems

The CMV system provides inherently three-dimensional measurements of motion. Other metrology methods are one-dimensional (laser-Doppler vibrometry, Mössbauer) or two-dimensional (quadrature photodiodes). Measuring three-dimensional motions with such techniques requires repositioning the experimental setup for each measurement direction. Repositioning can be avoided by combining LDV and photodiode techniques (Hemmert et al., 2000), but these techniques must still be used sequentially. In addition, aligning the two measurement systems can be difficult. Also, because the quadrature photodiode technique is two-dimensional, axial motion of targets can cause brightness changes that are interpreted as lateral motion.

Because CMV is an image-based method, the information necessary for measuring motion is acquired simultaneously for every structure in the images. In contrast, LDV, Mössbauer, and photodiode techniques provide information about only a single point. The use of images has an additional benefit in that qualitative judgements of motion can be used as a cross-check on the quantitative measurements, and to facilitate interpretation of the motion measurement. Such cross-checks are not available with other techniques.

When imaging weakly-scattering tissue such as in the cochlea, CMV can measure the motions of structures deep within the tissue, such as the bases of hair bundles or nuclei of hair cells. LDV and Mössbauer techniques can only measure the motion of surface structures or highly reflective internal structures. CMV can also be used to measure motion on different scales — from the same set of images we can determine the motion of the entire basilar papilla, the rotation of a single hair bundle, and the relative deflection of stereocilia within a bundle (Davis and Freeman, 1995).

These advantages of CMV are paid for by the amount of time required to collect a set of images. It takes roughly 8 minutes to collect images of 3D motion of the alligator lizard cochlea at a single frequency. In contrast, LDV and Mössbauer methods are nearly instantaneous. However, the resulting CMV data set contains information

about the three-dimensional motion of every structure in a $200 \times 200 \times 80$ μm region. Measuring the motion of all such points in three dimensions with LDV or Mössbauer methods is prohibitively time-consuming.

In addition, CMV is limited to measuring periodic motions at multiples of the fundamental frequency of an applied stimulus. Thus it is not an appropriate technique for measuring, e.g., frequency glides in basilar membrane motion (deBoer and Nuttall, 1997; Recio et al., 1998) or spontaneous oscillations of hair bundles (Denk, 1989). Nonetheless, with a sufficiently fast camera (such as a line-scan camera), such motions could be studied with the CMV technique.

In summary, the Computer Microvision system is a sensitive technique for measuring the three-dimensional motions of many types of microscopic structures. CMV techniques are currently being used by several laboratories to study the micromechanical properties of mammalian cochleae (Karavitaki and Mountain, 1996; Richter, Evans, Hu and Dallos, 1998). We have also applied the system to measuring the motions of microfabricated micro-electromechanical systems (Freeman et al., 1998), and such measurements are now being done at several laboratories. The remaining chapters of this thesis describe the application of CMV to measurements of the motion of structures in the alligator lizard cochlea.

Chapter 4

The Alligator Lizard Basilar Papilla Has Two Modes of Motion

Abstract

Abstract

The hearing organ of lizards is the basilar papilla, which is homologous to the mammalian organ of Corti. Current models of cochlear function in the alligator lizard incorporate physically-derived models of middle ear and stereocilia mechanics, but treat the body of the basilar papilla as a simple rotational lever. However, previous measurements of the motion of *in vitro* preparations of this cochlea have suggested that the motion of the basilar papilla is more complex (Frishkopf and DeRosier, 1983; Holton and Hudspeth, 1983). To resolve this discrepancy, we measured three-dimensional motions of the basilar papilla in an *in vitro* preparation in response to sound stimulation as a function of frequency and location within the cochlea. Measurements were made using the Computer Microvision system developed in our laboratory (chapter 3). Our measurements show that the basilar papilla exhibits two simultaneous modes of motion: a rotational mode, and a translational mode perpendicular to the basilar membrane. The translational mode is independent of frequency, but the rotational mode has a peak in displacement near 5 kHz. This peak is largest at the basal end. This combination of modes makes the relative shearing displacement at the reticular lamina more uniform with lateral position than that which would result from pure rotation. From the measurements we derive a mechanical model of the basilar papilla. In the model, the admittance in the translational domain is represented as a compliance, while the admittance in the rotational domain is represented as a second order system. The impedance of this second-order system is dominated

by a compliance at low frequencies and by a moment of inertia at high frequencies. Damping in this model occurs only in the rotational domain. The parameters of this model are consistent with estimates based on anatomy; the translational compliance also matches that of a previous study (Rosowski et al., 1985). The transformation from translational to rotational motion in this cochlea introduces a frequency dependence that provides a physical basis for the mechanical low-pass filter hypothesized in models of this cochlea (Weiss and Leong, 1985a; Freeman and Weiss, 1990a).

Key words: Hearing, cochlea, basilar papilla, computer vision, alligator lizard, modal analysis.

4.1 Introduction

The sensitivity of the cochlea is determined by its ability to couple mechanical energy at the stapes to mechanical energy of hair bundle deflection. Clearly this coupling depends on the macromechanical properties of the cochlea — that is, the motion of the basilar membrane and basilar papilla* relative to surrounding bone (Patuzzi, 1996). In the mammalian cochlea, macromechanical motion is dominated by a traveling wave along the length of the cochlea (von Békésy, 1960). This traveling wave is amplified by a physiologically-dependent mechanism which is presumed to be outer hair cell motility. In the alligator lizard cochlea, in contrast, macromechanical motion is believed to be quite simple. The basilar membrane moves in phase along its length, with tuning similar to that of the stapes (Peake and Ling, 1980). In response to sound stimulation, the alligator lizard basilar papilla rotates about an axis near the neural edge of the basilar membrane (Frishkopf and DeRosier, 1983; Holton and Hudspeth, 1983). However, both of these studies qualitatively report an increase in the motion of the basal end of the papilla above 3 kHz, suggesting that the motion of the papilla is more complex than simple rotation.

The alligator lizard cochlea (figure 1-2) contains two regions: the apical tectorial region, in which hair bundles project into an overlying tectorial structure, and the

*We use the general term *basilar papilla* here to refer to the papillar structures of non-mammalian vertebrates as well as the organ of Corti of mammals.

basal free-standing region, in which hair bundles project freely into endolymph. In the free-standing region, hair bundles vary in height from over 30 μm at the apical end, where best frequencies are near 1 kHz, to about 12 μm at the basal end, where best frequencies are near 4 kHz (Mulroy, 1974; Weiss et al., 1976). Because of the planar structure of this cochlea, we can measure the sound-induced motion of nearly the entire basilar papilla over the frequency range of hearing of the lizard.

Most cochlear models assume that the cochlea has multiple modes of motion. Recent experiments show some evidence of multiple modes in the motion of the basilar membrane (Nilsen and Russell, 1999, but see Cooper, 2000), reticular lamina (Ulfendahl et al., 1995), tectorial membrane (Hemmert et al., 2000), and outer hair cells (Karavitaki and Mountain, 1997), as well as in neural responses (Lin and Guinan, 2000) of mammalian cochleae. The number of mechanical modes of vibration in the cochlea have not been determined, nor has the contribution of each mode to the function of the cochlea. The complexity of the structure of the mammalian cochlea and the major contribution of active, nonlinear processes to cochlear mechanics make modal analysis of the mammalian cochlea difficult. In this paper we examine the modes of motion of the alligator lizard basilar papilla. Because of the relative simplicity of this papilla, we can determine both the number of modes of motion and the contribution of multi-modal motion to the mechanical function of this cochlea.

4.1.1 Models require an additional low-pass filter

Although the basilar membrane shows no sharp frequency selectivity (Peake and Ling, 1980), both auditory nerve fibers (Weiss et al., 1976) and hair cells (Holton and Weiss, 1983b; Baden-Kristensen and Weiss, 1983) are sharply tuned, with best frequencies that vary with hair bundle height in the free-standing region (Holton and Weiss, 1983a). In the free-standing region, the motion of hair bundles varies with frequency (Holton and Hudspeth, 1983; Frishkopf and DeRosier, 1983; see also chapter 6), such that tall hair bundles are deflected more at low frequencies, and short hair bundles are deflected more at high frequencies. These results have led to models which combine simple rotation of the basilar papilla with mechanical resonance of

hair bundles. In these models, hair bundle rotation depends on viscous and inertial properties of the fluid; the fluid is driven by boundary-layer effects due to motion of the reticular lamina in the direction of hair bundle excitation. Such models are able to achieve reasonable fits to hair-cell and auditory nerve fiber tuning data (Weiss and Leong, 1985a; Freeman and Weiss, 1988; Freeman and Weiss, 1990a; Shatz, 1996). However, in order to fit the high-frequency slopes of hair-cell and neural tuning data, these models require an additional low-pass filter before the transduction nonlinearity. The models provide no physical explanation for this filter.

This paper presents measurements of the motion of the basilar papilla as a function of frequency in response to sound stimulation. These measurements used a computer microvision system developed in our laboratory (chapter 3), which can measure the three-dimensional motion of all structures in the cochlea with nanometer precision. From these measurements we derived a mechanical model to describe the motion of the basilar papilla. This model provides new insight into the function of the alligator lizard cochlea. Preliminary analyses of the results shown here have been presented previously (Aranyosi and Freeman, 2001; Aranyosi and Freeman, 2002).

4.2 Methods

A detailed description of the isolated cochlea preparation is in chapter 2, and a description of the computer microvision (CMV) system is provided in chapter 3. Here we provide a brief summary of those methods, and a detailed description of the experiment chamber for presenting acoustic stimuli to the cochlea.

4.2.1 Isolation of the cochlea

The alligator lizard cochlea (figure 1-2) was excised using a dorsal approach. The soft tissues of the cochlea, along with the 8th nerve and the lagena, were removed from their bony surround. Care was taken to minimize audio-frequency vibration of the tissue during extraction. The isolated cochlea was placed in a chamber (figure 4-1) and clamped over a hole between two fluid spaces. The fluid beneath the cochlea was

artificial perilymph (AP) and the fluid above the cochlea was artificial endolymph (AE). AP contains (in mM): Na^{+}, 168; K^{+}, 3; Ca^{+2}, 2; Mg^{+2}, 1.2; Cl^{-}, 174.9; SO_4^{-2}, 2; $H_2PO_4^{-}$, 0.5; D-glucose, 5; Hepes, 5. AE contains (in mM): Na^{+}, 2; K^{+}, 174; Ca^{+2}, 0.02; Cl^{-}, 171.5; SO_4^{-2}, 2; $H_2PO_4^{-}$, 0.5; D-glucose, 5; Hepes, 5. Both solutions contained MEM essential and non-essential amino acids, and were oxygenated immediately before use.

4.2.2 Experiment chamber

The experiment chamber (figure 4-1) was based on a design initially developed by Quentin Davis (Davis, 1997). The Plexiglas® experiment chamber allowed the cochlea to be clamped over a 0.74 mm hole separating two fluid spaces. The clamp was a thin slice of polyetheretherketone (PEEK) tubing (McMaster-Carr, NJ) with an 0.76 mm inner diameter. These dimensions match the size of the bony ring on which the cochlea sits *in vivo* (Mulroy, 1974; Freeman, 1990). The clamping ring encircled the triangular and neural limbi to avoid direct contact with the basilar membrane or sensory hair cells. Figure 4-2 shows a photograph of the chamber.

Several designs for securing the clamp were attempted. In the final design (figure 4-3), the clamp was glued to a stainless steel tube which is attached on the distal end to a cantilevered piece of shim steel. The shim steel acts as a spring holding the clamp above the hole. A threaded rod with a glued-on nut pushes down on the shim steel when the rod is turned, allowing the clamp to be raised and lowered slowly. The rod contains a 90° bend near the top, creating a lever arm. This lever arm allows the rod to be turned by hand, so the vertical motion of the clamping ring is about 1/60th of the motion of the tip of the rod. This reduction in motion allowed the ear to be clamped gently, reducing potentially damaging vibrations.

The chamber was designed to allow separate fluids to be perfused above and below the cochlea. This separation of fluids simulates that of the *in vivo* cochlear environment. AP was perfused below the cochlea and AE was perfused above the cochlea. During these studies, perfusion was typically done intermittently between motion measurements, roughly every 5–10 minutes. To reduce acoustic losses through

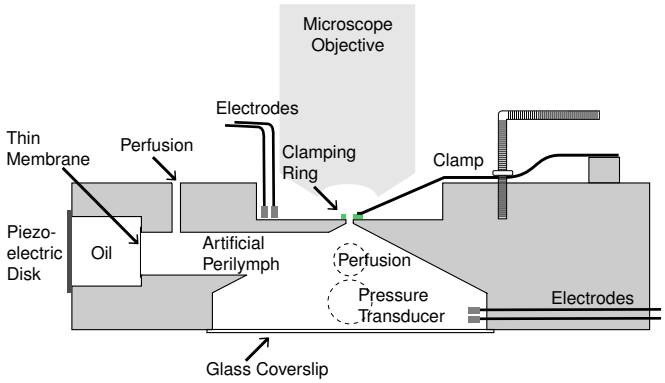

Figure 4-1: Schematic drawing of the experiment chamber. The papilla was held by a clamping ring over a hole separating two fluid spaces. A piezoelectric disk generated pressures in the fluid below the cochlea, and the resulting pressures were sensed with a pressure transducer (the dashed circles indicate structures coming out of the plane of view). To reduce electrical crosstalk, the piezoelectric disk was shielded from the electrolytic fluid by a small volume of oil and a thin plastic membrane. The fluids above and below the cochlea could be perfused continuously. Two electrodes in each fluid compartment allowed voltage- and current-clamp measurements. The chamber was designed so that both the objective and condenser can be brought into focus on the specimen. In addition, the inverted v-shape underneath the basilar papilla was designed to allow the widest angles of light coming from the condenser to reach the basilar papilla without being distorted by the Plexiglas® chamber. Some features of this drawing have been exaggerated for visibility.

the perfusion system, the influx and efflux tubes for the fluid below the cochlea contain 40 cm lengths of PEEK tubing (0.76 mm i.d.) to form a high acoustic resistance. The isolation of the two fluid spaces was verified by perfusing red food dye in the fluid below the cochlea and blue food dye in the fluid above the cochlea at the end of one experiment. No red dye was seen in the fluid above the cochlea, nor was blue dye seen in the fluid below the cochlea. After washing out the dye, the tissue of the basilar papilla (exposed to the fluid below the cochlea) was stained red, and the auditory nerve (outside the clamping ring in the fluid above the cochlea) was stained blue. The neural limbus contained both red and blue stain.

A piezoelectric disk (Panasonic EFR Series, Matsushita, Japan) generated sound pressure in the fluid below the cochlea. The disk was electrically shielded with aluminum foil, and was separated from the saline by a small oil-filled chamber. A hydrophone (Model EPB-126W-100G, Entran Devices, Inc., Fairfield NJ) measured

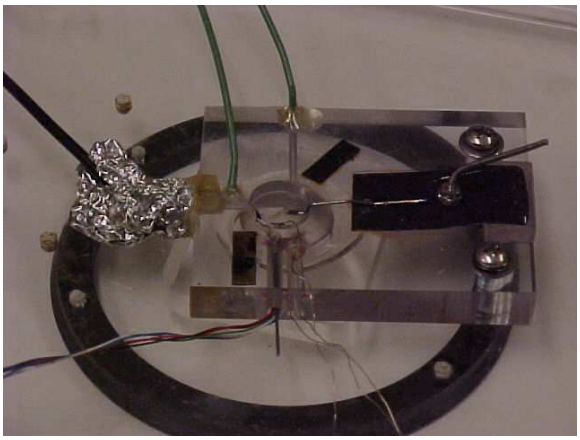

Figure 4-2: Photo of the experiment chamber. The papilla was placed in the indented area in the center of the picture, and held in place by a clamping ring. This clamping ring is glued to a steel rod, which extends to the right and is attached to a piece of shim steel (black). The piezoelectric disk (left, shielded by aluminum foil) generated sound pressures in the fluid below the cochlea. The yellowish region inside the chamber next to the disk contains oil, which electrically isolates the piezoelectric disk from the fluid. The green tubes extending upwards allow perfusion of the fluid below the cochlea. Perfusion tubes for the fluid above the cochlea are held magnetically on the thin black areas near the indented area. The wires for the microphone extend down and to the left. The wires for the electrodes extend down and to the right. The black ring underneath attaches to the microscope stage.

the resulting pressure in the fluid below the cochlea. The piezoelectric disk generated roughly 100 dB SPL in fluid per V_{rms}.

The fluid space above the cochlea is wide enough to allow a 63x water immersion objective to focus on the cochlea. This space is indented into the chamber to allow the condenser to be positioned close enough for Köhler illumination (section 3.2.1). The space below the cochlea is tapered so that light from the condenser passes only through fluid and glass coverslip, and not through Plexiglas®. The bottom surface of the chamber is sealed with a glass coverslip.

A pair of electrodes is mounted in each fluid space to allow voltage-clamp and current-clamp measurements of the electrical response of the cochlea. Voltage-clamp measurements were routinely made in earlier experiments. However, after many such measurements revealed no electrical response to sound (see chapter 2), the measurements were discontinued.

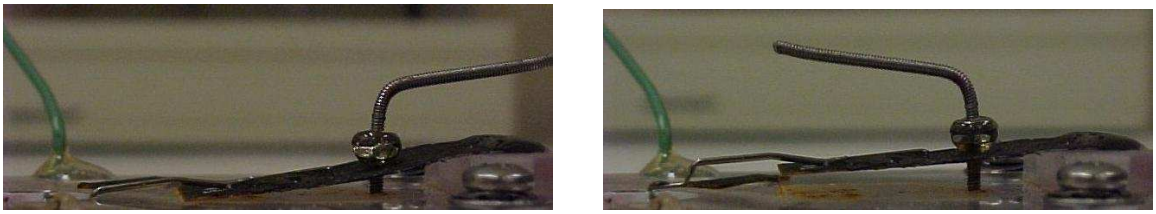

Figure 4-3: The clamping mechanism. The figure on the left shows the clamp in its lowered state, the figure on the right shows the clamp raised. The shim steel (black) is glued to a Plexiglas® block on the right. Turning the threaded rod clockwise moves the nut downwards, which pushes on the shim steel. When the clamp is down (left image), the tip of the shim on the left touches the Plexiglas®, pushing the clamp onto the bottom surface of the chamber. When the clamp is raised (right image), the tip of the shim is above the surface of the Plexiglas®. A small rust spot can be seen where the shim contacted the Plexiglas®; the shim was later painted black to prevent further rusting.

4.2.3 Image acquisition and analysis

The cochlea was viewed from above with a 63x, 0.9 NA water-immersion objective. A green LED (Nichia, Tokushima, Japan) was strobed with a 1/8 duty cycle at the frequency of the sound stimulus. The resulting image, which shows the position of the cochlea at a chosen phase of the sound stimulus, was captured with a 12-bit CCD camera (Dalsa CA-D7-1024A). Eight such images were taken at eight evenly-spaced stimulus phases. This process was repeated at 60-100 focal planes separated by 1 μm. The focus was changed using a piezoelectric focusing device (PIFoc P-721, Physik Instrumente, Waldbronn, Germany). The resulting data set is a sequence of three-dimensional images taken at different stimulus phases, where each voxel in the images has dimensions of $0.19 \times 0.19 \times 1.0$ μm.

Computer vision algorithms (Horn and Weldon Jr., 1988; Davis and Freeman, 1998a) were used to measure the motion of structures between images. These algorithms are based on the assumption that the brightness of the structure being imaged does not change as the structure moves. If the brightness of a given point at a given time is $E(x, y, z, t)$, and that point moves by Δx, Δy, Δz in time Δt, then

$$E(x, y, z, t) = E(x + \Delta x, y + \Delta y, z + \Delta z, t + \Delta t). \tag{4.1}$$

Taking the first-order terms of the Taylor series expansion of the right side gives

$$\frac{\partial E}{\partial x}\Delta x + \frac{\partial E}{\partial y}\Delta y + \frac{\partial E}{\partial z}\Delta z + \frac{\partial E}{\partial t}\Delta t = 0. \tag{4.2}$$

The least-squares solution to equation 4.2 over a region of the image describes the average motion of that region.

Noise in the measurements was due to ambient vibrations, drift of the tissue, and noise inherent in the imaging system (see chapter 3). This noise was aliased by the measurement process to the stimulus frequency and its harmonics. Most measurements showed primarily sinusoidal motion; in addition, the motions seen by eye in the microscope were primarily sinusoidal. Consequently, to eliminate noisy measurements, we accepted measurements only when higher harmonics of motion were at least 10 dB smaller than the fundamental component.

4.3 Measurements of basilar papilla motion

4.3.1 Measurements of displacement vs. lateral position

Figure 4-4 shows trajectories of displacement for four lateral positions on the body of the basilar papilla in one preparation. The image in the background shows an xz cross-section of the papilla (section 3.2.1), with the neural side on the right and the abneural side on the left[†]. The circles show the position of each measured location at each of eight phases of the 5 kHz sound stimulus; the filled circles indicate the location at the peak of the electrical stimulus driving the piezoelectric disk. At each location, the papilla moved in an elliptical pattern. In this plot the displacements have been magnified by a factor of 5 relative to the positions of structures to make the elliptical trajectories more evident. Displacements in each direction were nearly sinusoidal; higher harmonics were more than 40 dB below the fundamental component. The solid

[†]These cross-sectional images are computed from images taken at different focal planes. They represent thin slices through the tissue rather than side views of the tissue. Such images were used for visualization, but not for quantitative analysis.

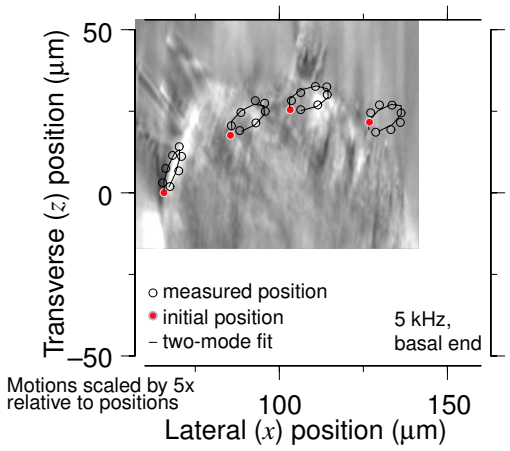

Figure 4-4: Two-dimensional trajectories of displacement of the basilar papilla. The background of this plot shows an xz view of the basilar papilla. Circles show the displacement of four points on the papilla as a function of stimulus phase. The displacements are centered at the location at which they were measured, but the motions are magnified by a factor of five to improve visibility. The solid circle indicates the measured position at the peak of the electrical stimulus. Lines represent the least-squares fit to the data as described in section 4.4.1. The fit had 0.79 μm z translation, 0.85 μm x translation, and 1.123 degrees rotation about the center of the papilla. Rotation and x translation were in phase, and lagged z translation by 0.162 cycle. The rms error of the fit was 0.130 μm. Stimulus was 120 dB SPL in fluid at 5 kHz.

lines in the figure denote the best fit of a rigid-body model of papilla displacement to the measurements. This fit is discussed further in section 4.4.1.

Figure 4-5 shows similar trajectories from five preparations. Each trajectory was measured near the basal end of the papilla, at a stimulus frequency between 3 and 4 kHz. In each preparation, the papilla moved elliptically, although the shapes of these ellipses varied across preparations. In each preparation, the shapes of the elliptical motions varied with position in a systematic manner. For each preparation, the major axis of the ellipses was largely in the z direction near the abneural edge of the papilla, and largely in the x direction near the neural edge. In addition, the ellipses were more nearly circular near the neural edge than near the abneural edge. When viewed with the neural side of the papilla on the right, the elliptical motion was typically in a clockwise direction; that is, x displacement lagged z displacement.

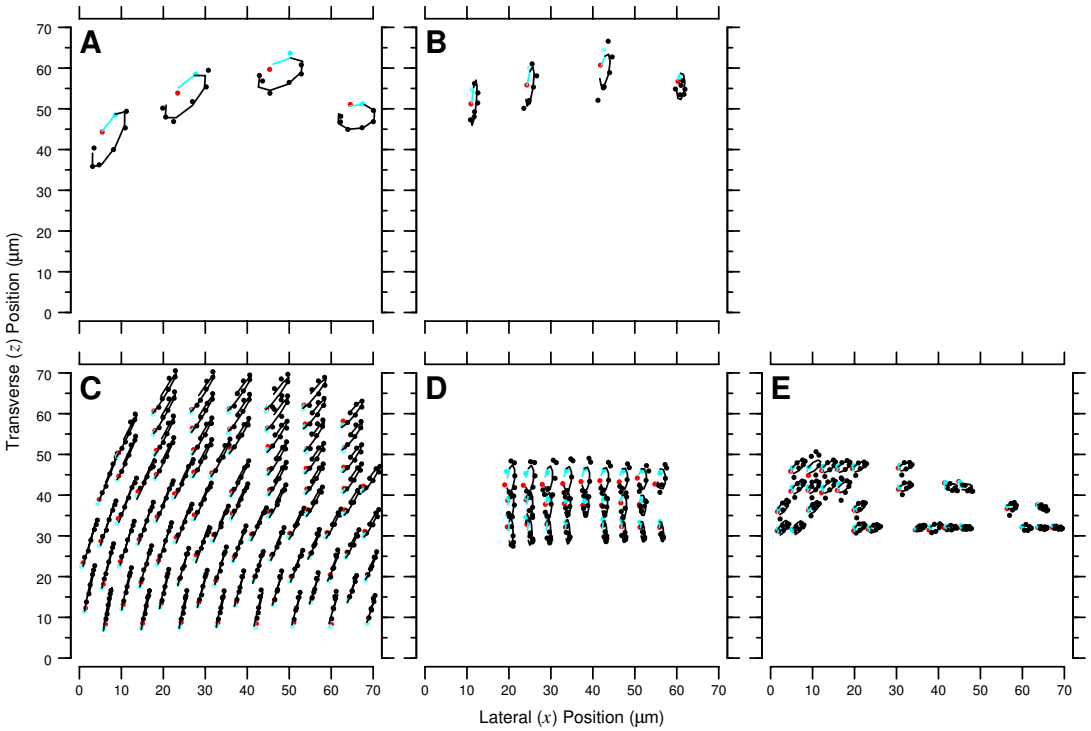

Figure 4-5: Elliptical motion of the basilar papilla in five preparations. These plots show the measured displacement of multiple locations at the basal end of the basilar papilla. In each plot, the neural edge of the papilla is to the right. The motion at each location was primarily elliptical. The tallest ellipses were typically at the abneural edge, and the widest were typically at the top center of the papilla. Symbols are as in figure 4-4, Dots show the measured displacements. Red (dark gray) dots are the position at the peak of the electrical stimulus; cyan (light gray) dots are the position at the next measured phase. Motions are magnified by a factor of ten relative to positions, except in figure **C**, for which the magnification is a factor of five. Stimuli were sound pressures at 3981 Hz (**A**), 3746 Hz (**B**), 3834 Hz (**C**), 3000 Hz (**D**), 3464 hz (**E**), 120 dB SPL. Solid lines show the best fit of a rigid-body model, described in section 4.4.1. The cyan (light gray) portion of the line connects the first two phases. Measurements at some locations were omitted for clarity.

4.3.2 Frequency dependence of motion of the basilar papilla

The displacement of the basilar papilla was frequency dependent in each preparation. Figure 4-6 shows the fundamental component of motion of the abneural edge of the basilar papilla as a function of frequency for four preparations (for experiment **D**, our noise criterion rejected most measurements at the abneural edge). Displacements were measured at the basal end of the basilar papilla. Although there was significant variability across preparations, several trends are evident. First, x displacement peaked at a frequency between 3.5 and 6 kHz for each preparation. Peaks in x displacement in this frequency range were also observed qualitatively in at least twelve prepara-

tions. Second, z displacement was either largely independent of frequency or had a frequency dependence similar to that of x displacement. Third, at low frequencies x and z displacement were in phase, but at higher frequencies x displacement lagged z displacement by as much as 0.5 cycles. Motion in the y direction was typically near the noise floor of our measurements, and is not shown here.

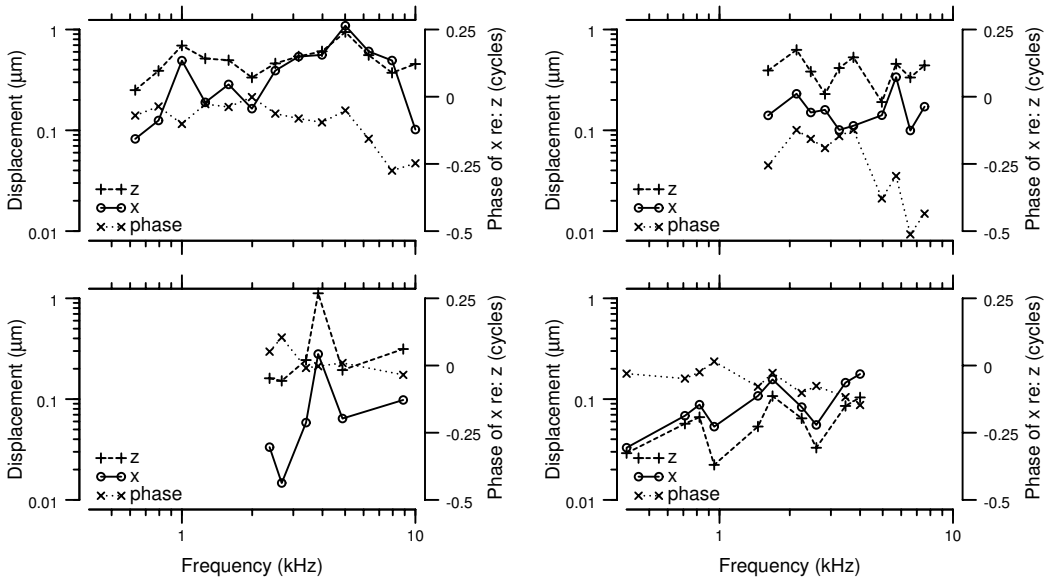

Figure 4-6: Displacement of the basal end of the basilar papilla vs. frequency. Plots show the measured displacement near the abneural edge of the papilla near the basal end from four preparations. The three curves on each plot show x and z displacement magnitude, and the phase of x relative to z displacement for each preparation. The left axis shows the scale for the displacement magnitudes, the right axis shows the scale for the phase. For each preparation, x displacement had a peak between 3.5 and 6 kHz. For some preparations, z displacement was independent of frequency; for others, z displacement had a frequency dependence similar to that of x displacement. At low frequencies, x and z displacement were in phase; at higher frequencies, x increasingly lagged z.

4.3.3 Motion of the basilar papilla vs. longitudinal position

Figure 4-7 shows the displacement of the basilar papilla, measured at the abneural edge, as a function of longitudinal position. Measurements are shown for the five preparations of figure 4-5, at the stimulus frequencies reported in that figure. The magnitude of x motion varied by nearly an order of magnitude across preparations. For most preparations, however, x displacement at the basal end was between 0.1 and

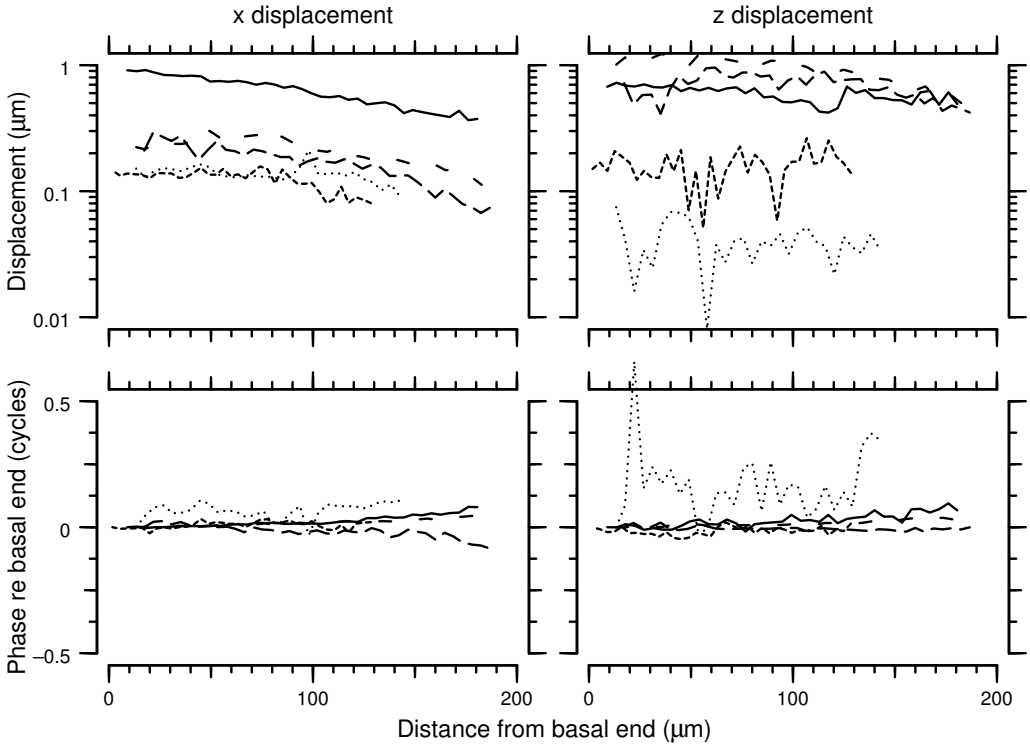

Figure 4-7: Displacement of the basilar papilla vs. longitudinal position. Plots show the measured displacement near the abneural edge of the papilla as a function of longitudinal position for five preparations. Measurements were made at a frequency between 3 and 4 kHz for each preparation. The plots on the left show x displacement, those on the right show z displacement. For each preparation, motion in both x and z directions was largest at the basal end, and decreased by a factor of two to three along the length of the papilla. The phase of motion was relatively constant along the length of the papilla, with a slight tendency for the apical end to lead the basal end.

0.3 μm. The magnitude of z displacement also varied significantly, but was typically between 0.7 and 1 μm near the basal end. For each preparation, x and z displacements were largest at the basal end, and decreased by a factor of 2–3 along the length of the papilla. In most preparations, both x and z displacements at the basal end lagged those at the apical end, but this lag was less than 0.125 cycles.

4.3.4 Phase of x relative to z displacement

Figure 4-8 shows the phase lag from z to x displacement for all of the measurements used in this study. For 75.4% of the measurements, x displacement lagged z displacement. For 4.6% of the measurements, x displacement led z displacement by more than $\frac{1}{16}$ of a cycle. The remaining 20% had x leading z displacement by less than

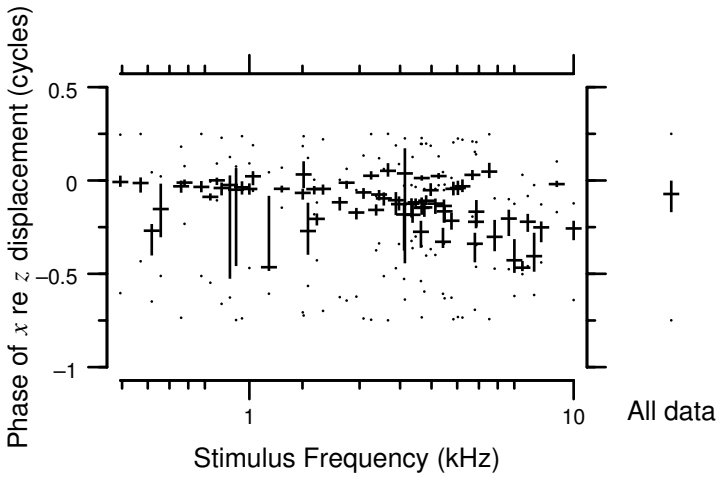

Figure 4-8: Phase of x relative to z displacement. This plot summarizes the phase lag from z to x displacement as a function of frequency for the papillae in this study. For each papilla at each frequency, measurements from all radial and longitudinal positions were combined into a histogram. The horizontal bar for each histogram indicates the median value, the vertical bar indicates the interquartile range, and the dots represent the full range of measurements. Phases that fell above 0.25 or below -0.75 cycles were wrapped into this range. The median values and interquartile ranges were almost all at or below 0 cycles, indicating that x displacement typically lagged z displacement. A total of 75594 measurements are included here, of which 56976 had a relative phase less than zero, and 3453 had a relative phase $> \frac{1}{16}$ cycle. The box-and-whisker plot to the right of the right-hand axis shows the histogram for all 75594 measurements.

$\frac{1}{16}$ cycle. There is a trend for the phase lag to increase with frequency. A lag of x displacement relative to z displacement corresponds to clockwise elliptical motion of the basilar papilla.

4.4 Rigid-body fits to the motion

4.4.1 Fitting elliptical motion with the sum of translational and rotational motion

As seen in figures 4-4 and 4-5, each point in a radial cross-section of the papilla traced out a closed loop during a cycle of motion. The shapes of these ellipses varied with lateral position. These trajectories can be modeled by considering the papilla to be a rigid body with a translational and a rotational component of motion. When the

rotations are small enough that $\sin x \approx x$, the resulting trajectories are described by

$$\begin{aligned} x_p(t) &= x_r \cos(\omega t) + x_i \sin(\omega t) + (p_z - c_z)(\Theta_r \cos(\omega t) + \Theta_i \sin(\omega t)) \\ z_p(t) &= z_r \cos(\omega t) + z_i \sin(\omega t) + (c_x - p_x)(\Theta_r \cos(\omega t) + \Theta_i \sin(\omega t)), \end{aligned} \tag{4.3}$$

where $x_p(t)$ and $z_p(t)$ are the lateral and transverse displacements of point p as a function of time, p_x and p_z are the x and z positions of point p (which can be assumed constant if the motions are small compared to the distance from p to the center of rotation c), c_x and c_z are the center of rotation of the rotational mode, Θ_r and Θ_i are the real and imaginary components of rotation, x_r and x_i are the real and imaginary components of x motion, z_r and z_i are the real and imaginary components of z motion, and ω is the angular frequency of motion. Each of these equations can be written in the form $A\cos(\omega t + \phi)$, so equations 4.3 are the parametric equations for an ellipse.

Equations 4.3 have eight free parameters: the real and imaginary components of x, z, and Θ motion, and the center of rotation (c_x, c_z). To find the best-fit values of these parameters, we perform a least-squares fit of equations 4.3 to the measured displacements of several points at each longitudinal position (as in figures 4-4 and 4-5). The values of Θ_r and Θ_i are uniquely determined by the least-squares fit; however, the other parameters are not. Changes in c_x can be offset by changes in z_r and z_i, and changes in c_z can be offset by changes in x_r and x_i. To find the best fit, we fix the center of rotation in the center of the papilla and fit the other six parameters.

Figures 4-4 and 4-5 show the best fit of equations 4.3 (solid lines) to the measured motions. The best-fit parameter values for each preparation are shown in table 4.1. For each fit, the rms error is smaller than the rms displacement, indicating that this rigid-body model captures a large fraction of the motion of the basilar papilla. Equations 4.3 provided similarly good fits to measured motions at other frequencies and longitudinal positions.

Figure 4-9 shows the normalized error of the fit as a function of the rms displacement of the basilar papilla. The error was computed separately for each frequency and longitudinal position. The rms error is computed as the rms difference between

Figure	Stimulus Frequency (Hz)	x Mag (μm)	x Phase (cycles)	z Mag (μm)	z Phase (cycles)	Θ Mag (degrees)	Θ Phase (cycles)	CV $\frac{\text{std.dev}}{\text{mean}}$
A	3981	0.445	0.308	0.466	0.167	0.510	0.273	0.16
B	3746	0.070	-0.104	0.440	0.227	0.368	-0.154	0.39
C	3834	0.374	0.092	0.862	-0.389	0.425	0.048	0.12
D	3000	0.043	-0.419	0.305	0.220	0.234	0.357	0.47
E	3464	0.096	-0.432	0.092	0.338	0.172	0.454	0.41

Table 4.1: Best-fit values of the parameters of equations 4.3 to the measured motions of figure 4-5. The first column refers to the plots in figure 4-5; the second column lists the stimulus frequency for those measurements. The next six report the magnitude and phase of the best-fit parameters. The final column reports the CV, which is the rms error of the fits divided by the rms displacement of the papilla. Magnitudes are reported in μm, except for the magnitude of Θ in degrees. Phases are reported in cycles.

the measured displacement and the best-fit displacement at each location for each of eight stimulus phases at the given frequency and longitudinal position. The normalized error is the rms error divided by the rms displacement. Although the normalized error varied somewhat with rms displacement, the median value was typcally below 0.3, and the interquartile ranges were below 0.5. Most of the error seems to come from a few outlying points (see figure 4-5).

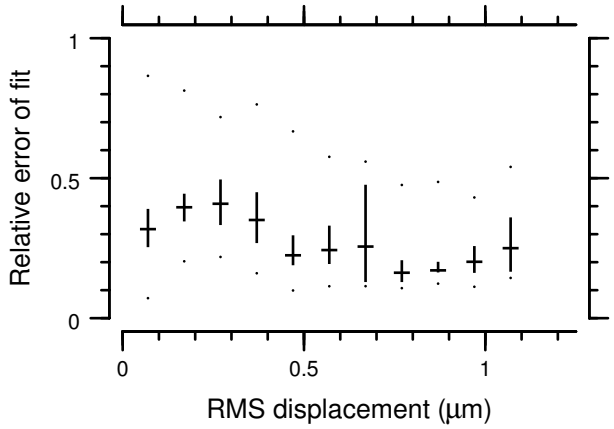

Figure 4-9: Normalized errors of the fits. This plot shows the median (horizontal line), interquartile range (vertical line), and full range (dots) of the normalized error of the fit as a function of rms displacement of the papilla. The normalized error is the rms error divided by the rms displacement of the papilla. Although the normalized error varied with frequency, the median values were all ≤ 0.4, and the interquartile ranges were ≤ 0.5.

4.4.2 Frequency dependence of translational and rotational components

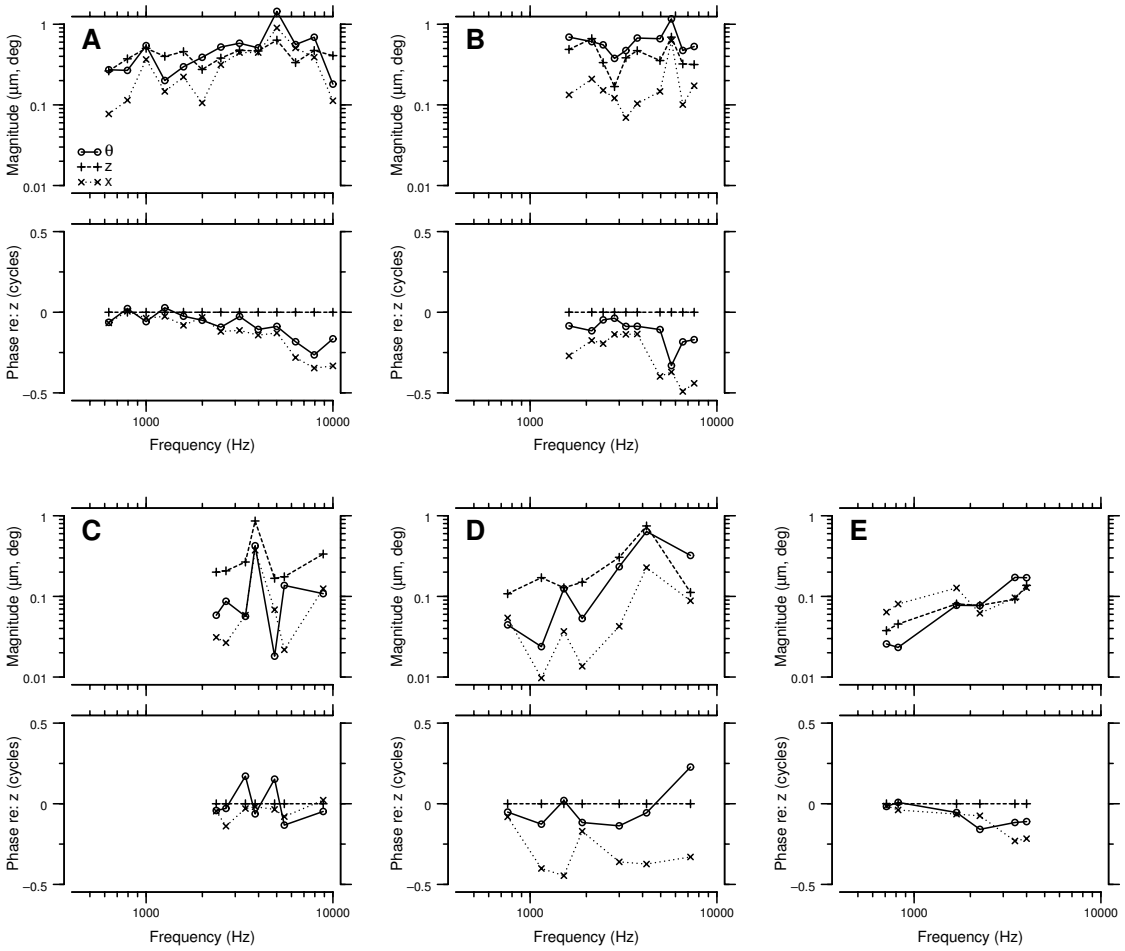

Figure 4-10: Best-fit translational and rotational components of motion of the basilar papilla vs. frequency. Plots show the magnitude and phase of the fits of equation 4.3 to the measured motions as a function of frequency. The five plots are for the same preparations as in figure 4-5. Phase is measured relative to the phase of z displacement.

The fitting procedure described above was repeated at each longitudinal position as a function of frequency for five preparations. The resulting parameters for the fits are shown in figure 4-10. The frequency dependence is similar to that seen in figure 4-6; however, whereas figure 4-6 shows measured x and z displacement at a single location vs. frequency, figure 4-10 shows the best-fit rigid body motion of x, z, and Θ to all measured locations at one longitudinal position.

For each preparation, Θ has a peak in magnitude between 3.8 and 5.7 kHz. For

four of the five, this peak is between 5 and 5.7 kHz (in preparations **D** and **E**, these peaks are not evident in figure 4-10; however, qualitative observations made during the experiment place the peak frequency near 5.5 and 5.2 kHz, respectively, for the two experiments). The frequency dependence of x is similar to that of Θ. The magnitude of z also has a peak at the same frequency as Θ, but this peak tends to be somewhat less sharp. In addition, Θ and z are in phase at low frequencies, but Θ typically lags z by up to 0.25 cycles at high frequencies.

4.5 A mechanical model of the basilar papilla

4.5.1 Deriving the model from anatomy and measurements

The anatomy of the alligator lizard basilar papilla suggests a simple mechanical model which is consistent with the results shown in sections 4.3 and 4.4. The basilar membrane on which the basilar papilla rests is asymmetric; the neural side is about half as wide and twice as thick as the abneural side (figure 1-3). Consequently, pressure across the basilar membrane can induce translation as well as rotation of the basilar papilla. The amount of translation is determined by the compliance of the basilar membrane, the mass of the basilar papilla, and the viscous damping of the fluid. The amount of rotation is determined by the rotational compliance of the basilar membrane, the moment of inertia of the basilar papilla, and the viscous damping of the fluid. Thus the anatomy suggests that both translation and rotation should each have the frequency dependence of a second-order system, but that these frequency dependences may differ. Figure 4-11 shows a schematized representation of this mechanical system.

The measurements in section 4.3 show that the phase lag from translation to rotation increases with frequency. This difference in the frequency dependences of translation and rotation suggests that the basilar papilla has two modes of motion. By teasing apart the modes, we can more accurately define a mechanical model of the basilar papilla. If we assume that the two modes correspond to translation and

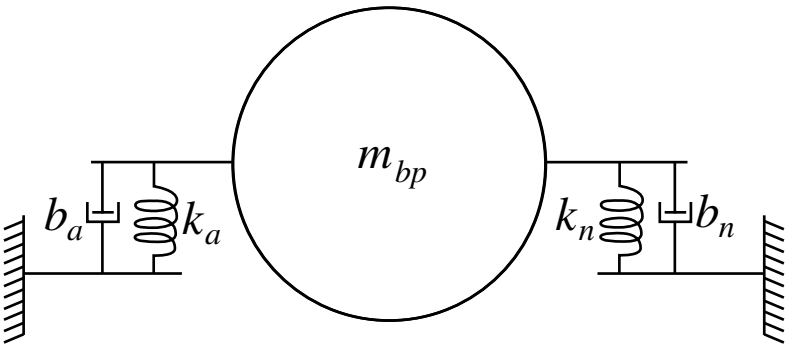

Figure 4-11: A mechanical model of the basilar papilla. The basilar papilla is represented as a circular structure with a mass m_{bp}. This mass is supported by two springs, k_a and k_n, representing the stiffness of the basilar membrane on the abneural and neural sides, respectively. These two springs need not have the same stiffness. Damping elements b_a and b_n are included to represent the viscous damping of the fluid in response to basilar papilla motion. The model allows the central mass to undergo both translational and rotational motion. Although the element names are chosen here to represent structures in the alligator lizard cochlea, the model represents the mechanical behavior of any mass supported by two compliant structures.

rotation, the task of separating them is simplified. The rotational component of motion then clearly represents the rotational mode. The translational component of motion, however, includes both the translational and rotational modes of motion. The reason for this is that the center of rotation was fixed at the center of the papilla. If we allow the center of rotation to vary, we can subtract a multiple of the rotational motion from the translational motion, as described in equation 4.3.

The x component of translation has a frequency dependence similar to Θ in both magnitude and phase. Thus subtracting a multiple of the Θ component from the x component should make the x component negligible. The magnitudes of the z component are often similar to those of the Θ component, but the phases differ. Thus subtracting a multiple of the Θ component from the z component will not eliminate z. Typically, rotation lags translation in the z direction. For this reason, and because previous measurements of basilar membrane motion show little frequency dependence, we expect that the translational mode is largely independent of frequency. Thus we can separate the modes by finding a new center of rotation which

1. minimizes the mean magnitude of x translation, and

2. minimizes the variance of z translation.

Figure 4-12 shows the result of the modal decomposition process described above. The x translation component was not completely eliminated; however, the magnitude of x translation was reduced. The phase of x translation shows no systematic pattern with frequency, although x translation typically lagged z translation. The z translational mode is nearly independent of frequency, with a phase near 0 cycles. The magnitude of the z translational mode varies significantly across preparations. The Θ rotational mode has a frequency dependence that is unchanged compared to that of figure 4-10. As a result of this modal decomposition, the center of rotation was typically shifted in the positive z direction and towards the neural edge of the basilar papilla.

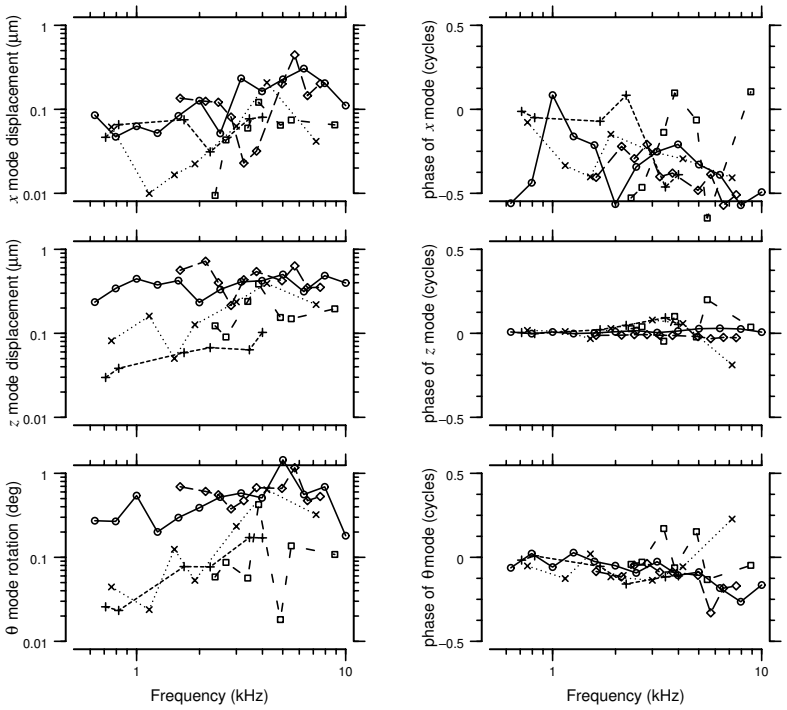

Figure 4-12: Modal decomposition of basilar papilla motion. The plots in this figure show the individual modes isolated from the data in figure 4-10. Translation in the x direction had a magnitude typically below 0.2 μm, with a phase that shows no clear trends with frequency. Translation in the z direction had a magnitude that was largely independent of frequency, with a phase near 0 cycles. Rotation has a peak in magnitude near 5 kHz, with a phase lag that increases with frequency.

Based on this modal decomposition, we model the translational admittance as a

compliance and the rotational admittance as a compliance, moment of inertia, and damping element in series. The second-order model of the rotational compliance is evident from the frequency dependence of the Θ component. The compliant model of the translational compliance is evident from the fact that rotation lags translation, so the resonant frequency for translation must be higher than that for rotation. Below the resonant frequency, the admittance will be dominated by the compliance. A compliant translational mode is also supported by the fits shown in figure 4-10 plot **A**. In this plot, the rotational mode has a prominent peak at 5 kHz, but the translational mode does not; by a fortunate choice of the center of rotation, the modes are already separated. In this case the translational mode is independent of frequency, consistent with a compliance.

The mechanical model described in the previous paragraphs and shown in figure 4-11 can be represented by an equivalent electrical circuit, as shown in figure 4-13. In this model, the pressure difference P across the basilar membrane acts on the area of the basilar membrane to generate a force F. This force acts on the compliance C_m of the basilar membrane to cause a velocity V_{BM}. The same force, via an effective lever arm L, applies a torque τ on the basilar papilla in the rotational domain to cause a rotational velocity $\dot{\theta}$. At low frequencies most of the torque acts on the compliance C_r to rotate the papilla. At high frequencies, most of the torque acts on the moment of inertia J_r. At the resonant frequency, the torque is resisted by fluid damping R_r.

4.5.2 Estimating model parameter values from measurements

The model in figure 4-13 has six parameters: C_m, C_r, J_r, R_r, A, and L. The input pressure was 120 dB SPL, or 28 $\mathrm{Pa_{peak}}$. If we estimate the two transformer ratios A and L, we can determine the other parameter values from the measurements. The area A of the basilar membrane has been measured to be 0.03 mm^2 (Rosowski et al., 1985). We can estimate L by assuming that the net force due to the acoustic stimulus acts on the center of the basilar membrane, and that the center of rotation is in the center of the papilla. From these assumptions and figure 1-3, we estimate $L = 7\mu\mathrm{m}$.

The compliance $C_m = \frac{P \times A}{|z|}$ can be estimated from the low-frequency asymptote

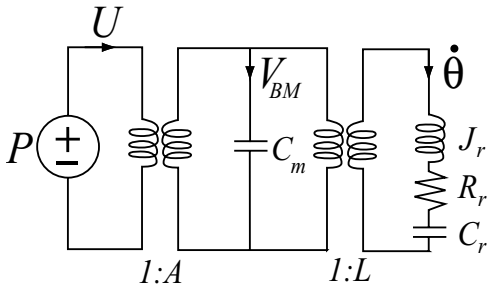

Figure 4-13: Circuit model of the basilar papilla. The circuit model contains three domains. The input to the system, on the left, is in the acoustic domain; the drive P is the pressure difference across the basilar membrane. The area of the basilar membrane, A, transforms the acoustic to the mechanical domain. In the mechanical domain, the basilar papilla looks like a compliance C_m; that is, displacement in the z direction is proportional to force. On the right, an effective lever arm L converts translational to rotational motion. In the rotational domain, the basilar papilla looks like a second order system consisting of a moment of inertia J_r, a rotational compliance C_r, and a viscous damper R_r.

of magnitude of the z component of motion, which is between 0.1 and 0.4 μm for most preparations. The resulting compliance is $0.12 \leq C_m \leq 0.48$ m/N. Similarly $C_r = \frac{P \times A \times L}{|\Theta|}$. The low-frequency asymptote of rotation is between 0.05° and 0.5°, so $1.04 \cdot 10^8 \leq C_r \leq 1.04 \cdot 10^9$ rad/N·m. From the peak frequency of rotation f_p, we can determine $J_r = \frac{1}{C_r (2\pi f_p)^2}$. The resulting estimates of J_r range from $1 \cdot 10^{-18}$ to $8.4 \cdot 10^{-18}$. At the peak frequency the net impedance of C_r and J_r is zero, so $R_r = \frac{P \cdot A \cdot l}{2\pi f_p |\Theta|}$. The resulting estimates of R_r range from $7.4 \cdot 10^{-15}$ to $3.3 \cdot 10^{-14}$ N·m·s/rad.

4.6 Discussion

4.6.1 Gross motions are comparable to those measured *in vivo*

Peake and Ling (1980) measured the velocity of the basilar membrane in the transverse direction using the Mössbauer technique, and found it to be a linear function of sound pressure. In response to a 75 dB SPL tone at 1.4 kHz, they measured a velocity of −25 dB re 1 cm/s, which corresponds to a peak displacement of 90 nm. Based on our estimate of a middle-ear pressure gain (figure 1-5) of 35 dB at this frequency, we

expect our stimuli to correspond to 85 dB SPL at the eardrum, which would result in a basilar membrane transverse displacement of 280 nm peak based on the Peake and Ling data. At 1585 Hz in one preparation, we measured basilar papilla transverse displacements of 330 and 550 nm peak on the neural and abneural sides, respectively. Thus the transverse motions measured in this study are roughly comparable to those measured *in vivo* using a different technique. However, there are many caveats to comparing these studies directly:

1. Our comparison uses a rough estimate of the middle ear pressure gain.

2. In some preparations, displacements in the transverse direction were considerably smaller than in others (figure 4-7).

3. The efficiency of coupling sound pressure to the papilla in our experiment chamber may differ from that *in vivo*.

4. Peake and Ling measured motion on the perilymphatic surface of the basilar membrane, but we measured motion on the endolymphatic surface of the basilar papilla.

5. The Mössbauer source used by Peake and Ling was $\sim 40 \times 40$ μm, much larger than our measurement regions; the motion of the $5 \times 5 \times 5$ μm regions measured here may differ from the average motion of a larger region.

4.6.2 *xz* cross-sections of the basilar papilla move as a rigid body

Equations 4.3 describe elliptical motion of a rigid body. If the motion of every point in a lateral cross-section of the basilar papilla satisfies these equations, then this lateral cross-section moves as a rigid body. Figures 4-4 and 4-5 show that to a first approximation, the motions of all measured points satisfy equations 4.3. The rms error of the fit in figure 4-4 is 0.175 μm. The average rms error of the fit for each frequency and longitudinal position across preparations was 0.108 ± 0.077 μm

(mean±s.d.). The largest rms error was 1.59 μm, but only 4 of 1665 fits had an rms error larger than 0.5 μm. Thus for any xz cross-section, the papilla can be accurately modeled as a rigid body undergoing translation and rotation.

4.6.3 The basilar papilla has multiple modes of motion

Points on the reticular lamina of the basilar papilla follow elliptical trajectories in response to sinusoidal sound stimulation. Elliptical motion in two dimensions is equivalent to sinusoidal motion in each dimension, with a relative phase difference between the motion in each dimension. Since the relative amplitudes and phases of the sinusoids change with position (that is, the shape and orientation of the ellipses change), as in figure 4-4, the motion is well fit by the sum of one translational and one rotational component, as described in equations 4.3.

Hemmert *et al.* (2000) point out that elliptical motion can result from phase errors in motion estimates. We believe that our measurements accurately describe the motion of the papilla for several reasons. First, the phase errors in the Hemmert *et al.* study resulted from their use of two different measurement techniques to measure motions in different directions; we use a single method to measure motions in all three dimensions. Second, elliptical motion is visible to the eye when viewing the images in sequence. Third, our measurements were typically at least 20 dB above the noise floor, and we rejected measurements which were non-sinusoidal; the phase error in the remaining measurements is small. Fourth, the shapes of the ellipses change systematically with position.

Elliptical motion alone is not sufficient evidence for multiple modes of motion (for example, the crankshaft of a car has a single, circular mode of motion). However, as shown in figure 4-10, the frequency dependence of the translational and rotational components of motion differ. This difference allowed us to separate the two modes of motion. These results demonstrate that a single cochlear structure can exhibit multiple modes of motion in response to sound stimulation.

4.6.4 Relative shearing deflection at the reticular lamina is enhanced by two-mode motion

Hair bundle deflection in this cochlea is believed to be driven by shearing deflection at the reticular lamina (Freeman and Weiss, 1990a; see also chapter 6) in the direction of maximum sensitivity (Shotwell et al., 1981). Because of the circular shape of the papilla in cross-section, the direction of shearing displacement at the surface of the papilla changes with lateral position on the papilla (Mulroy, 1968; Mulroy, 1974; see also figure 3-2). Thus the drive for hair bundle deflection depends not only on the magnitudes and phases of the two modes of papilla motion, but on the lateral position of the hair bundle.

In previous models of the basilar papilla (Weiss and Leong, 1985a), shearing displacement at the surface of the basilar papilla is driven by rotation of the papilla about a point (c_x,c_z) near the neural edge of the basilar membrane. For a papilla with radius R centered at (r_x,r_z), the shearing displacement at any location (p_x,p_z) on the surface due to rotation is given by

$$d_r = \frac{(p_z - r_z)(p_z - c_z) + (r_x - p_x)(c_x - p_x)}{R}\Theta. \tag{4.4}$$

The value of d_r depends strongly on position; for a location near the neural side of the basilar papilla, d_r will be zero. However, allowing the papilla to translate as well as rotate eliminates this problem; translation in z causes shearing displacement at all locations except the top center of the papilla. Thus all hair bundles are subjected to shearing displacement due to translation, rotation, or both.

Figure 4-14 shows the estimated relative shearing displacement at the surface of the basilar papilla as a function of position for the two cases described above. The prediction for pure rotation was calculated from equation 4.4. The prediction for two-mode motion was calculated using the parameters from figure 4-4. Except at the neuralmost edge, the relative shearing displacement is larger for two-mode motion than for pure rotation. However, there are no hair bundles at the neuralmost edge of the papilla (see figure 1-3). Thus the shearing displacement that drives hair bundle

deflection in the free-standing region is more uniform with position for two-mode motion than for pure rotation.

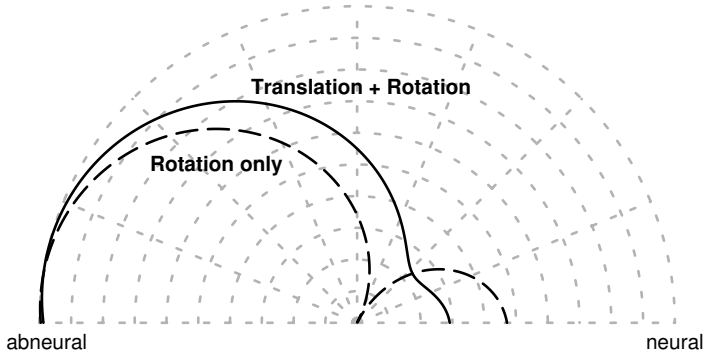

Figure 4-14: Shearing displacement at the reticular lamina. This plot shows the shearing displacement relative to that at the abneural edge as a function of polar position along the top half of the basilar papilla. The dashed line shows the predicted shearing displacement if the basilar papilla underwent pure rotation about a point near the neural edge of the basilar membrane. The solid line shows the estimated shearing displacement from the best fit to the motions in figure 4-4. Except near the neural edge, the relative shearing motion due to the sum of translation and rotation is larger than that due to rotation alone.

4.6.5 Comparison of estimated model parameters to measurements

From the measurements in this study we were able to derive a mechanical model that describes the motion of the basilar papilla. This model captured the basic features of basilar papilla motion in all preparations studied, but the model parameters varied significantly from one preparation to the next. To determine whether these model parameters are physiologically reasonable, we can compare them to estimates from anatomy and from previous studies on the alligator lizard cochlea.

Rosowski *et al.* (1985) present measurements of the acoustic impedance at the tympanic membrane before and after destroying the cochlear partition. From those measurements they derive a mechanical model in which the basilar papilla is represented as a compliance. This model is consistent with ours for two reasons. First, below 5 kHz the rotational domain is also dominated by a compliance, so at the frequencies used in their study the entire basilar papilla appears compliant. Second,

the impedance of the rotational domain in our model is large compared to that of the translational domain at all frequencies; thus the admittance seen at the tympanic membrane is dominated by the translational compliance. Rosowski *et al.* report an acoustic compliance of $5.7 \cdot 10^{-16}$ m^3/Pa. When reflected into the mechanical domain, this compliance is 0.63 m/N; however, they also report an "effective basilar membrane area" of 0.07 mm^2; using this value gives a mechanical compliance of 0.12 m/N. Thus the range of compliances estimated in the current study is roughly consistent with those estimated from measurements at the tympanic membrane.

For a cylinder rotating about a point at a distance d from the center, the moment of inertia J_r is given by

$$J_r = \rho l(\frac{\pi r^4}{2} + \pi r^2 d^2), \tag{4.5}$$

where ρ is the mass density of the cylinder, l is the length, and r is the radius. From this equation we can estimate the effective radius of the basilar papilla by assuming that the basilar papilla length is 400 μm, the density is that of water (ρ = 1000 kg/m^3) and the center of rotation is near the neural edge (d = 30 μm). With these values our estimate of J_r gives an effective radius of $35 \leq r \leq 60$ μm.

The effective radius predicted from the best-fit J_r is somewhat larger than the measured radius of the basilar papilla, which is roughly 30–35 μm. This difference is due partly to the entrained motion of fluid; at 5 kHz (the frequency at which J_r was determined), the boundary layer thickness is about 8 μm. In addition, the hair bundles that project from the basilar papilla entrain fluid. This entrained fluid increases the effective radius r, and also increases the effective distance d from the center of rotation to the center of mass; both effects would manifest as an increase in the estimate of r.

The drag force on a cylinder moving in fluid is (Munson et al., 1990)

$$\mathcal{D} = \frac{1}{2}\rho U^2 A C_D, \tag{4.6}$$

where ρ is the density of water (1000 kg/m^3), U is the velocity of water relative to the cylinder ($2\pi \cdot 5000$ s$^{-1} \times 1 \cdot 10^{-6}$ m), A is the area of the cylinder facing the fluid (400

μm $\times$ 30 μm), and C_D is the drag coefficient, given by $C_D = \frac{5.93}{\sqrt{\text{Re}}} + 1.17$, where Re is the dynamic Reynolds number (roughly 0.8 at 5 kHz for the displacements measured in this study). If we compute $\frac{\mathcal{P}}{U}$ and reflect it into the acoustic domain, we get a rotational resistance of $1.4 \cdot 10^{-16}$ N·m·s, more than an order of magnitude smaller than our estimate of R_r. Our estimate of R_r is almost certainly too large, since the frequency at which the peak was measured was probably not the actual resonant frequency f_p. Additional fluid drag is most likely introduced by the hair bundles. Therefore, this calculation suggests that most of the energy loss in this cochlea is due to viscous drag on the hair bundles rather than motion of the basilar papilla.

4.6.6 Phase lag between translational and rotational modes — the 'missing low-pass filter'

As mentioned in the introduction, models of this cochlea introduced a first-order mechanical low-pass filter, but did not specify the physical basis for this filter. This filter was necessary to explain the high-frequency slopes of tuning curves from hair cells in the free-standing region. In this study, we see an 0.25 cycle phase lag between the translational and rotational modes of motion. This phase lag suggests the presence of a low-pass filter between the translational and rotational modes. Our mechanical model includes a similar phase lag between translational and rotational components of motion. Thus the conversion from translational to rotational motion may provide a physical basis for the low-pass filter required by models. However, since at least some hair bundles are sensitive to the translational mode of motion, we expect variations of as much as 6 dB/octave in the high-frequency slopes of tuning curves of auditory nerve fibers. Indeed, such variations have been seen in auditory nerve fiber recordings (Weiss et al., 1976).

4.6.7 Papilla resonance is beyond range of best frequencies

The resonant frequency of the basilar papilla is typically at or above 5 kHz. This resonance is largest at the basal end. Hair cells in this region have best frequencies

between 3 and 4 kHz. Thus the papilla resonance at the basal end is just beyond the range of frequencies to which hair cells in this cochlea are most sensitive. By 5 kHz, hair cells with best frequencies of 3–4 kHz are 20–40 dB less sensitive than at CF (Weiss et al., 1976). Thus the mechanical resonance of the papilla does not appear to play a significant role in determining the frequency selectivity of the cochlea. However, since electrical responses to sound were measured in auditory nerve fibers at frequencies up to 12 kHz, the mechanical resonance of the papilla is likely to affect these high-frequency responses.

4.6.8 The relation between basilar membrane motion and basilar papilla motion

Although our measurements of the transverse component of basilar papilla motion correspond roughly to previous measurements of basilar membrane motion, the shearing displacement at the reticular lamina cannot be predicted from the transverse motion of the basilar membrane. The receptor organ, and hence the reticular lamina, demonstrates modes of motion that are not present in measurements of transverse motion of the basilar membrane, and these modes of motion play an important role in cochlear function. In the mammalian cochlea, our understanding of mechanics comes largely from measurements of basilar membrane motion. Given the complexity of the organ of Corti relative to the alligator lizard basilar papilla, it is likely that the mammalian cochlea also has multiple modes of motion (see section 1.2), some of which are likely to play an important role in cochlear function. Thus it may not be possible to infer cochlear function from measurements of basilar membrane motion alone.

Chapter 5

Micromechanics of the Tectorial Region

Abstract

Relations among motions of the reticular lamina (RL), tips of hair bundles, and endolymphatic surface of the tectorial membrane (TM) in the tectorial region of the excised cochlea of the alligator lizard (*Gerrhonotus multicarinatus*) were investigated. Sound stimuli from 105–140 dB SPL measured in the fluid adjacent to the basilar membrane (equivalent to approximately 90–105 dB SPL at the tympanic membrane), with frequencies from 40 Hz to 4 kHz, were used to excite cochleae in eight preparations. Images taken with a video microscopy system were analyzed to determine three-dimensional motions of cochlear structures. Motions of these structures were generally broadly tuned in frequency, with peak amplitudes smaller than 1 micrometer peak-to-peak. Four micromechanical relations were investigated as functions of frequency: (1) $\frac{\mathrm{TM}}{\mathrm{RL}}$, the motion of the endolymphatic surface of the TM normalized to RL motion; (2) $\frac{\mathrm{TM-RL}}{\mathrm{RL}}$, the shear between the endolymphatic surface of the TM and the RL, normalized to RL motion; (3) $\frac{\mathrm{Tip-RL}}{\mathrm{TM-RL}}$, the ratio of the deflection of the tips of hair bundles relative to the RL to shear between the endolymphatic surface of the TM and the RL; (4) $\frac{\mathrm{Tip-RL}}{\mathrm{RL}}$, the ratio of hair bundle deflection to RL motion. Although

there was considerable variation across preparations, two trends were evident. First, the magnitude of $\frac{\mathrm{TM}}{\mathrm{RL}}$ was less than 2. Second, none of the micromechanical relations showed evidence of sharp frequency selectivity in either the magnitude or phase. The measured magnitudes of $\frac{\mathrm{TM}}{\mathrm{RL}}$ are small compared to those predicted by resonant TM models of cochlear micromechanics. This difference suggests that TM resonance does not significantly contribute to the frequency selectivity of the alligator lizard cochlea. The frequency selectivity of the measured micromechanical relations is broad compared to that seen in responses of auditory nerve fibers innervating the TM region. Thus, mechanisms other than mechanical resonance most likely determine frequency selectivity in the tectorial region of the alligator lizard cochlea.

Key words: Hearing, cochlea, basilar papilla, auditory mechanics, tectorial membrane, hair cell, frequency selectivity, microscopy, computer vision, alligator lizard.

5.1 Introduction

The sensitivity, frequency selectivity, and nonlinearity of the cochlea all depend on the micromechanical interactions of structures within the cochlea. Although active processes are believed to play a large role in the mammalian cochlea, the passive mechanical properties of cochlear structures affect cochlear function in all species, including mammals. In addition, the mammalian cochlea may be passive at the lowest as well as the highest sound pressure levels (Ruggero et al., 1997). However, our current understanding of the mechanical properties of cochlear structures is limited, particularly at the frequencies of interest for hearing.

Although models can increase our understanding of cochlear function, the complexity of the cochlea requires modelers to make drastic simplifications in order for models to be computationally tractable. Consequently, no single model of cochlear mechanics captures all of the known mechanical behaviors of the cochlea while using physiologically reasonable parameters. In addition, many cochlear models are mutually contradictory. For example, one model (Allen, 1977; Allen, 1980) suggests

that the cochlea is passive and the TM is resonant, while another (Mammano and Nobili, 1993) includes active elements and treats the TM as a mass. To resolve these issues, it is important to measure the mechanical properties of the cochlea.

Observing the interactions of structures in an intact cochlea is the most direct way to understand cochlear micromechanics. Such observations are currently underway in several laboratories (ITER, 1989; Hu et al., 1995; Gummer et al., 1996; Karavitaki and Mountain, 1996; Hu et al., 1999; Hemmert et al., 2000). However, the time-consuming nature of the measurements, combined with the lability of the preparations, makes it difficult to obtain more than a few measurements on any single animal. In addition, geometrical constraints make it difficult to obtain high-resolution images of the mammalian cochlea. We have developed a preparation of the cochlea of the alligator lizard (*Gerrhonotus multicarinatus*) that allows us to overcome these problems. The alligator lizard cochlea is planar, so it can be isolated and imaged with high resolution. The cochlea can be maintained *in vitro* for several hours (chapter 2), allowing measurements three-dimensional motions of cochlear structures with nanometer accuracy (chapter 3).

The alligator lizard cochlea consists of two regions (figure 1-2): a free-standing region in which the hair bundles project freely into endolymph, and a tectorial region in which the bundles project into an overlying tectorial membrane. The frequency selectivity of auditory nerve fibers (ANFs) innervating the tectorial region is similar to that of mammalian ANFs with the same best frequencies, 200–800 Hz (Weiss et al., 1976). However, the alligator lizard cochlea is simpler than the mammalian cochlea in many ways, making it more tractable for study. The basilar membrane moves in phase over its length and is broadly tuned in frequency (Peake and Ling, 1980; but see chapter 4), so the micromechanical properties of the cochlea can be studied without the confounding influence of macromechanical tuning. The cochlea's planar structure allows high-resolution microscopy to image the tectorial membrane (TM), hair bundles, and individual stereocilia across the entire cochlea. From a series of such high-resolution images taken at multiple stimulus phases, the motions of all structures in the images can be determined. The relative motions of various

micromechanical structures can then be determined from the absolute motions.

5.1.1 Micromechanical transfer functions

By comparing the motion of different structures within the cochlea, we can derive a series of "micromechanical transfer functions" that characterize the mechanical properties of the region*. We define the variables TM, Tip, and RL to be the displacement of the TM, tips of hair bundles, and reticular lamina, respectively. Displacement of the TM is measured at the top (endolymphatic) surface. With these definitions, the transfer functions examined in this study are

$\frac{\mathrm{TM}}{\mathrm{RL}}$ the ratio of the displacement of the TM to the displacement of the RL. This ratio provides information about the mechanical properties of the TM, such as whether a mechanical resonance is present.

$\frac{\mathrm{TM-RL}}{\mathrm{RL}}$ the ratio of TM shear (TM − RL) to RL displacement. This ratio describes the transformation from absolute motion of the RL to the relative motion that drives hair bundle deflection.

$\frac{\mathrm{Tip-RL}}{\mathrm{TM-RL}}$ the ratio of hair bundle deflection (Tip−RL) to TM shear. This ratio describes the effectiveness of TM shear at driving hair bundle deflection. Hair bundles attached to the TM are believed to be driven by TM–RL displacement, while unattached hair bundles are believed to be driven by TM–RL velocity (Dallos et al., 1972), or by some combination of velocity and displacement (Freeman and Weiss, 1988).

$\frac{\mathrm{Tip-RL}}{\mathrm{RL}}$ the ratio of hair bundle deflection to RL displacement. This ratio characterizes the entire micromechanical stage of cochlear function.

In this paper, we show that each of these transfer functions is essentially independent of frequency in the tectorial region of the alligator lizard cochlea. Thus mechanical

*Such a derivation assumes that the mechanical properties of the cochlea are linear. Because we typically made measurements at only a single stimulus level for each cochlea, we were not able to assess linearity directly.

tuning does not appear to play a role in determining the frequency selectivity of this region. There is a caveat to this conclusion. Hair cells in this region of the cochlea typically develop blebs when isolated (see chapter 2). Blebs form adjacent to the stereocilia, and may have large effects on the mechanical properties of this region. In addition, we were unable to measure an electrical response to sound in the isolated cochlea. Consequently, the measurements reported in this study may not be indicative of the motions of the cochlea *in vivo*.

A preliminary analysis of these measurements was presented previously (Aranyosi et al., 1998).

5.2 Methods

5.2.1 Biological preparation

Adult alligator lizards (20-49 g) were sacrificed by decapitation and pithing. The dorsal skin and muscle were removed. A scalpel was used to penetrate the posterior semicircular canal and remove the bone covering the sacculus. The saccular membrane was peeled away with fine forceps, and the saccular otoconia were removed by gentle suction. A razor blade shard was used to cut the 8th nerve. Hydraulically actuated forceps mounted on a micromanipulator were used to lift the cochlea out by the 8th nerve. The cochlea was transferred (through air in earlier experiments, through saline in later ones) to the stimulus chamber, which was filled with artificial perilymph. Artificial endolymph was perfused over the apical surface before the vestibular membrane was removed.

Artificial perilymph contained (in mM): Na^{+}, 168; K^{+}, 3; Ca^{+2}, 2; Mg^{+2}, 1.2; Cl^{-}, 174.9; SO_4^{-2}, 2; $H_2PO_4^{-}$, 0.5; D-glucose, 5; Hepes, 5. Artificial endolymph contained (in mM): Na^{+}, 2; K^{+}, 174; Ca^{+2}, 0.02; Cl^{-}, 171.5; SO_4^{-2}, 2; $H_2PO_4^{-}$, 0.5; D-glucose, 5; Hepes, 5. Solutions were adjusted to a pH of 7.30, and had an osmolality of 342$\pm$8 mmol/kg. Both solutions contained MEM essential and non-essential amino acids, and were oxygenated immediately before use. In some experiments Liebowitz' L-15

was used in place of artificial perilymph. All chemicals were purchased from Sigma Chemical Company (St. Louis, MO).

5.2.2 Measurement system

Experiment chamber

The Plexiglas® experiment chamber (figure 4-1) allowed the cochlea to be clamped over a hole separating two fluid spaces. Artificial perilymph was perfused through the basolateral fluid space and artificial endolymph was perfused through the apical fluid space. This separation of fluids allowed us to simulate the *in vivo* cochlear environment. Because perfusion increased the noise of the mechanical measurements, the cochlea was typically perfused between measurements (roughly every 5–10 minutes). The clamping ring encircled the neural limbus and triangular limbus to avoid clamping the basilar membrane or basilar papilla. A piezoelectric disk (Panasonic EFR Series) generated sound waves in the basolateral fluid, and a hydrophone (Model EPB-126W-100G, Entran Devices, Inc., Fairfield NJ) measured the resulting pressure. The bottom surface of the chamber was sealed with a glass coverslip.

Video microscopy

The video microscopy system has been described in detail elsewhere (Davis and Freeman, 1998b; see also chapter 3). The chamber was placed on the stage of a microscope and viewed using brightfield transmitted light illumination. The specimen was viewed through a 63x, 0.9 NA water immersion objective, with a transmitted-light condenser with an NA of 0.8. Images were collected with a 12-bit, 1024x1024 pixel CCD camera (CAD7-1024A, Dalsa Inc., Waterloo, Ontario)[†].

The cochlea was illuminated with an LED (AND190HYP, Purdy Electronics, CA). The light source was synchronized to the acoustic stimulus, allowing us to stop the apparent motion of the cochlea at arbitrary stimulus phases. We typically took images

[†]Early experiments used a 40x, 0.75 NA objective, an 0.6 NA condenser, and a 12-bit, 576x384 pixel CCD camera (CH250A, Photometrix Inc., Tucson, AZ).

at eight evenly-spaced stimulus phases. This process was repeated at several focal planes to give us three-dimensional information about the positions of cochlear structures. We applied a two-point flat fielding technique (Hiraoka et al., 1987; Healey and Kondepudy, 1994) to the images to correct for spatial inhomogeneities in the imaging system. The resulting corrected images have pixel values that are proportional to the brightness of the specimen.

Image analysis

From a series of images of the cochlea at different phases of the sound stimulus, we can determine the motions of cochlear structures with nanometer accuracy. Motion measurements were made using computer vision algorithms (Davis and Freeman, 1998a; Davis and Freeman, 1998b; Timoner and Freeman, 2001) based on ones originally developed by Horn (Horn, 1986; Horn and Weldon Jr., 1988). These algorithms are based on the assumption that the brightness of a moving object does not change; only the spatial distribution of brightness changes. By tracking changes in the spatial distribution of brightness over time, we can measure motions as small as two nanometers in the plane of focus and 40 nanometers in the axial direction (see chapter 3).

By computing the displacement of an object between images taken at successive stimulus phases, we determined the motion of cochlear structures at the stimulus frequency and its harmonics. We made separate measurements for each hair bundle, and for each region of the TM above and RL below the bundle.

5.3 Results

5.3.1 Images of the cochlea

Figure 5-1 shows a typical image of the tectorial region of the alligator lizard cochlea taken with our measurement system. We viewed the cochlea from the endolymphatic side. In this image the bases of some hair bundles, the tips of others, and the edge of

the TM are visible. Individual stereocilia can be seen within each bundle. However, unlike in the mammalian cochlea, no internal structure of the TM is visible.

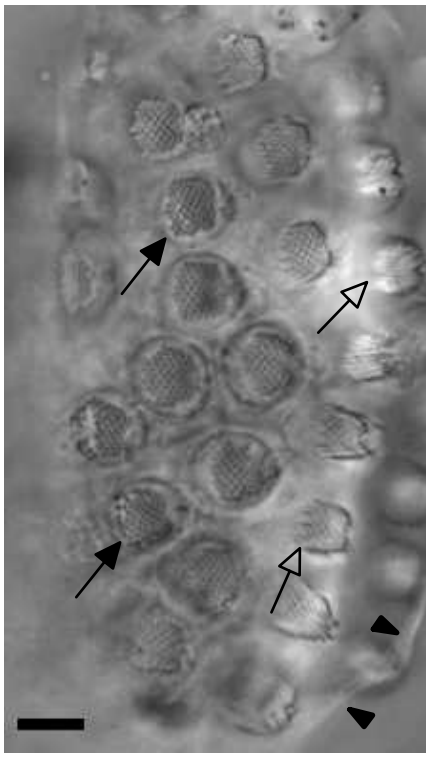

Figure 5-1: The tectorial region of an alligator lizard cochlea. This light microscope image shows the cochlea as seen during our experiments. At this plane of focus the bases of some hair bundles are visible on the left (solid arrows), the tips of other bundles are visible in the middle (hollow arrows), and the TM is visible on the right (arrowheads). Individual stereocilia and the edge of the TM are both clearly visible. Scale bar = 10 μm.

5.3.2 Gross motion

Figure 5-2 shows the displacement of the RL at the base of one hair bundle in response to a 500 Hz, 120 dB SPL tone[‡]. Positive x is in the excitatory direction for the hair bundle, which is also the lateral direction described in chapter 1. The fundamental component of the displacement, determined from the Fourier transform of the data points, was 0.15 μm peak. Higher harmonics were more than 26 dB smaller.

[‡]Sound pressures reported here are measured in the fluid beneath the cochlea. The middle-ear pressure gain is about 27 dB at this frequency (see figure 1-5), so this stimulus corresponds to a sound pressure of 93 dB SPL at the eardrum.

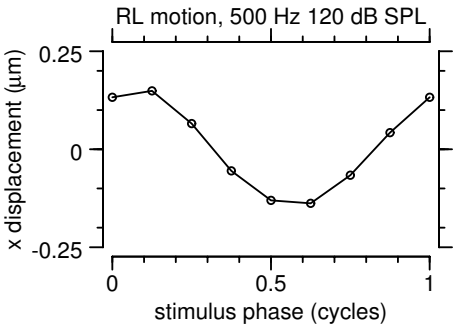

Figure 5-2: Displacement of the reticular lamina (RL) in response to a 500 Hz, 120 dB SPL tone. Displacement was measured along the axis running from the shortest stereocilia to the kinocilium. The motion was computed from eight images taken at evenly-spaced phases of the sinusoidal stimulus. The fundamental component of motion was 0.15 μm with a phase of -0.07 cycles. The second harmonic had a magnitude of 6 nm; higher harmonics were smaller.

Figure 5-3 shows the displacement of the tip of one hair bundle, the TM above it, and the RL at the bundle base as a function of frequency in response to tones at 120 dB SPL. Each point represents the magnitude of the fundamental component of motion for a displacement curve like the one in figure 5-2. The displacements varied by less than 20 dB over the frequency range examined. In addition, although the displacement of the hair bundle tip was comparable to that of the TM, both were smaller than the displacement of the RL.

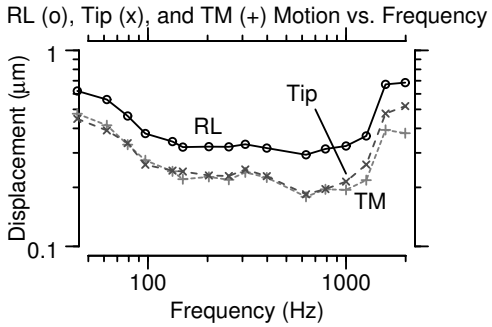

Figure 5-3: Frequency dependence of displacements of the reticular lamina (RL, $\circ$ symbol), hair bundle tips (Tip, $\times$ symbol) and tectorial membrane (TM, + symbol) for one hair bundle. The magnitude of the fundamental component of motion is plotted. Displacement of the tip and TM are comparable, and are smaller than displacement of the RL at all frequencies. These motions are all broadly tuned in frequency compared to the sharp frequency selectivity of auditory nerve fibers innervating this region. The magnitude of the displacement of each structure at each frequency was measured from time waveforms such as figure 5-2.

5.3.3 Micromechanical transfer functions

$\frac{\mathbf{TM}}{\mathbf{RL}}$. Figure 5-4 shows the magnitude and phase of the ratio of TM to RL displacement. This ratio describes how much the TM moves for a given displacement of the RL. For each cell, the ratio $\frac{\mathrm{TM}}{\mathrm{RL}}$ was roughly constant with frequency. Because of the

similarity across different cells, results have been pooled for 140 hair cells from nine cochleae. The plot shows the median (horizontal bar), interquartile range (vertical line), and full range (dots) of measured ratios. The median magnitude and interquartile range of the ratios were less than one at all frequencies, indicating that the TM moved less than the RL. The interquartile range of magnitudes spanned less than one order of magnitude, and the full range spanned less than three. The median phase was near 0 cycles at all frequencies.

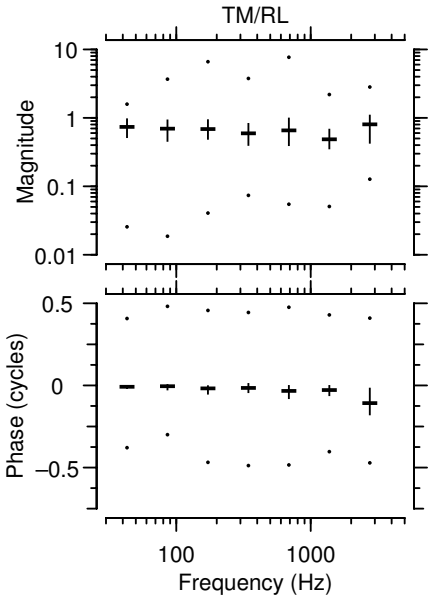

Figure 5-4: $\frac{\mathrm{TM}}{\mathrm{RL}}$ vs. Frequency. This plot shows the magnitude and phase of the ratio of TM to RL motion as a function of frequency for 140 hair cells from nine lizards. The horizontal bars indicate the median value of the ratio over the frequency range indicated. The vertical lines indicate the interquartile range of the ratio values. The dots indicate the full range of ratio values. Note that the median magnitude was less than one at all frequencies, and the median phase was near zero at all frequencies. The median values were nearly independent of frequency.

$\frac{\mathbf{TM-RL}}{\mathbf{RL}}$. Figure 5-5 shows the magnitude and phase of TM shear (TM–RL) normalized to RL displacement. This ratio describes the relative shear of the TM as seen by a hair cell (i.e., TM–RL) for a given RL displacement. The median magnitude was less than one at all but the highest frequencies, and was nearly independent of frequency. As with $\frac{\mathrm{TM}}{\mathrm{RL}}$, the interquartile range of magnitudes spanned less than one order of magnitude, and the full range spanned less than three orders of magnitude.

The phase was near −0.5 cycles at all frequencies; that is, TM shear was 180° out of phase with RL displacement.

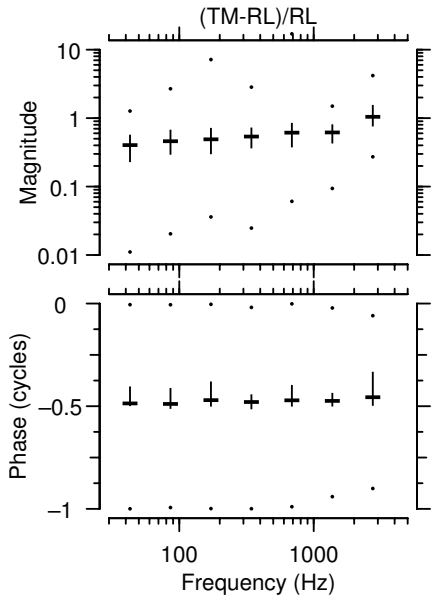

Figure 5-5: $\frac{\text{TM}-\text{RL}}{\text{RL}}$ vs. Frequency. The magnitude and phase of the ratio of TM–RL motion (i.e., TM shear) to RL motion as a function of frequency is plotted for the same 140 hair cells as in figure 5-4. Symbols are as in figure 5-4. The median magnitude was less than one and shows a slight increase with frequency. The median phase was near −0.5 cycles, independent of frequency.

$\mathbf{\frac{Tip-RL}{TM-RL}}$**.** Figure 5-6 shows the magnitude and phase of hair bundle deflection (Tip–RL) normalized to TM shear (TM–RL). This ratio describes the extent to which TM shear drives hair bundle deflection. The ratio was roughly constant with frequency, with a median value slightly less than one and a phase near 0 cycles. As with the other measures, the interquartile range of magnitudes spanned less than one order of magnitude, and the full range spanned about three.

$\mathbf{\frac{Tip-RL}{RL}}$**.** Figure 5-7 shows the magnitude and phase of hair bundle deflection (Tip–RL) normalized to RL displacement. This ratio was roughly constant with frequency, with a median value between 0.1 and 0.5. The interquartile range spanned just over one order of magnitude, while the full range spanned about three. The phase was nearly constant with frequency, with a median value near −0.5 cycles.

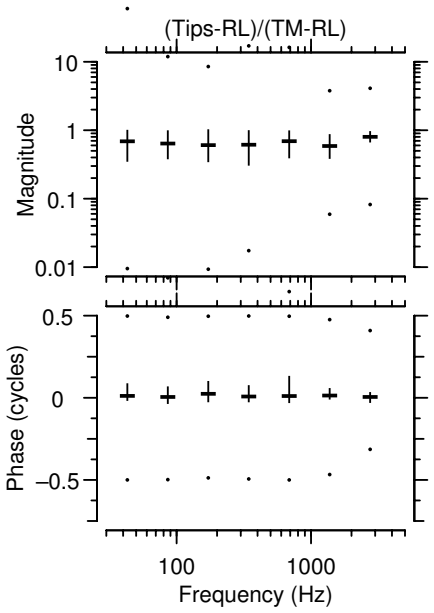

Figure 5-6: $\frac{\text{Tip}-\text{RL}}{\text{TM}-\text{RL}}$ vs. Frequency. This plot shows the magnitude and phase of the ratio of Tip–RL motion (i.e., hair bundle deflection) to TM–RL motion (i.e., TM shear) as a function of frequency for 140 hair cells. Symbols are as in figure 5-4. The median magnitude of this ratio was less than one, and the median phase was near 0 cycles. Both magnitude and phase median values are essentially independent of frequency.

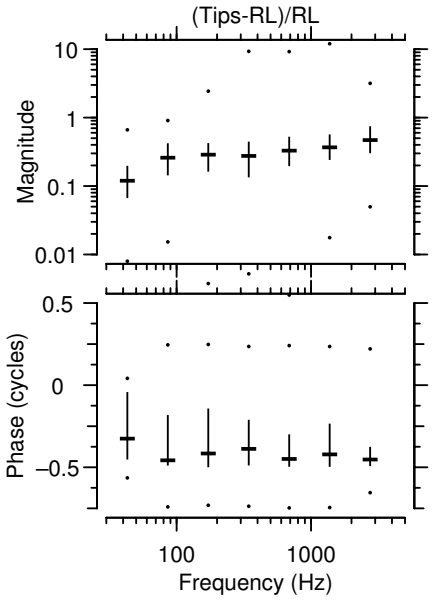

Figure 5-7: $\frac{\text{Tip}-\text{RL}}{\text{RL}}$ vs. Frequency. The median magnitude of this ratio increased with frequency with a slope of about 10 dB/decade, and was less than one at all frequencies. The phase of this ratio was near -0.5 cycles at all frequencies; that is, hair bundle deflection was out of phase with RL motion.

5.4 Discussion

5.4.1 Are observed motions indicative of *in vivo* motions?

These results represent some of the first measurements of sound-induced motions of hair bundles and the overlying tectorial membrane. It is important to evaluate whether the observed motions accurately reflect the *in vivo* mechanics. In response to sinusoidal sound stimulation, the basilar papilla, hair bundles, and tectorial membrane all move sinusoidally. The basilar papilla rocks about the longitudinal axis, as has been seen in previous studies (Frishkopf and DeRosier, 1983; Holton and Hudspeth, 1983; see also chapter 4), with displacements comparable to basilar membrane motion measured *in vivo* (Peake and Ling, 1980). This rocking causes deflections of hair bundles primarily in the direction of hair cell excitation. The displacement of the tips of hair bundles is typically less than that of the RL, so that in response to a 120 dB SPL tone (in fluid, corresponding to roughly 80–90 dB SPL at the eardrum), hair bundle deflection is on the order of 0.1–0.25 μm_{peak}. This deflection is sufficient to saturate the hair cell response in hair cells from other species (Corey and Hudspeth, 1983; Crawford and Fettiplace, 1985), consistent with the saturated responses measured *in vivo* at these sound pressure levels. These results show that the observed motion is roughly consistent with the expected motions of structures in this cochlea.

However, we were not successful in measuring a cochlear microphonic potential in this preparation, so we cannot establish with certainty that the observed motions generate electrical responses similar to those measured *in vivo*. In addition, the condition of the preparations was less than ideal, as judged by the presence of blebs on the hair cells of the tectorial region (chapter 2). Blebs may directly affect the mechanical response to sound by blocking hair bundle motion, or by pushing the TM up and off of the hair bundles. In addition, blebbing may also be associated with other cellular responses to acoustic trauma, such as reductions of the stiffness of hair bundles (Flock, 1982; Saunders et al., 1986; Szymko et al., 1995; Chan et al., 1998; Duncan and Saunders, 2000). Thus the mechanical interactions of cochlear structures measured in this preparation may not entirely correspond to the interactions *in vivo*.

Finally, these studies relied primarily on 2D measurements of motion. Although 3D studies of the basilar papilla suggest that axial motion is relatively independent of frequency in the tectorial region (see chapter 4), it is possible that relative axial motion between the TM and the RL is frequency dependent, and thus may affect mechanical tuning.

5.4.2 Lack of frequency dependence

The most striking result of this study is the lack of frequency dependence of both the absolute and relative motions of cochlear structures. Both the individual measurements and the aggregate measurements of micromechanical transfer functions show little variation with frequency. If the system were mechanically resonant, the measured transfer functions would show increasing phase lag for frequencies above the range of resonant frequencies seen in auditory nerve fibers innervating this region (roughly 800 Hz). No such increase in phase lag is seen, indicating that no mechanical resonances are present. Thus passive micromechanical tuning does not appear to play a significant role in the frequency selectivity of the tectorial region of the alligator lizard cochlea. This result is in sharp contrast to the micromechanical tuning of the free-standing region (Frishkopf and DeRosier, 1983; Holton and Hudspeth, 1983; see also chapter 6), in which frequency selectivity is determined largely by the mechanical properties of the hair bundle and surrounding fluid.

In another lizard species, the Tokay gecko, the presence of tectorial structures is believed to reduce the resonant frequency and increase the quality factor of resonance (Authier and Manley, 1995; Manley, 2000a), as compared to hair bundles that project freely into endolymph. In the alligator lizard, however, resonance of the TM/hair-bundle complex does not appear to play a role in mechanical tuning. It is tempting to model the TM/hair-bundle complex as a resonant system whose resonant frequency is below 50 Hz, so hair bundle deflection is proportional to RL displacement. However, such a model predicts that $\frac{\mathrm{TM}}{\mathrm{RL}}$would have a magnitude near zero with a phase near -0.5 cycle, which is inconsistent with our measurements. A more appropriate model is to treat the TM and hair bundles as stiffnesses connected

by levers. With such a model, the displacement of the RL, tips of hair bundles, and TM are in phase, and differ only by a scaling factor. Such a model is consistent with the lever model of cochlear mechanics originally proposed by Davis (Davis, 1957).

5.4.3 Lack of TM resonance

The TM has been modeled as a resonant structure both in mammals (Hubbard and Mountain, 1996, for review) and in lizards (Authier and Manley, 1995). Some evidence for TM resonance has been seen in measurements of motions at the cochlear apex in mammals (Gummer et al., 1996; Hemmert et al., 2000), although a similar study by another group found no evidence of TM resonance (Ulfendahl et al., 1995). In this study, we also find no evidence to support the idea of a resonant TM in the alligator lizard. However, the interaction of the TM with hair bundles may be altered by the presence of blebs on hair cells.

In mammalian cochleae, outer hair cells are believed to be stimulated by TM–RL displacement, while inner hair cells are believed to be driven by TM–RL velocity (Dallos et al., 1972) or by a combination of TM–RL velocity and displacement (Freeman and Weiss, 1988). In the alligator lizard tectorial region, hair bundle deflection is proportional to TM–RL displacement, as would be expected if the bundles were attached to the TM. However, hair bundle deflection is typically smaller than TM–RL displacement. This result may be due to shear within the TM, since TM displacement was measured at the top of the TM. However, shear is typically associated with viscous coupling, which would introduce a phase lag that was not seen in our measurements. An alternate hypothesis is that the TM rotates about a separate attachment point as proposed by Davis (Davis, 1957).

5.4.4 The origin of sharp frequency selectivity

The observed mechanical properties of the cochlea show no significant frequency dependence over the range of frequencies to which hair cells of this region are most sensitive. Measurements from auditory nerve fibers innervating this region, however,

demonstrate sharp frequency selectivity, with Q_{10dB} values ranging from one to five. The question remains as to the origin of this sharp frequency selectivity. In the tectorial region, frequency selectivity may be determined by electrical resonance, as it is in the turle cochlea (Fettiplace and Fuchs, 1999). Although electrical resonance has not been studied in hair cells of the tectorial region, hair cells of the free-standing region are electrically resonant at frequencies more appropriate for the tectorial region (Eatock et al., 1993). If hair cells in the tectorial region are similarly electrically resonant, such resonance may be the basis for frequency selectivity in this region. Alternately, frequency selectivity may be determined by active hair bundle motility, as is believed to be the case in other lizard species (Manley and Köppl, 1998; Manley et al., 2001). Indeed, these two mechanisms may be coupled (Weiss, 1982). The results of this study demonstrate only that frequency selectivity does not come from mechanical tuning in this region. In combination with the results presented in chapter 6, these results suggest that two distinct mechanisms for conferring frequency selectivity act in different frequency regions of the same cochlea.

Chapter 6

Frequency Dependence of Motion of Free-Standing Hair Bundles

Abstract

Although there has been a long-standing debate about whether hair bundles can be mechanically resonant, existing measurements (Frishkopf and DeRosier, 1983; Holton and Hudspeth, 1983) are not sufficient to resolve the issue. Freeman and Weiss developed a two-dimensional model to demonstrate that a mechanical resonance of hair bundles was physically possible (Freeman and Weiss, 1990a-d). Their model, which describes the transformation $H_\mu(f)$ from reticular lamina velocity to hair bundle rotation, contains two free parameters, the height and the rotational compliance of the hair bundle. These parameters determine the frequency and quality factor of the resonance, while the low- and high-frequency slopes of $H_\mu(f)$ are determined by fluid properties. A three-dimensional model (Shatz, 2000), showed that these slopes were independent of the shape of the hair bundle. To test this model, we have made detailed measurements of the motion of free-standing hair bundles as a function of frequency. These measurements were made using the computer microvision system developed in our laboratory. The measured $H_\mu(f)$ was fit with the Freeman and Weiss model, varying only the rotational compliance; hair bundle height was measured from

images. The fits accurately represent the measurements for almost all hair bundles, confirming the model's basic tenet that fluid mass and viscosity play a key role in hair bundle mechanics. The fits fell into two categories. In the first category, the peak of $H_\mu(f)$ fell within the frequency range expected for these hair cells (0.5–5 kHz). The best-fit compliance for these hair bundles was somewhat smaller than the measured compliance of hair bundles from other reptile species. In the second category, the peak of $H_\mu(f)$ fell below the measured frequency range. The best-fit compliance for these hair bundles was significantly larger, and could not be determined precisely. The hair bundles of this second group may have suffered more damage from surgical extraction. Given the simplicity of the Freeman and Weiss model, and the use of only a single free parameter, the accuracy of the fits is striking.

Key words: Hearing, cochlea, basilar papilla, auditory mechanics, micromechanics, hair bundle, frequency selectivity, microscopy, computer vision, alligator lizard.

6.1 Introduction

The conversion of sound from mechanical vibrations to electrical signals takes place in the hair cells of the cochlea. Deflections of the hair bundles of hair cells open mechanically-gated ion channels called transduction channels, modulating the flow of current into the cells (Hudspeth and Corey, 1977). Although some hair cells are electrically resonant (Crawford and Fettiplace, 1985), the receptor potential of most hair cells is driven primarily by the gating of transduction channels. Consequently, the frequency dependence of hair bundle deflection is a primary determinant of the frequency selectivity of the hair cell.

Hair cells are components of many organs that sense acoustic and vibratory stimuli over a wide range of frequencies, from near-DC to more than 100 kHz. The macromechanical properties of the organ in which the hair cell is embedded determine the types of stimuli and the range of frequencies that drive hair bundle deflection. However, the hair bundle itself, along with structures and fluids surrounding it, constitutes a

micromechanical system that can play a large role in determining the sensitivity and frequency selectivity of the hair cell. Lizard cochleae provide a unique opportunity to study the mechanical properties of hair bundles. Unlike most hair cell organs, in which hair bundles project into overlying gelatinous structures, certain lizard cochleae have hair cells whose bundles project freely into endolymph. Because the mechanical properties of the fluid are known, this system provides a simpler context in which to study the dynamics of hair bundles at audio frequencies.

6.1.1 Models of hair bundle mechanics

Since free-standing hair bundles in the alligator lizard cochlea are surrounded by fluid, the motion of the fluid is believed to play a significant role in determining the motion of the hair bundle. An early model of hair bundle mechanics suggested that hair bundles of inner hair cells, which are believed not to be attached to the tectorial membrane (TM), are driven by fluid viscosity and thus are sensitive to the velocity of the reticular lamina (RL) relative to the TM (Dallos et al., 1972). Similarly, outer hair cells, believed to be attached to the TM, were considered to sense RL displacement relative to the TM. This model did not describe the mechanical properties of hair bundles with no overlying tectorial structure.

As part of an effort to model the entire cochlear mechanical pathway of the alligator lizard, Weiss and Leong (1985) derived a model transfer function $H_\mu(f)$ relating the deflection of free-standing hair bundles to the velocity of the RL. Their model suggested that free-standing hair bundles could be mechanically resonant. Below the resonant frequency, $H_\mu(f)$ increases with frequency by 10 dB/decade, while above resonance, $H_\mu(f)$ decreases with frequency by 20 dB/decade. With an additional low-pass filter, this model was able to match iso-rate tuning curves of free-standing hair cells. The primary difficulty with this model was the use of simple approximations to describe the fluid mechanics, leaving the model's fundamental conclusions open to question.

A subsequent model (Freeman and Weiss, 1988; Freeman and Weiss, 1990a-d) implemented a complete solution of the Navier-Stokes equation in two dimensions

for a simplified system consisting of a hinged flap attached to a moving plate by a rotational spring. The flap represents the hair bundle, while the plate, which moves orthogonal to the plane of the flap, represents the reticular lamina. This model qualitatively gave the same results as the Weiss and Leong model. The viscosity and density of endolymph are assumed to be those of water (Money et al., 1966; Steer et al., 1967; Rauch and Rauch, 1974), as in the Weiss and Leong model. If the mass of the flap itself is ignored, then this model has only two free parameters — the height of the flap and the compliance of its attachment to the plate. Because this model is two-dimensional, fluid is constrained to go over rather than around the moving flap. Thus this model most likely overestimates the effect of fluid inertia.

An extension of the Freeman and Weiss model to three dimensions (Shatz, 1996; Shatz, 2000) allows fluid to flow around the bundle as well as over the top. This model predicts that at low frequencies, $H_\mu(f)$ varies as the cube rather than the square of hair bundle height, but otherwise makes predictions that match those of the earlier models. However, this model requires a third parameter to describe hair bundle shape (tall and thin vs. short and fat), and lacks a closed-form solution over most of the frequency range of interest in this study.

The most striking result of all three models of free-standing hair bundle motion is that at low frequencies, hair bundle rotation is proportional not to RL velocity, but to a linear combination of RL velocity and acceleration. This combination gives $H_\mu(f)$ a low-frequency slope of +10 dB/decade, with a phase of +1/8 cycle; that is, hair bundle rotation leads RL velocity. This result stems from the fact that the thickness of the fluid boundary layer decreases with frequency, so the fluid shear which drives hair bundle motion depends on both viscous and inertial properties of the fluid (Freeman and Weiss, 1988; Freeman and Weiss, 1990c).

6.1.2 The Freeman and Weiss 'flap' model in more detail

Although the models described above all make similar predictions, the Freeman and Weiss model is the only one which is both hydrodynamically accurate and for which solutions are available for all relevant frequencies. In addition, the free-standing hair

bundles of the alligator lizard cochlea are arranged in rows, and so are similar in appearance to the two-dimensional 'flap' of the Freeman and Weiss model. For this reason we will compare measured hair bundle motions to the predictions of this model.

The model is illustrated in figure 6-1. A basal plate, immersed in water, moves in the x direction with a velocity U_b. A rigid flap of height L is attached to the plate by a specific compliance (compliance per meter of the flap) C_z. Motion of the basal plate causes the flap to rotate through an angle θ. The flap is acted on by hydrodynamic forces due to fluid motion, and by the reactive force of the compliant attachment. The hydrodynamic forces are predominantly linear in the range of sound intensities typically seen in the cochlea (Freeman and Weiss, 1990a). Consequently the hydrodynamic forces due to motion of the basal plate can be considered separately from those due to rotation of the flap. The rotation of the flap is then described by an equation balancing the torques due to hydrodynamic forces, the compliance of the attachment, and the inertia of the flap. From this equation, the transfer function $\frac{\theta}{U_b}(f)$ can be determined as a function of frequency.

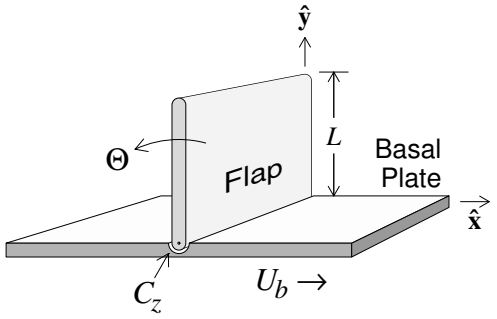

Figure 6-1: The Flap model of Freeman and Weiss. The flap projects from the basal plate moving at velocity U_b in the x direction. Motion of the basal plate causes the flap to rotate through an angle θ. The model describes the transformation $\frac{\theta}{U_b}(f)$ as a function of frequency. The two free parameters in the model are L, the height of the flap, and C_z, the specific compliance of the attachment of the flap to the plate. The properties of the fluid around the flap are taken to be those of water. Figure taken from Freeman and Weiss, 1990d.

At low frequencies, the torques due to inertia and the rotation of the flap are negligible, so the hydrodynamic torque due to motion of the basal plate is balanced by the torque due to the compliant attachment. The torque due to motion of the plate at low frequencies results from the rate of fluid shear within the viscous boundary layer,

which depends on both viscous and inertial properties of the fluid. Consequently, at low frequencies $\frac{\theta}{U_b}(f)$ increases with frequency with a slope of 10 dB/decade and a phase angle of $+\frac{1}{8}$ cycle (Freeman and Weiss, 1990b). Since the hydrodynamic torque is balanced by the torque due to the compliance, the magnitude of $\frac{\theta}{U_b}(f)$ is directly proportional to C_z in this frequency range. Hydrodynamic torque also depends on flap height, so the magnitude of $\frac{\theta}{U_b}(f)$ is directly proportional to L as well.

At high frequencies, the compliance of the attachment provides negligible torque. In addition, the boundary layer is infinitesimally small. Consequently, the fluid forces acting on the flap are predominantly inertial. As a result, rotation of the flap is proportional to displacement of the basal plate; the flap rotates about a virtual pivot point that lies between $\frac{3L}{2\pi}$ and $\frac{2L}{3}$, depending on the mass of the flap (Freeman and Weiss, 1990c,d). The high-frequency asymptote of $\frac{\theta}{U_b}(f)$ falls by 20 dB/decade with a phase angle of -1/4 cycle. The magnitude of $\frac{\theta}{U_b}(f)$ at high frequencies is determined by fluid inertia, and is thus inversely proportional to L.

$\frac{\theta}{U_b}(f)$ has a maximum at an intermediate frequency. This maximum is due to a resonance between the mass of moving fluid and the compliance of the flap attachment. Unlike in a traditional mechanical resonance, however, the mass is not constant; it depends on both frequency and the height of the flap. Increasing L decreases the resonant frequency, but does not significantly affect the sharpness of tuning. Increasing C_z decreases both the resonant frequency and the sharpness of tuning. The model includes an additional parameter, M_z, which is the mass per unit length of the flap. Increasing this mass decreases the resonant frequency and increases the sharpness of tuning. These three variables — L, C_z, and M_z — provide the only degrees of freedom in the model. We assume M_z is negligible, so the model as used in this study has only two free parameters. The effect on the model predictions of changing each of these parameters is shown in figure 6-2.

6.1.3 Measurements of hair bundle mechanics

Although several studies have measured the static or low-frequency mechanical properties of hair bundles (Crawford and Fettiplace, 1985; Saunders, Canlon and Flock,

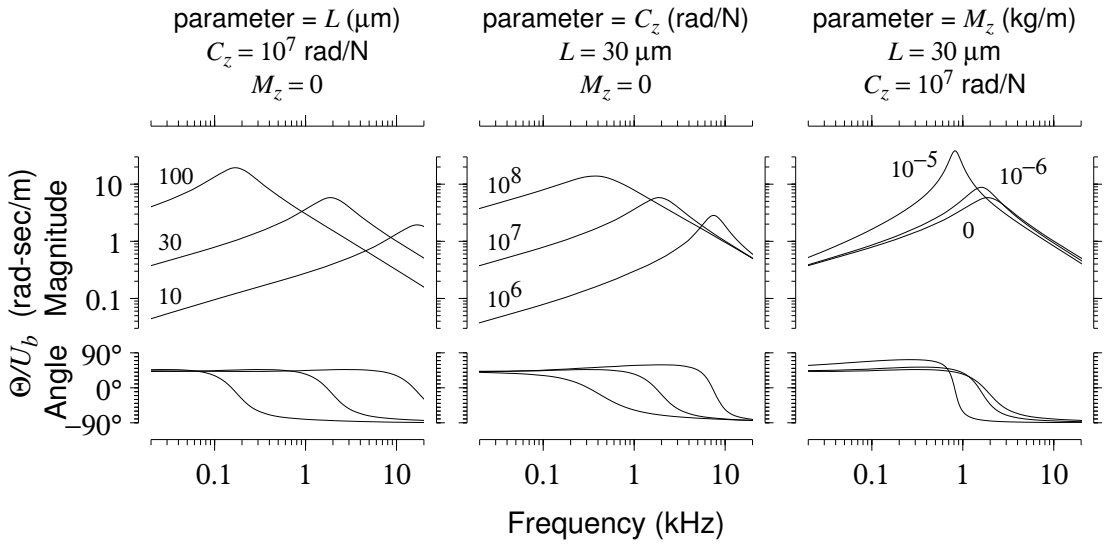

Figure 6-2: Dependence of flap model on model parameters. The left-hand plot shows how the model prediction changes as L is varied, with C_z and M_z held constant. Increasing L decreases the resonant frequency, but does not affect the sharpness of tuning. The center plot shows how the model prediction changes with C_z. Increasing C_z decreases the resonant frequency and decreases the sharpness oftuning. The right-hand plot shows how the model prediction depends on M_z. Increasing M_z decreases the resonant frequency slightly, and significantly increases the sharpness of tuning. Figure taken from Freeman and Weiss, 1990d.

1986; Howard and Ashmore, 1986; Howard and Hudspeth, 1988, among others), few experimental measurements of sound-induced hair bundle motion at audio frequencies have been made. Frishkopf and DeRosier (1983) measured the difference in the phase of motion of the tips and bases of hair bundles in the alligator lizard. At low frequencies, the tips and bases moved in phase. As the frequency was increased, the tip increasingly lagged the base, with lags as large as 0.5 cycle by 3 kHz (figure 1-6). In addition, taller bundles at more apical locations showed greater phase lag at a given frequency than shorter bundles. These results provide some evidence that free-standing hair bundles are mechanically resonant. However, without measurements of the magnitude of motion, phase differences between the tip and base do not provide sufficient information to characterize $H_\mu(f)$. The relative phase between tip and base position is biased towards zero by common motion of the two locations, and so does not accurately describe hair bundle rotation. Holton and Hudspeth (1983) measured the magnitude and phase of motion, but only for two hair bundles — one at the low-frequency end and one at the high frequency end of the cochlea (figure 1-7). These

measurements were made at only two frequencies, resulting in a total of four measurements of hair bundle rotation. Two of these measurements were below the noise floor of their measurement system. Thus from their measurements we can conclude only that tall hair bundles rotate more at 1.2 kHz, and short hair bundles rotate more at 3.8 kHz. While these measurements confirmed that the motion of free-standing hair bundles was indeed frequency dependent, they did not provide enough information to evaluate mechanical models, or to determine whether the frequency selectivity seen in electrical measurements of hair cells can be explained by micromechanical tuning.

In this study we performed detailed measurements of the motion of several hair bundles and their underlying reticular lamina in response to sound stimulation. These measurements used a computer microvision system developed in our laboratory (chapter 3), which can measure the three-dimensional motion of all structures in the cochlea with nanometer precision. From these measurements we can compute $H_\mu(f)$ for comparison with models. A preliminary analysis of some of these results was presented previously (Aranyosi and Freeman, 2000; Freeman et al., 2000).

6.2 Methods

6.2.1 Biological preparation

Adult alligator lizards (20-49 g) are sacrificed by decapitation and pithing. The dorsal skin and muscle are removed. A scalpel is used to penetrate the posterior semicircular canal and remove the bone covering the sacculus. The saccular membrane is peeled away with fine forceps, and the saccular otoconia are removed by gentle suction. A razor blade shard is used to cut the 8th nerve. Hydraulically actuated forceps mounted on a micromanipulator are used to lift the cochlea out by the 8th nerve. The cochlea is transferred (through air in earlier experiments, through saline in later ones) to the stimulus chamber, which is filled with artificial perilymph. Artificial endolymph is perfused over the apical surface before the vestibular membrane is removed.

Artificial perilymph contains (in mM): Na^+, 168; K^+, 3; Ca^{+2}, 2; Mg^{+2}, 1.2; Cl^-,

174.9; SO_4^{-2}, 2; $H_2PO_4^-$, 0.5; D-glucose, 5; Hepes, 5. Artificial endolymph contains (in mM): Na^+, 2; K^+, 174; Ca^{+2}, 0.02; Cl^-, 171.5; SO_4^{-2}, 2; $H_2PO_4^-$, 0.5; D-glucose, 5; Hepes, 5. Solutions were adjusted to a pH of 7.30, and had an osmolality of 342±8 mmol/kg. Both solutions contained MEM essential and non-essential amino acids, and were oxygenated immediately before use. In some experiments Liebowitz' L-15 was used in place of artificial perilymph. All chemicals were purchased from Sigma Chemical Company (St. Louis, MO).

6.2.2 Measurement system

Experiment chamber

The Plexiglas® experiment chamber (figure 4-1) allows the cochlea to be clamped over a hole separating two fluid spaces. Artificial perilymph is perfused through the basolateral fluid space and artificial endolymph is perfused through the apical fluid space. This separation of fluids allows us to simulate the *in vivo* cochlear fluid environment. The clamping ring encircles the neural limbus and triangular limbus to avoid clamping the basilar membrane or basilar papilla. A piezoelectric disk (Panasonic EFR Series) generates sound waves in the basolateral fluid, and a hydrophone (Model EPB-126W-100G, Entran Devices, Inc., Fairfield NJ) measures the resulting pressure. The bottom surface of the chamber is sealed with a glass coverslip.

Video microscopy

The video microscopy system has been described in detail elsewhere (Davis and Freeman, 1998b; see also chapter 3). The chamber is placed on the stage of a microscope and viewed using brightfield transmitted light illumination. The specimen is viewed through a 63x, 0.9 NA water immersion objective, with a transmitted-light condenser with an NA of 0.8. Images are collected with a 12-bit, 1024x1024 pixel CCD camera (CAD7-1024A, Dalsa Inc., Waterloo, Ontario)*.

*Early experiments used a 40x, 0.75 NA objective, an 0.6 NA condenser, and a 12-bit, 576x384 pixel CCD camera (CH250A, Photometrix Inc., Tucson, AZ).

The cochlea is illuminated with a green LED (Nichia, Tokushima, Japan). The light source is synchronized to the acoustic stimulus, allowing us to stop the apparent motion of the cochlea at arbitrary stimulus phases. We typically take images at eight evenly-spaced stimulus phases. This process is repeated at several focal planes to give us three-dimensional information about the positions of cochlear structures. We apply a two-point flat fielding technique (Hiraoka et al., 1987; Healey and Kondepudy, 1994) to the images to correct for spatial inhomogeneities in the imaging system. The resulting corrected images have pixel values that are proportional to the brightness of the specimen.

Image analysis

From a series of images of the cochlea at different phases of the sound stimulus, we can determine the motions of cochlear structures with nanometer accuracy. Motion measurements are made using computer vision algorithms (Davis and Freeman, 1998a; Davis and Freeman, 1998b; Timoner and Freeman, 2001) based on ones originally developed by Horn (Horn, 1986; Horn and Weldon Jr., 1988). These algorithms are based on the assumption that the brightness of a moving object does not change; only the spatial distribution of brightness changes. By tracking changes in the spatial distribution of brightness over time, we can measure motions as small as two nanometers in the plane of focus and 40 nanometers in the axial direction (see chapter 3).

By computing the displacement of an object between images taken at successive stimulus phases, we determine the motion of the object at the stimulus frequency and its harmonics. We make separate measurements of the motion of the tip and base of each hair bundle. The rotation angle θ is determined by subtracting motion of the tip from that of the base, dividing by the height L of the hair bundle as measured from the images, inverting the sign[†] and computing the arctangent. The velocity U_b is determined from the displacement of the base. Both θ and U_b are taken to

[†]The sign is inverted because in the Freeman and Weiss model, positive θ is in the direction for which the base moves more than the tip; see figure 6-1.

be the component of motion along the axis pointing from the shortest to the tallest stereocilia.[‡] The fundamental components of θ and U_b are determined from Fourier transforms, and the transfer function $H_\mu(f) = \frac{\theta(f)}{U_b(f)}$ is computed as the ratio of these components. This transfer function is the same one used in models of this cochlea. Fundamental components of motion were used because in response to sinusoidal sound stimulation, cochlear structures typically moved sinusoidally (see section 6.3.2), both when observed visually in the microscope and when viewed in images.

6.2.3 Model fits

The best least-squares fit of the Freeman and Weiss model of $H_\mu(f)$ was computed for each hair bundle measured. This model has two free parameters — L, the length of the hair bundle, and C_z, the rotational compliance of the bundle attachment. The length of each hair bundle was measured from the images by finding the distance from the tip of the tallest stereocilim to the base of that stereocilium. Consequently, the model fits were allowed only a single free parameter, C_z. No arbitrary gain adjustment was allowed. Fits to the same data were also made while allowing both L and C_z to vary. Fits were computed using all measured magnitudes. The phase data were not used for these fits because phase measurements are more susceptible to noise. Since several magnitude measurements were also corrupted by noise, additional fits were computed on selected subsets of the measurements, referred to hereafter as the filtered data set. Data points were included in the filtered set based on two criteria:

- The peak-to-peak displacement of both the tip and base of the hair bundle in the direction of bundle sensitivity was at least 50 nm.
- The magnitude of the fundamental component of motion of both the tip and the base was at least 10 dB larger than that of any higher harmonics.

The rejection of certain data points was based on the observation that sound-induced motions were typically sinusoidal, but measurement noise due to drift of the tis-

[‡]The orientation of hair bundles reverses direction along the midline of the cochlea; this reversal was ignored in determining the direction of positive motion.

sue or ambient vibrations was not. Drift and ambient noise have a larger effect on small motions, so the first criterion rejects measurements that are more susceptible to noise. We have empirically observed sinusoidal motions of the tissue under low-noise conditions, but drift and ambient noise become aliased to higher harmonics of the stimulus frequency by our measurement system (section 3.5.1). The second criterion is designed to reject measurements that are likely to be corrupted by noise. Fits of the Freeman and Weiss model to the filtered data set were computed twice; once by fitting only the magnitudes, and once by fitting the real and imaginary components. Both fits are reported in the results.

The Freeman and Weiss model rather than the Shatz model was used to fit the data for two reasons. First, the Freeman and Weiss model can be solved at all relevant frequencies, while the Shatz model cannot. Second, the predictions of the Freeman and Weiss and the Shatz models are not significantly different; although the dependence of $H_\mu(f)$ on bundle height at low frequencies differs for the two models, the differences between the two models can only be compared if the compliance of hair bundles is known. Since the compliance is a free parameter in the fits, the two models are essentially equivalent.

6.3 Results

6.3.1 Measured hair bundle heights

Figure 6-3 shows the heights of hair bundles measured in this preparation as a function of distance from the basal end of the cochlea. For many hair bundles near the apical end, the basal end was not visible in the images, and so the distance had to be estimated. This process resulted in a consistent underestimate of the distance for these bundles; the length of the free-standing region of this cochlea as measured in other studies is between 250 and 300 μm, but our measurements are all below 200 μm. Nonetheless, there is a clear trend for hair bundle height to increase with distance from the basal end. The line in figure 6-3 shows hair bundle heights measured from

transverse sections of fixed tissue (Mulroy, 1974). The measured bundle heights in this study were consistently larger than those of Mulroy by up to 10 μm, but both show the same trend with position.

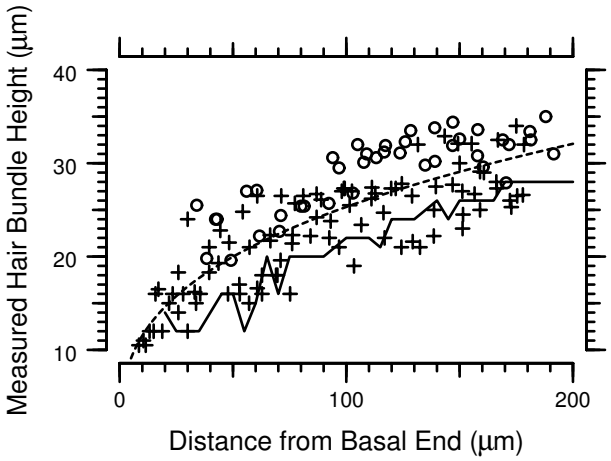

Figure 6-3: Measured hair bundle heights vs. longitudinal position. Hair bundle heights were measured from images of the unfixed tissue. Longitudinal positions were sometimes estimated, since the basal end of the basilar papilla was not always visible. The pluses show the measured heights of hair bundles oriented primarily in the axial direction of the microscope, circles show the measured heights of hair bundles oriented primarily in the plane of focus of the microscope. The dashed line shows the least-squares power-law fit to the data, $L = 5.25d^{0.34}$, r=0.85 (n=136). The solid line shows measurements of hair bundle height in fixed tissue (Mulroy, 1974).

6.3.2 Motion of a typical hair bundle

Figure 6-4 shows the displacement of both the tip of one hair bundle and the RL (base of the hair bundle) in response to a 1687 Hz, 120 dB SPL stimulus[§]. The displacements were largely sinusoidal; higher harmonics were more than 20 dB smaller than the fundamental component. At this frequency, the tip moved less than the RL and lagged the RL by 0.190 cycles. The difference of tip and RL motion, which is hair bundle deflection, was slightly larger than motion of the RL, and lagged the RL by 0.377 cycles.

The measurements of figure 6-4 were typical in that displacement of the tip lagged that of the RL, and hair bundle deflection lagged both tip and RL displacement.

[§]This stimulus corresponds to 85–100 dB SPL at the tympanic membrane.

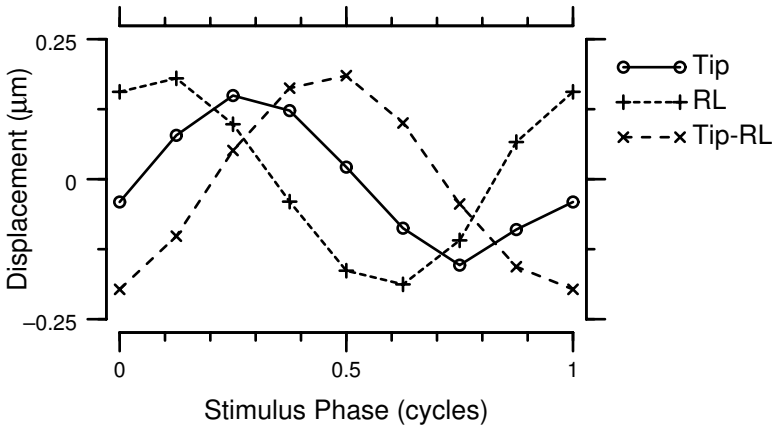

Figure 6-4: Motion of the tip and RL of one hair bundle (bundle 118) in response to a 1687 Hz, 120 dB SPL stimulus. The RL moved by 0.191 μm peak. The tip moved 0.145 μm peak, and lagged the RL by 0.190 cycles. By subtracting motion of the RL from that of the tip, we get a measure of hair bundle deflection (labeled 'Tip–RL'). The hair bundle was deflected by 0.193 μm peak, and bundle deflection lagged motion of the RL by 0.377 cycles. This bundle had a height of 22 μm, so peak bundle rotation was 0.50°.

Displacement of the tip was typically smaller than or equal to that of the RL, with the exceptions being at the lowest frequencies. In contrast, hair bundle deflection was often larger than displacement of the RL, depending on the phase lag from RL to tip displacement.

Figure 6-5 shows the ratios $\frac{\text{Tip}}{\text{RL}}$ and $\frac{\text{Tip}-\text{RL}}{\text{RL}}$ as a function of frequency for the hair bundle of figure 6-4. The magnitude of $\frac{\text{Tip}}{\text{RL}}$ decreased by about a factor of two between 400 Hz and 4 kHz. At most frequencies, the tip moved less than the RL. The phase of $\frac{\text{Tip}}{\text{RL}}$ showed increasing lag with frequency, with a lag greater than 1/4 cycle at the highest frequencies. The magnitude of $\frac{\text{Tip}-\text{RL}}{\text{RL}}$ increased by about a factor of three between 400 Hz and 4 kHz. The phase of $\frac{\text{Tip}-\text{RL}}{\text{RL}}$ showed greater lag than that of $\frac{\text{Tip}}{\text{RL}}$, approaching a lag of 1/2 cycle at the highest frequencies.

6.3.3 Measurements of the phase of the tip relative to the phase of the base of the hair bundle

Frishkopf and DeRosier (1983) estimate the characteristic frequency (CF) of the hair bundle by measuring the difference between the phase of motion of the tip and the phase of motion at the base of a hair bundle. They choose CF to be the frequency at

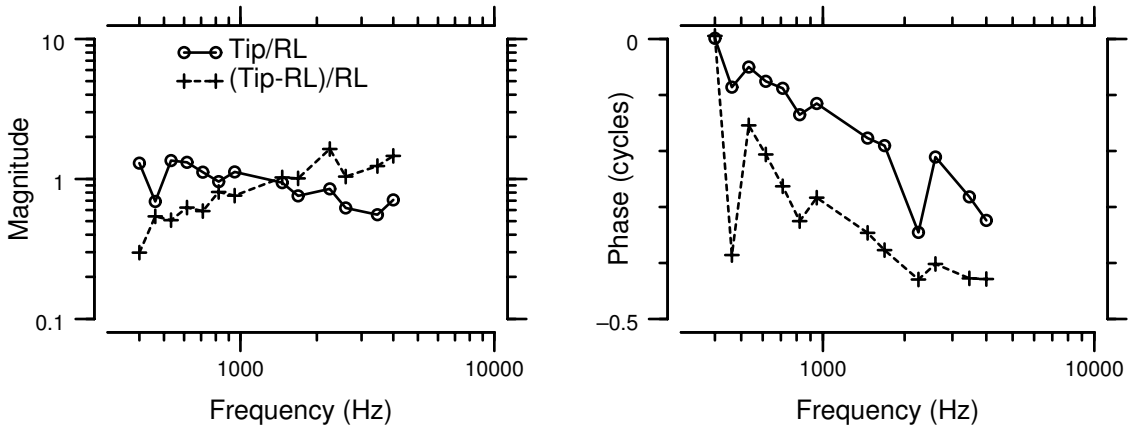

Figure 6-5: Ratio of tip motion and bundle deflection to RL motion vs. frequency, for the bundle in figure 6-4. The ratio of $\frac{\text{Tip}}{\text{RL}}$ motion decreased slightly with frequency, with a phase that fell with frequency to below $-1/4$ cycles. The magnitude of $\frac{\text{Tip}-\text{RL}}{\text{RL}}$ increased slightly with frequency. Bundle deflection lagged RL motion by more than 1/4 cycles at all but the lowest frequencies, with a phase that approached $-1/2$ cycles at high frequencies.

which the tip lags the base by 1/4 cycle. For comparison with their measurements, we estimated CF using the same technique for 136 hair bundles from four preparations. For twenty-five of these bundles, the phase lag was less than 1/4 cycle over the entire frequency range measured, so no CF could be determined by this method. The estimated CF of the remaining 111 bundles is shown in figure 6-6. The solid line shows the least-squares power-law fit to the measurements; the dashed line shows the fit of Frishkopf and DeRosier to their data. Both fits have similar slopes, but the fit to these data has a larger offset. Most of the estimates of CF fall near the best-fit line, showing that the estimated CF is inversely correlated to bundle height. The CF values estimated from our measurements all fell on or above the best-fit line from the Frishkopf and DeRosier study. The distribution of estimated CF values is biased toward high frequencies; sixteen bundles had estimated CF values larger than 1.5 times that predicted by the best-fit line, but only two bundles had estimated CF values less than 0.6 times that predicted by the best fit.

6.3.4 Measurements of $H_\mu(f)$

The Freeman and Weiss model predicts the micromechanical transfer function $H_\mu(f)$from RL motion to hair bundle rotation. We compute $H_\mu(f)$ by measuring $\frac{\theta}{U_b}(f)$, the ratio

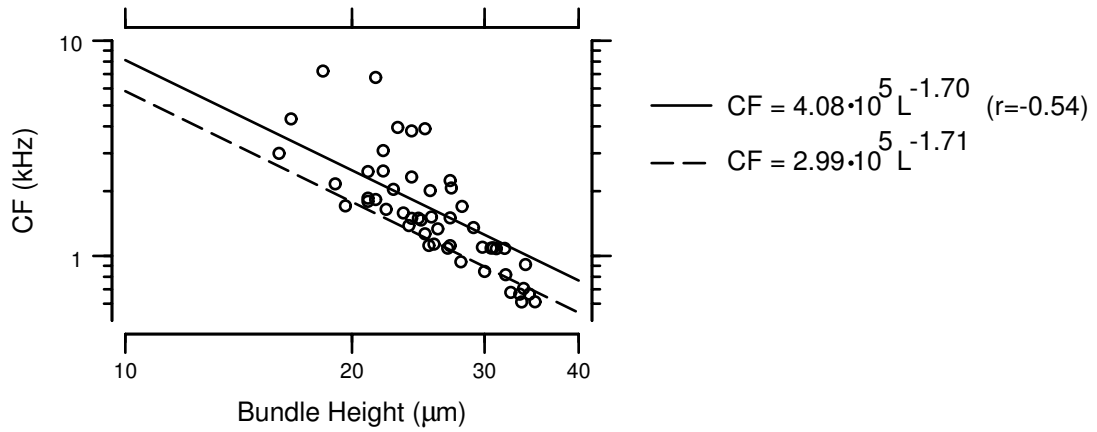

Figure 6-6: CF estimated from phase measurements. The data points show the frequency (CF) at which the phase of motion of the tip of the hair bundle lags that of the base of the bundle by 1/4 cycle. CF is inversely correlated to hair bundle height. The solid line shows the least-squares power-law fit to these measurements. The dashed line shows the least-squares power-law fit of Frishkopf and DeRosier to their measurements.

of hair bundle rotation (in radians) to velocity of the RL at the base of the bundle (in cm/sec). The magnitude of $\frac{\theta}{U_b}(f)$ is equal to that of $\frac{\text{Tip}-\text{RL}}{\text{RL}}$ divided by $L\omega$, where L is the hair bundle height and $\omega = 2\pi f$ is the angular frequency of the sound stimulus. The phase of $\frac{\theta}{U_b}(f)$ leads that of $\frac{\text{Tip}-\text{RL}}{\text{RL}}$ by 1/4 cycle. Since the measured motions of hair bundles were predominantly sinusoidal, calculations of $\frac{\theta}{U_b}(f)$ were based on the fundamental components of Tip−RL and RL motion.

Figure 6-7 shows measurements of $\frac{\theta}{U_b}(f)$ as a function of frequency for two hair bundles. The plots on the left are for the same bundle shown in section 6.3.2, those on the right are for a different bundle. The circles show the measured values of $\frac{\theta}{U_b}(f)$. The magnitudes were mostly between 0.01 and 0.1, and decreased with frequency at high frequencies. At low frequencies, magnitudes were constant or increased with increasing frequency. The phase rolled off from at or above 0 cycles at low frequencies to $-1/4$ cycles at high frequencies. The solid lines show the best fit of the model of Freeman and Weiss (Freeman and Weiss, 1988; Freeman and Weiss, 1990a) to the magnitudes, and are discussed in section 6.3.5. These plots show data from two hair bundles for which measurements were available over a wide frequency range, and represent some of the best fits of the Freeman and Weiss model to the measurements.

Appendices A, B, and C show measured $\frac{\theta}{U_b}(f)$ values for 136 hair bundles from four

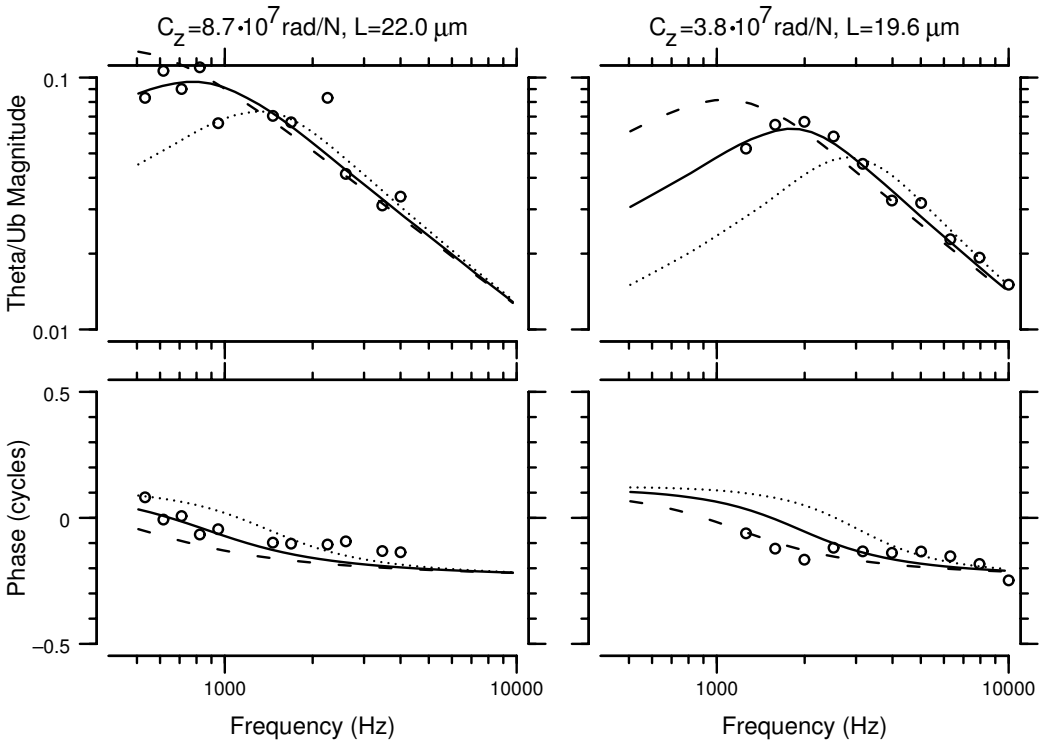

Figure 6-7: $\frac{\theta}{U_b}(f)$ vs. frequency for two hair bundles (bundle 118 on the left, 97 on the right). The top plots show the magnitude of $\frac{\theta}{U_b}(f)$, the bottom plots show the phase. Circles show the measured points, solid lines are the best fits of the model of Freeman and Weiss using a single free parameter. The measured data points generally fall near the best-fit line of the model. Dotted lines show the model prediction for twice the best-fit specific compliance, dashed lines show predictions for half the best-fit specific compliance. The parameters C_z and L are those used in the model; L is the hair bundle height as measured from images, C_z is the best-fit rotational specific compliance of the bundle.

preparations. The left-hand plot for each bundle shows the magnitude and phase of all measured $\frac{\theta}{U_b}(f)$ values as a function of frequency. Several of these measurements were corrupted by measurement noise and drift of the preparation. To reduce the effect of these artefacts, we created a filtered data set containing only the measurements that met the two criteria listed in section 6.2.3. These criteria eliminated 494 of 1624 $\frac{\theta}{U_b}(f)$ measurements; thirteen because of small magnitudes, 357 because of non-sinusoidal motions, and 124 due to both criteria. The center and right-hand plots in the appendices show the filtered subset of $\frac{\theta}{U_b}(f)$ measurements.

For nearly all hair bundles, except some of those in appendix A, $\frac{\theta}{U_b}(f)$ falls with frequency at high frequencies. The high-frequency slope of $\frac{\theta}{U_b}(f)$ is typically near -20

dB/decade. The phase of $\frac{\theta}{U_b}(f)$ approaches $-1/4$ cycles at high frequencies. In other words, at high frequencies hair bundle rotation θ is proportional to the displacement X_b of the base of the bundle.

Hair bundles for which low-frequency measurements of $\frac{\theta}{U_b}(f)$ were available largely fell into two categories. In the first category, the magnitude of $\frac{\theta}{U_b}(f)$ fell with frequency at all frequencies, and the phase of $\frac{\theta}{U_b}(f)$ was near $-1/4$ cycles at all frequencies measured. For these hair bundles, the largest value of $\frac{\theta}{U_b}(f)$ was typically at the lowest frequency measured. In the second category, $\frac{\theta}{U_b}(f)$ was constant or increasing with frequency at low frequencies, with a phase near or above 0 cycles. For these hair bundles, the largest value of $\frac{\theta}{U_b}(f)$ was typically at a frequency between 500 Hz and 5 kHz.

6.3.5 Model fits of $H_\mu(f)$

In addition to the measured $\frac{\theta}{U_b}(f)$ values, figure 6-7 shows fits of the Freeman and Weiss model to the measurements. These fits were computed by finding the value of the single free parameter C_z that minimizes the difference between the measured magnitudes and the model predictions in a least-squares sense[¶]. The solid lines show the best fit of the model to the data. For the left-hand plot, the model accurately predicts the phase; for the right-hand plot, the model predicts the phase at high frequencies, but underestimates phase lag at low frequencies. The dashed line shows the prediction of the model for twice the best-fit specific compliance. The dotted line shows the prediction of the model for half the best-fit specific compliance. The largest differences between the different model predictions are at low frequencies.

The Freeman and Weiss model was fit to measurements of $\frac{\theta}{U_b}(f)$ for the 136 hair bundles described in section 6.3.4. These fits are shown in the appendices. The left-hand plots show the least-squares fits of the model to all the measured magnitudes. The center plots show the least-squares fits of the model to the magnitudes of the filtered subset of data. The right-hand plots show the least-squares fits of the model

[¶]Model fits in which both C_z and L were allowed to vary are described in section 6.3.7.

to the real and imaginary components of the filtered subset of data. In subsequent figures, analyses of these three fits are shown side-by-side for comparison.

It is important to stress that these fits were found by adjusting only a single free parameter, the specific compliance C_z. There is no overall gain parameter in the model fits. Doubling or halving the best-fit C_z respectively increases (dotted lines) or decreases (dashed lines) the modeled $\frac{\theta}{U_b}(f)$ at low frequencies, while having very little effect at high frequencies. The high-frequency predictions of the model are determined primarily by the measured bundle height L, and so are completely constrained by the model. The best-fit specific compliance and the measured hair bundle height are listed at the top of each plot in the appendices.

The fits let us divide the hair bundles into three groups. The three appendices are sorted based on the fit of the Freeman/Weiss model to the real and imaginary components of the filtered data set. Appendix A contains twenty-four measurements which were not well fit by the model; the best fits to these measurements had RMS errors more than 0.5 times the mean $\frac{\theta}{U_b}(f)$ magnitude. Fourteen of these 24 came from the extreme basal end of the papilla in one preparation. The hair bundles in this group will not be described further in the results section. Appendix B contains 32 measurements which were well fit by the model with the peak frequency of the fit below 500 Hz. Appendix C contains 80 measurements which were well fit by the model with the peak frequency of the fit between 500 Hz and 10 kHz.

For the hair bundles in appendices B and C, the measured $\frac{\theta}{U_b}(f)$ values at high frequencies typically fall close to the predictions of the Freeman/Weiss model. The one free parameter in the model, C_z has almost no effect on the model predictions at high frequencies. Thus $\frac{\theta}{U_b}(f)$ at high frequencies can be predicted from the Freeman/Weiss model knowing only the hair bundle height L.

For the hair bundles in appendix B, a wide range of C_z values resulted in nearly identical fits to the measurements. These fits typically gave relatively high C_z values, often as high as permitted by the fitting procedure (10^{14} rad/N). For these bundles, the Freeman/Weiss model fits were linear with a slope of -20 dB/decade for all frequencies above 500 Hz.

For the hair bundles in appendix C, the measurements constrain C_z more tightly. The best fit of the model to these measurements has a peak frequency in the range 0.5–10 kHz. Below this peak frequency, the magnitude of the fit rises with frequency at 10 dB/decade, while the phase falls from +1/8 cycle to about 0 cycles. Above the peak frequency, the magnitude of the fit falls at -20 dB/decade, and the phase approaches -1/4 cycle.

To evaluate the accuracy of the fits, we compared the error in the best fit of the Freeman/Weiss model to the error in a linear fit to the magnitudes. Figure 6-8 shows the comparison for the 113 bundles in appendices B and C. The three plots in the figure correspond to the three fits for each bundle in the appendices. The left-hand plot shows the error in the fits to all the magnitudes. The center plot shows the error in the fits to the magnitudes of the filtered data set. The right-hand plot shows the error in the fits to the real and imaginary components of the filtered data set. In each case, the error in the fit of the Freeman/Weiss model is comparable to that of a linear fit, even though the linear fit has two free parameters compared to the one in the Freeman/Weiss model. The error in the fit of the Freeman/Weiss model is larger for the right-hand plot, because the error is computed to both real and imaginary components, while the error in the linear fit is computed using the magnitude.

Dependence of model parameters on bundle height

The parameters C_z and L (rotational specific compliance and height of the hair bundle) characterize the model fit. Since L was measured from the images, C_z was the only free parameter in the fit. Figure 6-9 shows the best-fit C_z as a function of bundle height L for the 112 bundles that were well fit by the model. For each symbol, the horizontal bar marks the best-fit C_z, and the vertical bar shows the range of C_z values for which the error in the fit is within 10% of the minimum error. The grey symbols are for bundles for which the best frequency was below 500 Hz; the black symbols are for bundles for which the best frequency was between 500 Hz and 10 kHz. For the right-hand figure, these symbols correspond to the bundles in appendices B and C, respectively. In general, the bundles in grey are well fit by any specific compliance

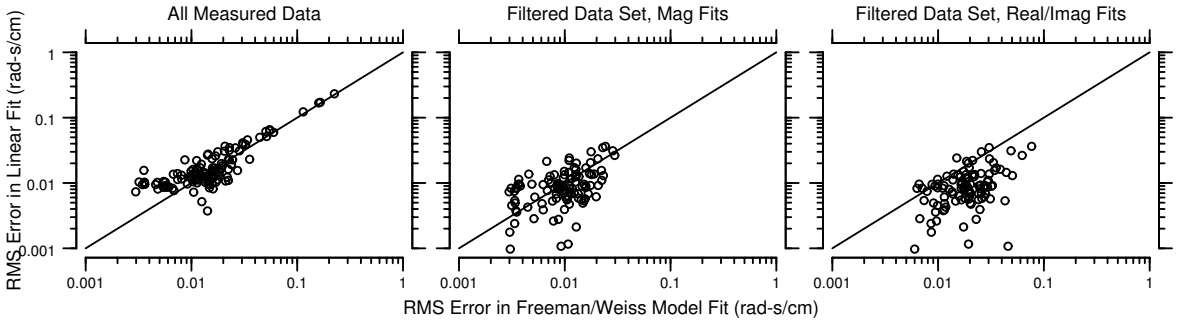

Figure 6-8: RMS errors of fits of the Freeman and Weiss model vs. RMS errors of linear fits. Circles show the RMS error in the best linear fit vs. the RMS error in the best fit of the Freeman and Weiss model. For data points above the line, the error in the linear fit is larger; for data points below the line, the error in the Freeman/Weiss fit is larger. The left-hand plot shows the errors in the fits to the magnitudes of all measured data. The center plot shows the errors in the fits to the magnitudes of the filtered data set. The right-hand plot shows the errors in the fits to the real and imaginary components of the filtered data set. Nine hair bundles had only one or two data points in the filtered data set; these bundles are not shown in the center and right-hand plots, since the error in the linear fit for these bundles is zero.

larger than about 5×10^8 rad/N. The measurements for the bundles in black more tightly constrain C_z. For these bundles, the range of C_z values for which the error is within 10% of the minimum is typically smaller than a factor of two. For most of these bundles, the best-fit C_z is within 10^7 and 10^8 rad/N. For a hair bundle width of 8 μm, these values correspond to rotational compliances in the range $1.25 \cdot 10^{12}$–$1.25 \cdot 10^{13}$ rad/N-m. In the fits to the magnitudes of $\frac{\theta}{U_b}(f)$ measurements (left and center plots), C_z is inversely correlated to bundle height for the bundles for which C_z is constrained by the data. For the fit to the real and imaginary components of $\frac{\theta}{U_b}(f)$, however, no such trend is evident. The next several figures will show results only for the bundles plotted in black in this figure.

The fits of the Freeman and Weiss model shown in figure 6-7 have a prominent peak at a particular frequency f_p. Figure 6-10 plots f_p as a function of hair bundle height for the hair bundles plotted in black in figure 6-9. The peak frequency f_p falls between 500 Hz and 3 kHz for nearly all hair bundles. When the Freeman/Weiss model is fit to just the magnitudes of the measurements, f_p is only loosely correlated to bundle height. When the model is fit to the real and imaginary components of the

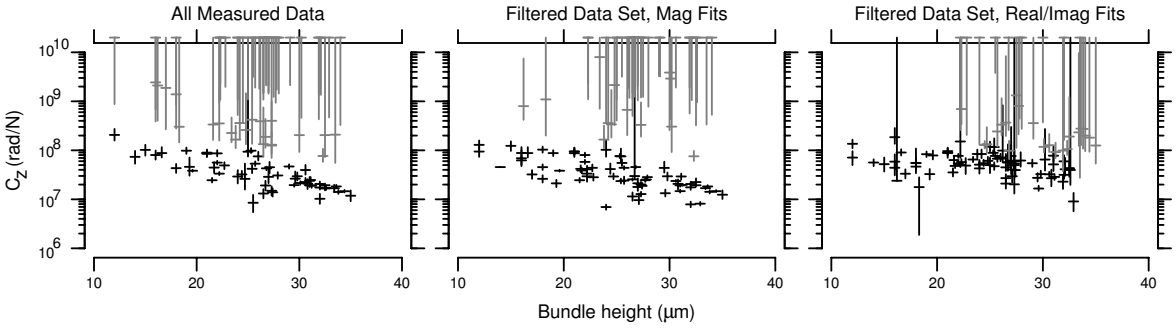

Figure 6-9: Best-fit C_z vs. bundle height. This figure plots the C_z value that best fits the magnitudes of all the measurements (left), the magnitudes of the filtered data set (center), and the real and imaginary components of the filtered data set (right). The horizontal line for each data point shows the best-fit C_z plotted against measured hair bundle height. The vertical line shows the range of C_z values for which the error in the fit is less than 10% larger than the best-fit error. Black symbols are for hair bundles for which $\frac{\theta}{U_b}(f)$ has a magnitude peak between 500 Hz and 10 kHz; grey symbols are for hair bundles for which $\frac{\theta}{U_b}(f)$ peaks at a lower frequency. In general, the fits plotted in black have lower best-fit C_z values and smaller ranges than fits plotted in grey.

filtered data set (right-hand plot), f_p is inversely correlated to bundle height to the $\frac{3}{2}$ power.

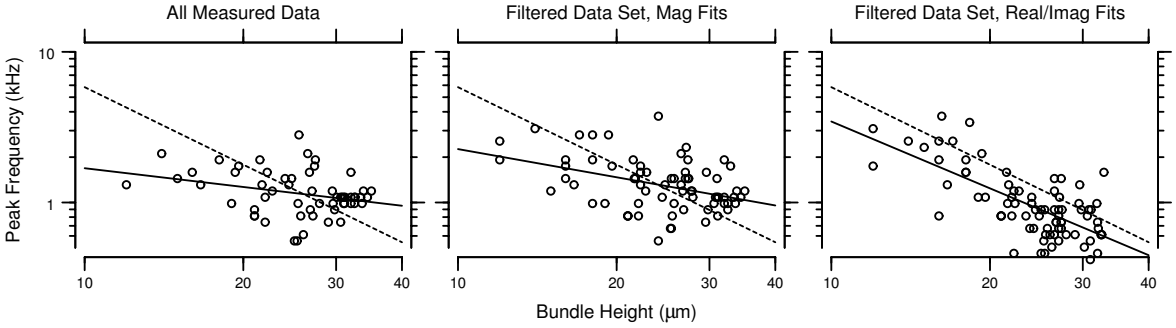

Figure 6-10: Peak frequency of $\frac{\theta}{U_b}(f)$ vs. bundle height. The arrangement of plots is as in figure 6-9. Circles show the peak frequency for each hair bundle. The solid lines show the least-squares power law fit to the data points. On the left, the fit is $f_p = 4.38L^{-0.41}$ (r=−0.30). In the center, the fit is $f_p = 9.46L^{-0.62}$ (r=−0.41). On the right, the fit is $f_p = 103L^{-1.47}$ (r=−0.70). The dashed line in each plot shows the fit to the data of Frishkopf and DeRosier from figure 6-6.

Since we know the location of each hair bundle, we can also look at the distribution of peak frequency along the length of the papilla. This distribution is shown

in figure 6-11. For all three types of fits, peak frequency is inversely correlated to distance from the basal end of the papilla. This correlation is strongest for the fits in the right-hand plot. The dashed line in each plot shows a predicted frequency-to-place map based on neural measurements (Holton and Weiss, 1983a), assuming that distance across the nerve maps directly to distance along the papilla. Most of the best frequencies seen in this study fall below this prediction.

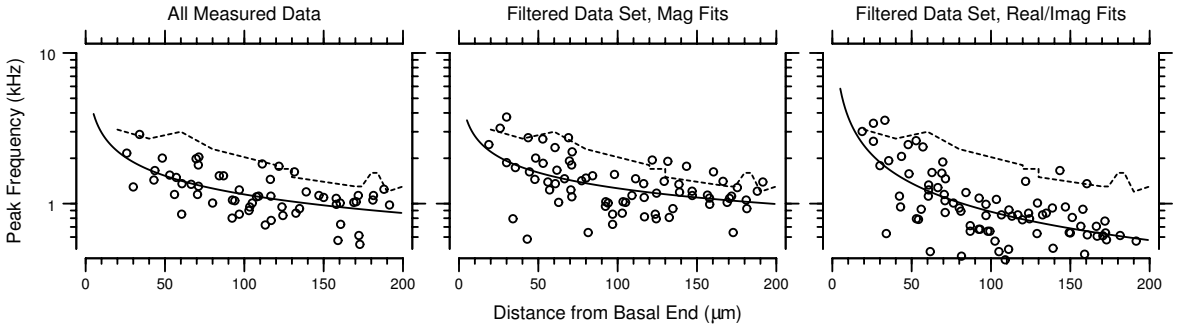

Figure 6-11: Peak frequency of $\frac{\theta}{U_b}(f)$ vs. longitudinal position d. The arrangement of plots is as in figure 6-9. Circles show the peak frequency for each hair bundle. The solid lines show the least-squares power law fit to the data points. On the left, the fit is $f_p = 7.63d^{-0.41}$ (r=−0.60). In the center, the fit is $f_p = 6.25d^{-0.35}$ (r=−0.49). On the right, the fit is $f_p = 15.9d^{-0.63}$ (r=−0.67). The dashed lines show a frequency-to-place map predicted from the neural data of Holton and Weiss (1983a). Nearly all of the best frequencies in this study fall below the prediction from neural neural measurements.

Figure 6-12 shows the peak frequency of f_p vs. the best-fit C_z for the same hair bundles as in the previous figures. The data are widely scattered. Although there is a trend for best frequency to be inversely correlated to best-fit compliance, the correlation is not strong.

The frequency selectivity of a resonant system is often represented by the quality factor Q. Figure 6-13 shows the Q_{10dB} as measured from the best fit of the Freeman and Weiss model as a function of hair bundle height. The Q_{10dB} values are all between 0.1 and 0.4. These Q_{10dB} values are all lower than those of the electrical responses of hair cells (Holton and Weiss, 1983b; Holton and Weiss, 1983a) or the neural responses of auditory nerve fibers (Weiss et al., 1976), which range from 0.5 to 5. For all three types of fits, Q_{10dB} is correlated with hair bundle height.

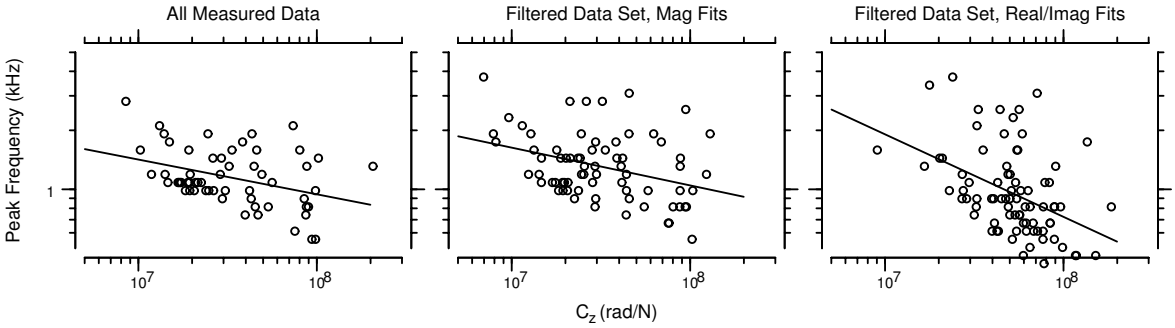

Figure 6-12: Peak frequency of $\frac{\theta}{U_b}(f)$ vs. C_z. The arrangement of plots is as in figure 6-9. Circles show the peak frequency for each hair bundle. The solid lines show the least-squares power law fit to the data points. On the left, the fit is $f_p = 24.7C_z^{-0.18}$ (r=−0.38). In the center, the fit is $f_p = 36.5C_z^{-0.19}$ (r=−0.35). On the right, the fit is $f_p = 1690C_z^{-0.42}$ (r=−0.44). Peak frequency is weakly correlated to C_z.

6.3.6 Analysis of a 'golden' experiment

One experiment, conducted on October 18, 2001, yielded a large number of low-frequency measurements with little noise. These measurements (bundles 113–136 in appendix C) were fit quite well by the Freeman/Weiss model. The best-fit C_z values were tightly constrained by the low-frequency measurements; C_z was $6.6 \cdot 10^7 \pm 2.1 \cdot 10^7$ rad/N (n=21). Figure 6-14 shows the peak frequency for these hair bundles as a function of both bundle height and distance from the basal end, as determined by the fits to both real and imaginary components of the filtered data set. Both curves show similar trends to those seen in figures 6-10 and 6-11, but with significantly less scatter. These plots show that the trends seen in the combined data set are also evident in results from individual experiments.

6.3.7 Two-parameter fits

Measurements of hair bundle height allow us to fit the Freeman and Weiss model to our measurements using only a single free parameter. We can also evaluate the model by allowing flap height to be a free parameter, and comparing the measured and fit heights. Figure 6-15 plots the best-fit flap height vs. the measured bundle height. For many hair bundles, the best fit was relatively insensitive to the flap

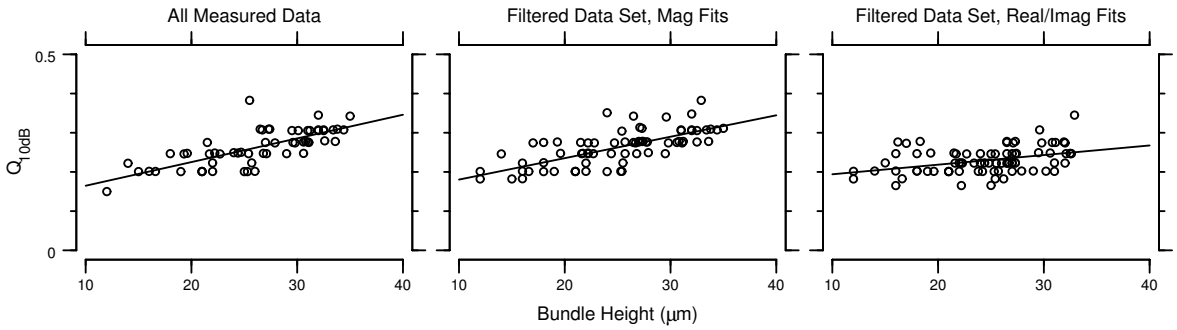

Figure 6-13: Q_{10dB} of model fits vs. hair bundle height. Q_{10dB} was measured from the least-squares fit of the Freeman and Weiss model to the measured $\frac{\theta}{U_b}(f)$. The values fall between 0 and 0.5 for nearly all hair bundles measured. The arrangement of plots is as in figure 6-9. Circles show $Q_{10dB}$for each hair bundle. Lines show the least-squares linear fit to the data points. On the left, the fit is $Q_{10dB}= 6.0 \cdot 10^{-3}L + 0.10$ (r=0.74). In the center, the fit is $Q_{10dB}= 5.5 \cdot 10^{-3}L + 0.13$ (r=0.70). On the right, the fit is $Q_{10dB}= 2.5 \cdot 10^{-3}L + 0.17$ (r=0.39).

height. Figure 6-15 shows only the bundles for which the range of bundle heights over which the error was within 10% of the minimum was less than 4 μm. In the left-hand plot, 38 hair bundles satisfied this criterion. In the center and right-hand plots, 55 hair bundles satisfied the criterion. For all three types of fits, best-fit flap height is loosely correlated to measured bundle height. For the fits to the real and imaginary components of the filtered data set, the best-fit line has a slope near 1 and an offset near zero. For the other two types of fits, the slope is lower and the offset is larger.

The best-fit bundle heights from the two-parameter fits in figure 6-15 are not well correlated to the measured bundle heights, although they were tightly constrained for a fixed C_z. With two-parameter fits, it is possible to have a situation where each parameter is tightly constrained when the other is fixed, but the two parameters can covary without significantly increasing the error of the fit. To investigate this possibility, we plotted the error in the two-parameter fit for a range of L and C_z values for each bundle. Figure 6-16 shows a contour plot of this error for one hair bundle. Contour plots for other hair bundles were similar in appearance — simultaneously increasing L and decreasing C_z had little effect on the error in the fit. When either

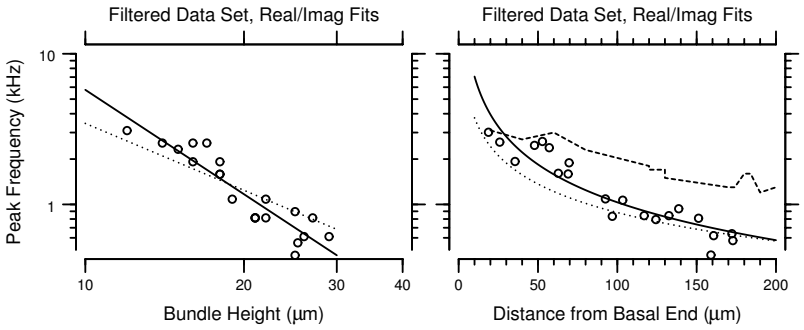

Figure 6-14: Peak frequency of $\frac{\theta}{U_b}(f)$for a 'golden' experiment. The left-hand graph plots the peak frequency of the best fit of the Freeman/Weiss model as a function of measured hair bundle height. The solid line is the least-squares power law fit to the data points, $f_p = 1.15 \cdot 10^6 L^{-2.30}$ (r=−0.92). The dotted line is the least-squares fit from the right-hand plot of figure 6-10. The right-hand graph plots the peak frequency as a function of distance from the basal end. The solid line is the least-squares power law fit, $f_p = 48250 d^{-0.83}$ (r=−0.92). The dashed and dotted lines are repeated from the right-hand plot of figure 6-11.

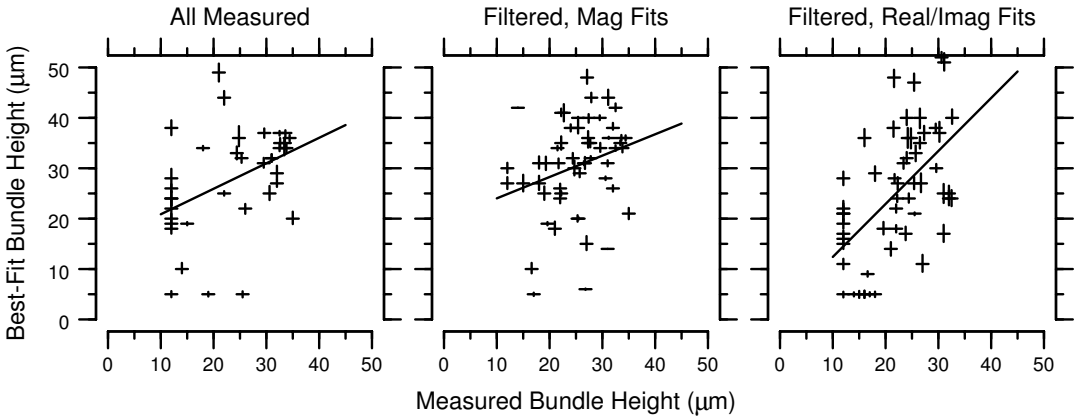

Figure 6-15: Comparison of measured and fit bundle heights. The best-fit flap height of the Freeman and Weiss model is plotted vs. measured hair bundle height. The arrangement of plots is as in figure 6-9. For each symbol, the horizontal line indicates the flap height of the best least-squares fit when both flap height L and compliance C_z are allowed to vary. The vertical line indicates the range of flap heights for which the error in the fit is within 10% of the minimum error. Only hair bundles for which this range was less than 4 μm are included in this plot. This restriction gave 38 hair bundles for the left-hand plot, and 55 hair bundles for both the center and right-hand plots. Although there is a significant amount of scatter to the data, the best-fit flap height is correlated to the measured bundle height in all three fits. Lines show the least-squares linear fit to the data points. On the left, Fit Height = 0.51 Measured Height +15.8 (r=0.43). In the center, Fit Height = 0.42 Measured Height +19.8 (r=0.26). On the right, Fit Height = 1.05 Measured Height +1.9 (r=0.56). The best-fit height was weakly correlated to the measured height.

L or C_z is specified, the other parameter is tightly constrained. However, when neither is constrained there is a large range of parameter values for which the error is within 10% of the minimum. Thus small measurement errors can cause large changes in the best-fit parameter values for the two-parameter fits. Figure 6-17 shows the measured $\frac{\theta}{U_b}(f)$ values for bundle 128, along with model predictions for the four locations shown in figure 6-16. Note that the predictions all have nearly the same best frequency and phase, and differ only slightly in magnitude at high frequencies. The error in each fit was similar.

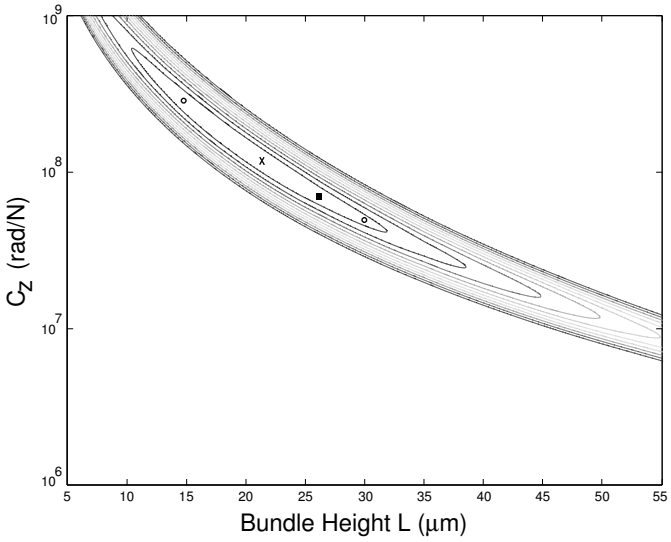

Figure 6-16: The error in a two-parameter fit as a function of L and C_z. This plot shows the best-fit values of L and C_z (marked by the $\times$), and contours at every 10% increase in error up to twice the minimum error. At a given L or C_z, the other parameter is tightly constrained. However, the two parameters can covary without significantly increasing the error in the fit. The $\times$ marks the parameters that best fit the data for a two-parameter fit. The square marks the best fit when the bundle height is specified. The circles mark two sets of parameters for which the model fit is shown in figure 6-17.

6.4 Discussion

6.4.1 Estimates of hair bundle height

As shown in figure 6-3, the height of hair bundles varies systematically along the length of the cochlea. However, our estimates were consistently larger than previous estimates made from fixed tissue. There are three potential causes of this discrepancy. First, the optical point spread function of the microscope tends to blur structures in

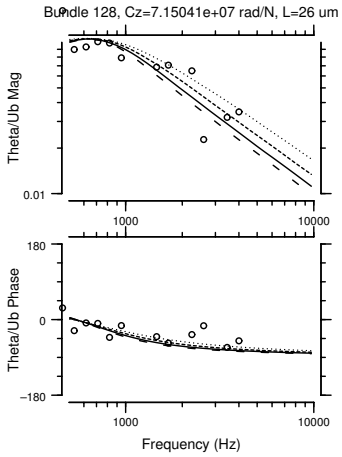

Figure 6-17: Model fits for four values of L and C_z for one hair bundle. The solid line shows the best one-parameter fit of the model using the measured hair bundle height. The short-dashed line shows the best fit of the model when both L and C_z are allowed to vary. The long-dashed and dotted lines show the best fit of the model with L equal to 15 and 30 μm, respectively. Note that all fits have nearly the same peak frequency and nearly the same phase. The magnitudes of the fits differ at high frequencies by less than a factor of two. The error in each fit was within 10% of the minimum error.

the axial direction, so that objects appear taller than their true height. If this were the reason for the overestimate, we would expect hair bundles oriented in the direction of the microscope axis to appear consistently taller than hair bundles oriented longitudinally. However, we do not see such a trend, so optical blurring is unlikely to be the reason for the difference. A more likely reason is that fixation tends to cause tissues to shrink, so estimates of bundle height from fixed tissue are consistently smaller. Another possible reason is that we measure hair bundle heights from the lowest point at which individual stereocilia can be recognized. This point is likely to be inside the cell, so the height of the stereocilia outside the cell in fixed tissue is smaller.

Fits of the Freeman and Weiss model to the measured $\frac{\theta}{U_b}(f)$ values used the measured hair bundle height to constrain the model to having a single free parameter. However, it is not necessarily clear that the measured bundle height is the best value to use for fitting. For most hair bundles, the model fits at high frequencies — which are determined entirely by L — are quite good, suggesting that using the measured height is appropriate. For some measurements, however, the model fits would be improved by choosing a different value for hair bundle height. In particular, for some hair bundles the absolute value of the fit at high frequencies — which is determined entirely by L — does not match the measurements, although the slopes are similar. There is some evidence that the presence of multiple hair bundles in close proximity can be

represented in the model as a change in the effective height of the flap (Freeman, unpublished). Model fits that allow L to vary result in best-fit values of L that can be quite different from the measured values. However, the measurements do not sufficiently constrain such two-parameter fits, so a large range of L values generate similarly good fits. Consequently, we reported C_z values from the one-parameter fits using the measured hair bundle height. To a first approximation, any difference between the measured hair bundle height and the effective height can be compensated by a change in C_z.

6.4.2 Hair bundle deflections are comparable to those predicted from *in vivo* measurements

Although we cannot directly assess the magnitude of hair bundle rotation *in vivo*, we can make predictions based on electrical recordings from hair cells. Measurements of electrical responses of free-standing hair cells (Holton and Weiss, 1983b) show that the response magnitude saturates near 80 dB SPL at the tympanic membrane. In turtle cochlear hair cells, bundle rotations of about 0.1° saturate the electrical responses of the cells (Crawford and Fettiplace, 1985). In our measurements, sound pressures of 120 dB SPL in fluid (which correspond to 84–100 dB SPL at the eardrum, as shown in figure 1-5) cause hair bundle deflections close to 0.5° peak. Assuming that alligator lizard cochlear hair bundles and frog saccular hair bundles are similarly sensitive to rotation (Pickles, 1993), our measurements of hair bundle deflection suggest that electrical responses of hair cells should saturate at sound pressures of 70–86 dB SPL. Thus the observed hair bundle deflections are roughly comparable to those expected *in vivo*.

6.4.3 Comparison to previous measurements

Frishkopf and DeRosier estimate the peak frequency of hair bundle motion by measuring the difference between the phase of displacement of the tip and the base of a hair bundle. Displacement of the tip is the sum of hair bundle deflection and

displacement of the base; the second term biases the phase difference toward zero. Consequently, this method results in an estimate of the peak frequency that is too high. In figure 6-5, the phase of $\frac{\text{Tip}}{\text{RL}}$ is -0.25 cycles at about 2 kHz; for the same hair bundle, the peak of $\frac{\theta}{U_b}(f)$ in figure 6-7 is below 1 kHz. Thus the best frequency found by fitting the Freeman and Weiss model is typically lower than that predicted by the phase-difference method, as shown in figure 6-10.

The peak frequency estimated from our measurements using this phase-difference method is at or above that measured by Frishkopf and DeRosier for all the hair bundles in our study. There are two likely reasons for this discrepancy. First, as stated above, the phase-difference method overestimates the peak frequency. This overestimate is likely to be larger for shorter hair bundles, because the basilar papilla moves more at the basal end at high frequencies (see chapter 4). Second, the cochleae in our study were typically more organized in appearance than in previous studies (Frishkopf, personal communication), suggesting that our preparations suffered less damage during extraction. Since one effect of hair bundle damage is an increase in compliance (Flock, 1982; Flock and Strelioff, 1984; Saunders et al., 1986; Canlon et al., 1987; Szymko et al., 1995; Chan et al., 1998; Duncan and Saunders, 2000), hair bundles that have suffered less damage will have higher peak frequencies.

6.4.4 Reliability of fits

Three types of fits of the Freeman and Weiss model to the data were performed. Fits of the model to all measured magnitudes are likely to be corrupted by noisy measurements, and therefore are probably not reliable. Filtering the data set to remove such measurements reduces the effect of noise. However, fits to the magnitudes of this filtered data set are extremely sensitive to measurement errors; particularly in the high-frequency region, large changes in C_z are necessary to make small changes in the magnitude of the fit. Fits to the real and imaginary components are less susceptible to minor variations in the measurements. For this reason we believe that the fits to the real and imaginary components of the filtered data set are the most reliable.

The Freeman and Weiss model has a third parameter, M_z, the mass per unit length of the flap. We set this parameter to zero in fitting our measurements. To verify the accuracy of this assumption, we need to estimate M_z for a hair bundle. The tallest stereocilia we measured were about 34 μm long, and the shortest stereocilia in those bundles were less than half that height. Thus the cross-sectional area of these bundles is less than 200 μm^2. If the hair bundles have the density of water (1000 kg/m^3), M_z would be $2 \cdot 10^{-7}$ kg/m. Figure 6-2 shows that an M_z value five times larger than this has a negligible effect on the predictions of the model. In other words, the mass of entrained fluid greatly exceeds that of the hair bundle. For this reason, we ignored the effect of hair bundle mass in our calculations.

When the hair bundle height L is fixed in the model, the measured $\frac{\theta}{U_b}(f)$ values generally tightly constrain C_z. Similarly, when C_z is fixed, the measurements tightly constrain L. However, when both parameters are allowed to vary, a wide range of parameter values provide similarly good fits to the measurements. Within this range, increasing L while decreasing C_z has little effect on the peak frequency. Although increasing L lowers the model prediction at high frequencies, decreasing C_z partially compensates for this lowering (see figure 6-2). Consequently, measurements of $\frac{\theta}{U_b}(f)$ by themselves do not provide sufficient information to tightly constrain the parameters of the Freeman and Weiss model.

6.4.5 Comparison of measured $\frac{\theta}{U_b}(f)$ to model predictions

The fits of the Freeman and Weiss model to our measurements are surprisingly accurate given the simplicity of the model. At high frequencies, the measured $\frac{\theta}{U_b}(f)$ almost always decreased with frequency with a slope near -20 dB/decade. The model accurately predicts not only the slope but also the magnitude of $\frac{\theta}{U_b}(f)$ at high frequencies, even though the only free parameter, C_z, has no effect on the model fit in this frequency range. In other words, with no degrees of freedom in this frequency range — not even a gain parameter — the model fit both the magnitude and phase of the measured $\frac{\theta}{U_b}(f)$. This result confirms one of the basic tenets of the Freeman and Weiss model, that free-standing hair bundles are sensitive to RL displacement at high

frequencies.

For 32 hair bundles, the slope of $\frac{\theta}{U_b}(f)$ was -20 dB/decade at low frequencies as well as high frequencies. The Freeman and Weiss model fit these measurements quite well for any value of C_z larger than about 10^8 rad/N. It is likely that these hair bundles were damaged by the dissection. Extensive damage can break the stereocilia rootlets, which would tend to make the hair bundles extremely compliant.

For 80 hair bundles, the best fit of the Freeman and Weiss model had a peak between 500 Hz and 10 kHz, with a positive slope vs. frequency for frequencies below the peak. The measured $\frac{\theta}{U_b}(f)$ magnitudes often showed the same trend, although relatively few reliable measurements were obtained below the peak frequencies of the fits. The measured $\frac{\theta}{U_b}(f)$ phases were in good agreement with the model for these hair bundles. In particular, $\frac{\theta}{U_b}(f)$ had a phase at or above zero cycles at low frequencies.

The consistent increase in phase lag with frequency seen in both the measurements and the models highlights the different mechanical processes at work at low and high frequencies. At high frequencies, both measured and modeled phase were near $-\frac{1}{4}$ cycle. This phase lag is consistent with the idea that at high frequencies, inertial properties of the fluid minimize motion of the hair bundle, so θ is proportional to reticular lamina displacement (Freeman and Weiss, 1990b). At low frequencies, both the measured and modeled phase were at or above 0 cycles. This phase lead is consistent with the idea that at low frequencies, hair bundle deflection is driven by boundary-layer effects which depend on both the velocity and acceleration of the reticular lamina (Freeman and Weiss, 1990c).

The model typically provided better fits to the magnitudes of $\frac{\theta}{U_b}(f)$ at high frequencies than at low frequencies. Because the bases and tips of hair bundles typically moved in phase at low frequencies, measurements of hair bundle rotation at low frequencies involved small differences of large motions. Consequently the low-frequency measurements contained a significant amount of noise, as can be seen by comparing measurements made at closely-spaced frequencies. The lack of reliable low-frequency measurements means that other models could provide good fits to the measured $\frac{\theta}{U_b}(f)$. In particular, the magnitudes — but not the phases — are well-fit

by modeling $\frac{\theta}{U_b}(f)$ as a low-pass filter with two free parameters, the DC gain and the cutoff frequency. However, such a model is a "black box", in that it has no direct physical basis. In comparison, the Freeman and Weiss model fits the data using a physically-based model with only a single free parameter. These features make the Freeman and Weiss model the most parsimonious interpretation of the data.

The best fits of the Freeman and Weiss model to our measurements provide estimates of C_z that range over a factor of five, from roughly $2 \cdot 10^7$ to 10^8. This large range of compliances is hard to reconcile with the fact that the bases of all free-standing hair bundles in this cochlea look remarkably similar. Some of this variability is probably due to errors in measuring hair bundle height, since the best-fit C_z varies with hair bundle height for a given set of measurements (figure 6-16). However, it is likely that some hair bundles suffered more damage than others during dissection. Since damage to hair bundles increases their compliance, the *in vivo* compliance of the bundles is thus more likely to match the lower end of the range measured in this study, and to be constant across the papilla.

6.4.6 Dependence of best frequency on best-fit model parameters

For the hair bundles for which the model fits had peak frequencies above 500 Hz, the peak frequency of the fit was inversely correlated to the measured bundle height. This correlation is clearly seen in figure 6-10, even though there is significant scatter in the data. The correlation is even more evident in the data of figure 6-14; the relationship between f_p and L for this one preparation was similar to the relationship for the pooled data, but with significantly less scatter. The best-fit lines in these plots show that f_p is inversely proportional to L raised to the $\frac{3}{2}$ to $\frac{5}{2}$ power. Hair bundle heights vary by about a factor of three in the free-standing region of this cochlea, while best frequencies of neural recordings from this region vary by about a factor of 4.5. Thus the prediction $f_p \propto L^{-\frac{3}{2}}$ is more likely representative of the *in vivo* relation.

In this study, no strong dependence of f_p on the best-fit compliance C_z was seen.

However, the lowest f_p values were never associated with the lowest C_z values; the lower-left corners of the plots in figure 6-12 are devoid of data points. This is not surprising, since all else being equal, higher C_z values lead to lower f_p values in the model. The weak correlation of f_p with C_z suggests that frequency selectivity in the free-standing region of this cochlea is determined by changes in hair bundle height rather than changes in the compliance of the attachment.

6.4.7 The mechanical frequency selectivity of hair bundles matches that of hair cell receptor potentials at high levels, but not low levels

Measurements of $\frac{\theta}{U_b}(f)$ in this study demonstrate that free-standing hair bundles are mechanically resonant. However, this mechanical resonance alone does not account for the frequency selectivity of hair cells and auditory nerve fibers in this region of the cochlea. In this study, f_p of the model fits ranged from about 0.5–3.5 kHz. Tuning curves measured in the auditory nerve of this lizard range from 1–4.5 kHz for fibers innervating the free-standing region. In addition, by assuming distance along the auditory nerve maps to distance along the basilar papilla, we derive a frequency-to-place map (figure 6-11) that predicts f_p values higher than measured. However, the neural tuning curves were measured near threshold, while our measurements were made at high levels. Measurements of the electrical responses of hair cells show that the peak frequency of the AC (but not DC) component of the receptor potential decreases as the stimulus level increases (Holton and Weiss, 1983a). This decrease can be as large as an octave. Such a shift is consistent with the lower f_p values in our study.

The Q_{10dB} values of the fits in this study are lower than those reported by Weiss *et al* (1976) and Holton and Weiss (1983), who measured Q_{10dB} values of 0.5 to 3 from hair cells in the free-standing region and auditory nerve fibers innervating this region. However, the sharpness of tuning decreases as level increases (Holton and Weiss, 1983b), so the Q_{10dB} values measured in response to high-level stimuli

are comparable to those seen in this study. The nonlinear mechanism that causes sharpness of tuning to change with stimulus level is unknown.

Saturation of the transduction channels reduces the sharpness of tuning at high levels, but does not account for the broadening of tuning curves measured below saturation, nor for the shift in f_p with level. In the Freeman and Weiss model, sharpness of tuning can be increased either by increasing L and decreasing C_z, or by assuming that the hair bundle itself has mass. Neither of these mechanisms depends on stimulus intensity, so the parameters that describe hair bundle motion at high intensities are equally applicable at low intensities. Manley and Köppl have provided some evidence of an active mechanism in the gecko cochlea (Manley and Köppl, 1998; Manley et al., 2001), and suggest that this mechanism is bundle motility. Adding active bundle motility to the Freeman and Weiss model may increase the sharpness of tuning in response to low-level stimuli, and may also cause f_p to shift to higher frequencies at low levels. However, there is currently no direct evidence for the presence of an active mechanism in the alligator lizard cochlea.

In summary, we have demonstrated that free-standing hair bundles have a passive mechanical resonance that determines the best frequency of the hair cell. The motion of hair bundles is well fit by the model of Freeman and Weiss, providing experimental verification of this model. The resonant frequency is determined by the interaction of the hair bundle compliance with the mass of the fluid entrained to move with the bundle; this mass varies with the height of the bundle. The mechanical resonances are highly damped by fluid viscosity, so the sharpness of tuning measured at the level of hair bundle deflection is lower than that measured at the level of hair cell electrical responses. The mechanism by which sharpness of tuning is increased at low levels has not been established.

Appendix A

$\frac{\theta}{U_b}(f)$ of hair bundles that were not well fit by the Freeman/Weiss model

The 24 hair bundles in this appendix had $\frac{\theta}{U_b}(f)$ values that were not well-fit by the Freeman/Weiss model. The best fit to the magnitudes of the filtered data set (center plots) had RMS errors more than 20 times larger than the mean magnitude of $\frac{\theta}{U_b}(f)$. Of these hair bundles, fourteen (bundles 46–49, 51, 81, 83, 85–89, 100, 101) came from the extreme basal end of the papilla in one experiment. The three plots for each hair bundle show different subsets of the data and different fits of the model. In each plot, the solid line shows the best fit, the dotted line shows the model prediction for twice the best-fit compliance, and the dashed line shows the model prediction for half the best-fit compliance. The left-hand plots show all the measured $\frac{\theta}{U_b}(f)$ values (circles), with the best fit of the magnitudes. The center plots show the subset of $\frac{\theta}{U_b}(f)$ values for which the magnitude of the fundamental component of motion was larger than 100 nm, and the magnitudes of higher harmonics were at least 20 dB smaller; the fits in these plots were made to the magnitudes only. The right-hand plots show the same data as the center plots, but with fits to both the real and imaginary components of $\frac{\theta}{U_b}(f)$.

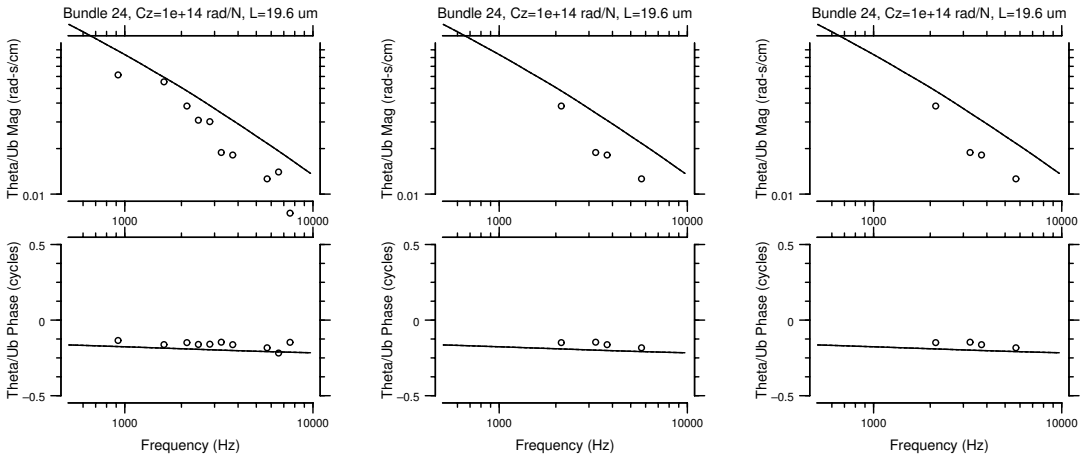

Figure A-1: Bundle 24

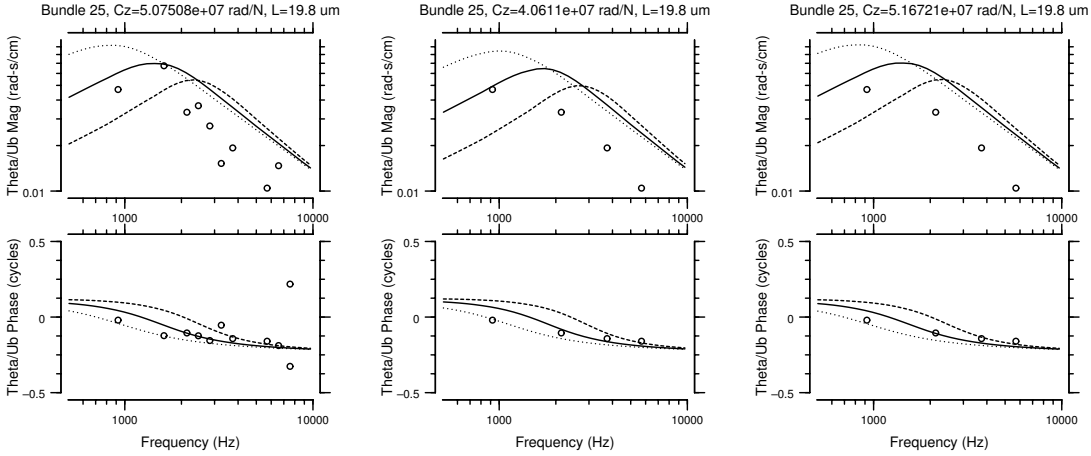

Figure A-2: Bundle 25

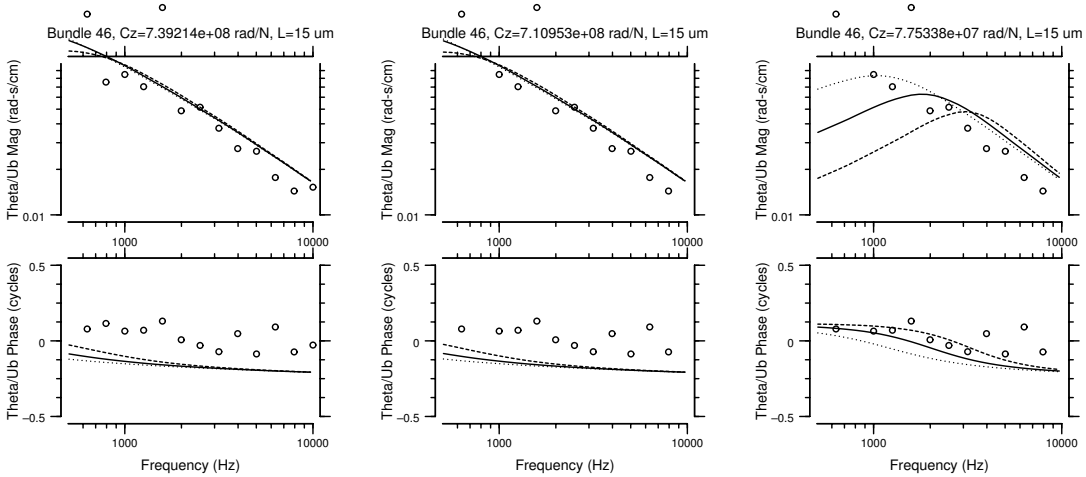

Figure A-3: Bundle 46

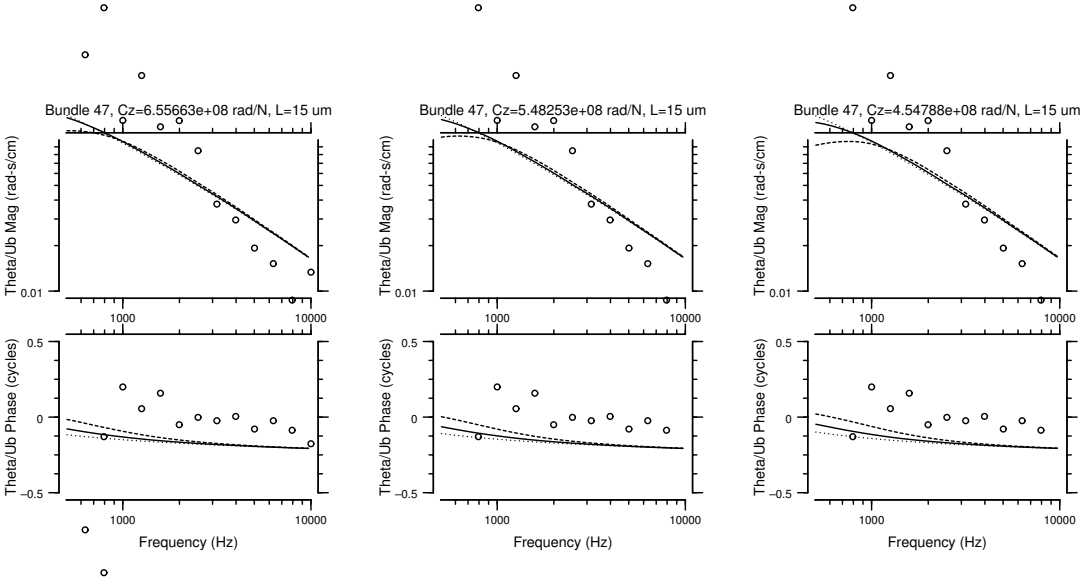

Figure A-4: Bundle 47

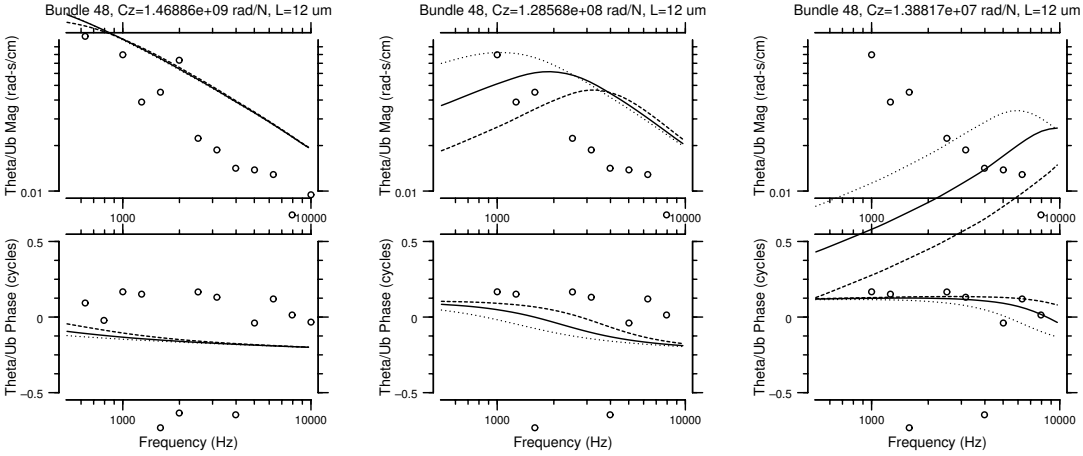

Figure A-5: Bundle 48

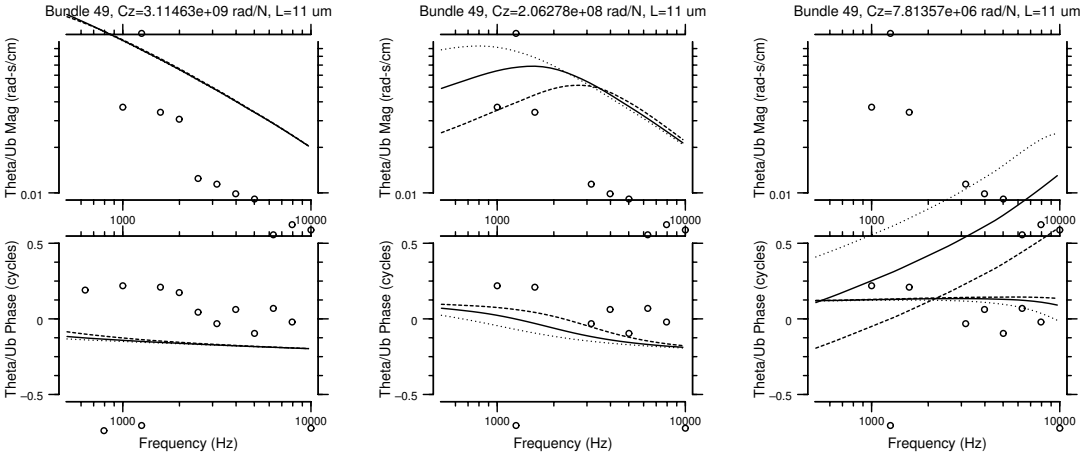

Figure A-6: Bundle 49

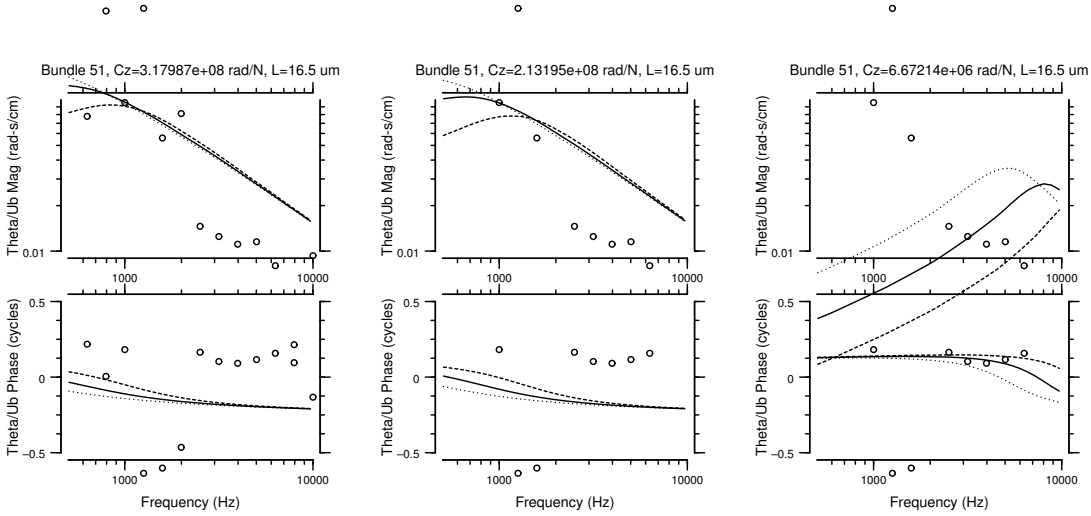

Figure A-7: Bundle 51

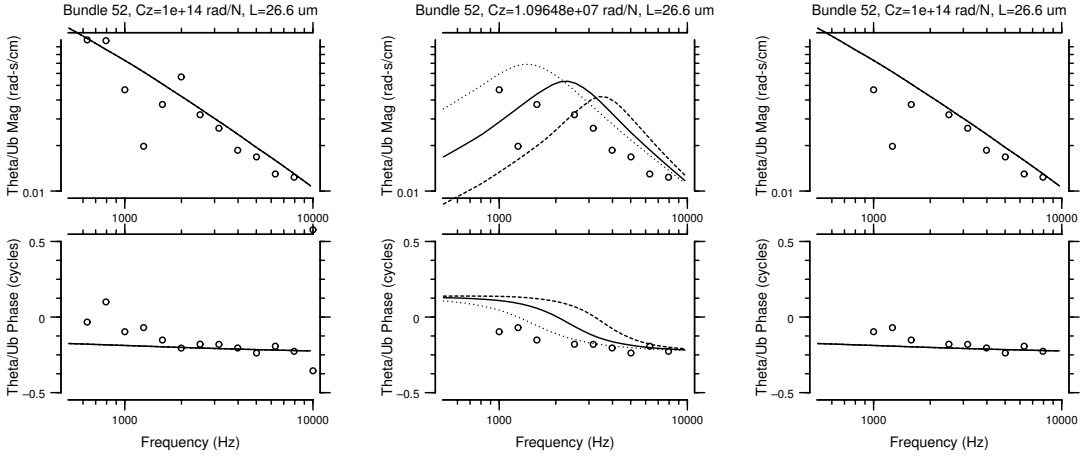

Figure A-8: Bundle 52

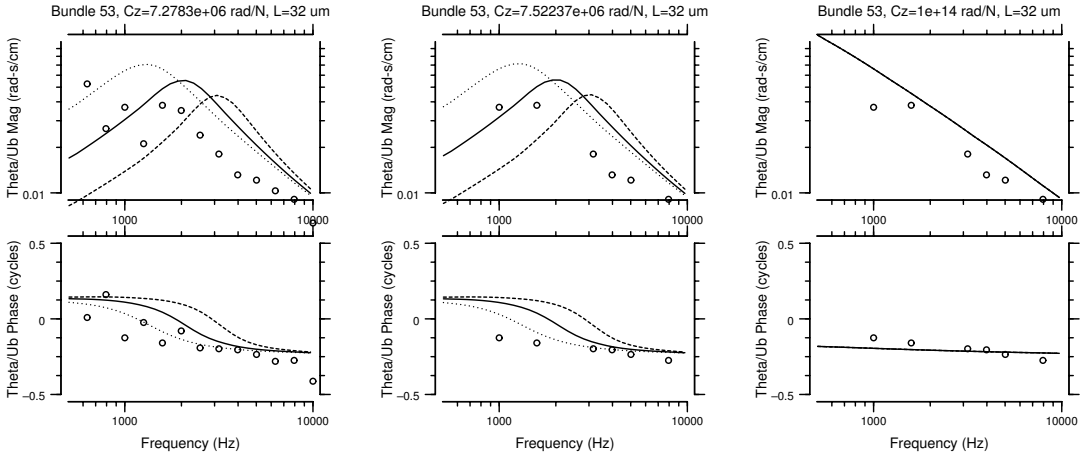

Figure A-9: Bundle 53

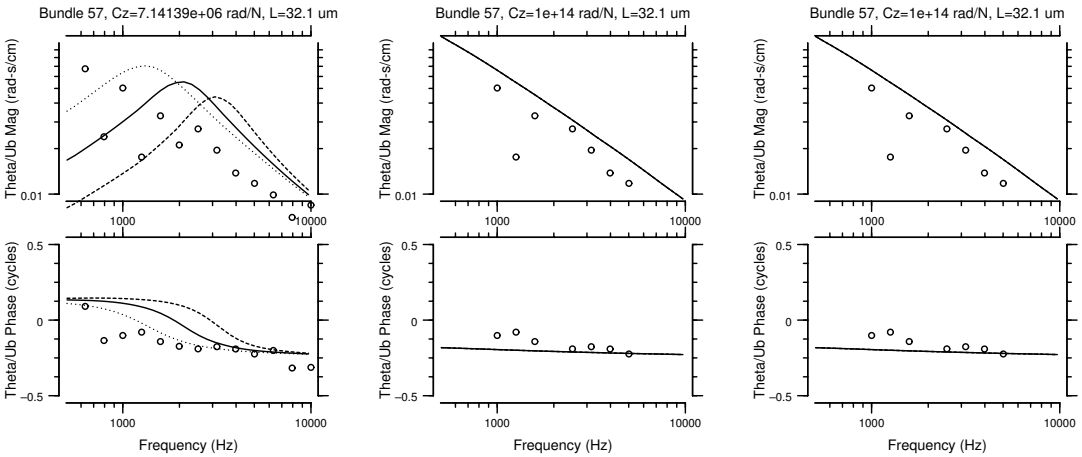

Figure A-10: Bundle 57

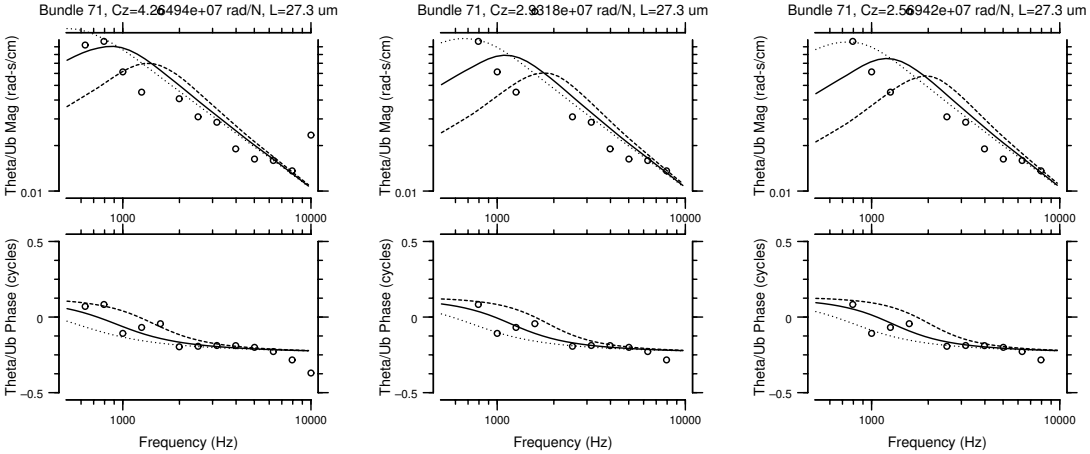

Figure A-11: Bundle 71

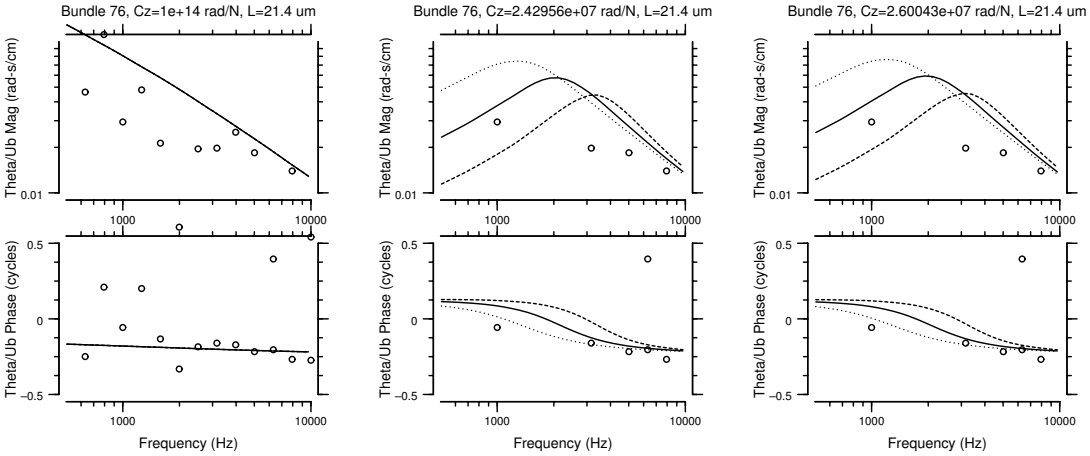

Figure A-12: Bundle 76

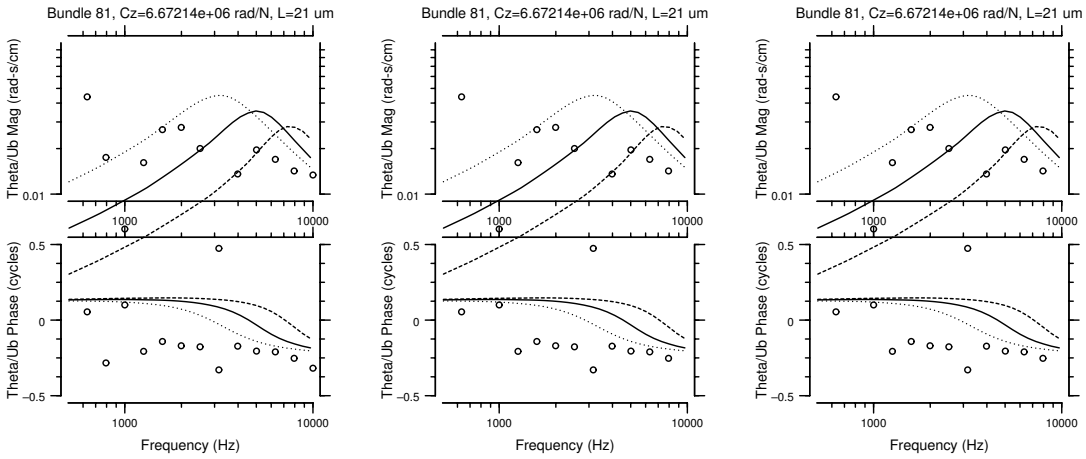

Figure A-13: Bundle 81

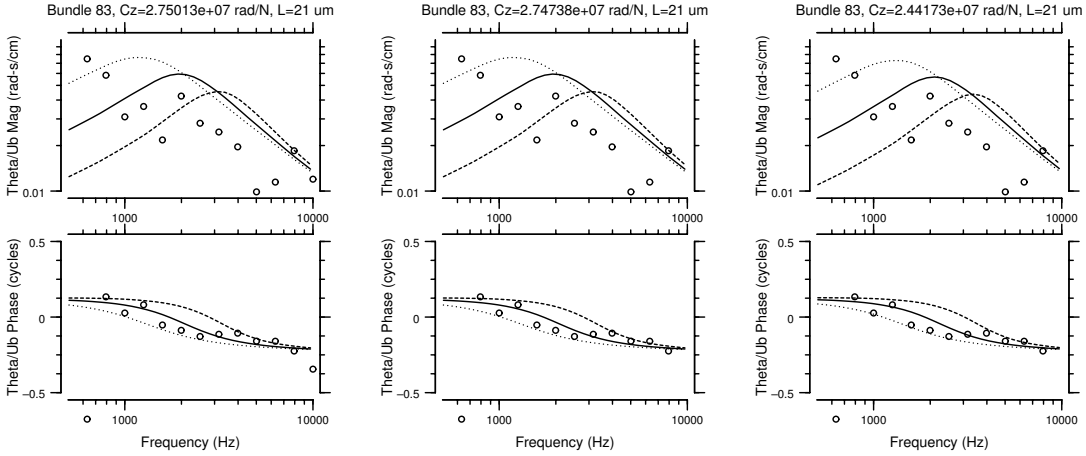

Figure A-14: Bundle 83

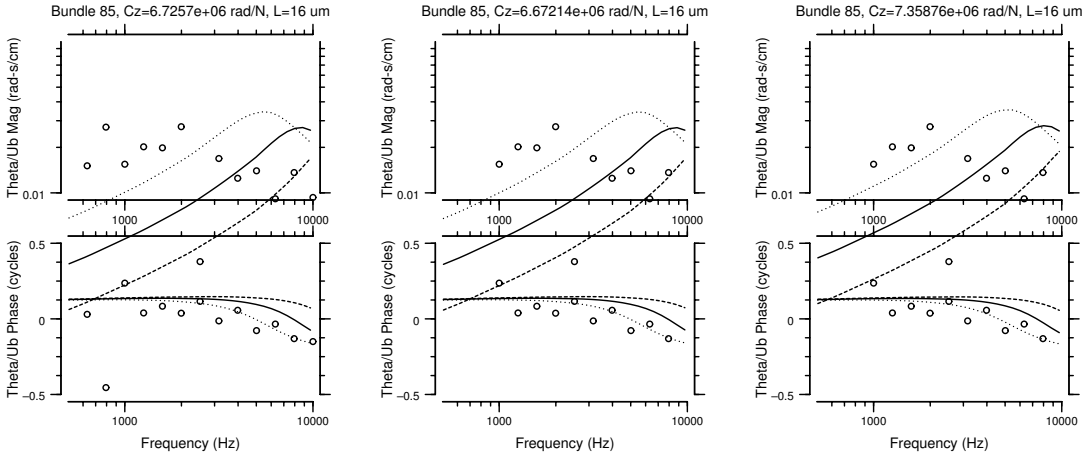

Figure A-15: Bundle 85

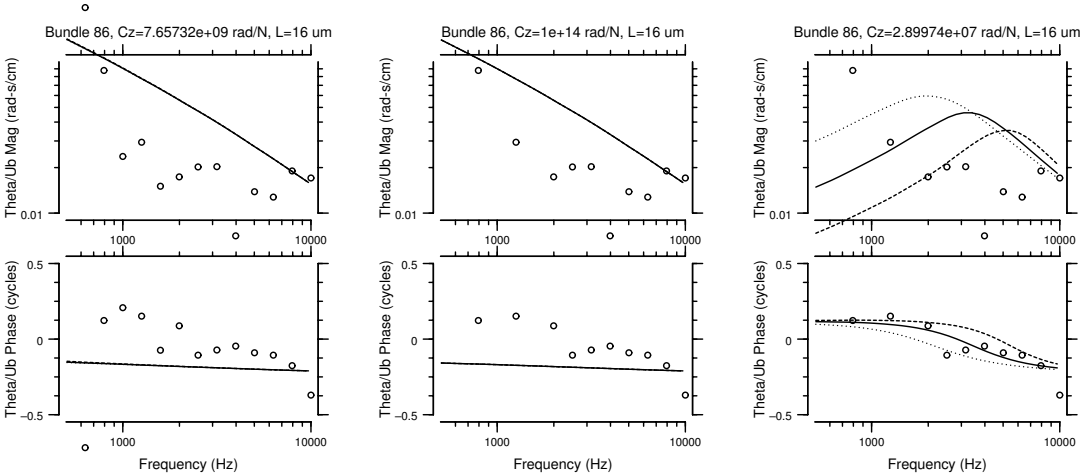

Figure A-16: Bundle 86

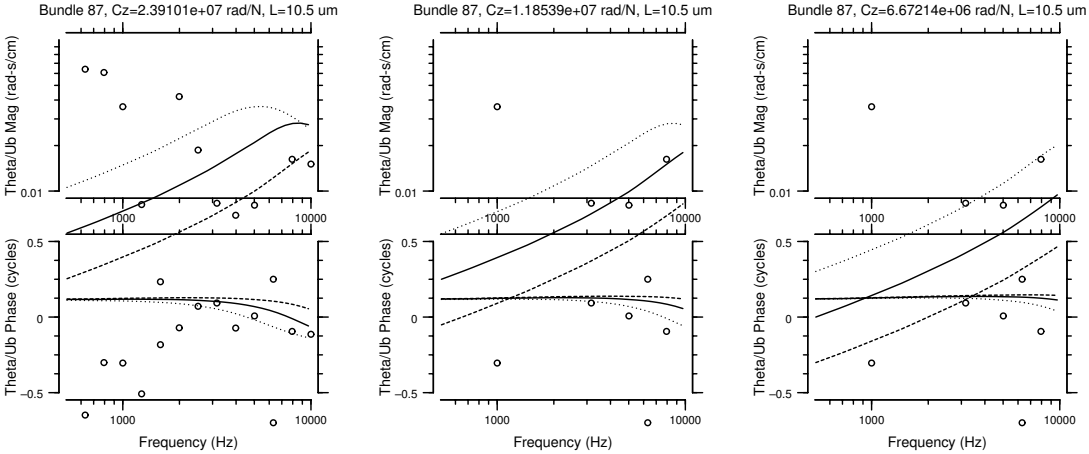

Figure A-17: Bundle 87

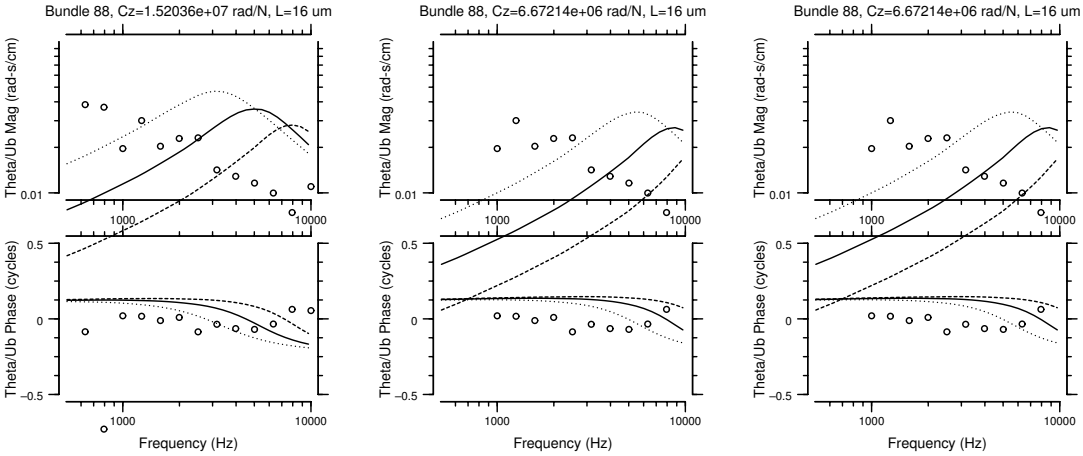

Figure A-18: Bundle 88

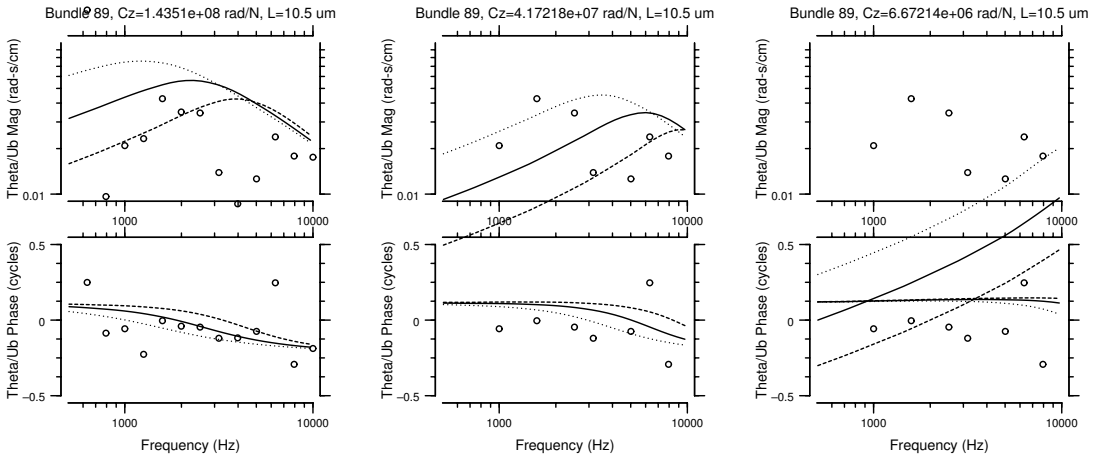

Figure A-19: Bundle 89

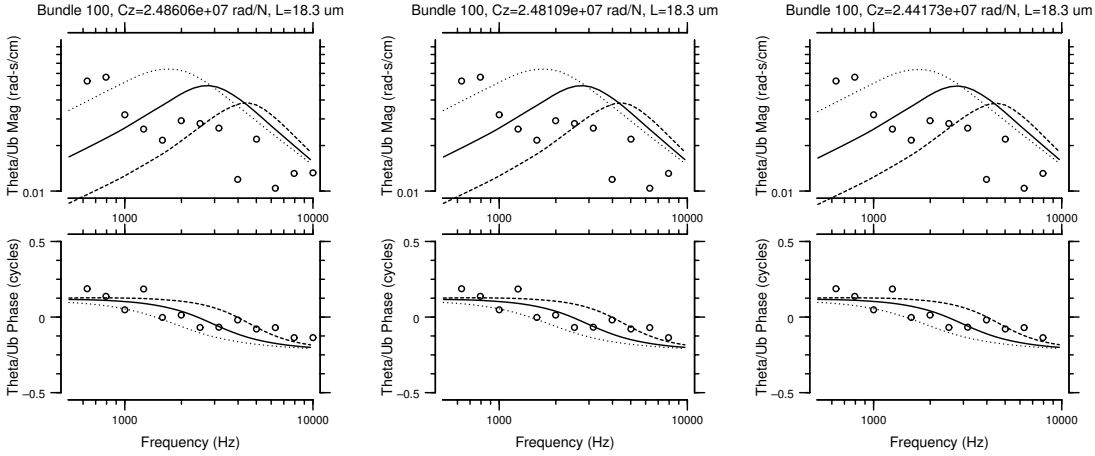

Figure A-20: Bundle 100

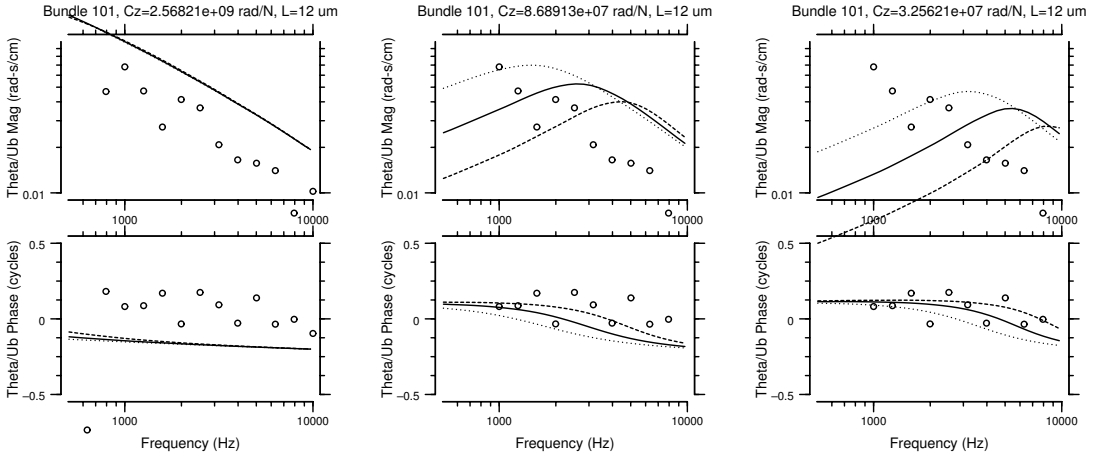

Figure A-21: Bundle 101

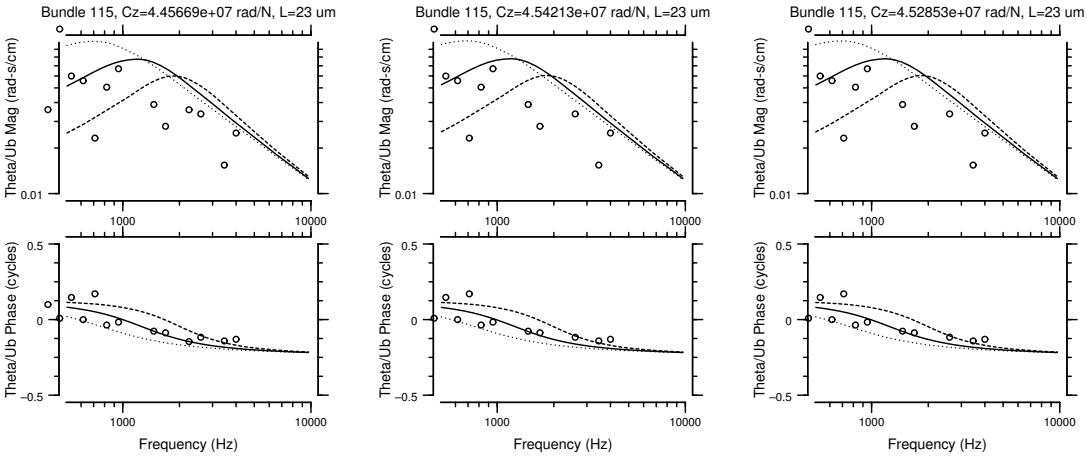

Figure A-22: Bundle 115

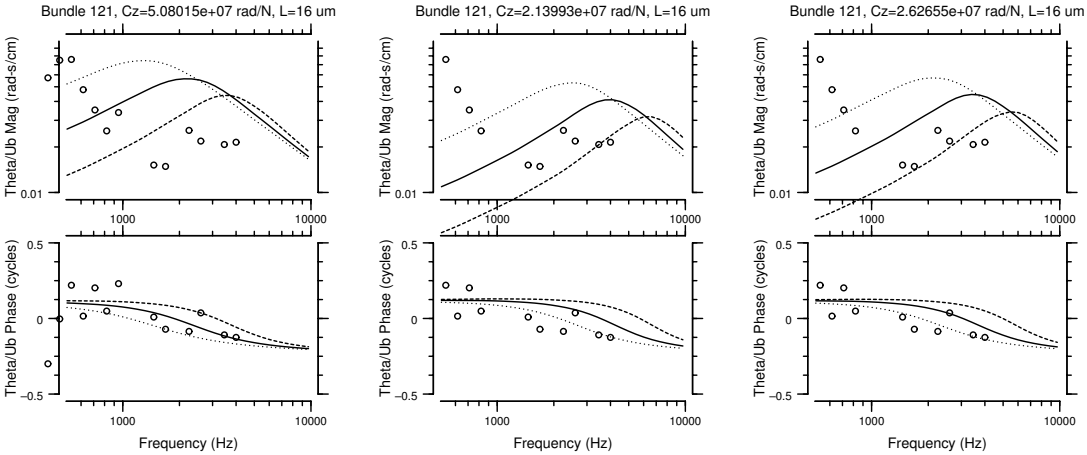

Figure A-23: Bundle 121

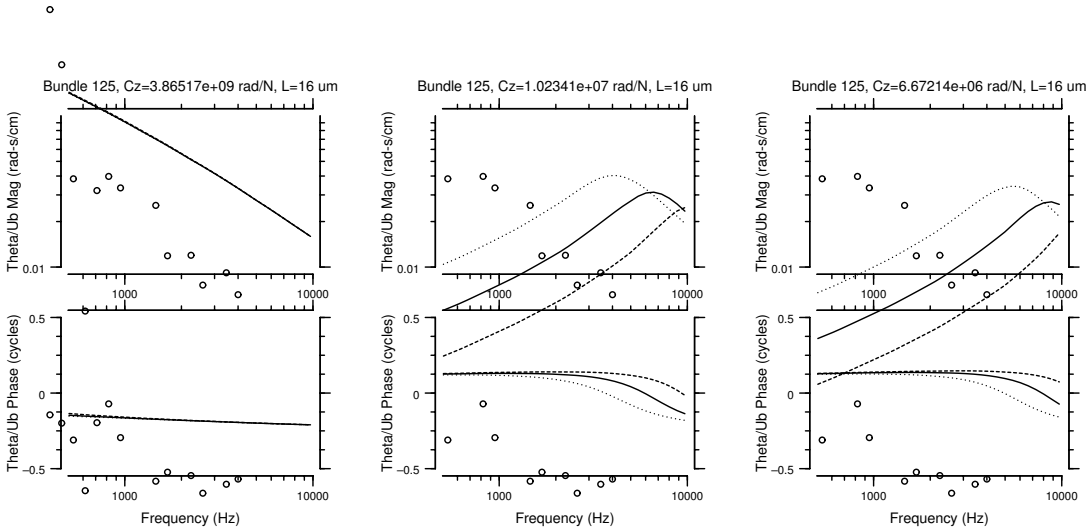

Figure A-24: Bundle 125

Appendix B

$\frac{\theta}{U_b}(f)$ of hair bundles that were well fit by the Freeman/Weiss model with a peak frequency below 500 Hz

The 32 hair bundles in this appendix had $\frac{\theta}{U_b}(f)$ values that were well-fit by the Freeman/Weiss model. The peak frequency of the fit to the real and imaginary components of the filtered data set (right-hand plots) fell below 500 Hz. The three plots for each hair bundle show different subsets of the data and different fits of the model. In each plot, the solid line shows the best fit, the dotted line shows the model prediction for twice the best-fit compliance, and the dashed line shows the model prediction for half the best-fit compliance. The left-hand plots show all the measured $\frac{\theta}{U_b}(f)$ values (circles), with the best fit of the magnitudes. The center plots show the subset of $\frac{\theta}{U_b}(f)$ values for which the magnitude of the fundamental component of motion was larger than 100 nm, and the magnitudes of higher harmonics were at least 20 dB smaller; the fits in these plots were made to the magnitudes only. The right-hand plots show the same data as the center plots, but with fits to both the real and imaginary components of $\frac{\theta}{U_b}(f)$.

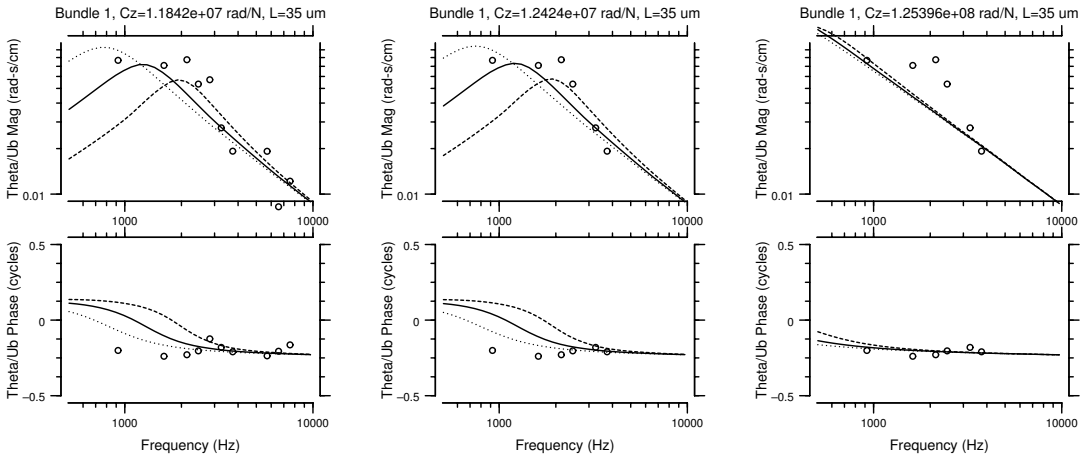

Figure B-1: Bundle 1

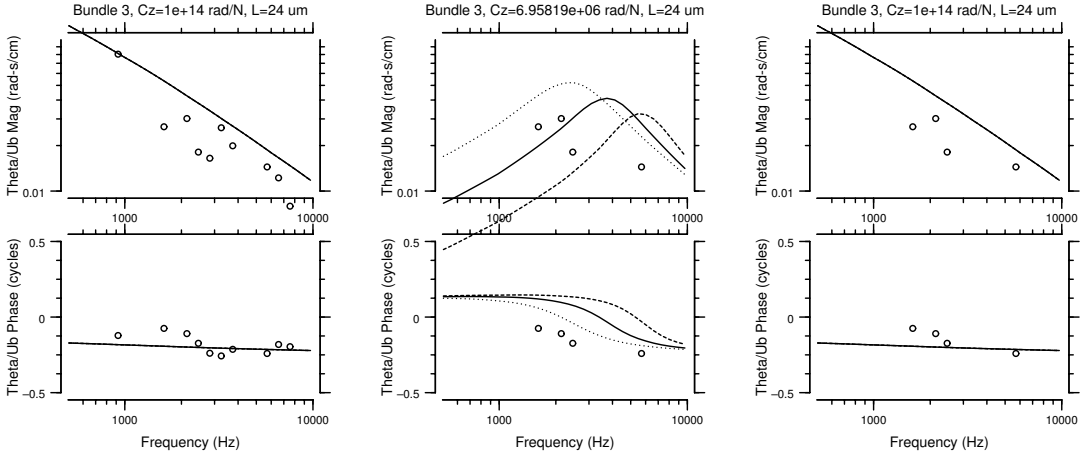

Figure B-2: Bundle 3

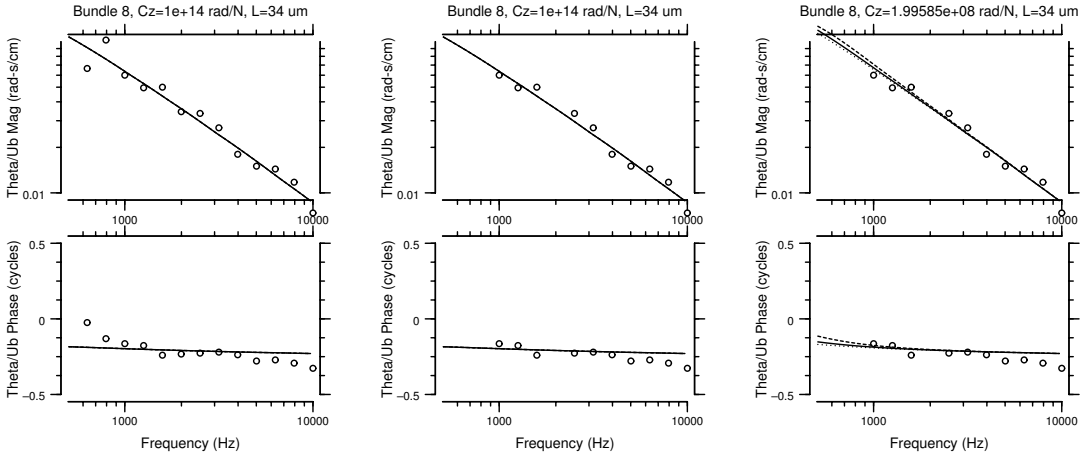

Figure B-3: Bundle 8

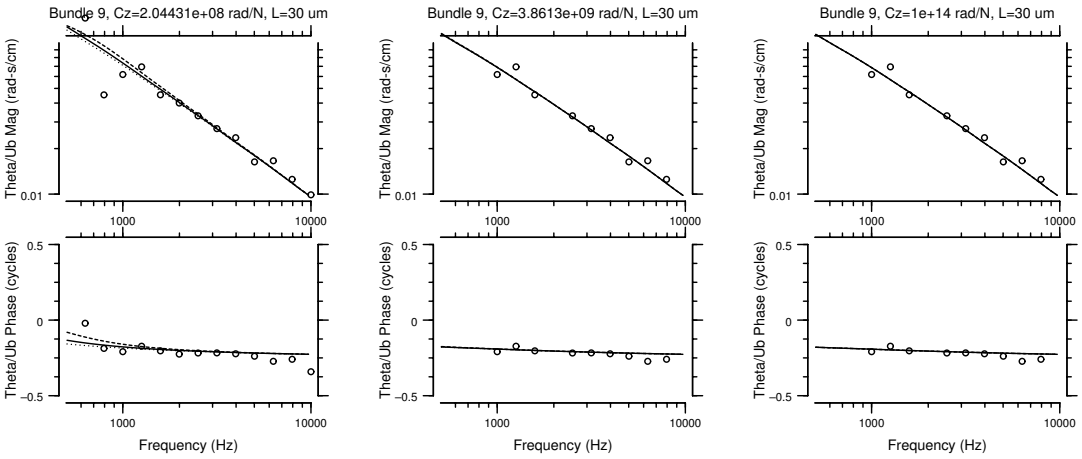

Figure B-4: Bundle 9

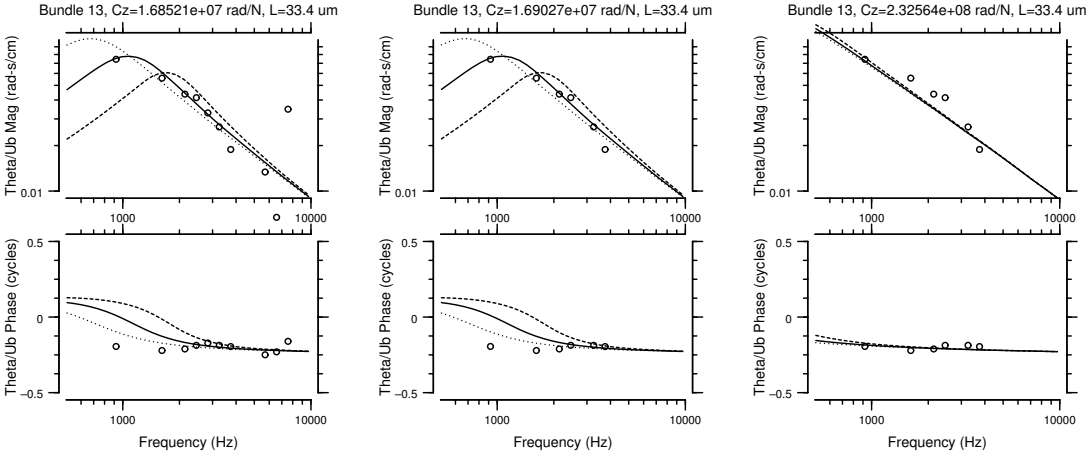

Figure B-5: Bundle 13

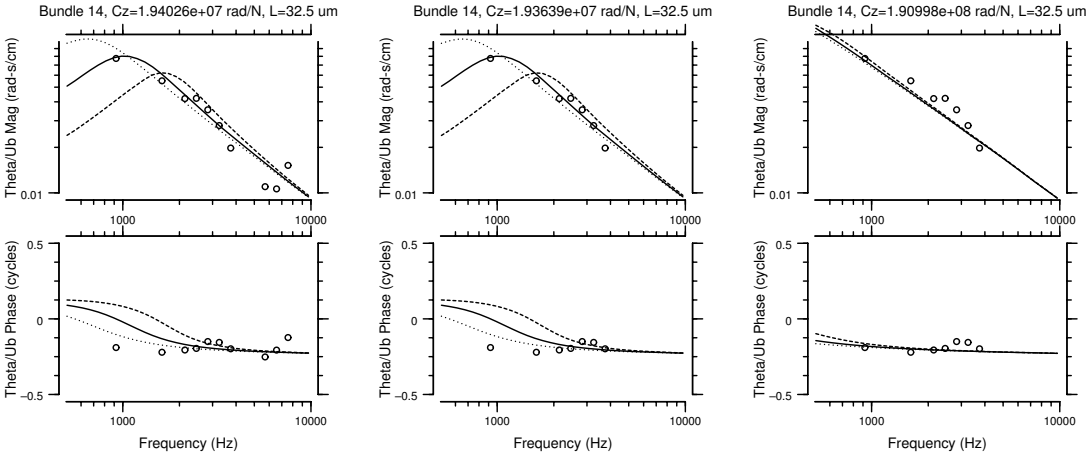

Figure B-6: Bundle 14

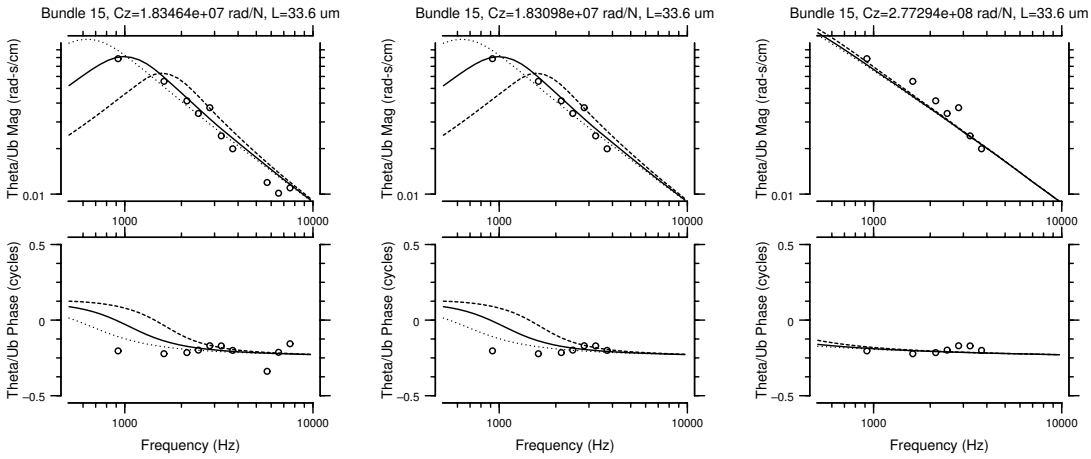

Figure B-7: Bundle 15

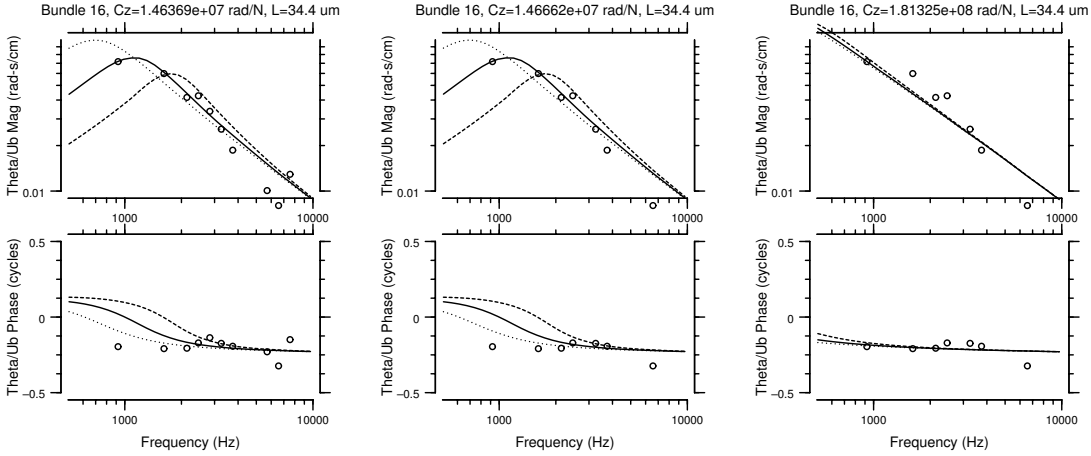

Figure B-8: Bundle 16

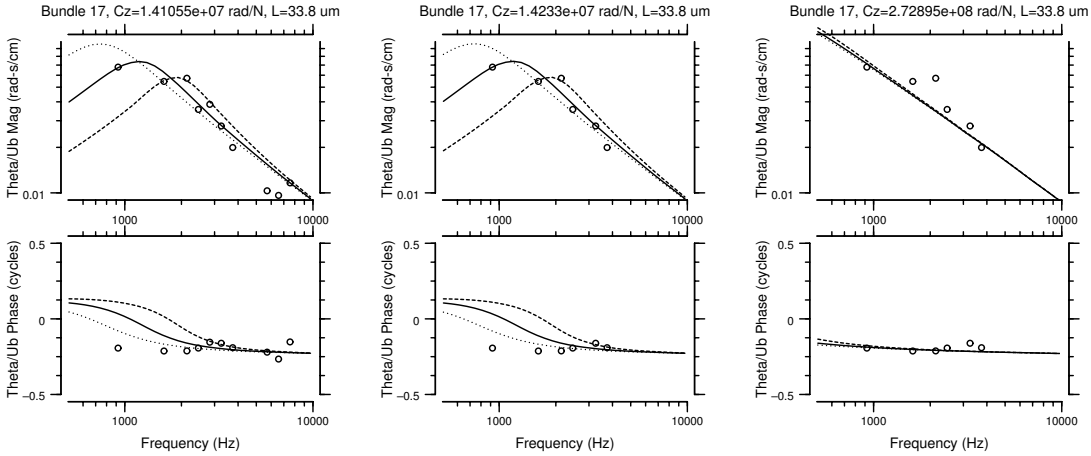

Figure B-9: Bundle 17

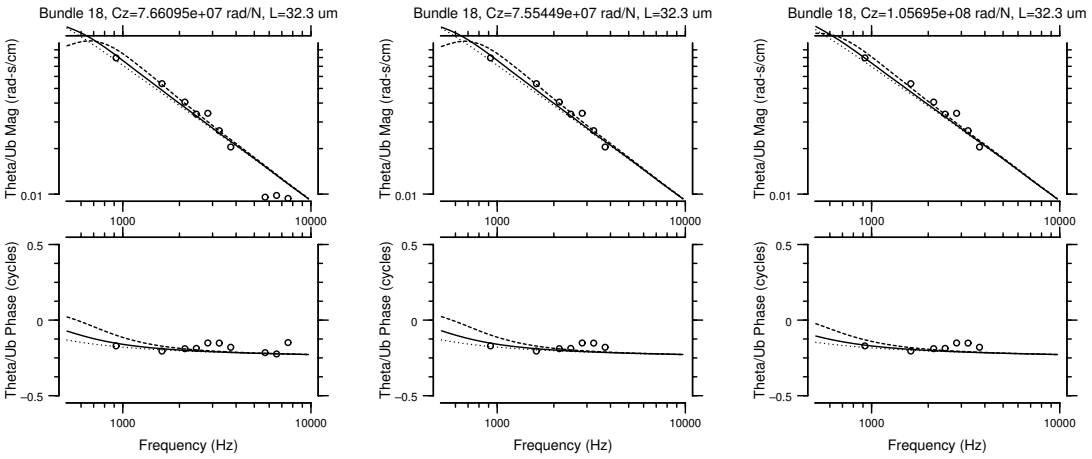

Figure B-10: Bundle 18

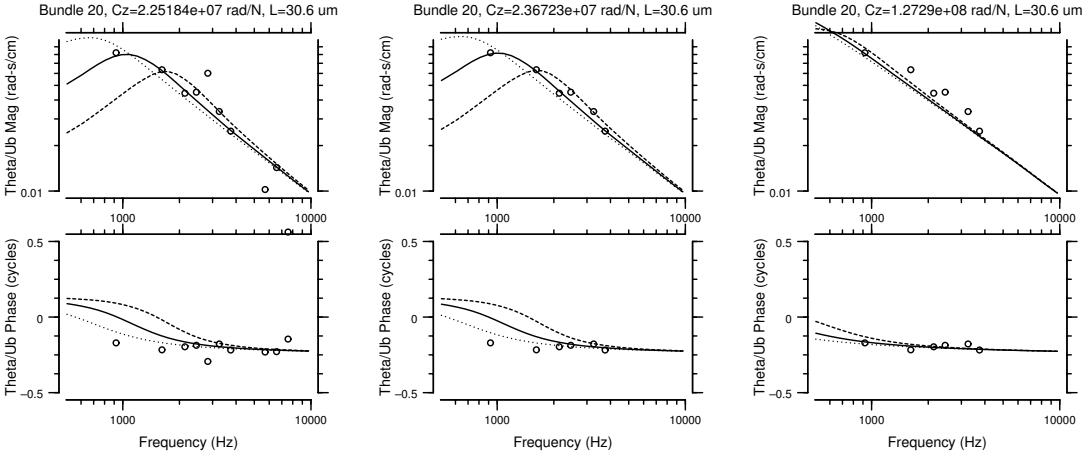

Figure B-11: Bundle 20

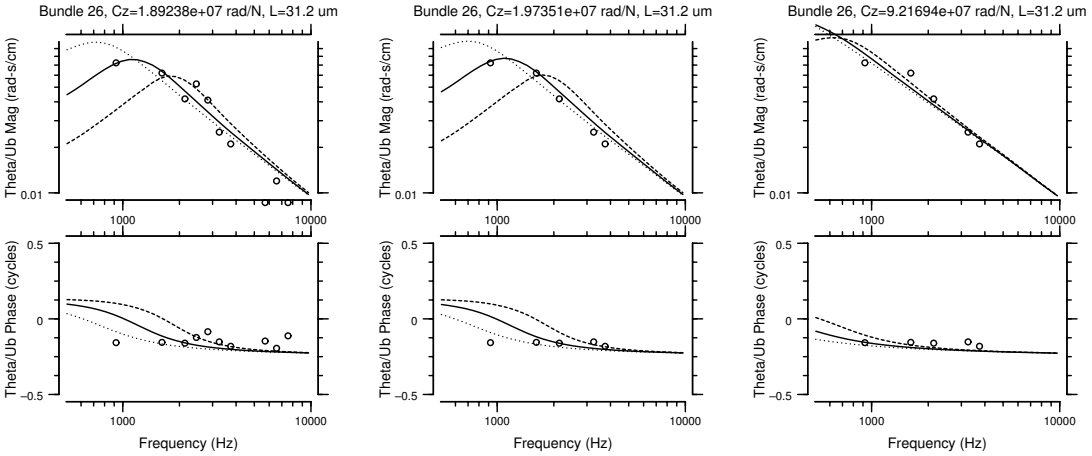

Figure B-12: Bundle 26

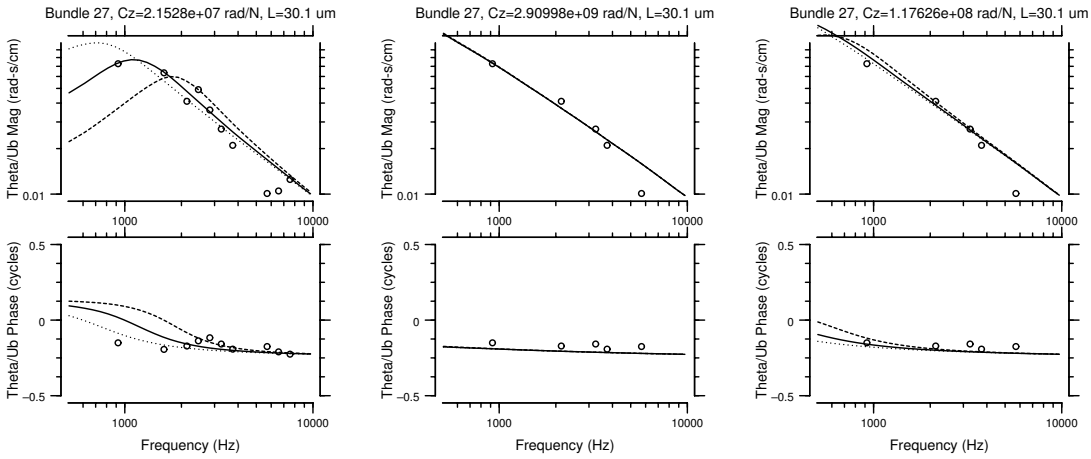

Figure B-13: Bundle 27

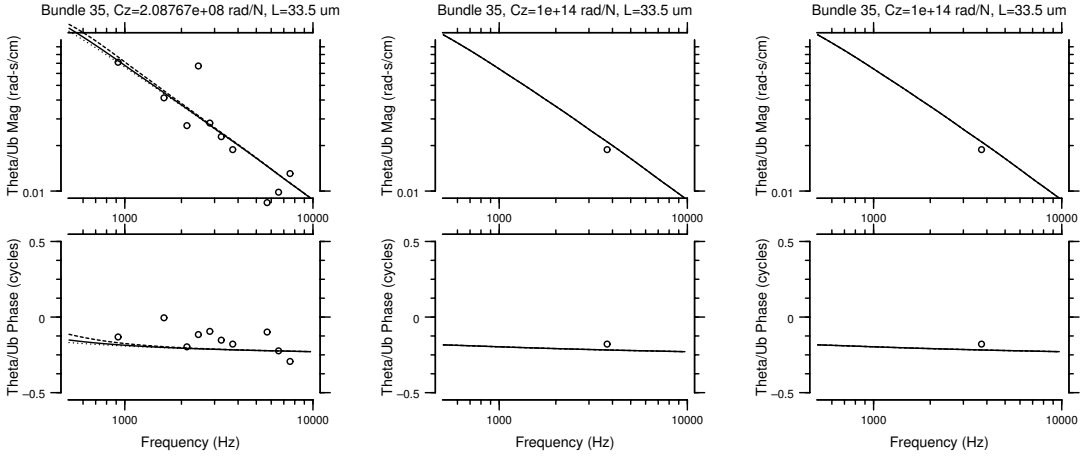

Figure B-14: Bundle 35

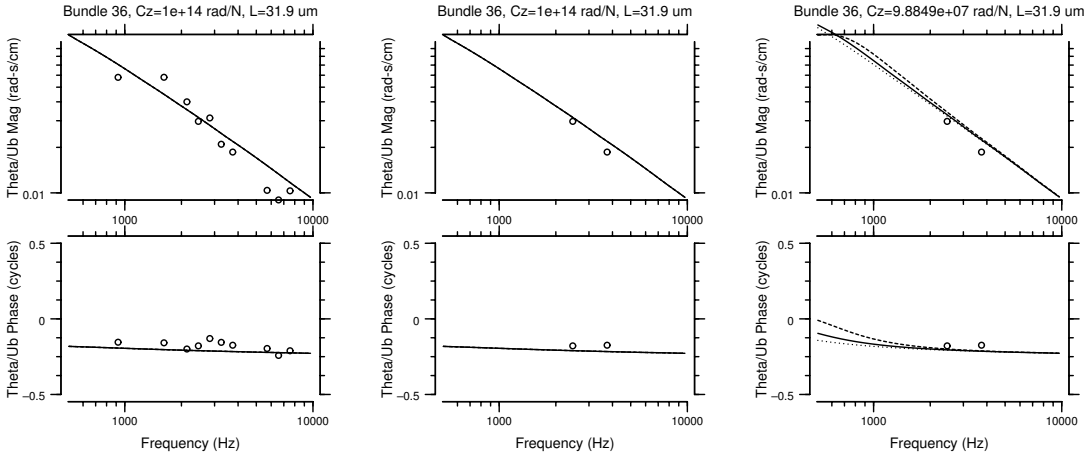

Figure B-15: Bundle 36

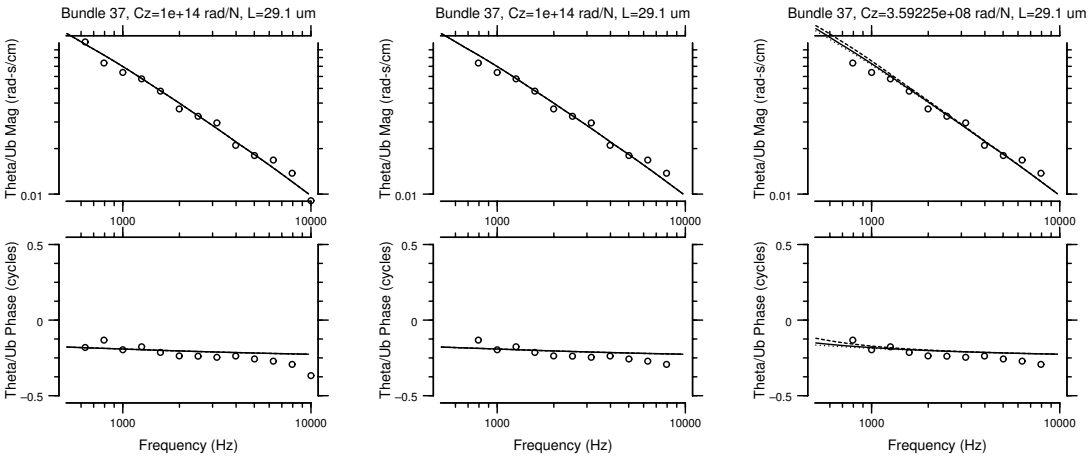

Figure B-16: Bundle 37

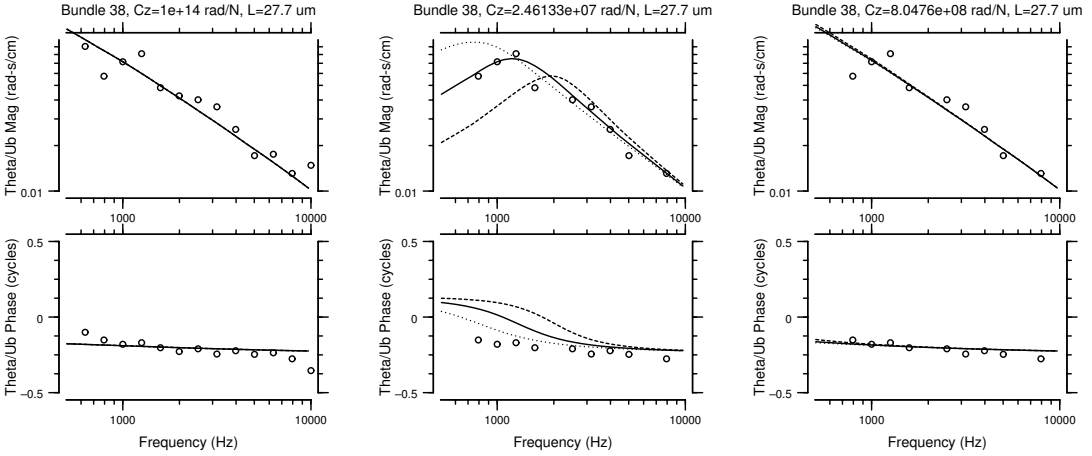

Figure B-17: Bundle 38

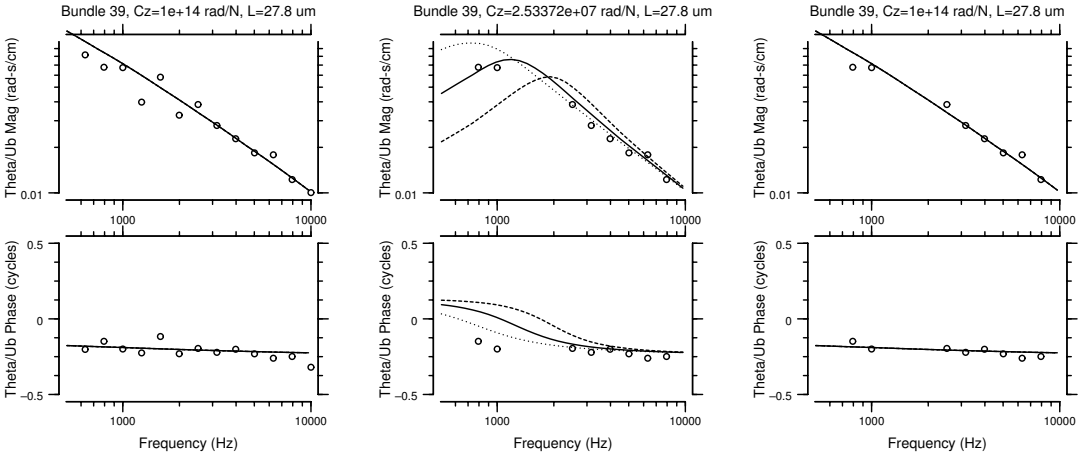

Figure B-18: Bundle 39

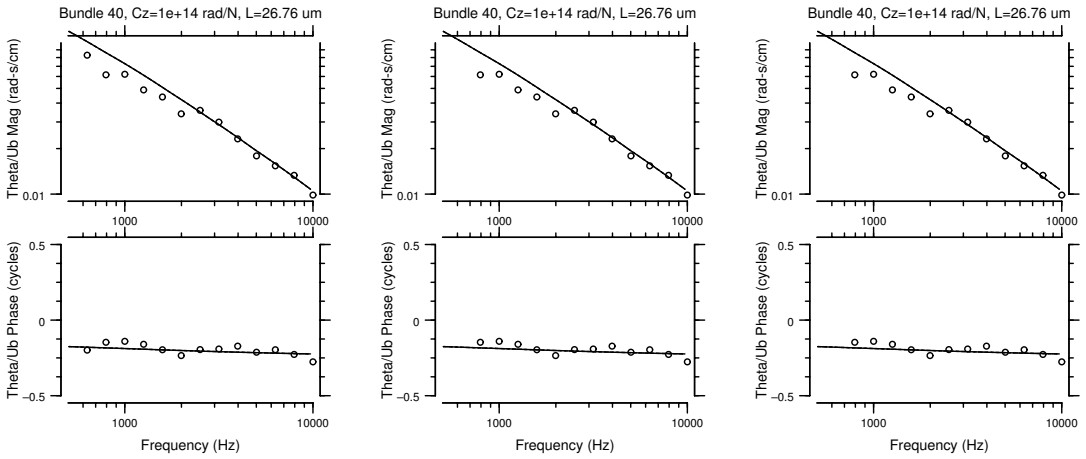

Figure B-19: Bundle 40

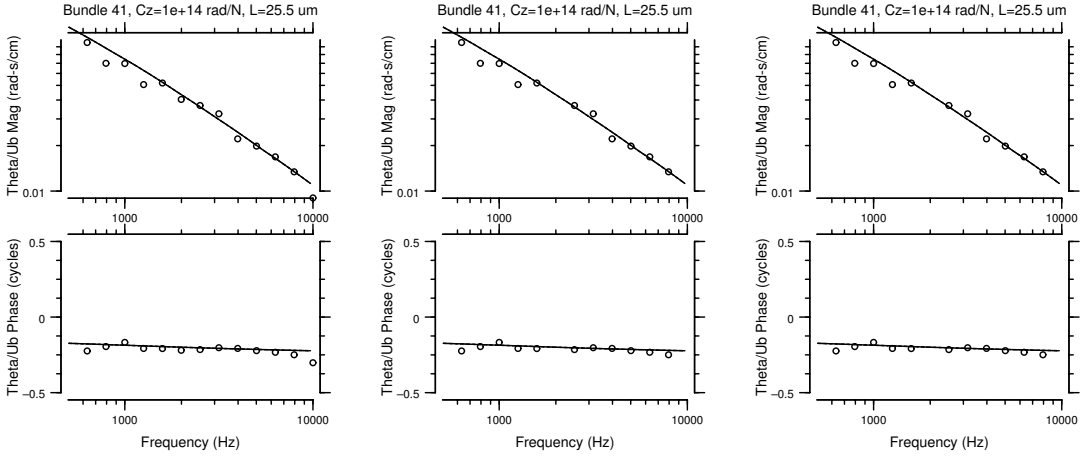

Figure B-20: Bundle 41

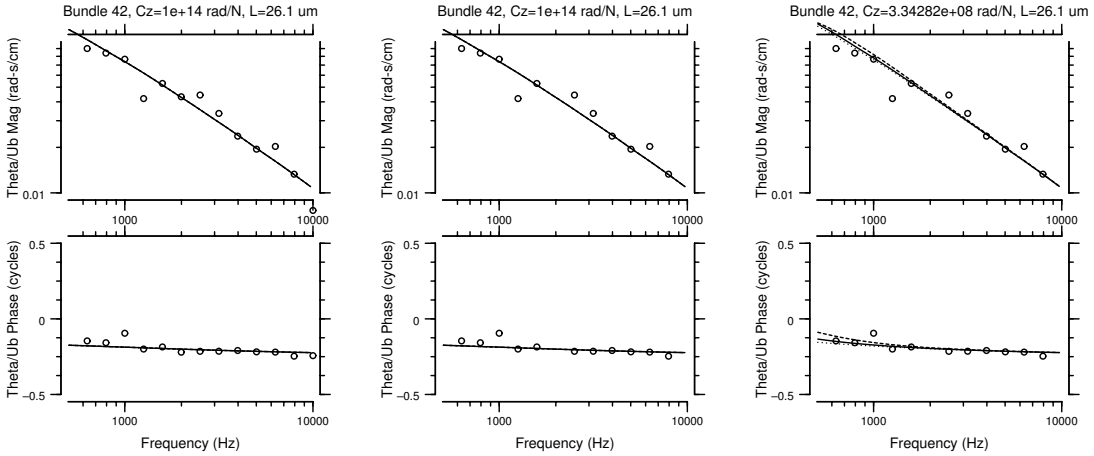

Figure B-21: Bundle 42

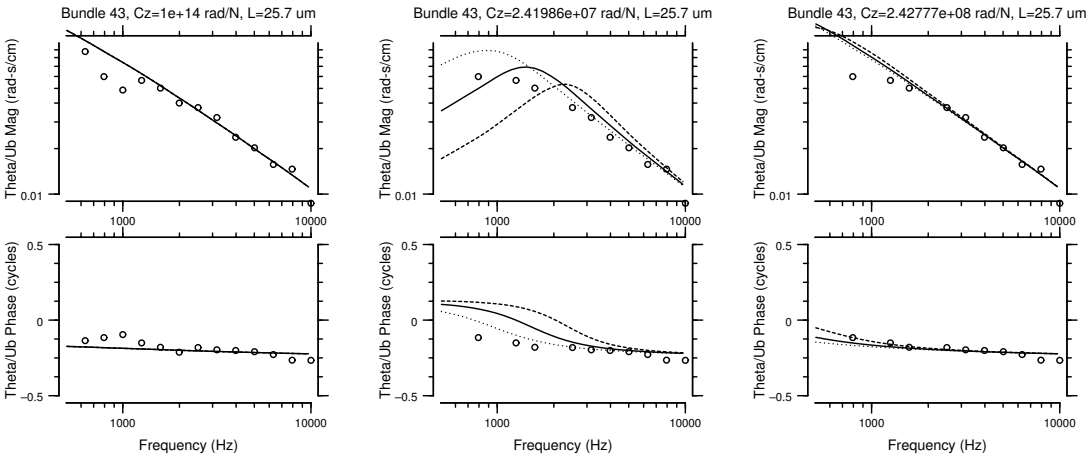

Figure B-22: Bundle 43

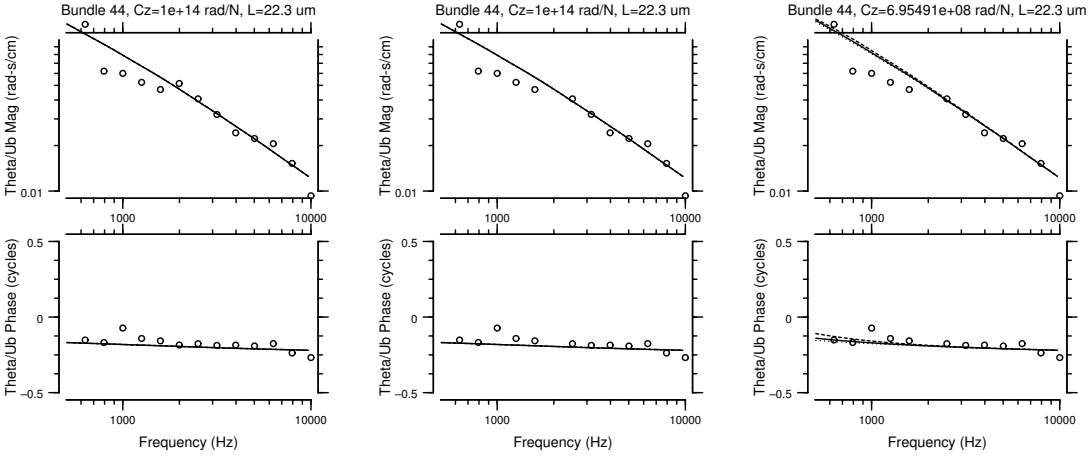

Figure B-23: Bundle 44

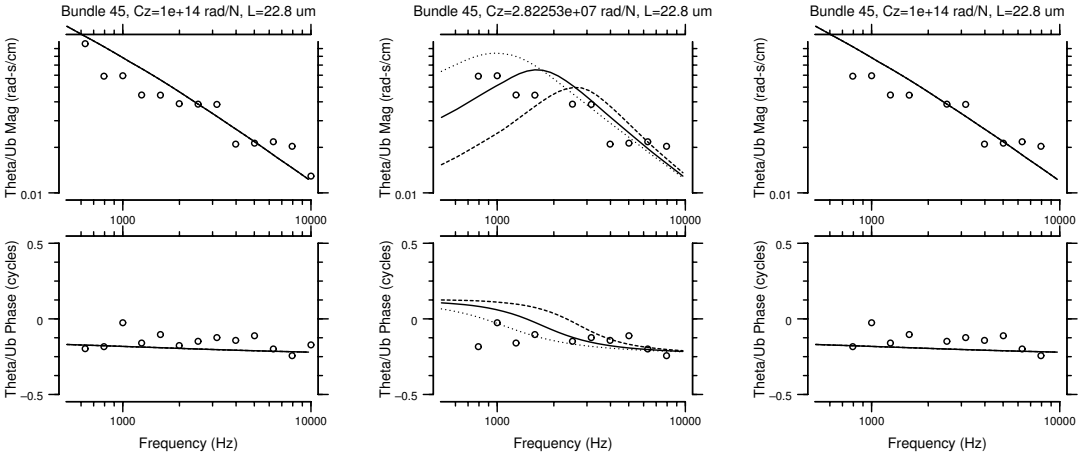

Figure B-24: Bundle 45

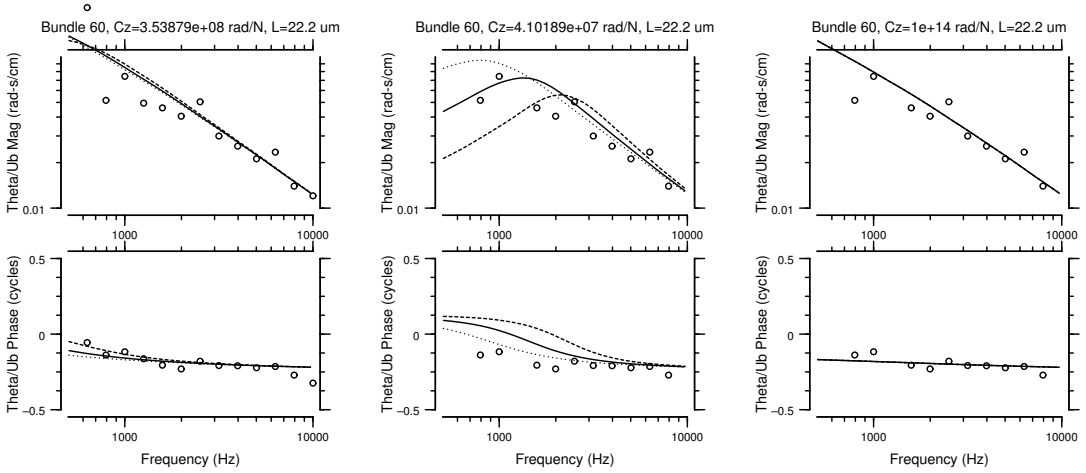

Figure B-25: Bundle 60

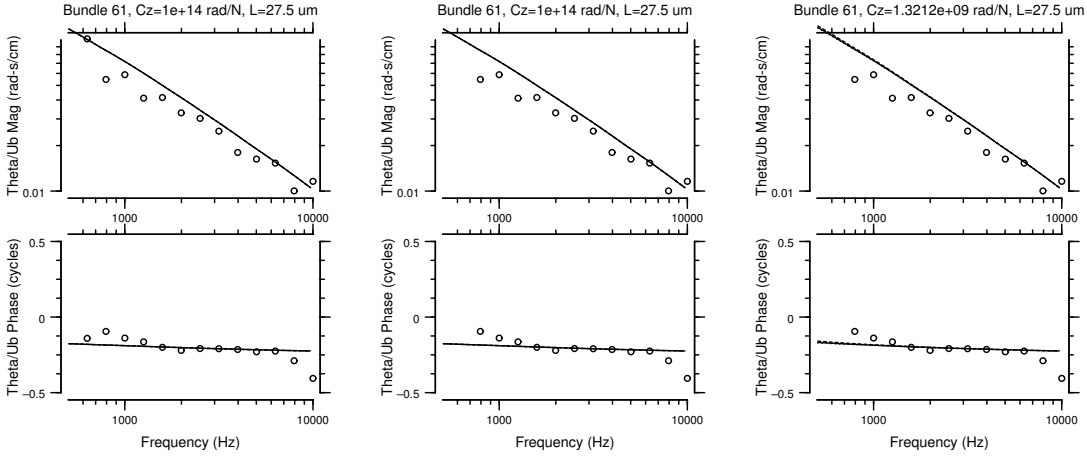

Figure B-26: Bundle 61

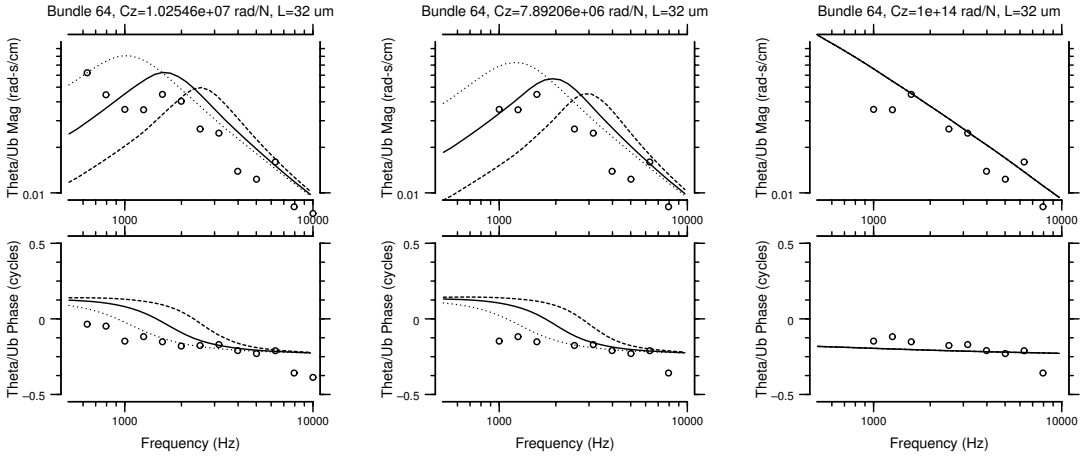

Figure B-27: Bundle 64

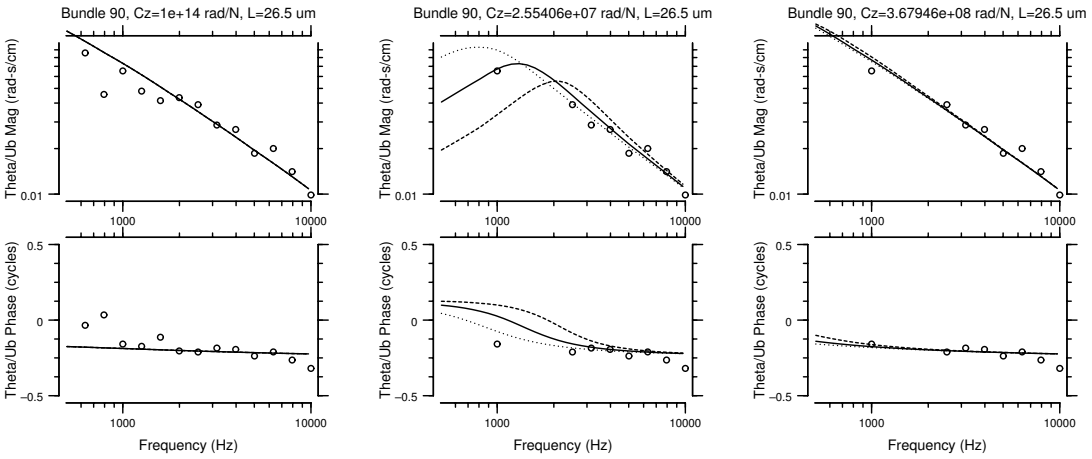

Figure B-28: Bundle 90

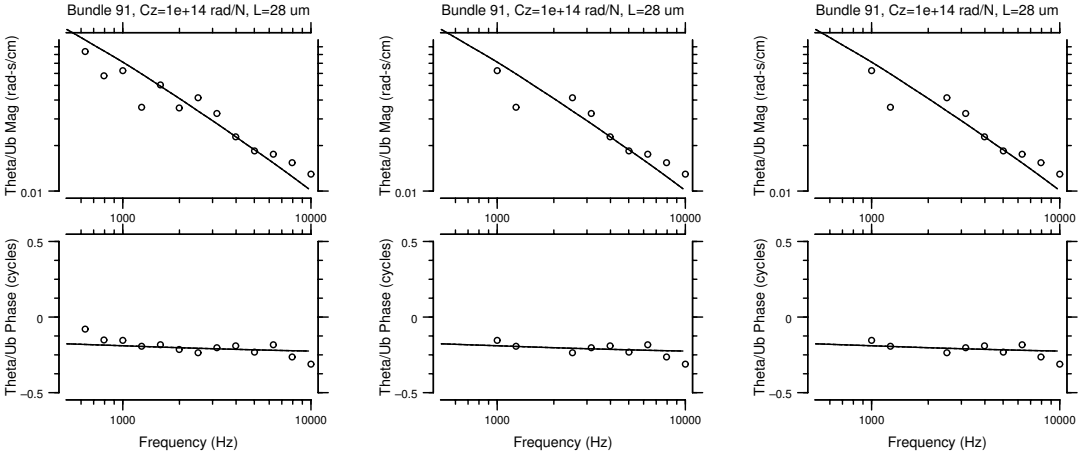

Figure B-29: Bundle 91

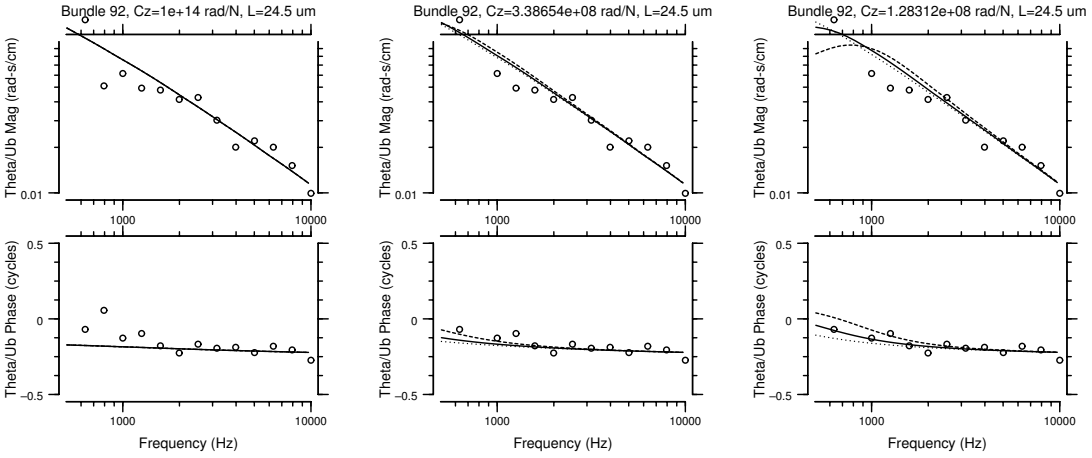

Figure B-30: Bundle 92

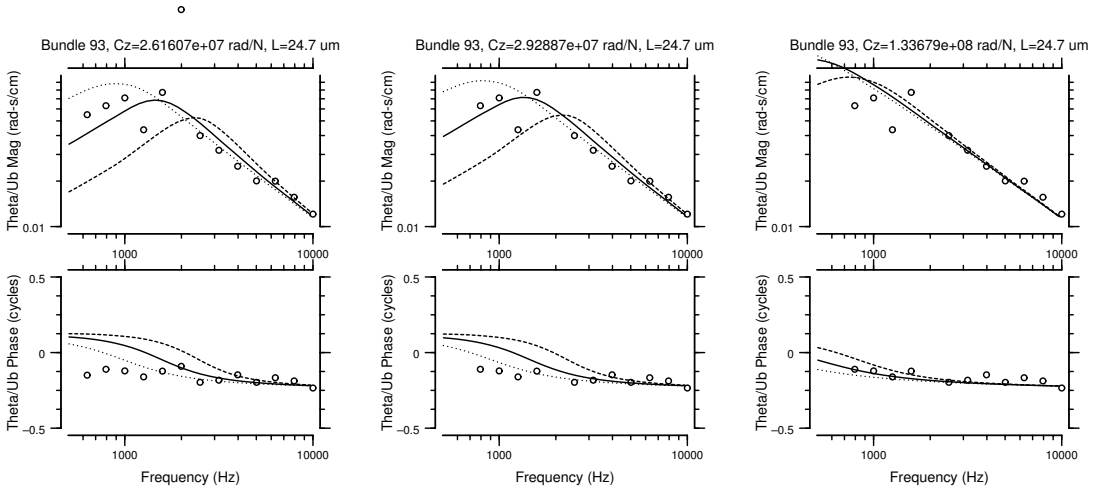

Figure B-31: Bundle 93

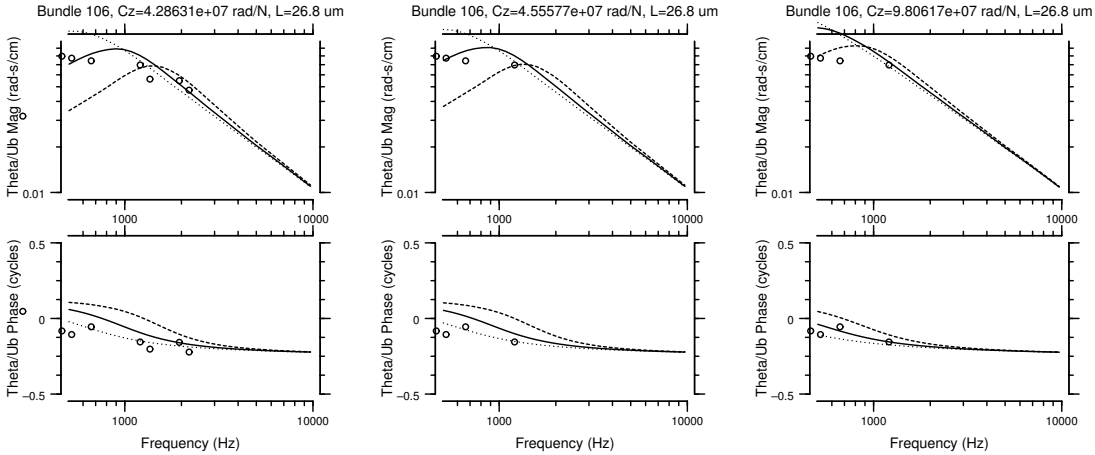

Figure B-32: Bundle 106

Appendix C

$\frac{\theta}{U_b}(f)$ of hair bundles that were well fit by the Freeman/Weiss model with a peak frequency between 500 Hz and 10 kHz

The 80 hair bundles in this appendix had $\frac{\theta}{U_b}(f)$ values that were well-fit by the Freeman/Weiss model. The peak frequency of the fit to the real and imaginary components of the filtered data set (right-hand plots) fell between 500 Hz and 10 kHz. The three plots for each hair bundle show different subsets of the data and different fits of the model. In each plot, the solid line shows the best fit, the dotted line shows the model prediction for twice the best-fit compliance, and the dashed line shows the model prediction for half the best-fit compliance. The left-hand plots show all the measured $\frac{\theta}{U_b}(f)$ values (circles), with the best fit of the magnitudes. The center plots show the subset of $\frac{\theta}{U_b}(f)$ values for which the magnitude of the fundamental component of motion was larger than 100 nm, and the magnitudes of higher harmonics were at least 20 dB smaller; the fits in these plots were made to the magnitudes only. The right-hand plots show the same data as the center plots, but with fits to both the real and imaginary components of $\frac{\theta}{U_b}(f)$.

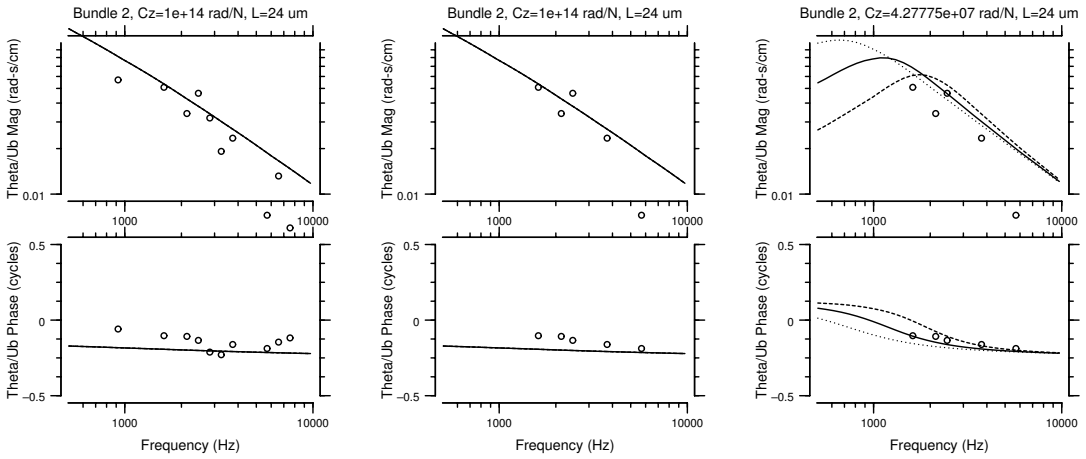

Figure C-1: Bundle 2

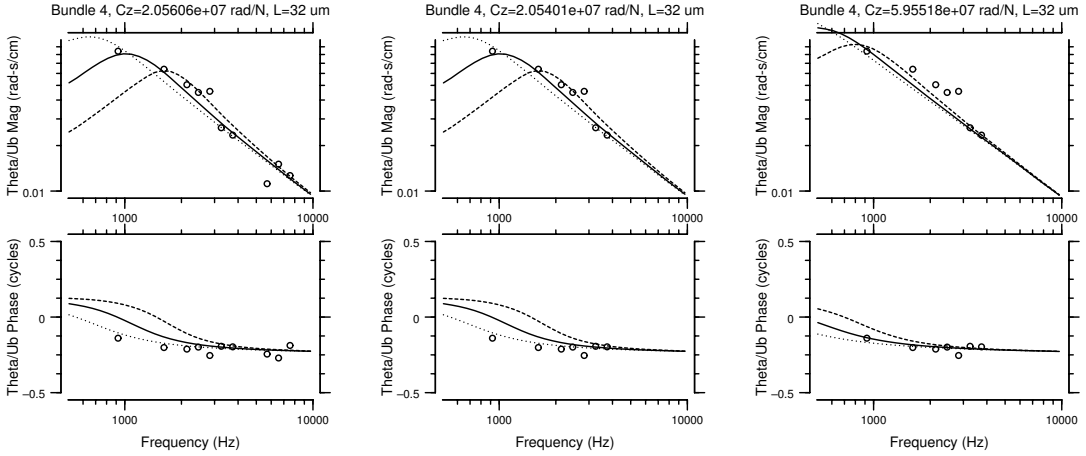

Figure C-2: Bundle 4

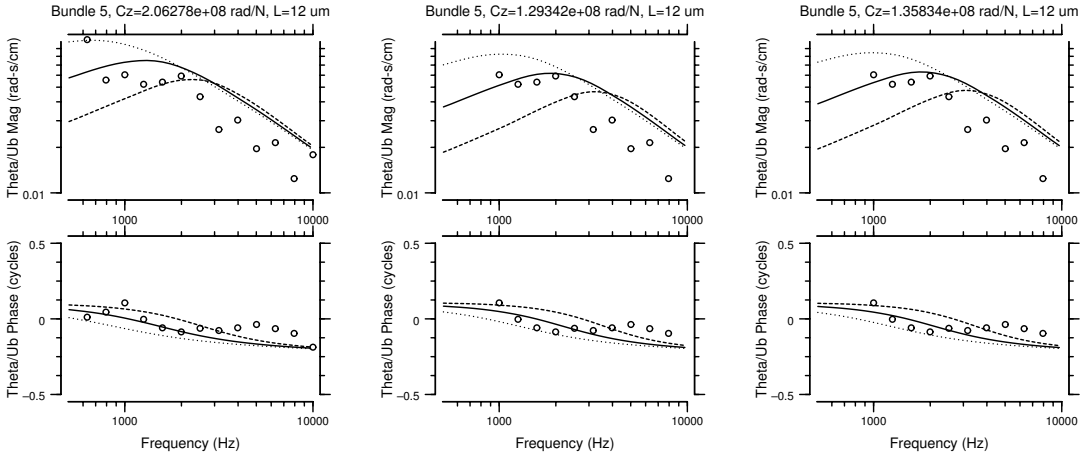

Figure C-3: Bundle 5

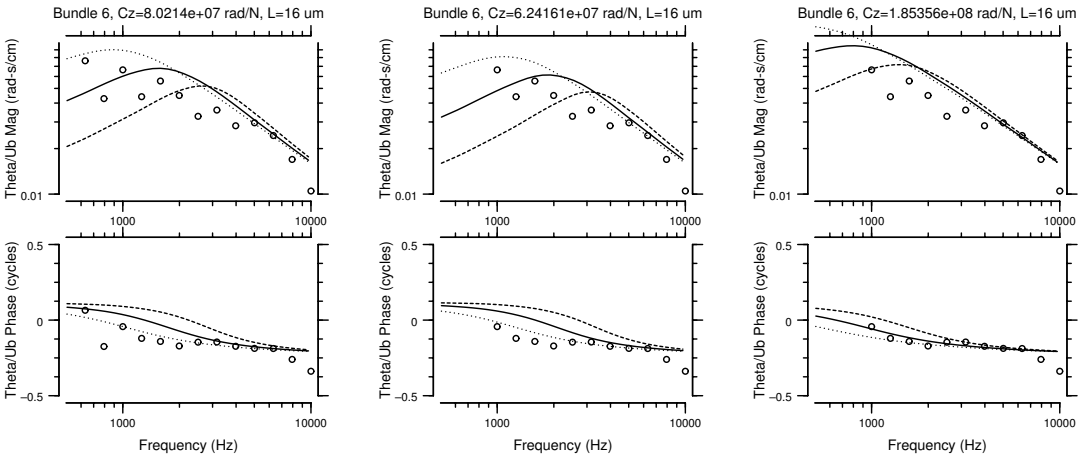

Figure C-4: Bundle 6

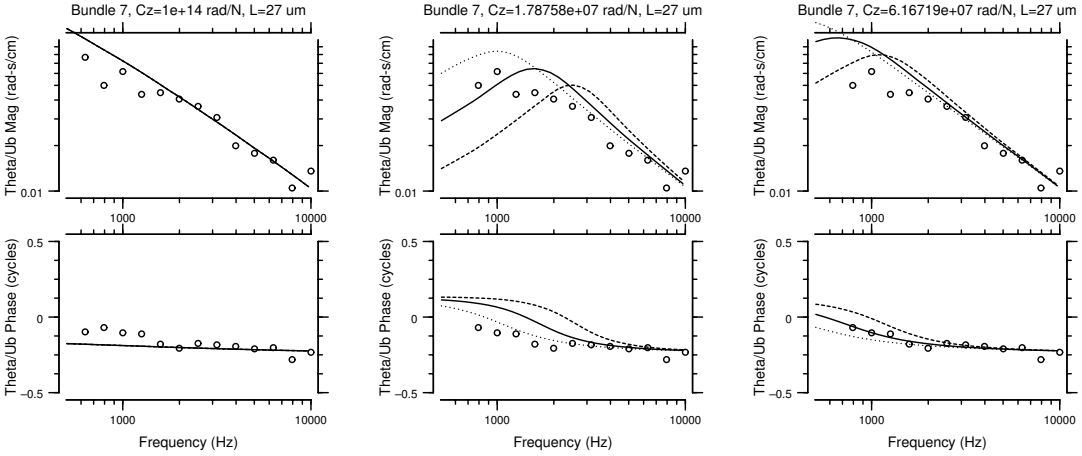

Figure C-5: Bundle 7

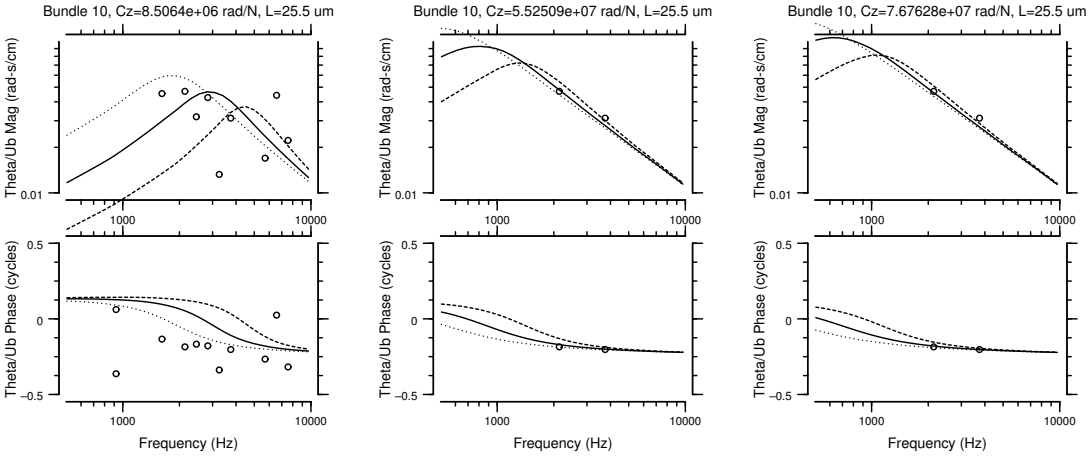

Figure C-6: Bundle 10

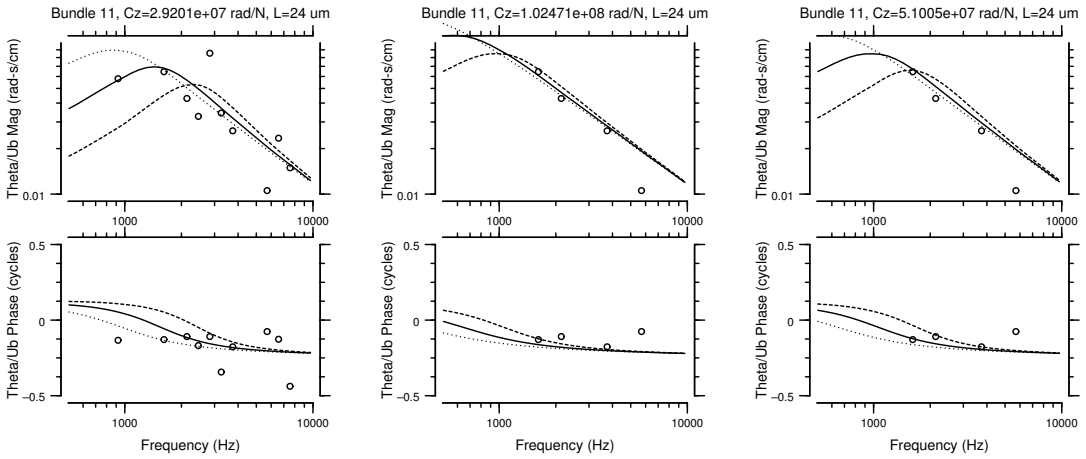

Figure C-7: Bundle 11

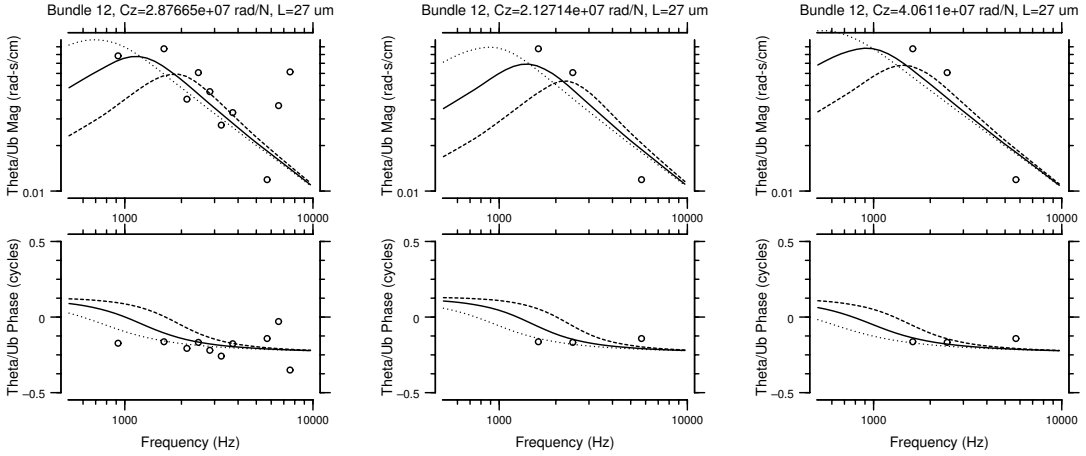

Figure C-8: Bundle 12

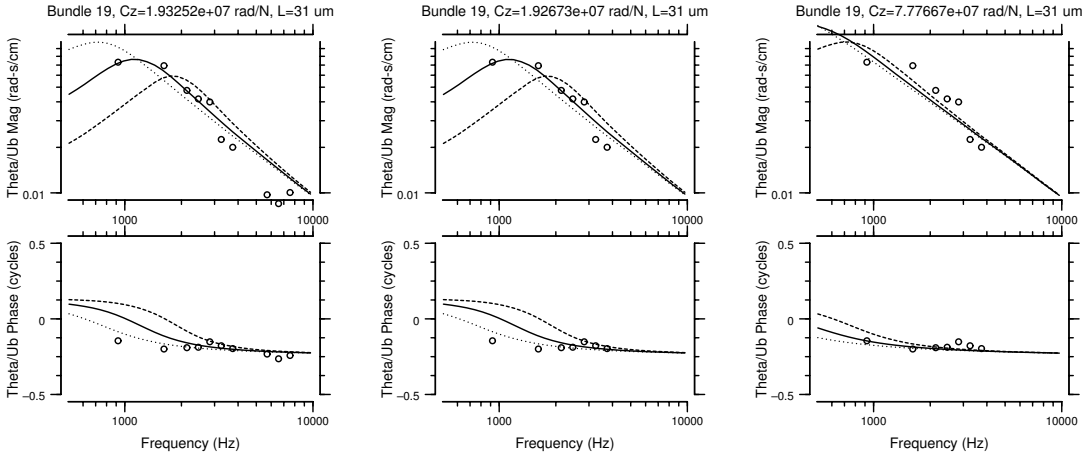

Figure C-9: Bundle 19

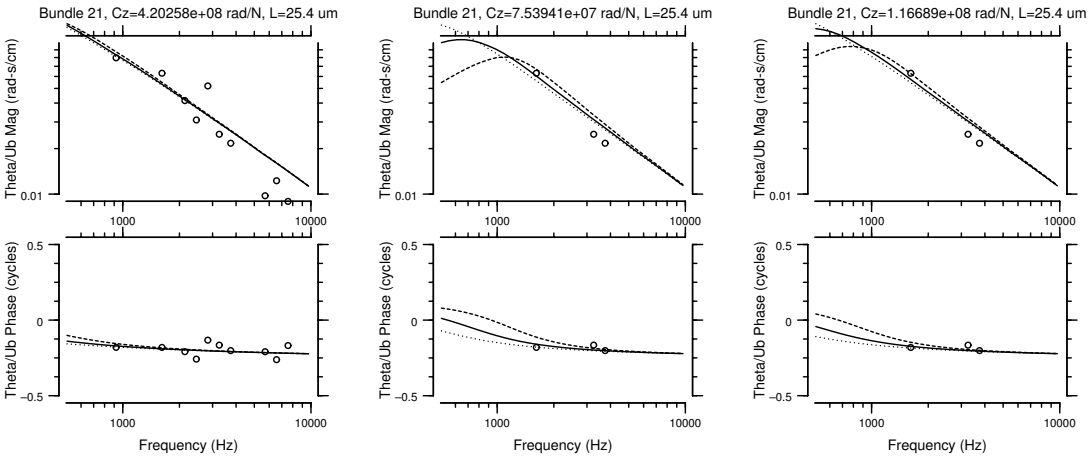

Figure C-10: Bundle 21

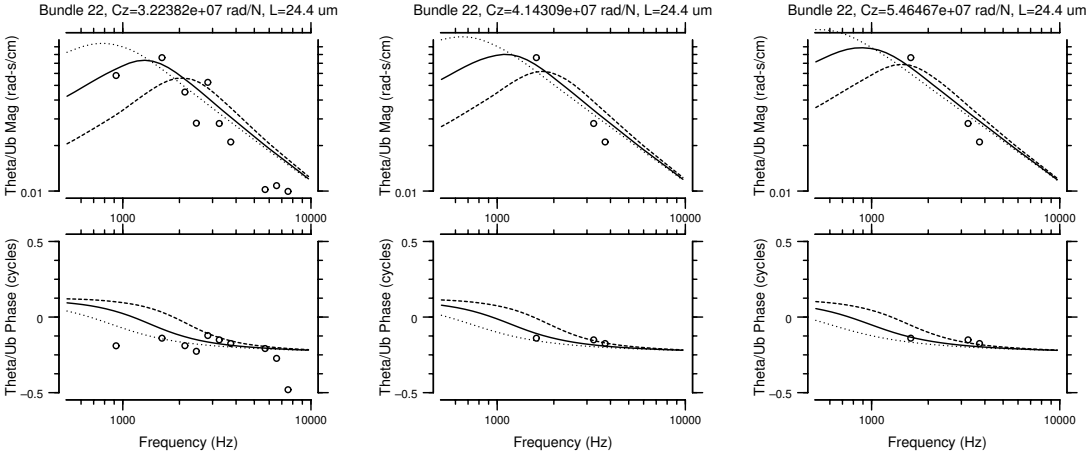

Figure C-11: Bundle 22

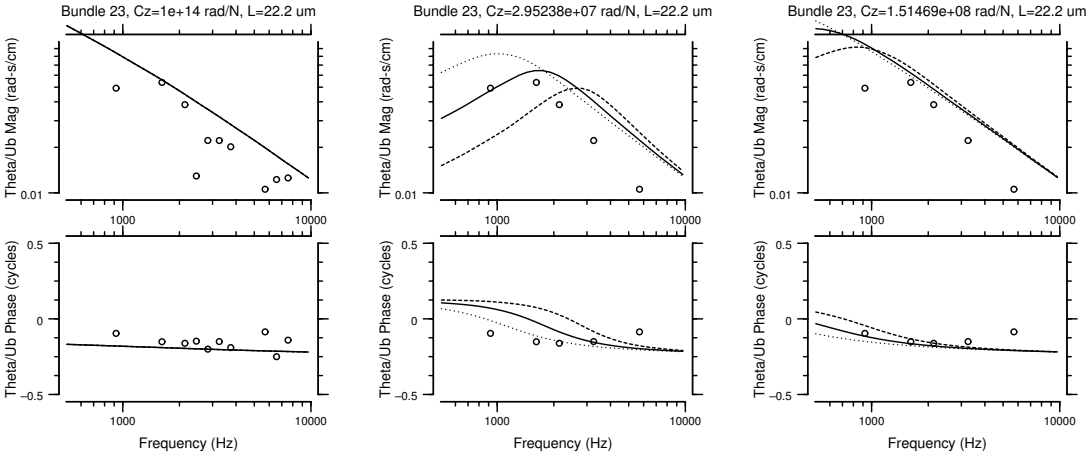

Figure C-12: Bundle 23

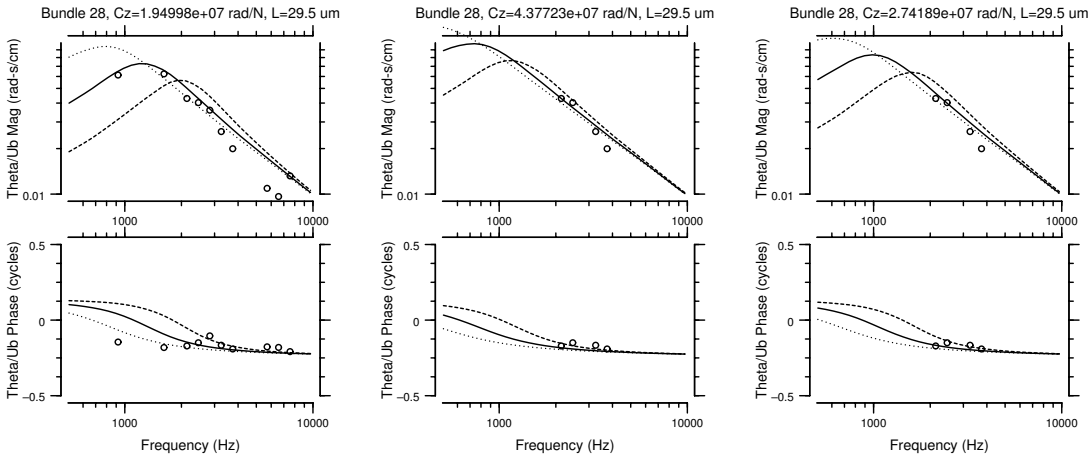

Figure C-13: Bundle 28

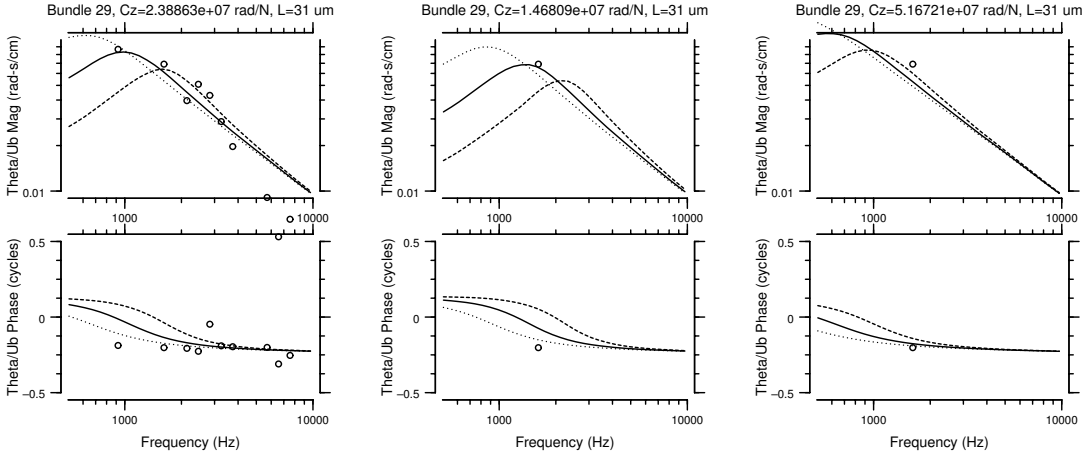

Figure C-14: Bundle 29

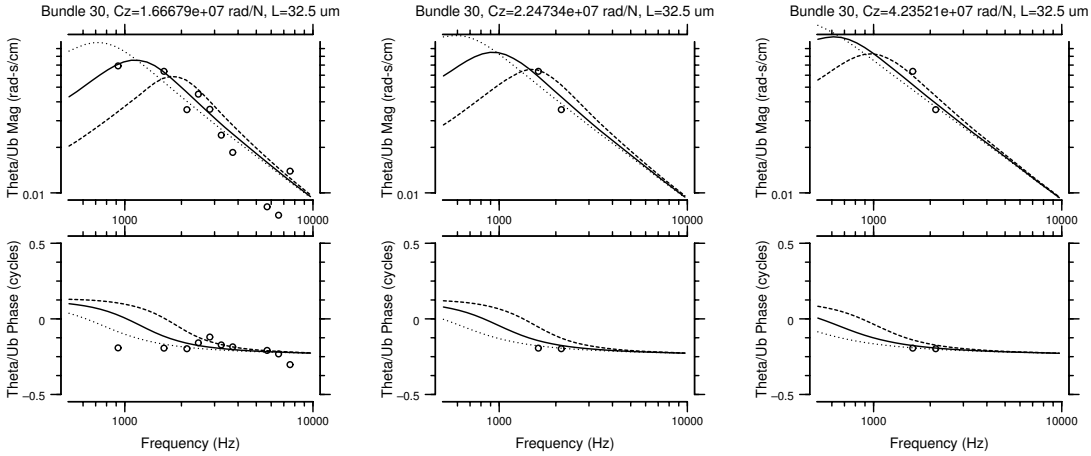

Figure C-15: Bundle 30

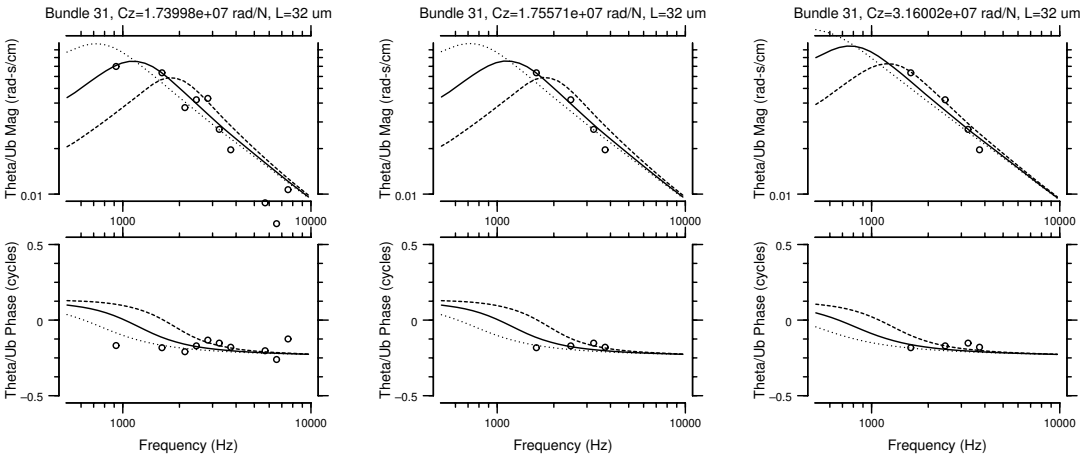

Figure C-16: Bundle 31

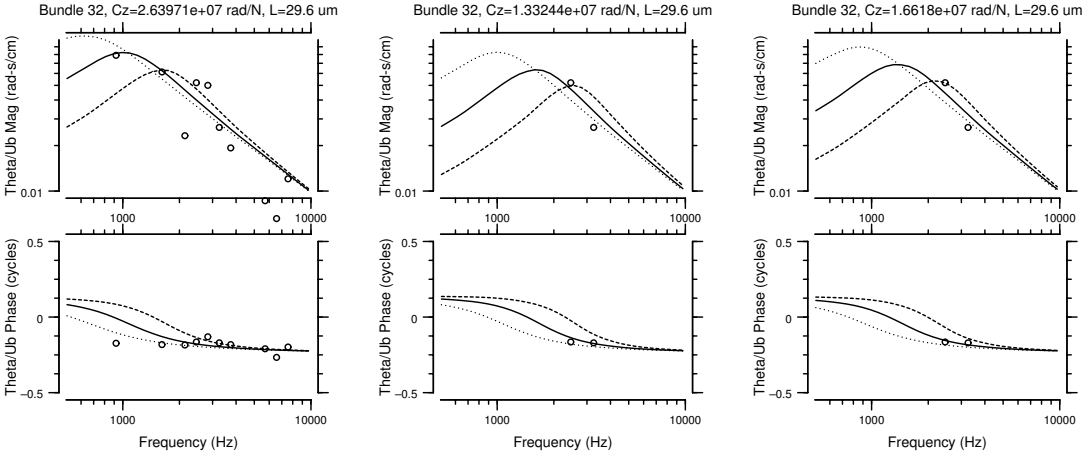

Figure C-17: Bundle 32

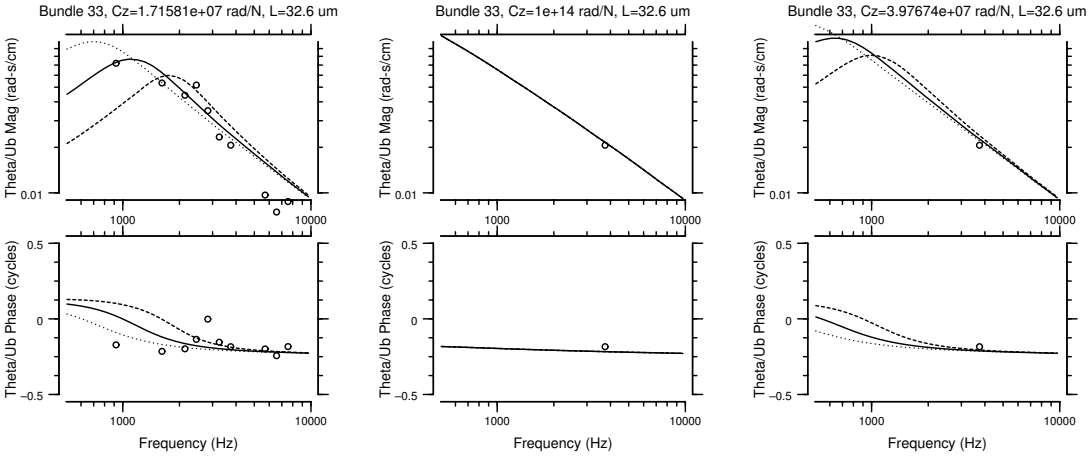

Figure C-18: Bundle 33

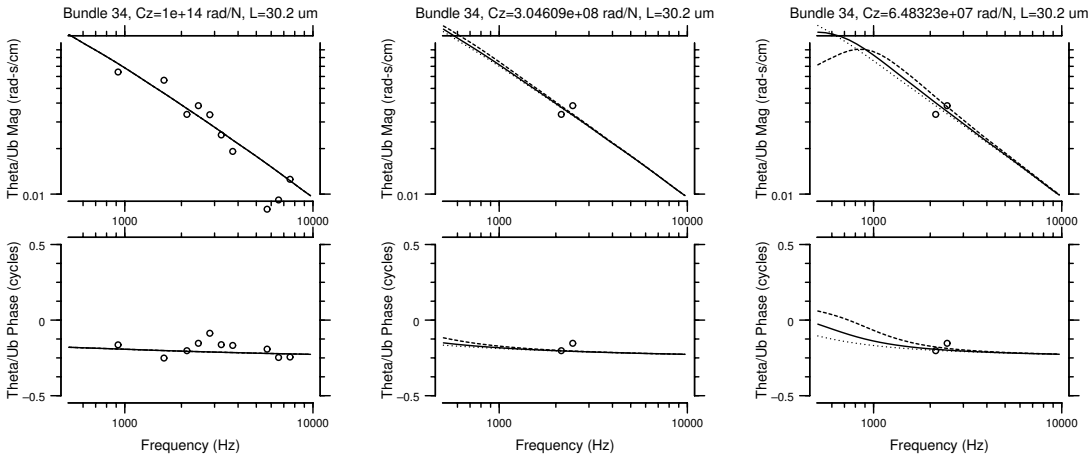

Figure C-19: Bundle 34

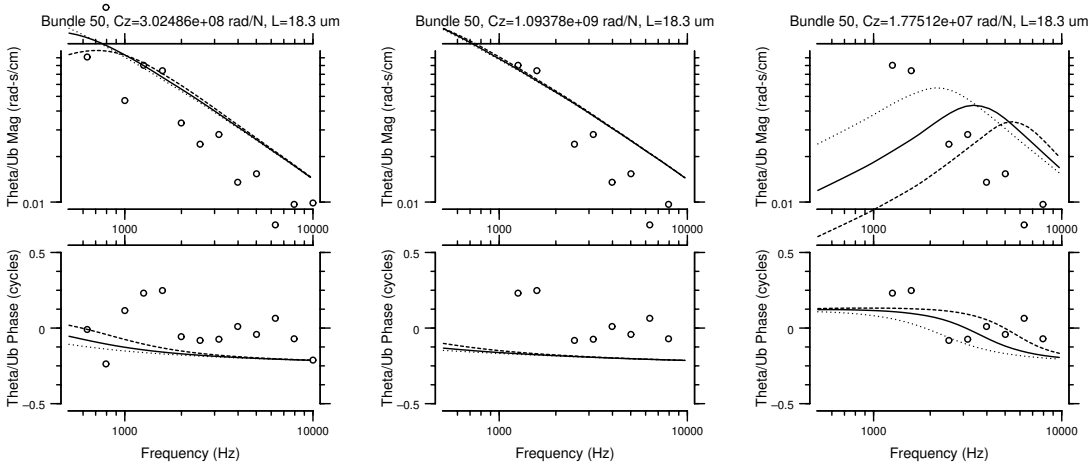

Figure C-20: Bundle 50

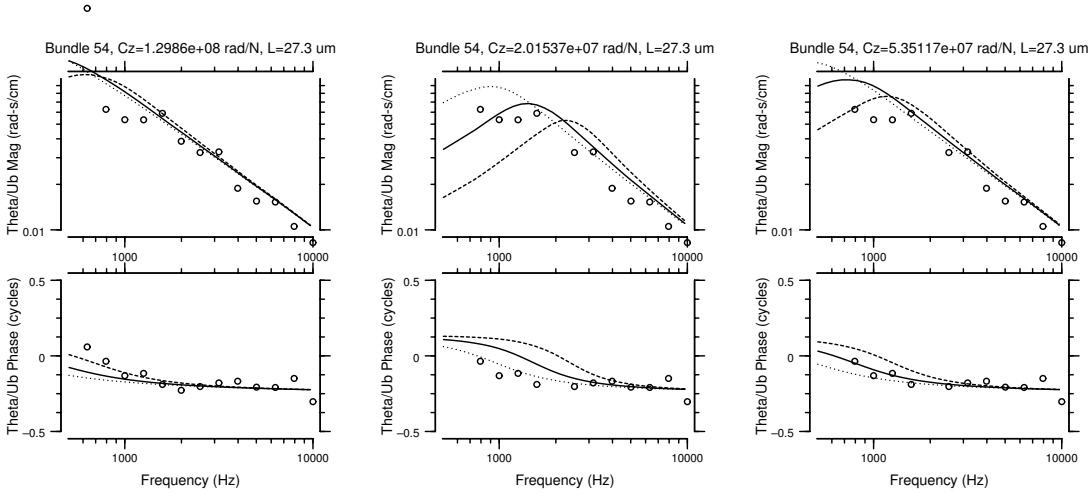

Figure C-21: Bundle 54

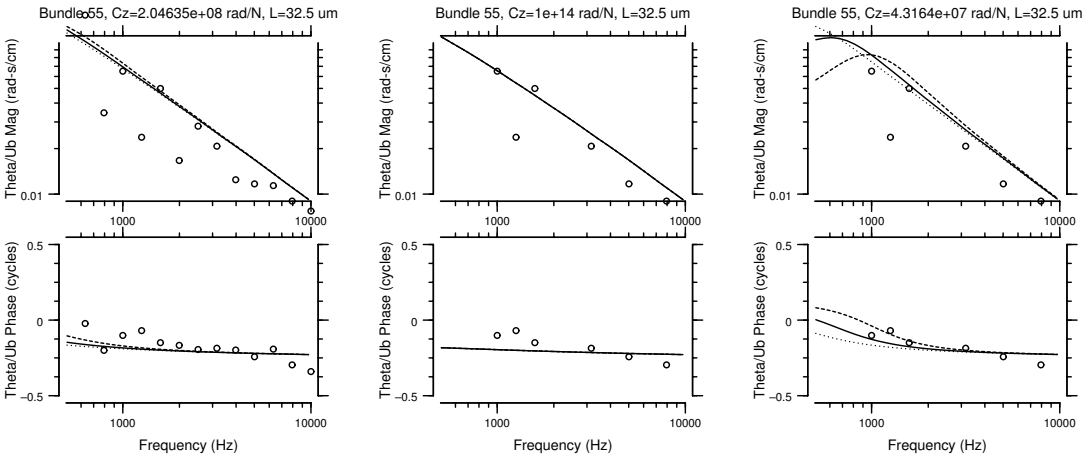

Figure C-22: Bundle 55

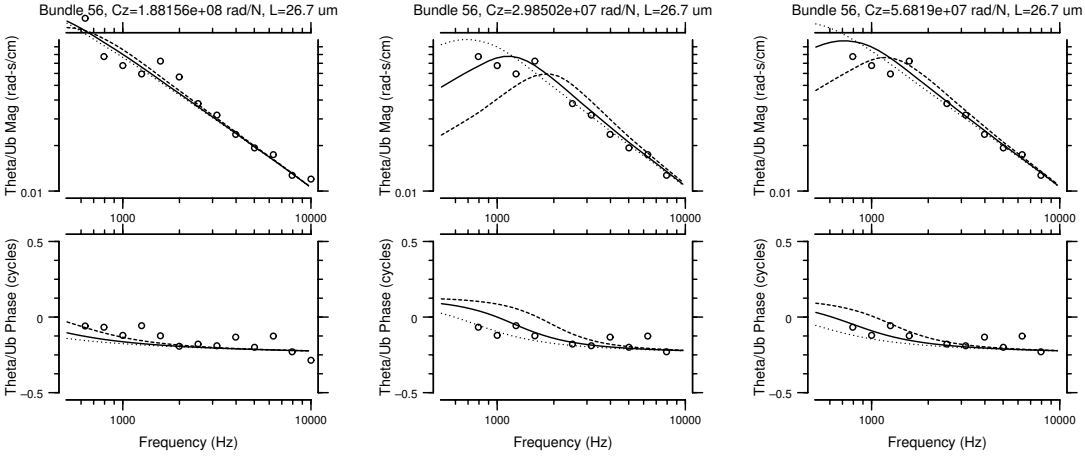

Figure C-23: Bundle 56

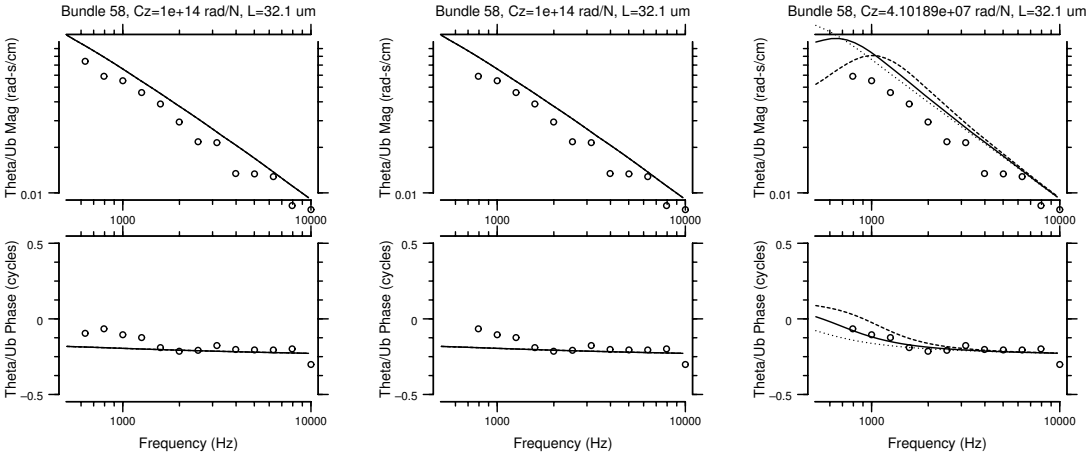

Figure C-24: Bundle 58

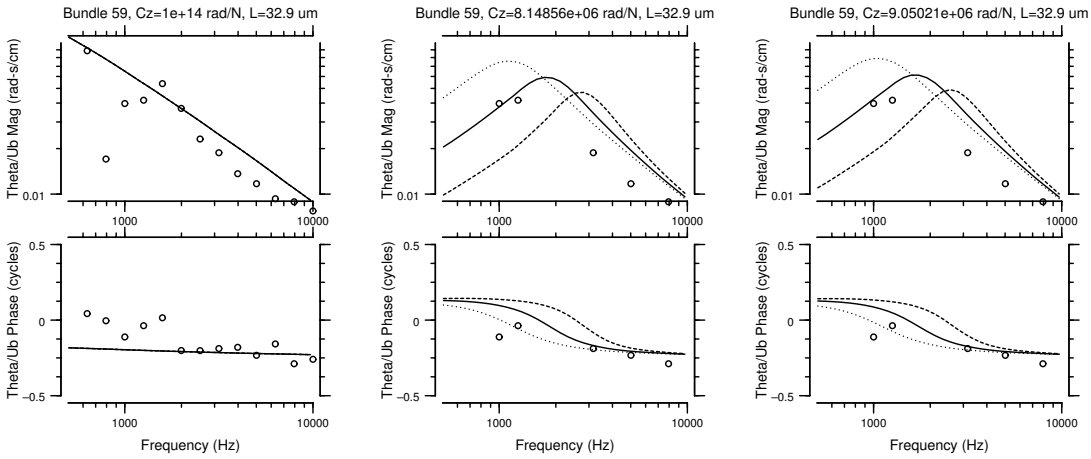

Figure C-25: Bundle 59

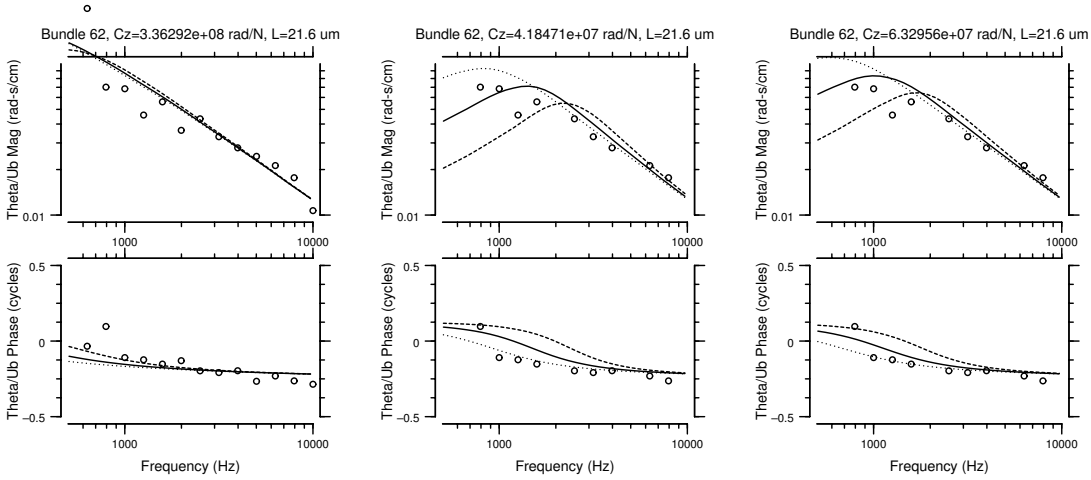

Figure C-26: Bundle 62

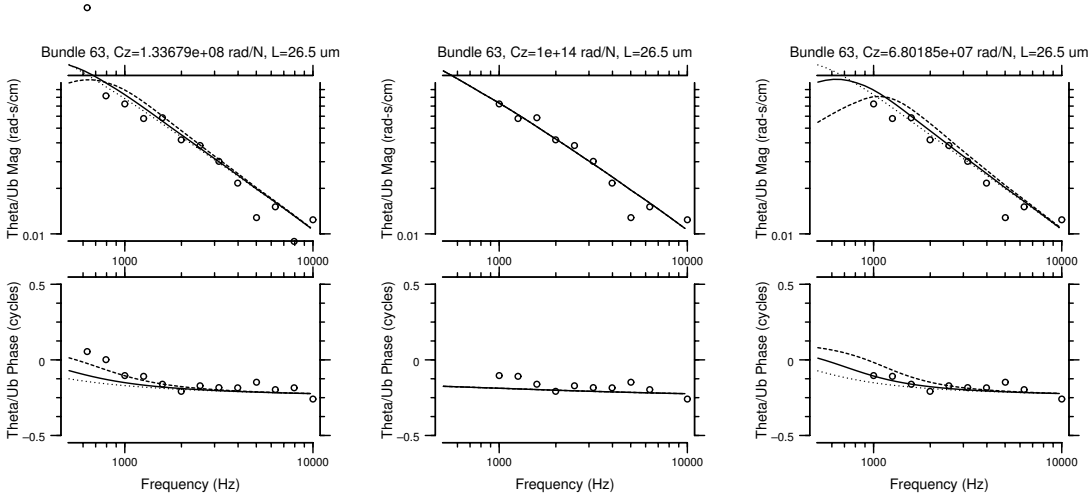

Figure C-27: Bundle 63

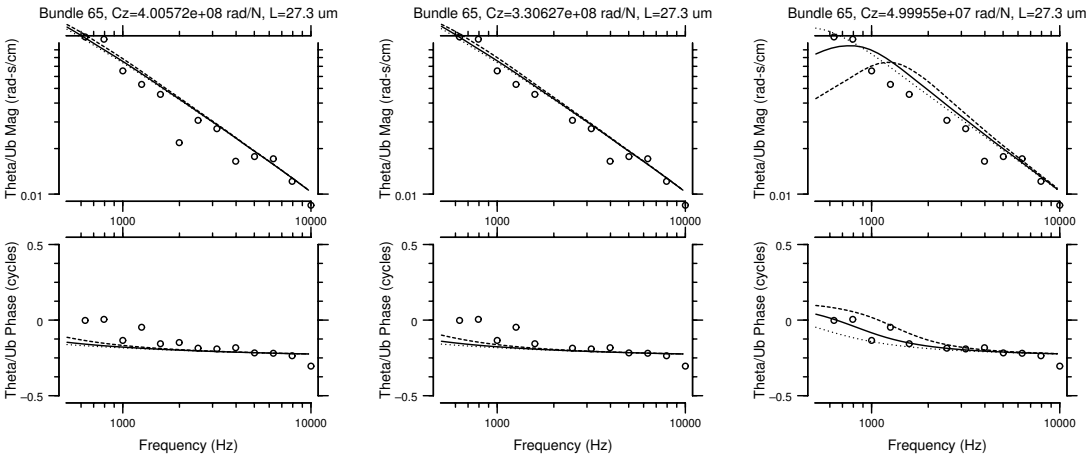

Figure C-28: Bundle 65

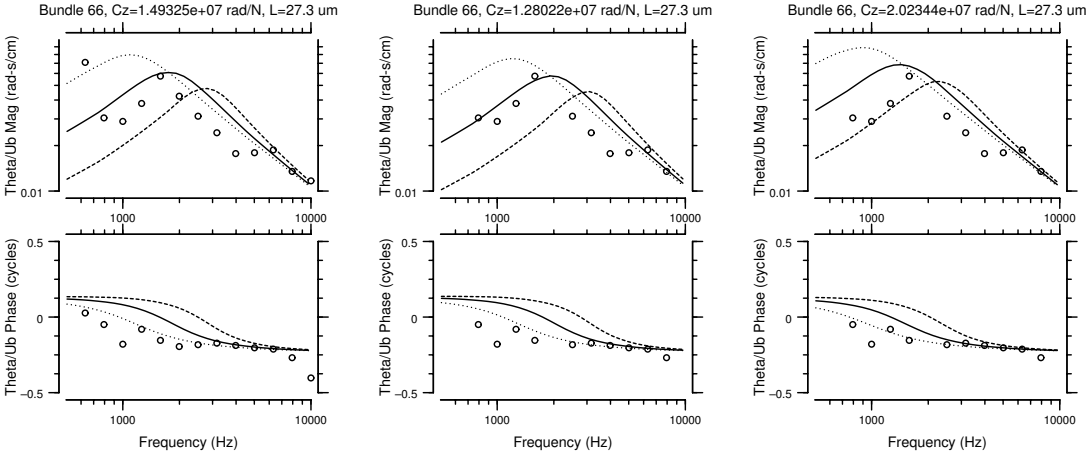

Figure C-29: Bundle 66

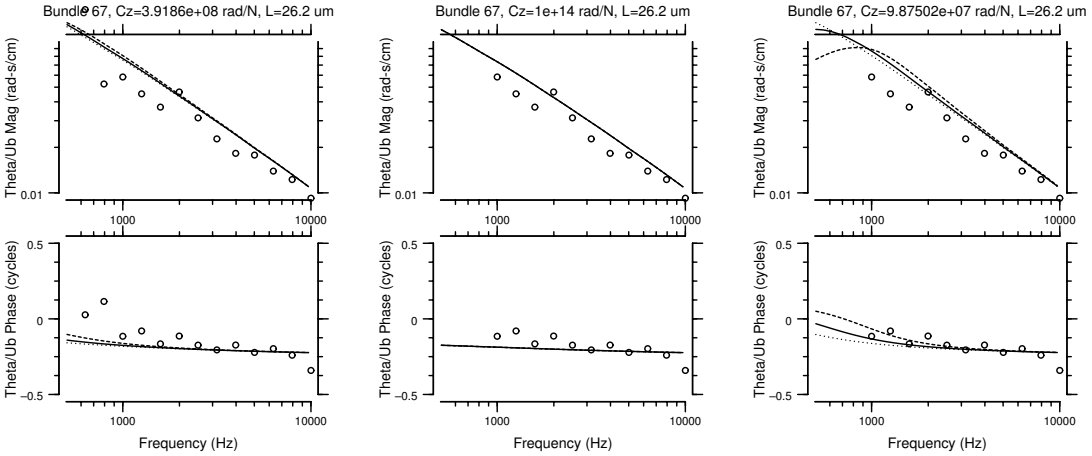

Figure C-30: Bundle 67

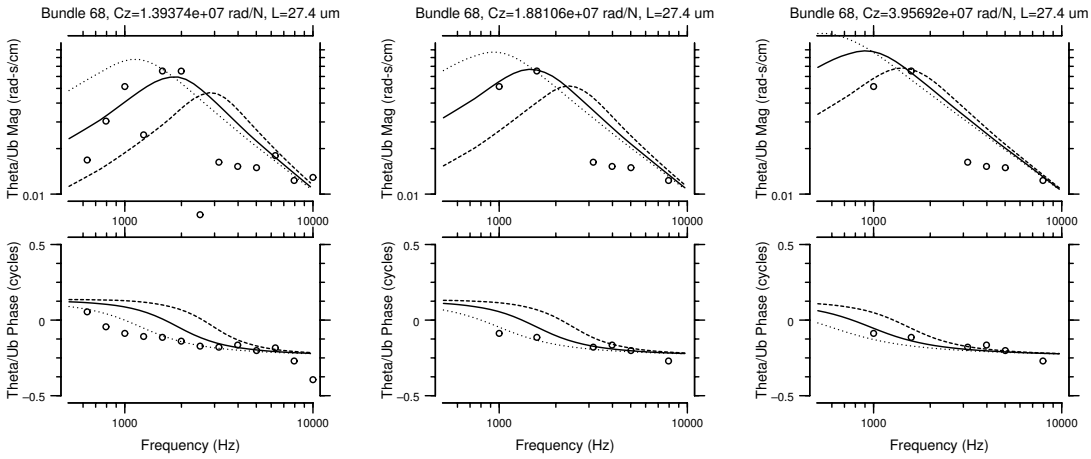

Figure C-31: Bundle 68

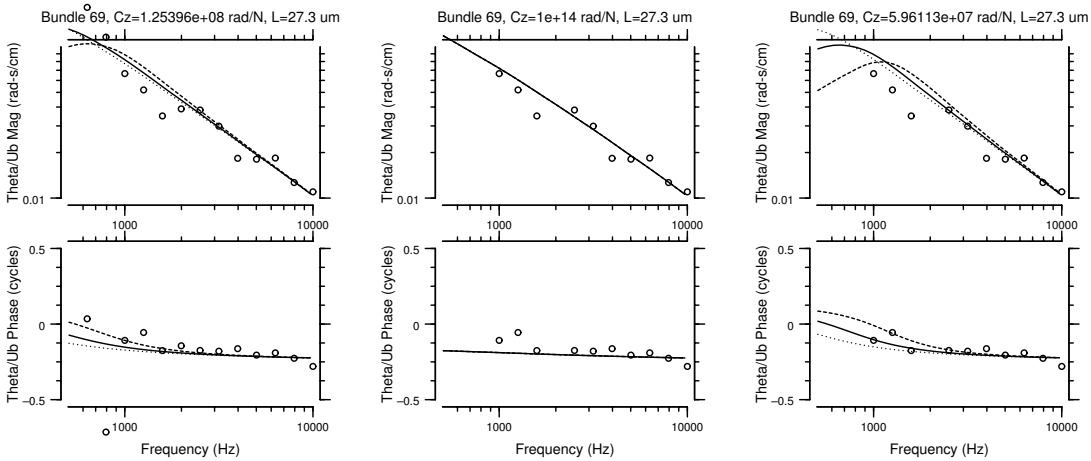

Figure C-32: Bundle 69

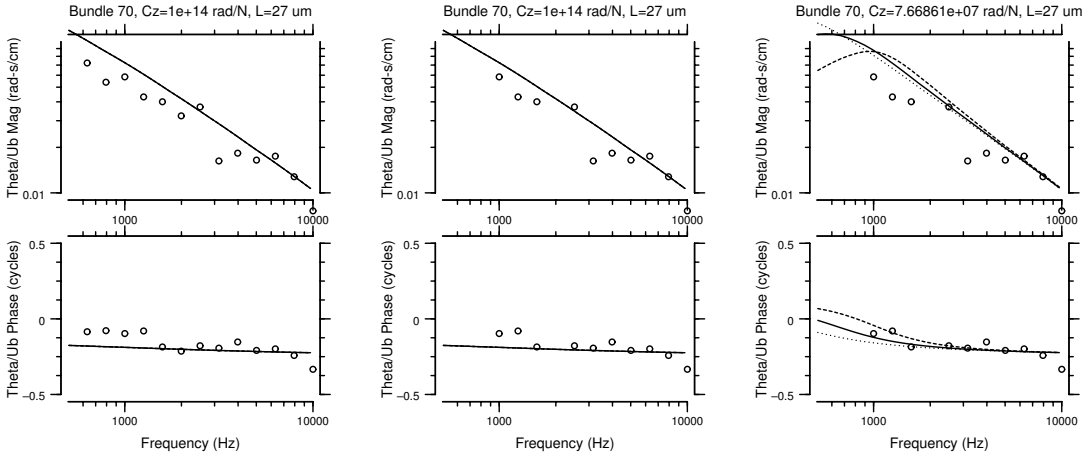

Figure C-33: Bundle 70

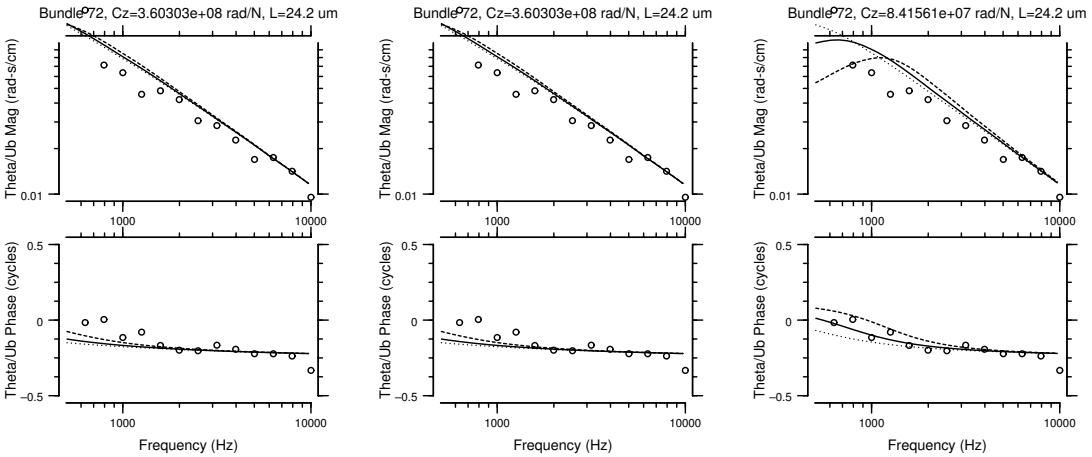

Figure C-34: Bundle 72

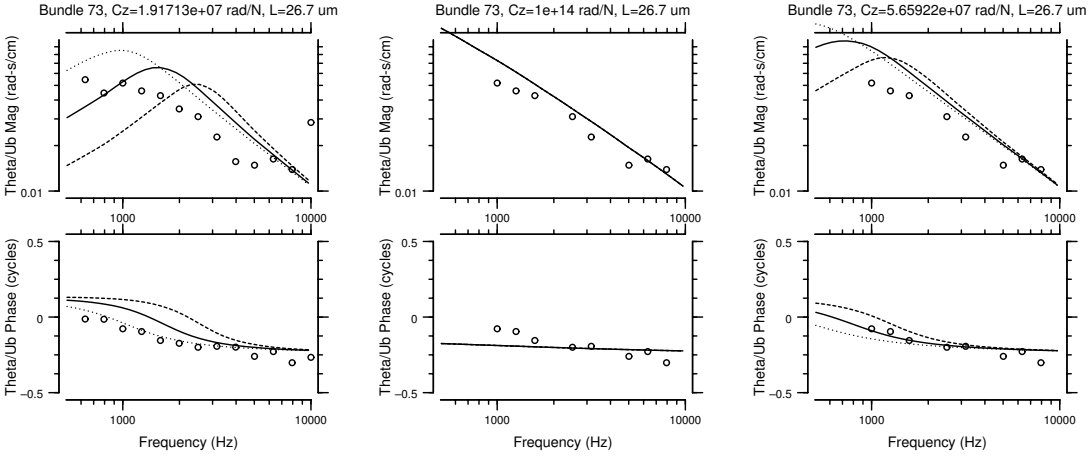

Figure C-35: Bundle 73

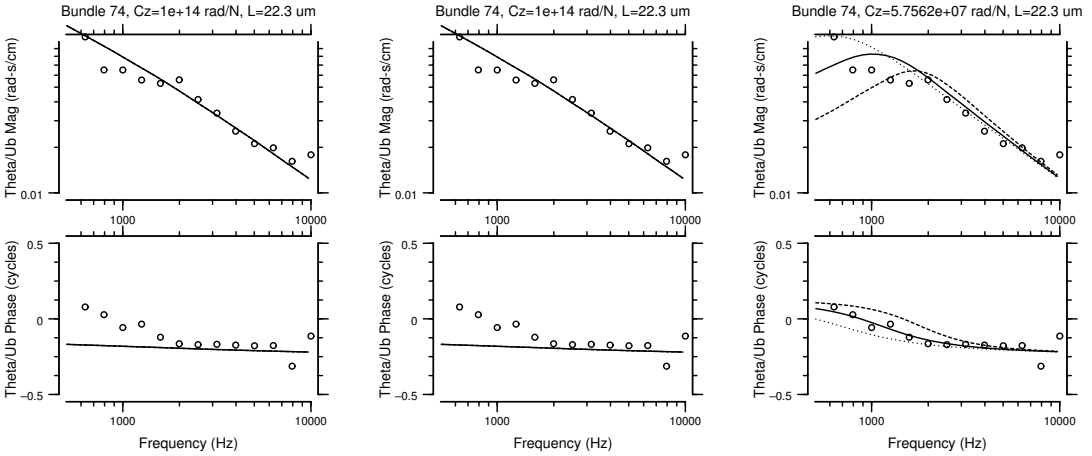

Figure C-36: Bundle 74

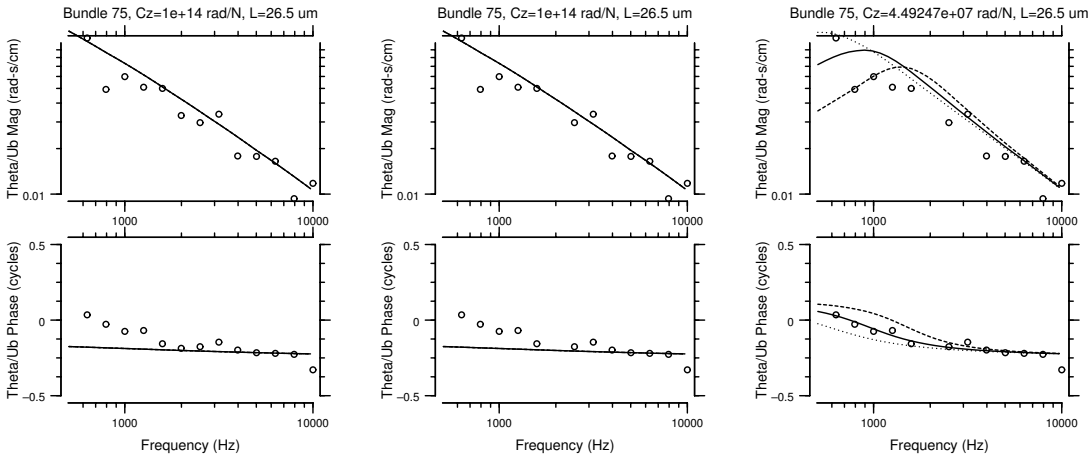

Figure C-37: Bundle 75

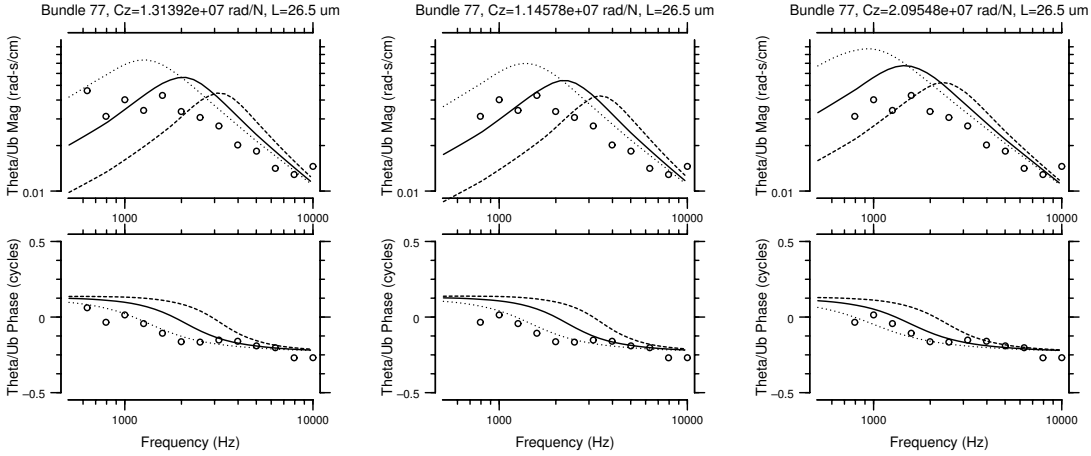

Figure C-38: Bundle 77

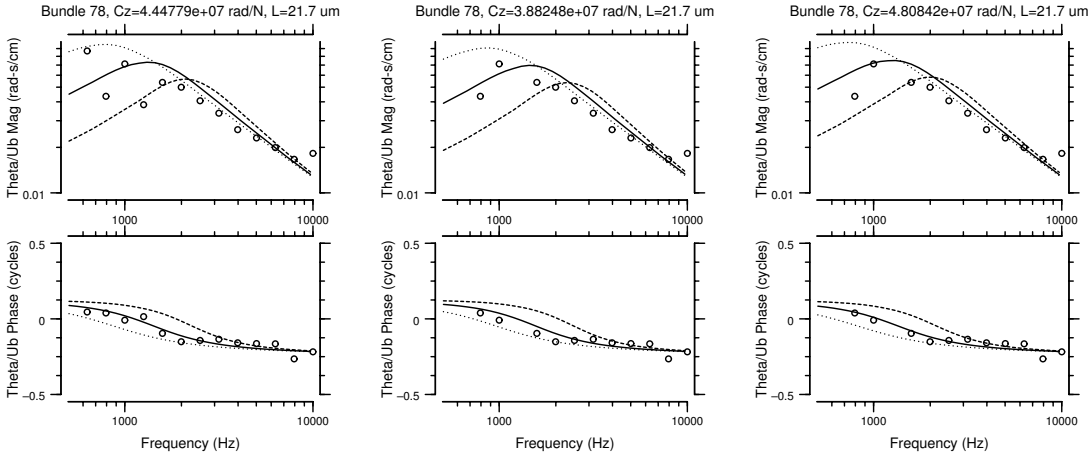

Figure C-39: Bundle 78

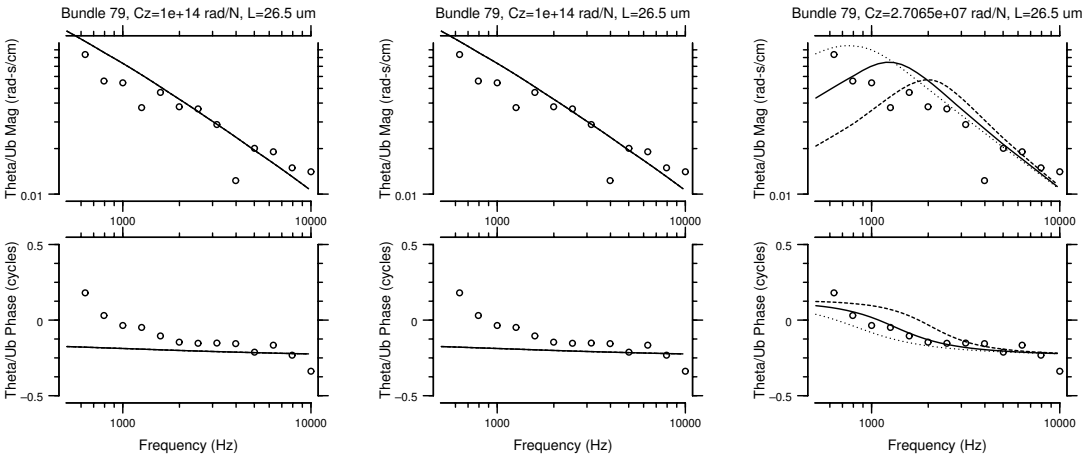

Figure C-40: Bundle 79

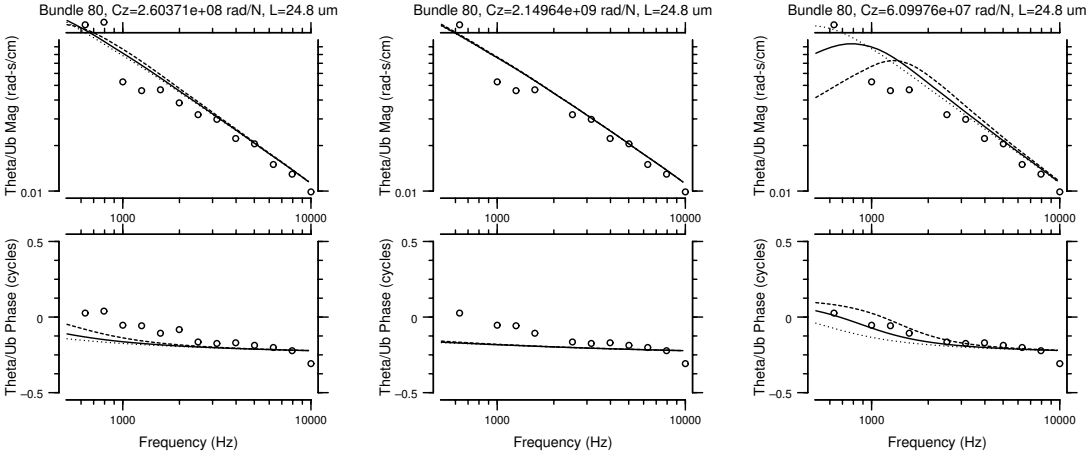

Figure C-41: Bundle 80

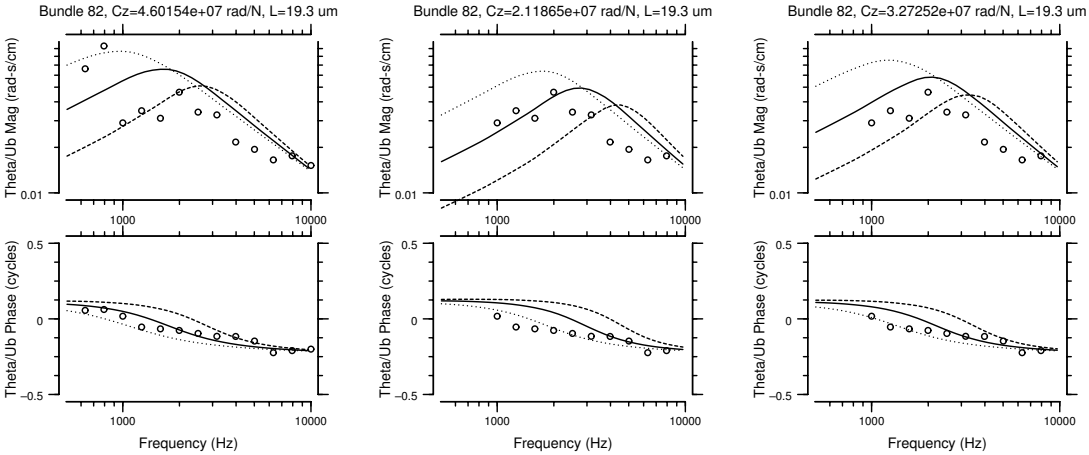

Figure C-42: Bundle 82

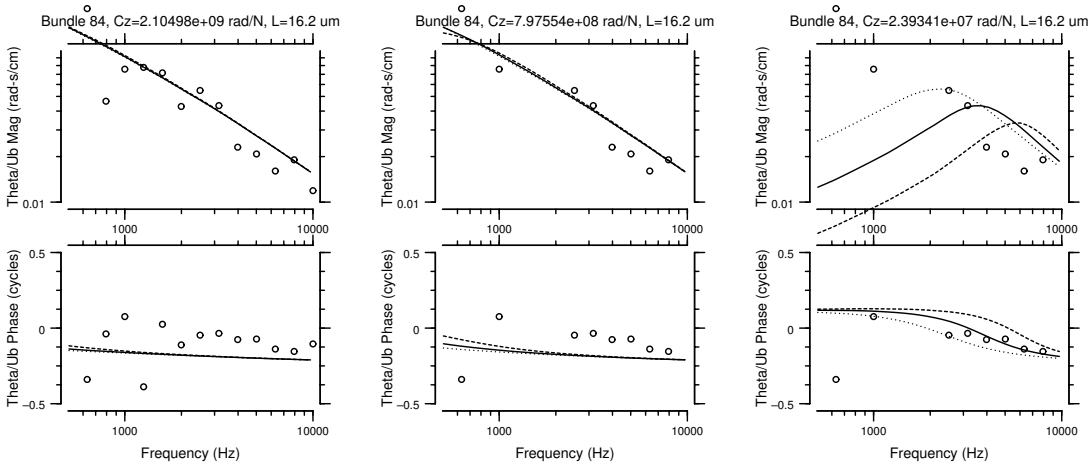

Figure C-43: Bundle 84

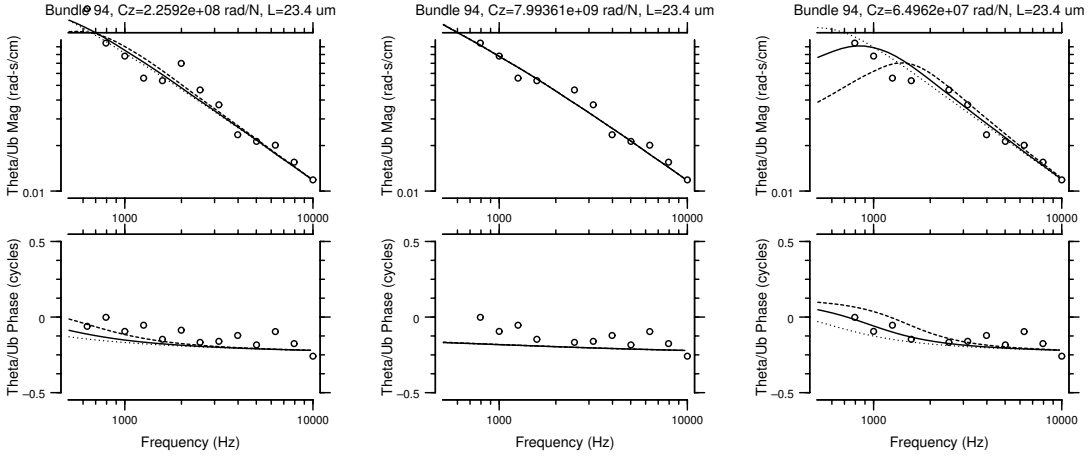

Figure C-44: Bundle 94

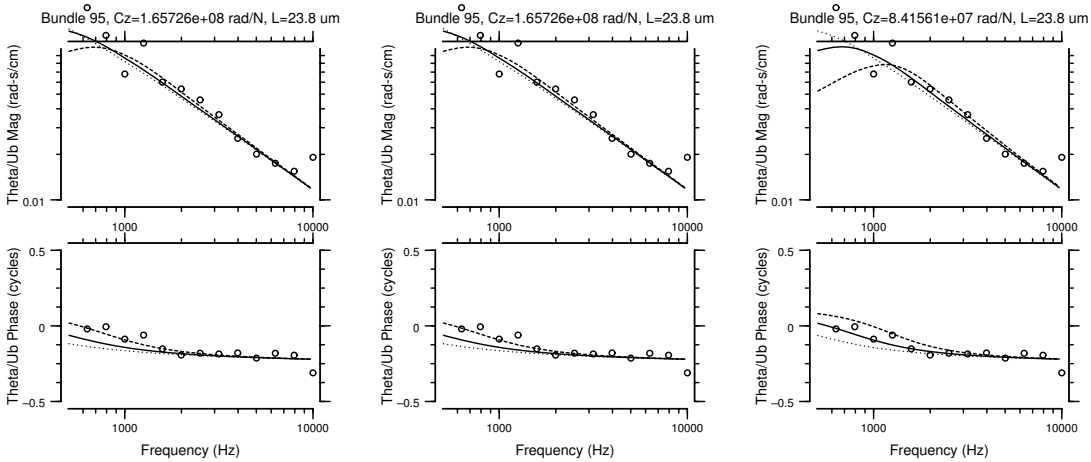

Figure C-45: Bundle 95

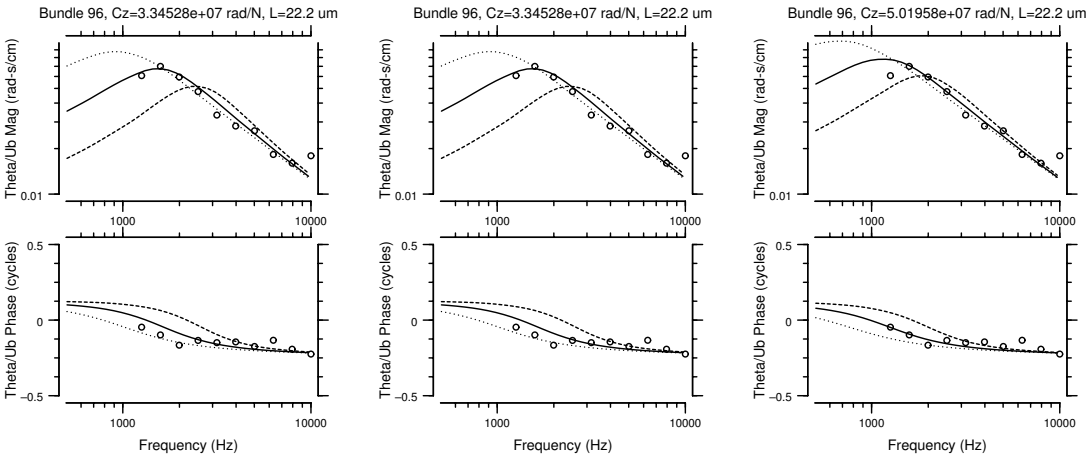

Figure C-46: Bundle 96

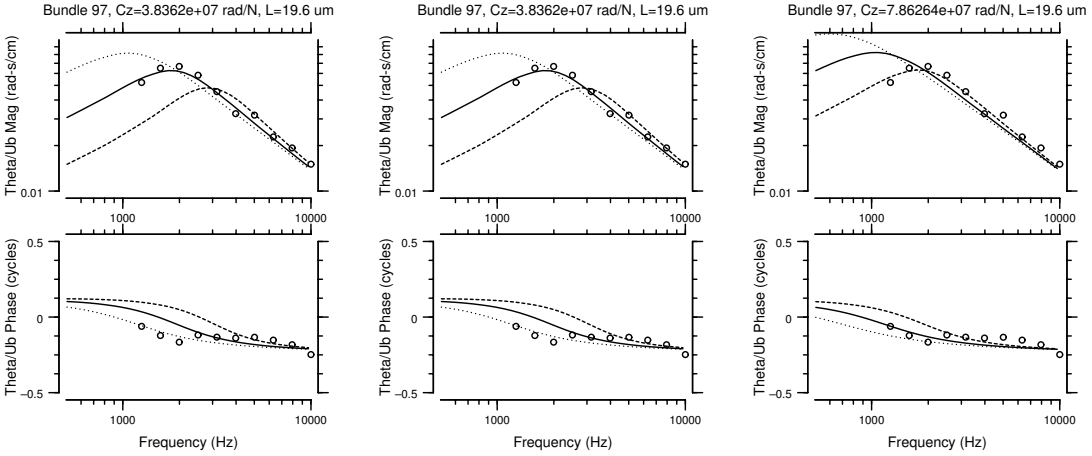

Figure C-47: Bundle 97

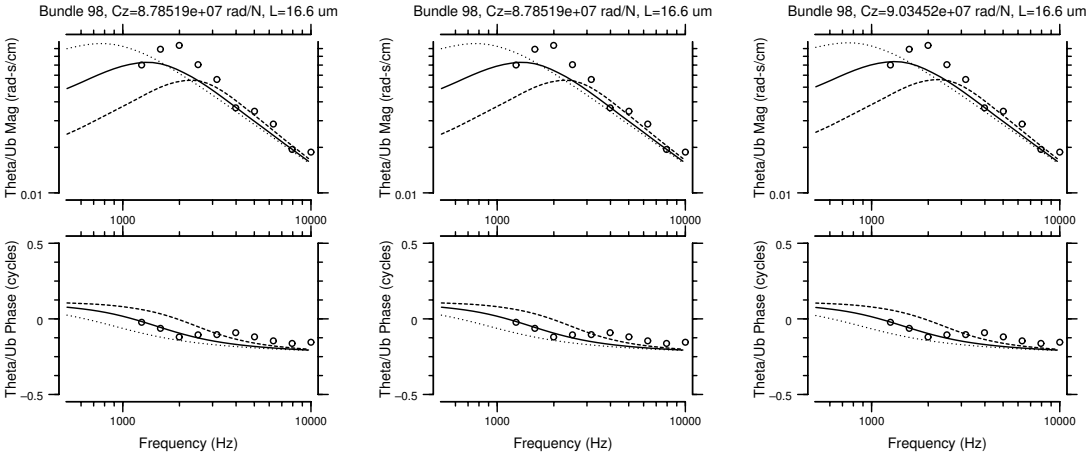

Figure C-48: Bundle 98

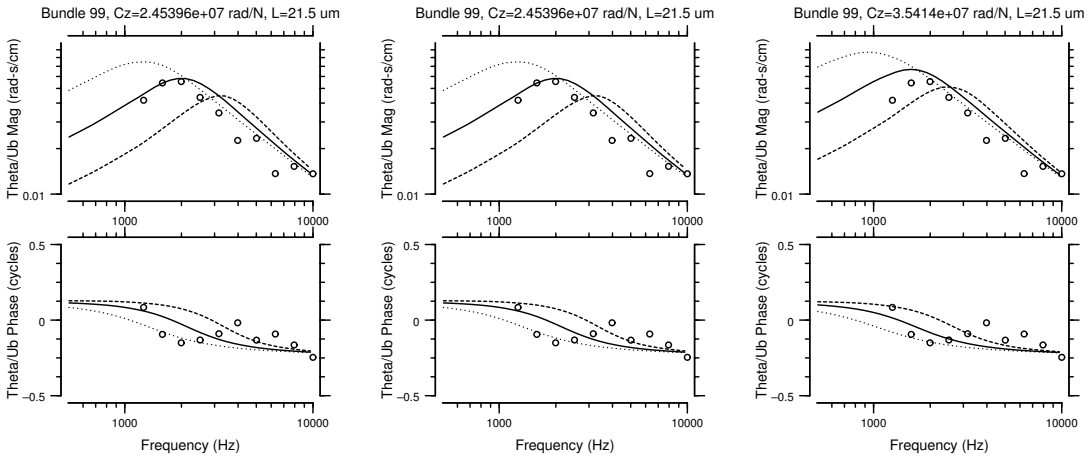

Figure C-49: Bundle 99

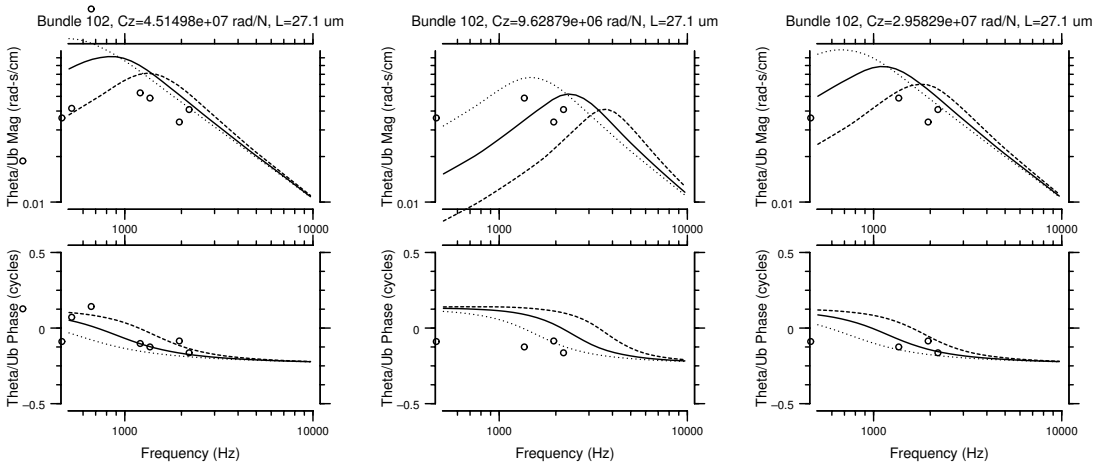

Figure C-50: Bundle 102

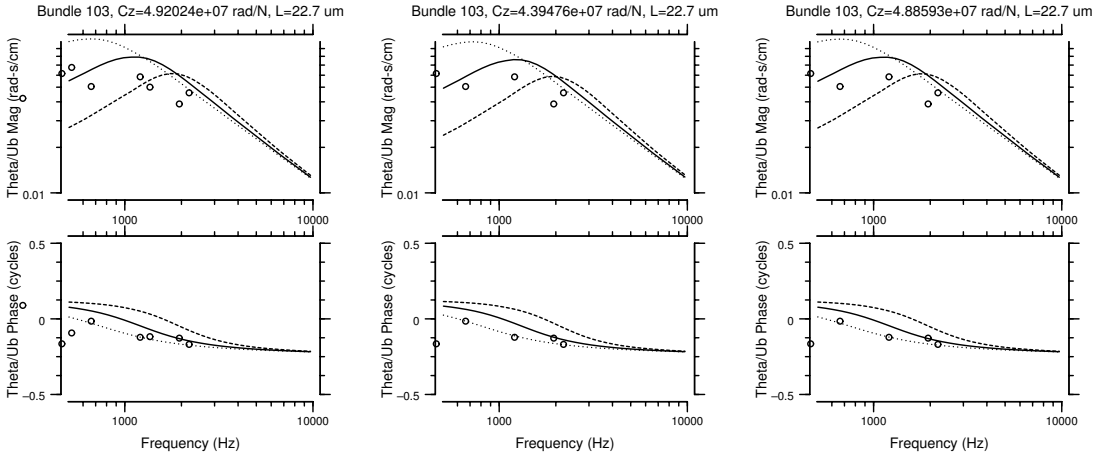

Figure C-51: Bundle 103

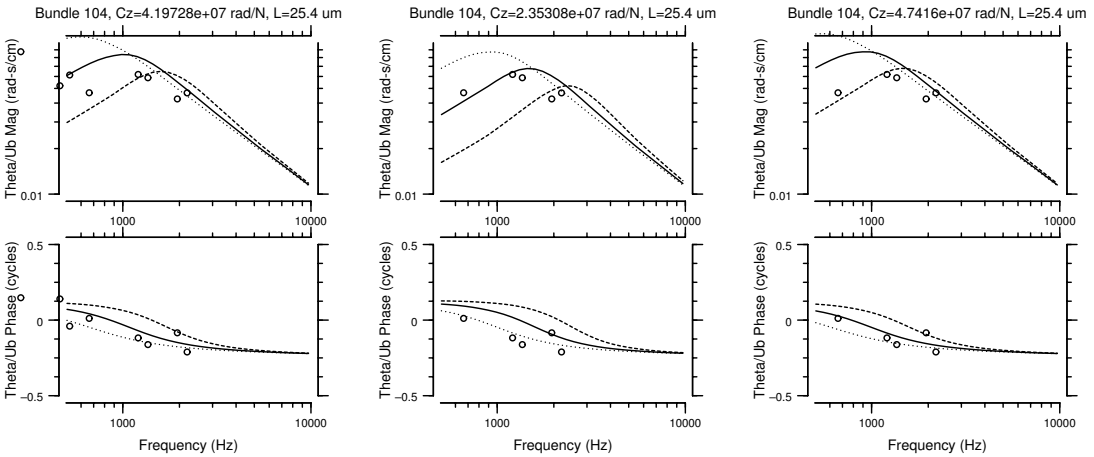

Figure C-52: Bundle 104

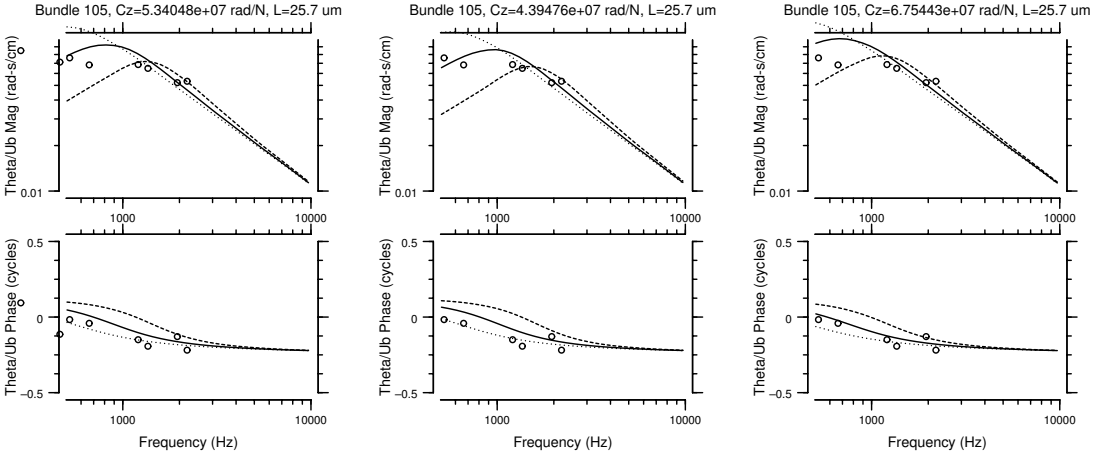

Figure C-53: Bundle 105

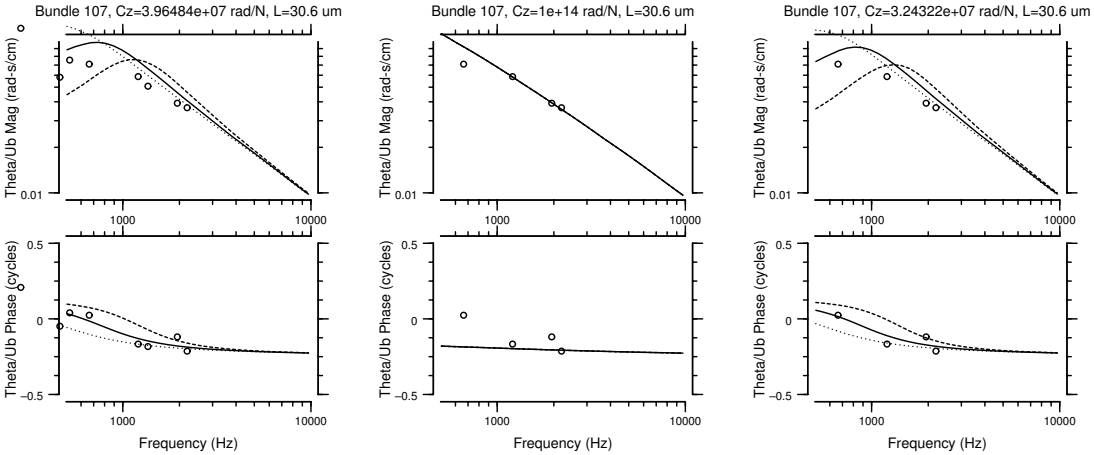

Figure C-54: Bundle 107

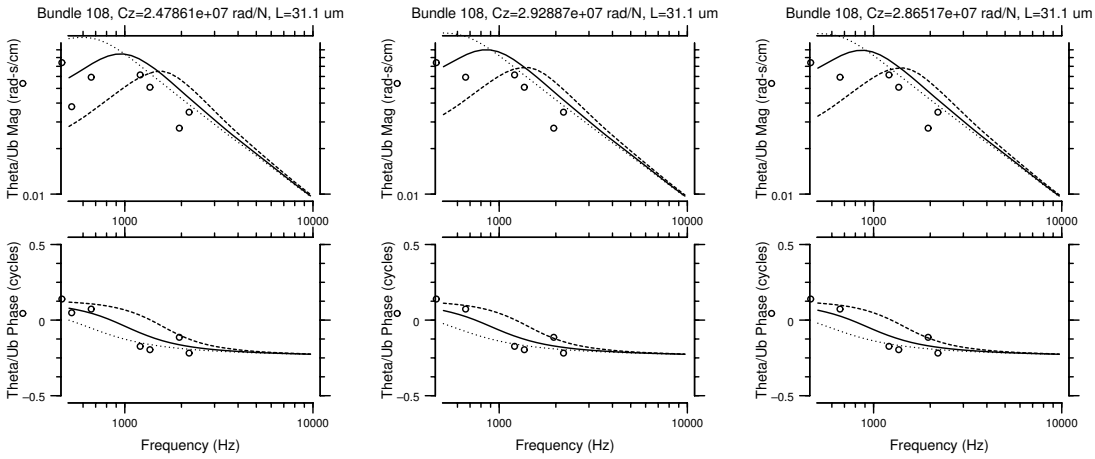

Figure C-55: Bundle 108

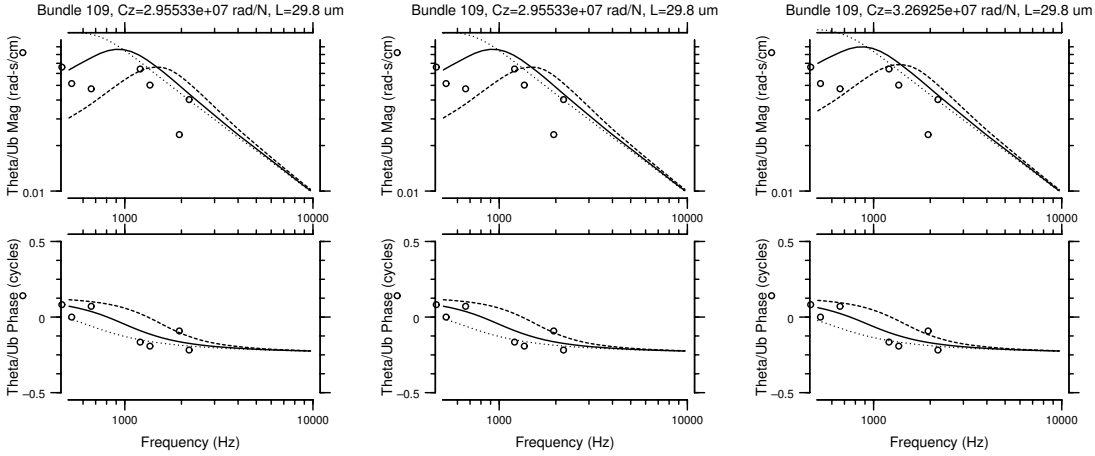

Figure C-56: Bundle 109

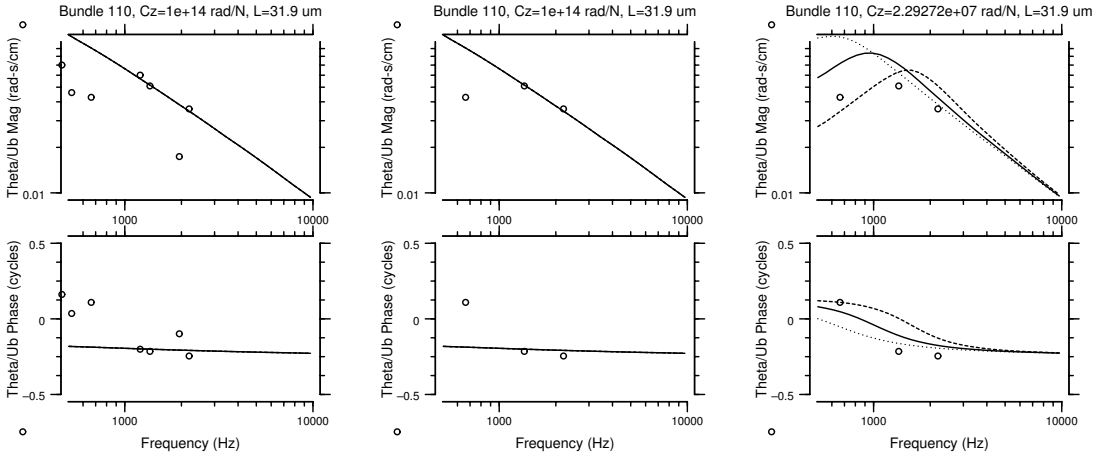

Figure C-57: Bundle 110

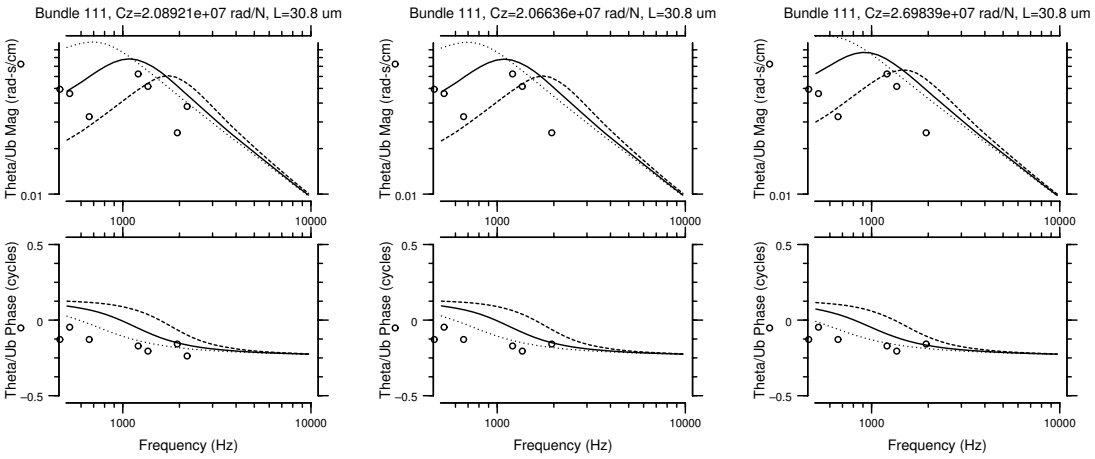

Figure C-58: Bundle 111

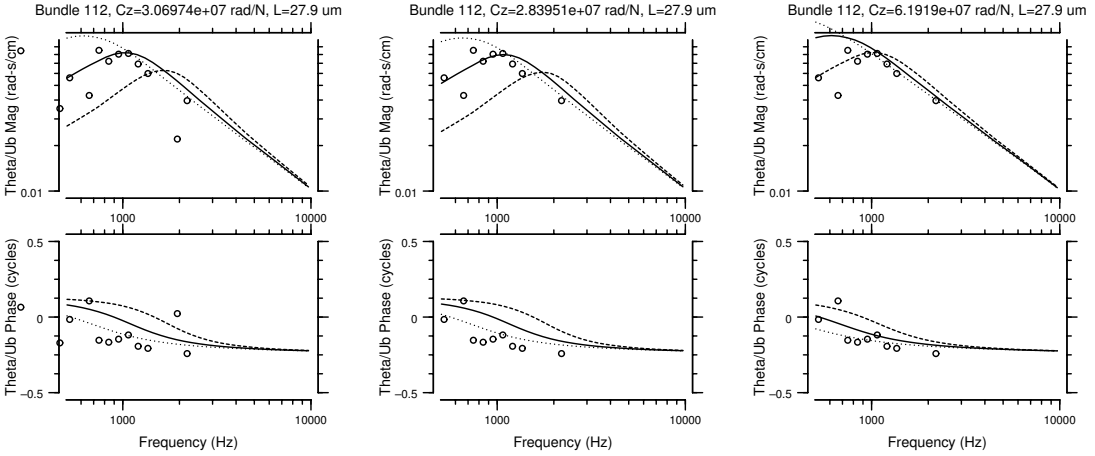

Figure C-59: Bundle 112

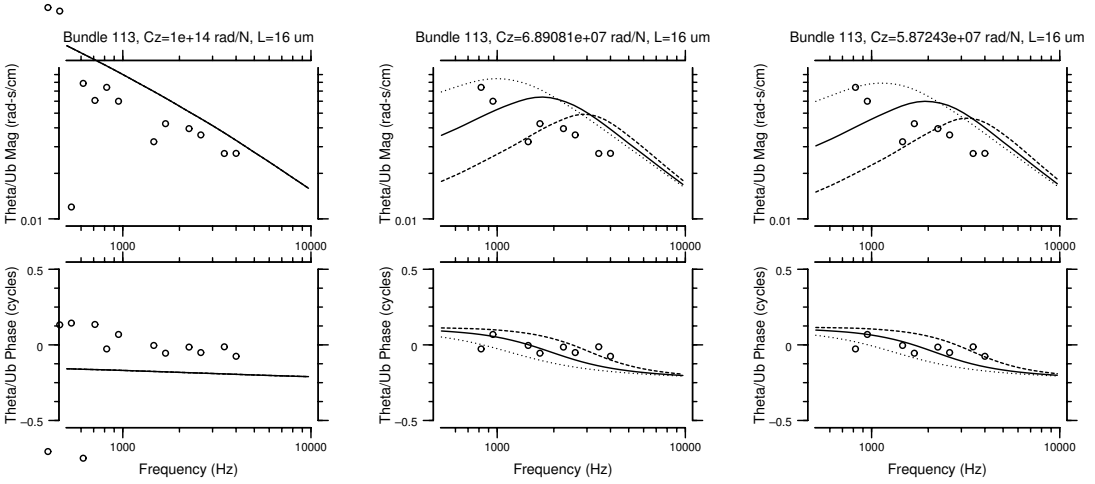

Figure C-60: Bundle 113

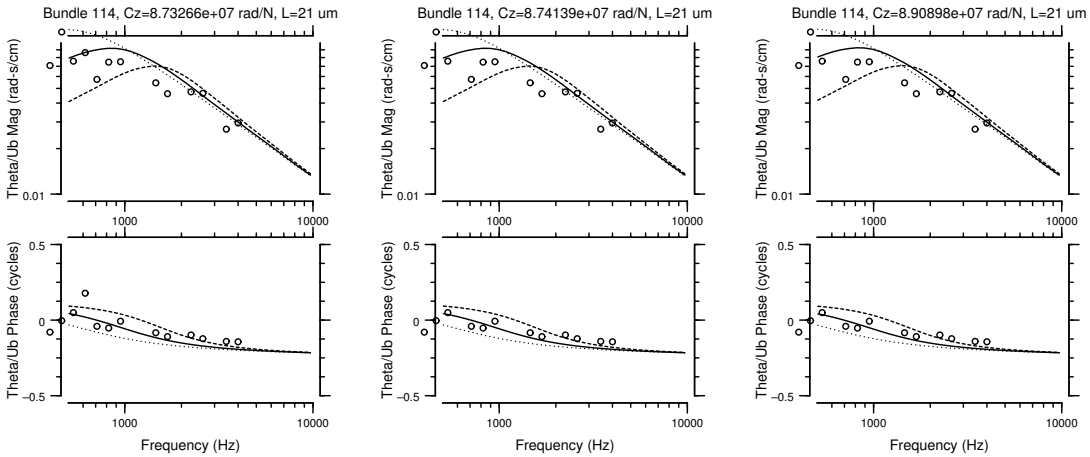

Figure C-61: Bundle 114

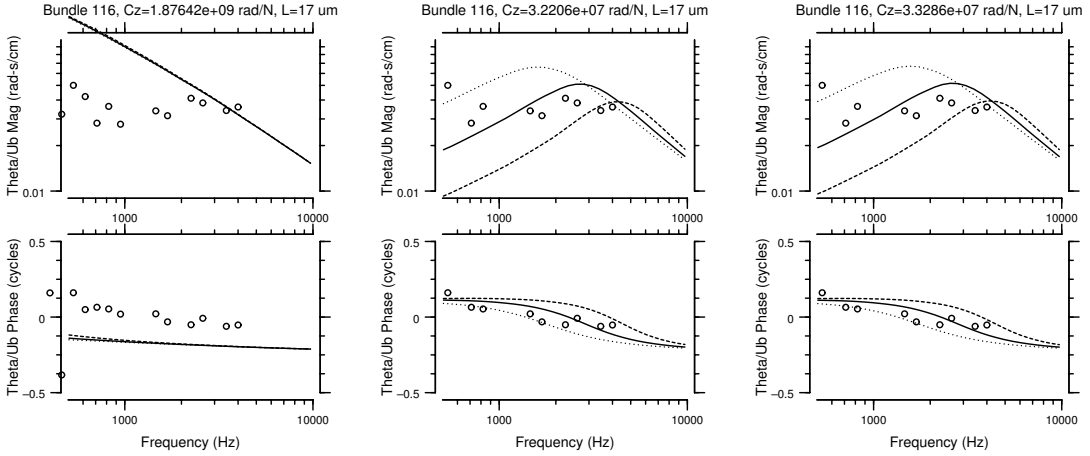

Figure C-62: Bundle 116

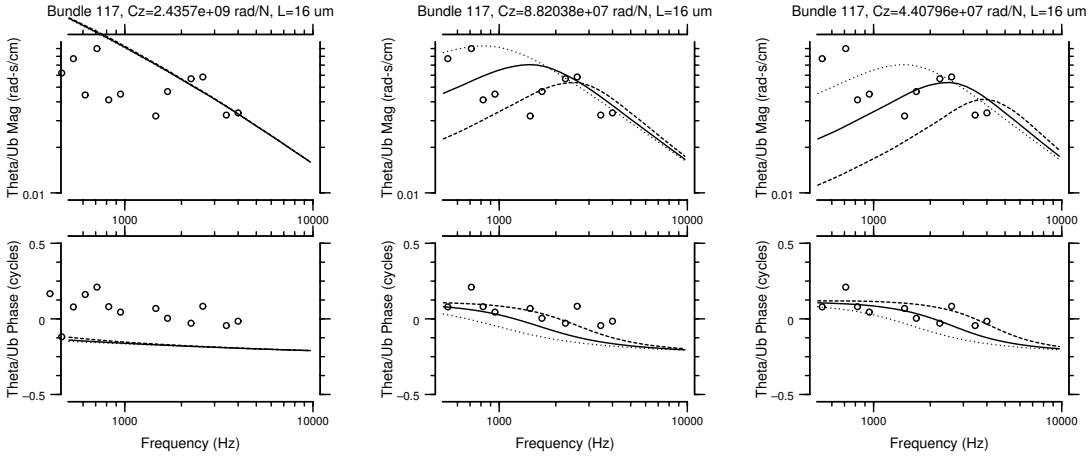

Figure C-63: Bundle 117

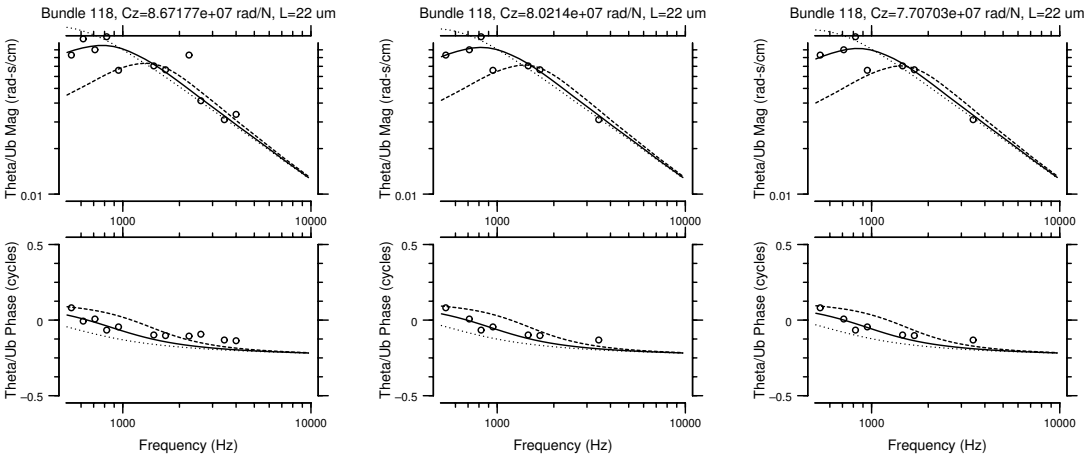

Figure C-64: Bundle 118

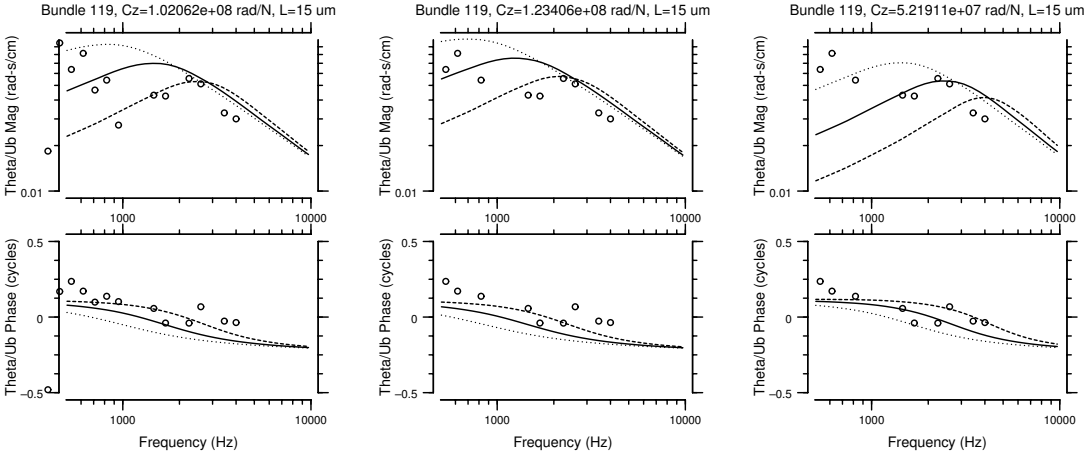

Figure C-65: Bundle 119

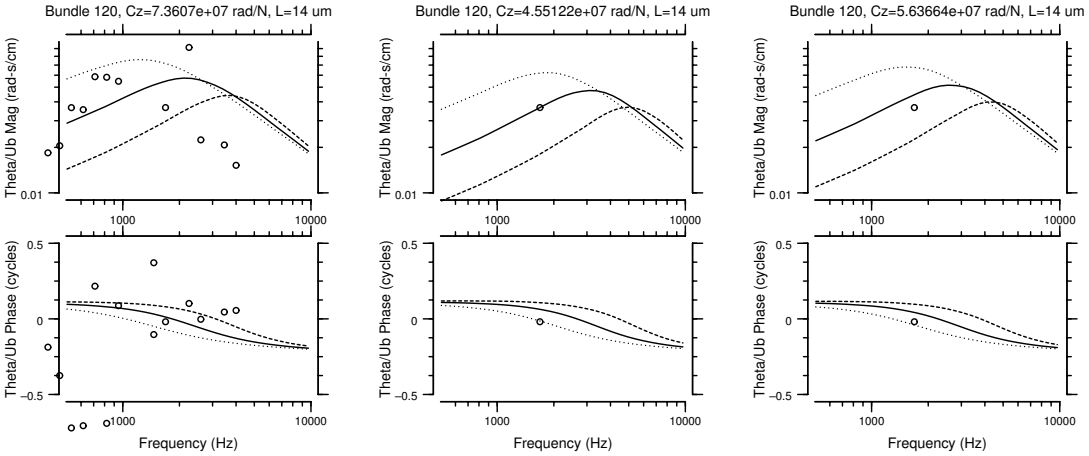

Figure C-66: Bundle 120

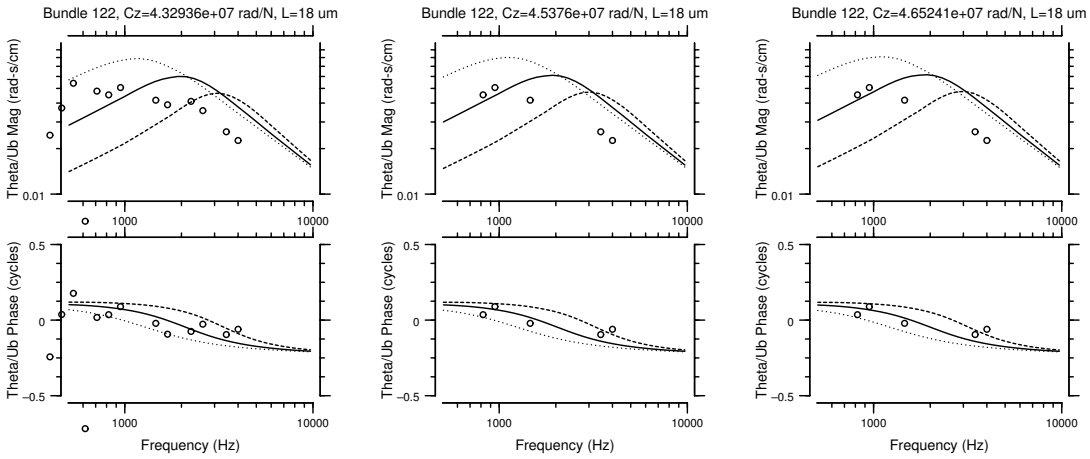

Figure C-67: Bundle 122

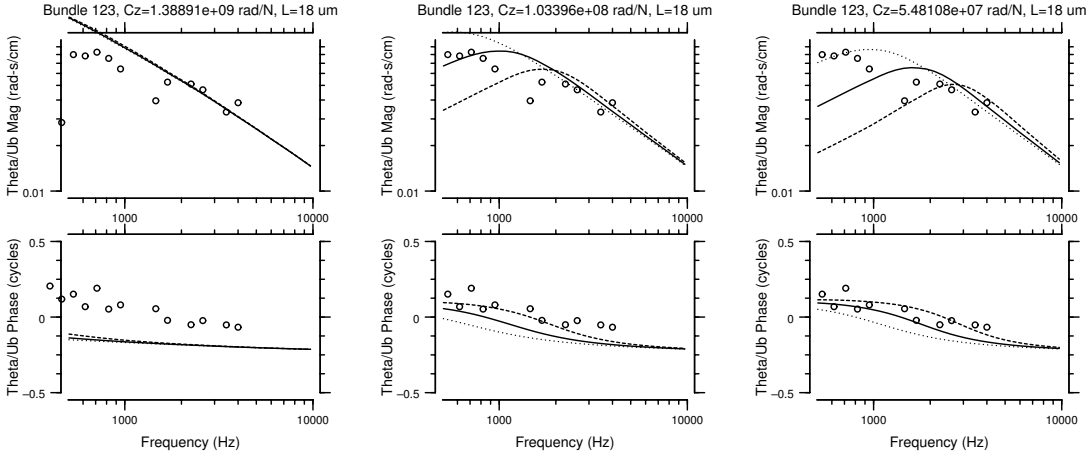

Figure C-68: Bundle 123

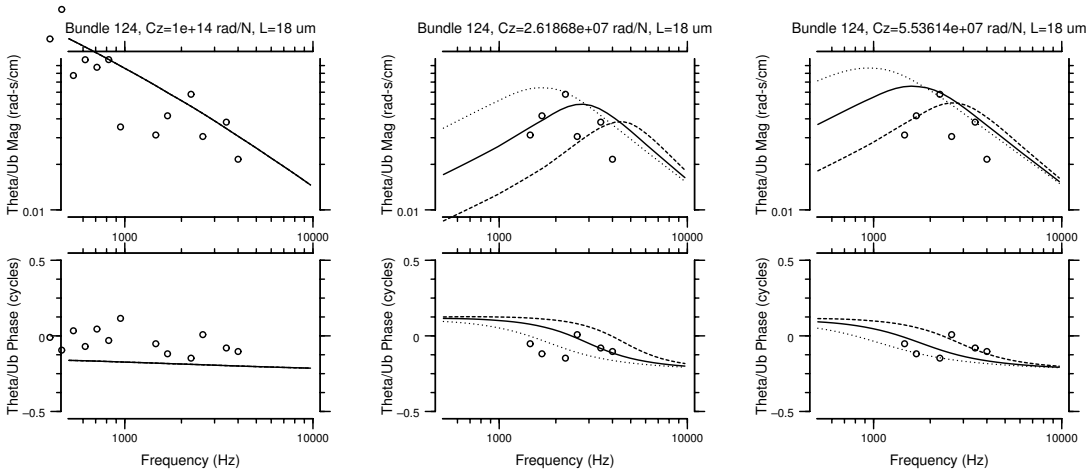

Figure C-69: Bundle 124

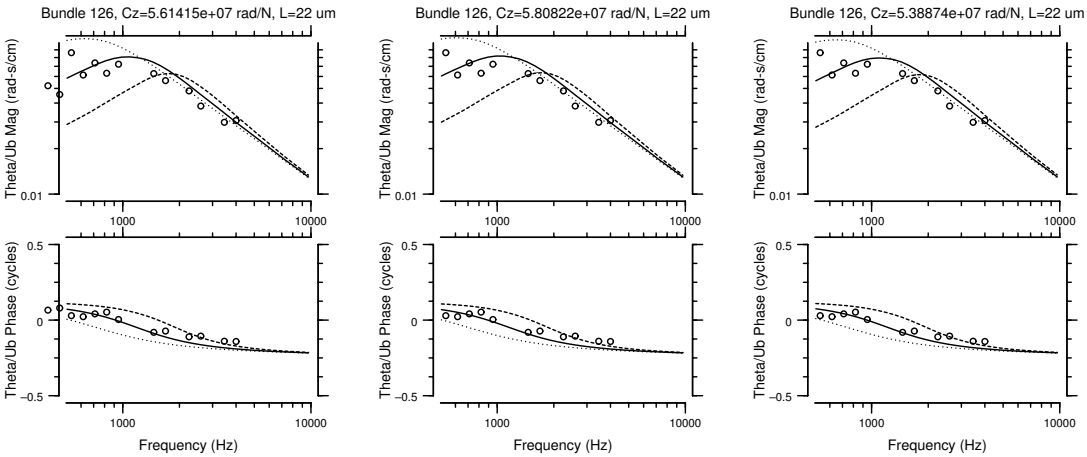

Figure C-70: Bundle 126

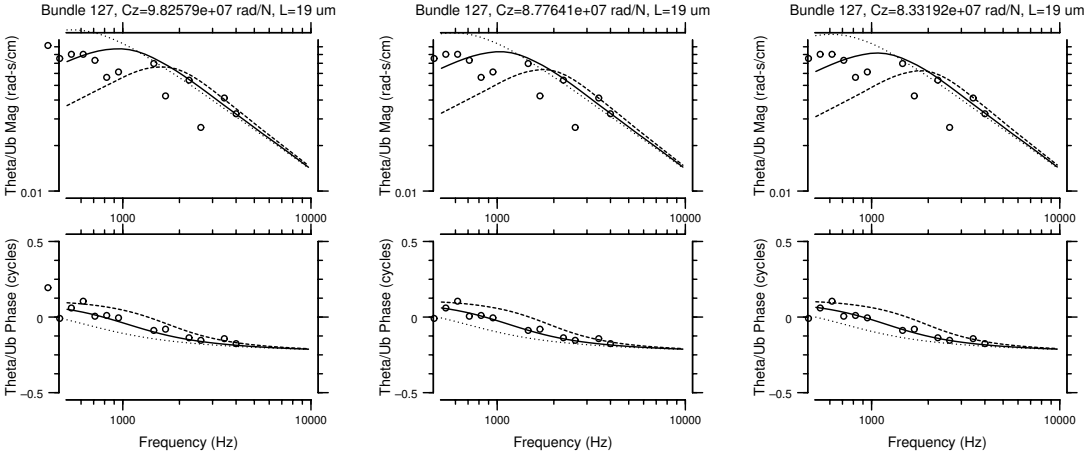

Figure C-71: Bundle 127

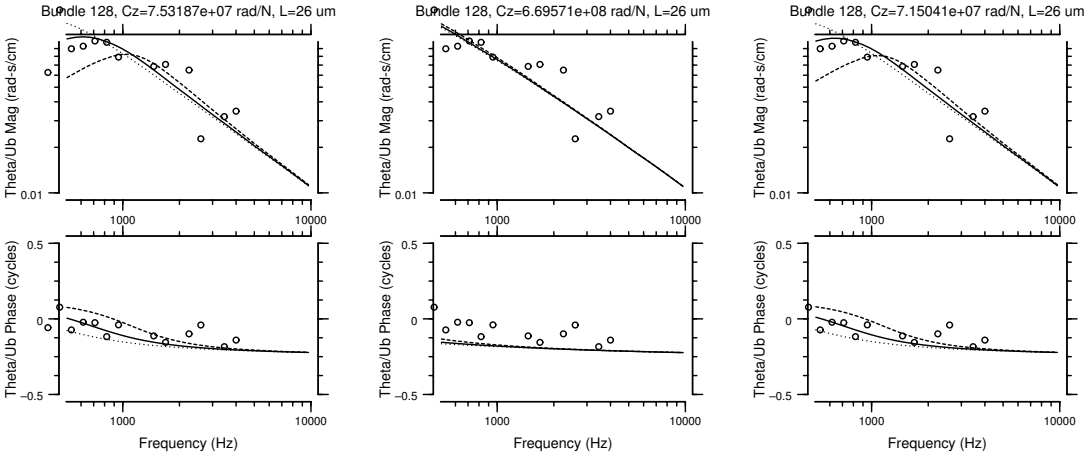

Figure C-72: Bundle 128

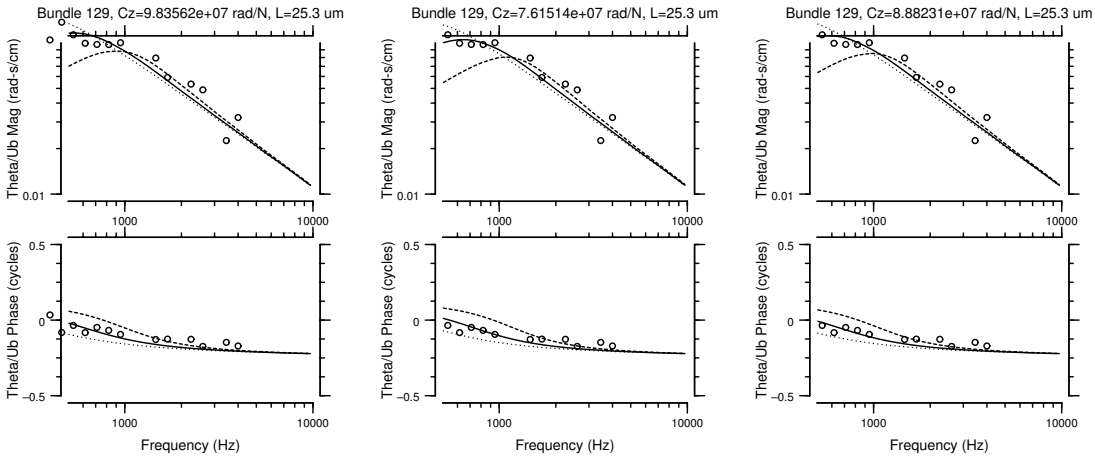

Figure C-73: Bundle 129

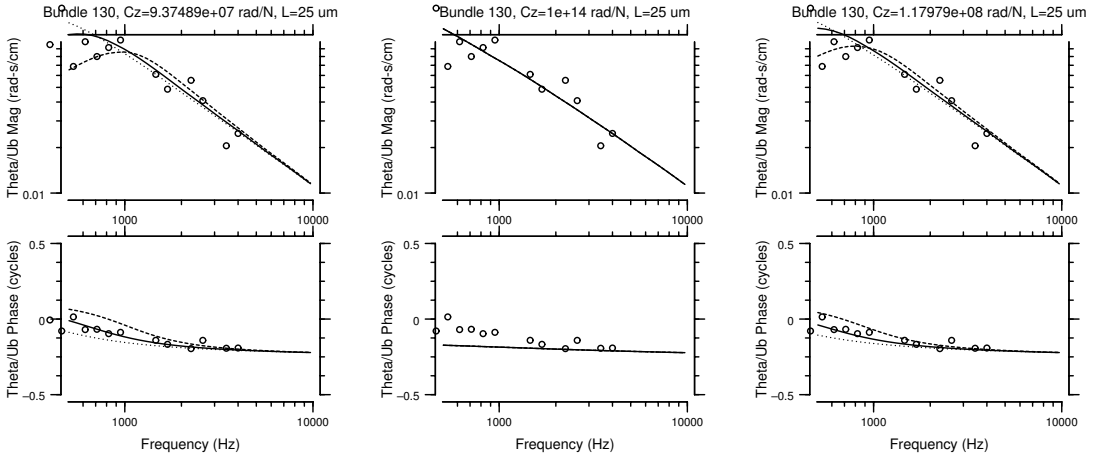

Figure C-74: Bundle 130

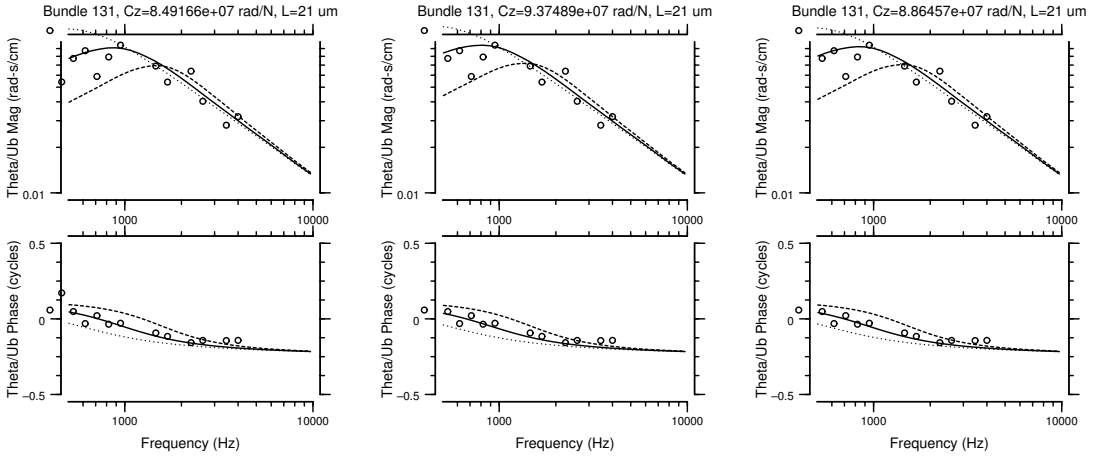

Figure C-75: Bundle 131

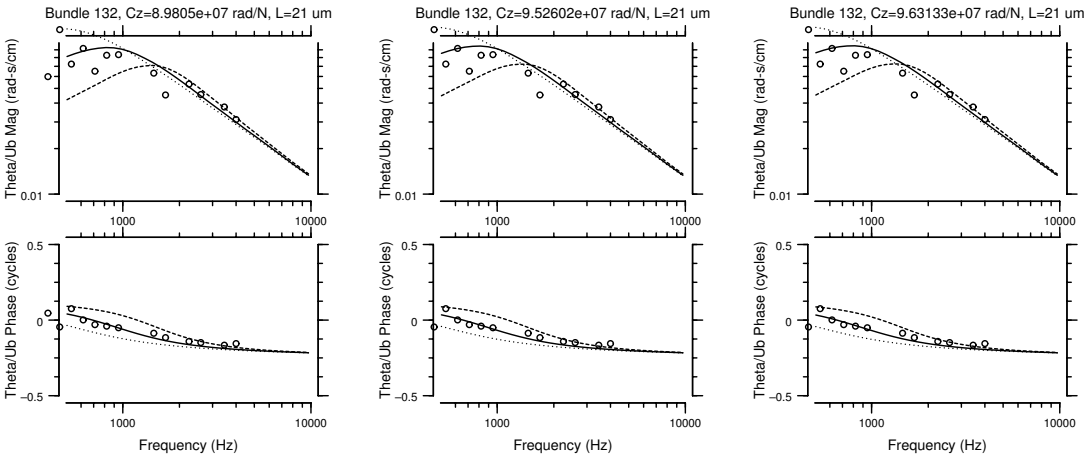

Figure C-76: Bundle 132

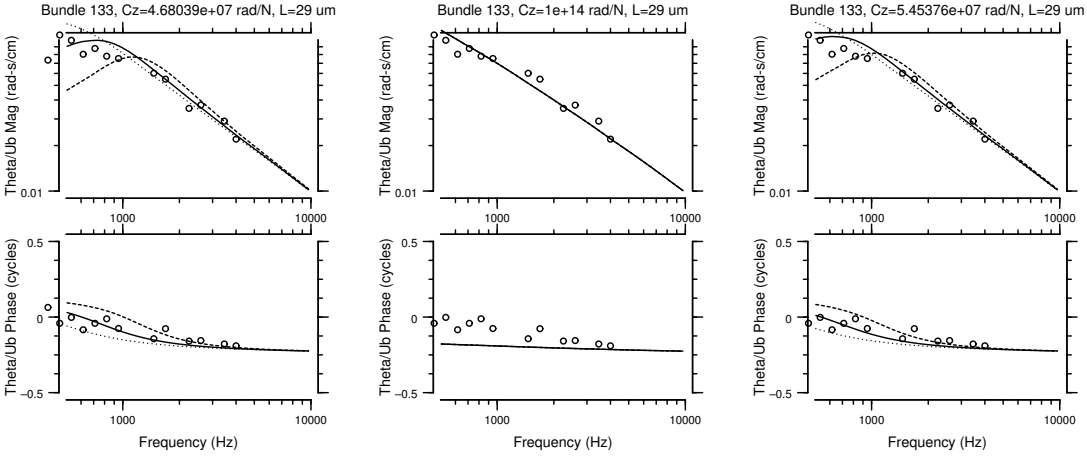

Figure C-77: Bundle 133

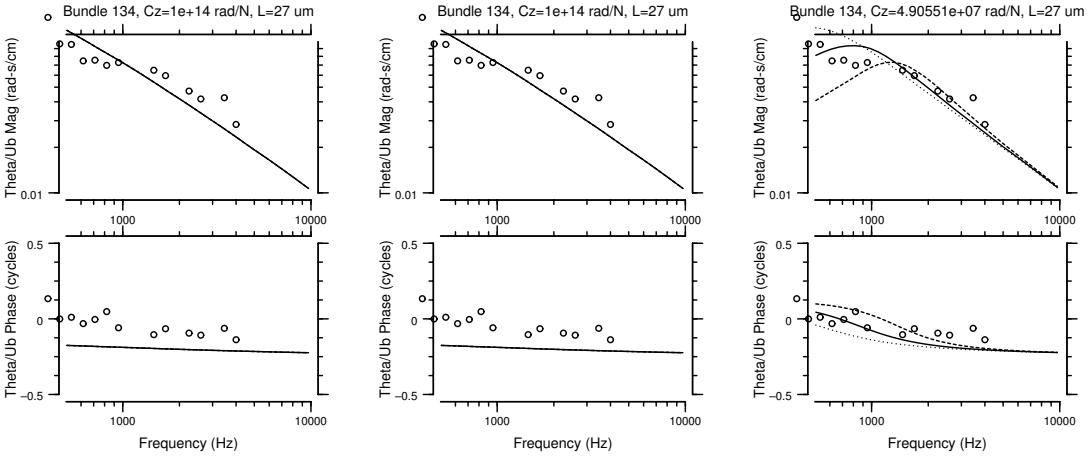

Figure C-78: Bundle 134

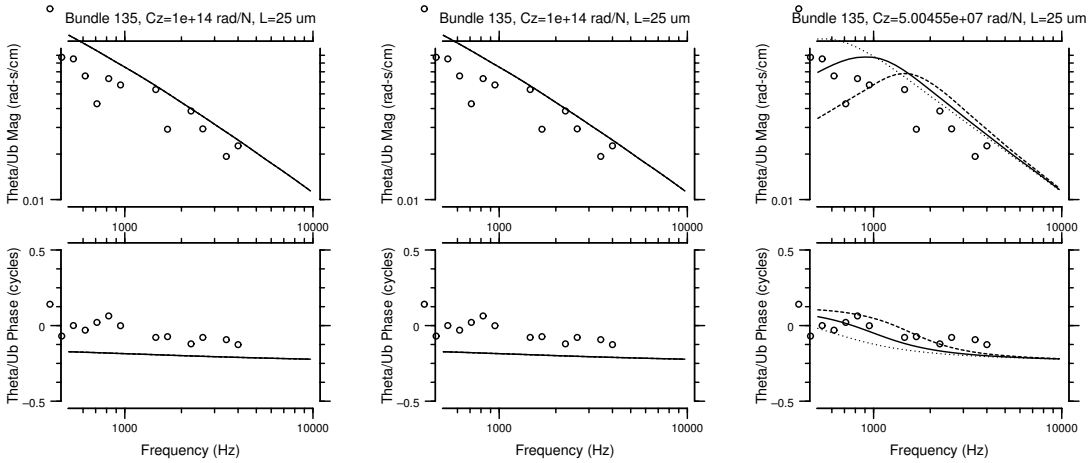

Figure C-79: Bundle 135

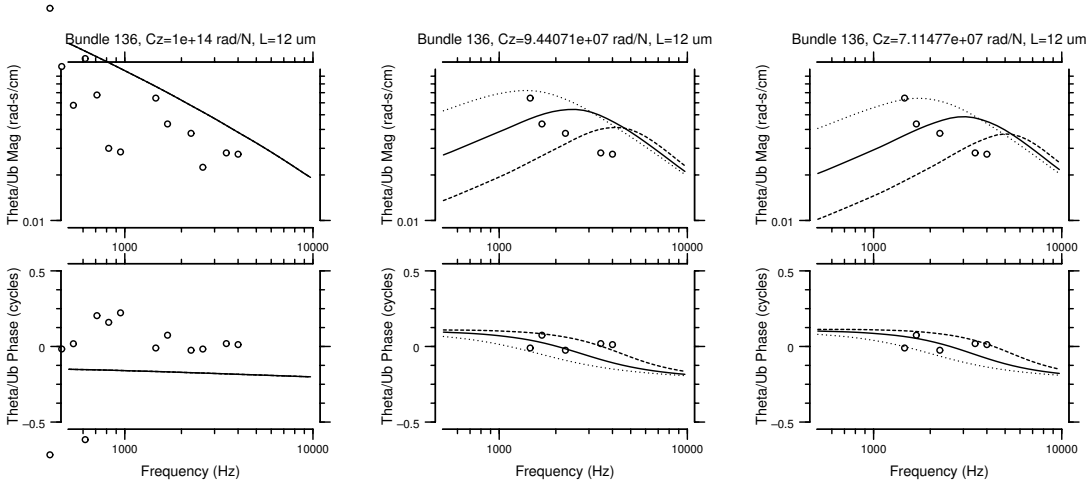

Figure C-80: Bundle 136

Bibliography

Allen, J. B. (1977). Cochlear micromechanics — a mechanism for transforming mechanical to neural tuning within the cochlea, *J Acoust Soc Am* **62**: 930–939.

Allen, J. B. (1980). Cochlear micromechanics — a physical model of transduction, *J Acoust Soc Am* **68**: 1660–1670.

Aranyosi, A. J., Davis, C. Q. and Freeman, D. M. (1998). Experimental measurements of micromechanical transfer functions in the alligator lizard cochlea, *Abstracts of the Twenty-First Midwinter Research Meeting*, Association for Research in Otolaryngology, St. Petersburg Beach, Florida.

Aranyosi, A. J. and Freeman, D. M. (1999). Media dependence of bleb growth in cochlear hair cells, *Abstracts of the Twenty-Second Midwinter Research Meeting*, Association for Research in Otolaryngology, St. Petersburg Beach, Florida.

Aranyosi, A. J. and Freeman, D. M. (2000). Tomographic reconstruction of three-dimensional cochlear motions, *Abstracts of the Twenty-Third Midwinter Research Meeting*, Association for Research in Otolaryngology, St. Petersburg Beach, Florida.

Aranyosi, A. J. and Freeman, D. M. (2001). Mechanical properties of the basilar papilla of alligator lizard, *Abstracts of the Twenty-Fourth Midwinter Research Meeting*, Association for Research in Otolaryngology, St. Petersburg Beach, Florida.

Aranyosi, A. J. and Freeman, D. M. (2002). A two-mode model of motion of the alligator lizard basilar papilla, *Abstracts of the Twenty-Fifth Midwinter Research Meeting*, Association for Research in Otolaryngology, St. Petersburg Beach, Florida.

Assad, J., Hacohen, N. and Corey, D. (1989). Voltage dependence of adaptation and active bundle movement in bullfrog saccular hair cells, *Proc Natl Acad Sci USA* **86**: 2918–2922.

Authier, S. and Manley, G. A. (1995). A model of frequency tuning in the basilar papilla of the tokay gecko, *Gekko gecko*, *Hear Res* **82**: 1–13.

Baden-Kristensen, K. and Weiss, T. F. (1983). Receptor potentials of lizard hair cells with free-standing stereocilia: responses to acoustic clicks, *J Physiol* **335**: 699–721.

Bohne, B. A. (1971). *Scar formation in the inner ear following acoustical injury: sequence of changes from early signs of damage to healed lesion*, PhD thesis, Washington University, St. Louis, MO.

Bohne, B. A. (1976). Mechanisms of noise damage in the inner ear, *in* D. Henderson, R. P. Hamernik, D. S. Dosanj and J. H. Mills (eds), *Effects of Noise on Hearing*, Raven, New York, pp. 41–68.

Bohne, B. A. and Rabbitt, K. D. (1983). Holes in the reticular lamina after noise exposure: implications for continuing damage in the organ of Corti, *Hear Res* **11**: 41–53.

Brändle, T. U., Glowatzki, E., Wild, K., Zenner, H.-P. and Ruppersberg, J. P. (1995). Expression of P2X-receptor sequences in different cell populations of the organ of Corti: detected by single-cell RT-PCR, *Proc Mol Biol Hear Deaf Symposium*, Bethesda, MD, p. 168.

Brownell, W. E., Bader, C. R., Bertrand, D. and de Ribaupierre, Y. (1985). Evoked mechanical responses of isolated cochlear hair cells, *Science* **227**: 194–196.

Cai, H., Richter, C.-P. and Chadwick, R. S. (2002). A new approach for optical flow analysis of cochlear motions, *Abstracts of the Twenty-Fifth Midwinter Research Meeting*, Association for Research in Otolaryngology, St. Petersburg Beach, Florida.

Canlon, B., Miller, J., Flock, Å. and Borg, E. (1987). Pure tone overstimulation changes the micromechanical properties of the inner hair cell stereocilia, *Hear Res* **30**: 65–72.

Chan, E., Suneson, A. and Ulfendahl, M. (1998). Acoustic trauma causes reversible stiffness changes in auditory sensory cells, *Neurosci* **83**: 961–968.

Chen, C., Skellett, R. A., Fallon, M. and Bobbin, R. P. (1998). Additional pharamacological evidence that endogenous ATP modulates cochlear mechanics, *Hear Res* **118**: 47–61.

Cooper, N. P. (2000). Radial variation in the sound-evoked vibrations of the cochlear partition, *Abstracts of the Twenty-Third Midwinter Research Meeting*, Association for Research in Otolaryngology, St. Petersburg Beach, Florida.

Corey, D. P. and Hudspeth, A. J. (1983). Analysis of the microphonic potential of the bullfrog's sacculus, *J Neurosci* **3**(5): 942–961.

Crawford, A. C. and Fettiplace, R. (1985). The mechanical properties of ciliary bundles of turtle cochlear hair cells, *J Physiol* **364**: 359–379.

Dai, J. and Sheetz, M. P. (1995). Regulation of endocytosis, exocytosis, and shape by membrane tension, *Cold Spring Harbor Symposia on Quantitative Biology*, Vol. LX, pp. 567–571.

Dallos, P., Billone, M. C., Durrant, J. D., Wang, C. and Raynor, S. (1972). Cochlear inner and outer hair cells: functional differences, *Science* **177**: 356–358.

Davis, C. Q. (1997). *Measuring nanometer, three-dimensional motions with light microscopy*, PhD thesis, Massachusetts Institute of Technology, Cambridge, MA.

Davis, C. Q. and Freeman, D. M. (1995). Direct observations of sound-induced motions of the reticular lamina, tectorial membrane, hair bundles, and individual stereocilia, *Abstracts of the Eighteenth Midwinter Research Meeting*, Association for Research in Otolaryngology, St. Petersburg Beach, Florida.

Davis, C. Q. and Freeman, D. M. (1998a). Statistics of subpixel registration algorithms based on spatio-temporal gradients or block matching, *Optical Engineering* pp. 1290–1298.

Davis, C. Q. and Freeman, D. M. (1998b). Using a light microscope to measure motions with nanometer accuracy, *Optical Engineering* pp. 1299–1304.

Davis, C. Q., Karu, Z. Z. and Freeman, D. M. (1995). Equivalence of subpixel motion estimators based on optical flow and block matching, *IEEE International Symposium for Computer Vision*, Coral Gables, Florida, pp. 7–12.

Davis, H. (1957). Biophysics and physiology of the inner ear, *Physiol Rev* **37**: 1–49.

deBoer, E. (1996). Mechanics of the cochlea: modeling efforts, *in* P. Dallos, A. N. Popper and R. R. Fay (eds), *The Cochlea*, Vol. 8 of *Springer Handbook of Auditory Research*, Springer-Verlag, New York.

deBoer, E. and Nuttall, A. L. (1997). The mechanical waveform of the basilar membrane. I. frequency modulations ("glides") in impulse responses and cross-correlation functions, *J Acoust Soc Am* **101**: 3583–3592.

Denk, W. (1989). *Biophysical studies of mechano-electrical transduction in hair cells*, PhD thesis, Cornell University, Ithaca, NY.

Duan, D., Winter, C., Cowley, S., Hume, J. R. and Horowitz, B. (1997). Molecular identification of a volume-regulated chloride channel, *Nature* **390**: 417–21.

Duncan, R. K. and Saunders, J. C. (2000). Stereocilium injury mediates hair bundle stiffness loss and recovery following intense water-jet stimulation, *J Comp Physiol* **186**: 1095–1106.

Eatock, R. A., Saeki, M. and Hutzler, M. J. (1993). Electrical resonance of isolated hair cells does not account for acoustic tuning in the free-standing region of the alligator lizard's cochlea, *The Journal of Neuroscience* **13**: 1767–1783.

Edge, R. M., Evans, B. N., Pearce, M., Richter, C. P., Hu, X. and Dallos, P. (1998). Morphology of the unfixed cochlea, *Hear Res* **124**: 1–16.

Fettiplace, R. and Crawford, A. (1978). The coding of sound pressure and frequency in cochlear hair cells of the terrapin, *Proc R Soc Lond B* **203**: 209–218.

Fettiplace, R. and Fuchs, P. A. (1999). Mechanisms of hair cell tuning, *Annu Rev Physiol* **61**: 809–834.

Flock, Å. (1982). Structure and function of the hearing organ: recent investigations of micromechanics and its control, *in* R. Carlson and B. Granström (eds), *The representation of speech in the peripheral auditory system*, Elsevier, Amsterdam, pp. 1–8.

Flock, Å. and Strelioff, D. (1984). Studies on hair cells in isolated coils from the guinea pig cochlea, *Hear Res* **15**: 11–18.

Franco, A. and Lansman, J. B. (1990). Stretch-sensitive channels in developing muscle cells from a mouse cell line, *J Physiol* **427**: 361–380.

Freeman, D. M. (1990). Anatomical model of the cochlea of the alligator lizard, *Hearing Research* **49**: 29–38.

Freeman, D. M., Aranyosi, A. J., Gordon, M. J. and Hong, S. S. (1998). Multidimensional motion analysis of MEMS using computer microvision, *1998 Solid-State Sensor and Actuator Workshop*, Hilton Head, South Carolina, pp. 150–155.

Freeman, D. M., Davis, C. Q., Aranyosi, A. J., Abnet, C. C. and Hemmert, W. (2000). Watching hearing: Using video microscopy to characterize cochlear micromechanics, *Abstracts of the Twenty-Third Midwinter Research Meeting*, Association for Research in Otolaryngology, St. Petersburg Beach, Florida.

Freeman, D. M. and Weiss, T. F. (1988). The role of fluid inertia in mechanical stimulation of hair cells, *Hearing Research* **35**: 201–208.

Freeman, D. M. and Weiss, T. F. (1990a). Hydrodynamic analysis of a two-dimensional model for micromechanical resonance of free-standing hair bundles, *Hearing Research* **48**: 37–68.

Freeman, D. M. and Weiss, T. F. (1990b). Hydrodynamic forces on hair bundles at high frequencies, *Hearing Research* **48**: 31–36.

Freeman, D. M. and Weiss, T. F. (1990c). Hydrodynamic forces on hair bundles at low frequencies, *Hearing Research* **48**: 17–30.

Freeman, D. M. and Weiss, T. F. (1990d). Superposition of hydrodynamic forces on a hair bundle, *Hearing Research* **48**: 1–16.

Frishkopf, L. S. and DeRosier, D. J. (1983). Mechanical tuning of free-standing stereociliary bundles and frequency analysis in the alligator lizard cochlea, *Hearing Res* **12**: 393–404.

Gale, J., Faucheux, F., Kennedy, H. and Richardson, G. (2000). FM1-43 loading of mouse cochlear hair cells in vitro is rapid, blocked by pretreating cultures with EGTA and recovers from Ca2+-chelation over 24 hours, *Abstracts of the Twenty-Third Midwinter Research Meeting*, Association for Research in Otolaryngology, St. Petersburg Beach, Florida.

Gall, V., Gall, D. and Hanson, J. (1971). Larynx-fotokymographie, *Arch Ohr-, Nas- und Kehlk Heilk* **20**: 34–41.

Gordon, M. J. (1999). *Rotation analysis of a microfabricated fatigue test structure*, Master's thesis, Massachusetts Institute of Technology, Cambridge, MA.

Gummer, A. W., Hemmert, W. and Zenner, H.-P. (1996). Resonant tectorial membrane motion in the inner ear: its crucial role in frequency tuning, *Proc Natl Acad Sci USA* **93**: 8727–8732.

Haugland, R. P. (1996). *Handbook of Fluorescent Probes and Research Chemicals*, 6th edn, Molecular Probes, Eugene, OR.

Healey, G. E. and Kondepudy, R. (1994). Radiometric CCD camera calibration and noise estimation, *IEEE Trans Pattern Anal Machine Intell* **16**: 267–276.

Hemmert, W., Zenner, H. P. and Gummer, A. W. (2000). Three-dimensional motion of the organ of Corti, *J Biophys* **78**: 2285–2297.

Hiraoka, Y., Sedat, J. W. and Agard, D. A. (1987). The use of charge-coupled devices for quantitative optical microscopy of biological structures, *Science* **238**: 36–41.

Holton, T. and Hudspeth, A. J. (1983). A micromechanical contribution to cochlear tuning and tonotopic organization, *Science* **222**: 508–510.

Holton, T. and Weiss, T. F. (1978). Two-tone rate suppression in lizard cochlear nerve fibers, relation to receptor organ morphology, *Brain Res* **159**: 219–222.

Holton, T. and Weiss, T. F. (1983a). Frequency selectivity of hair cells and nerve fibers in the alligator lizard cochlea, *J Physiol* **345**: 241–260.

Holton, T. and Weiss, T. F. (1983b). Receptor potentials of lizard cochlear hair cells with free-standing stereocilia in response to tones, *J Physiol* **345**: 205–240.

Horn, B. K. P. (1986). *Robot Vision*, MIT Press, Cambridge, MA.

Horn, B. K. P. and Weldon Jr., E. J. (1988). Direct methods for recovering motion, *Internatl J of Computer Vision* **2**: 51–76.

Housley, G. D. and Ashmore, J. F. (1992). Ionic currents of outer hair cells isolated from the guinea-pig cochlea, *J Physiol* **448**: 73–98.

Housley, G. D., Greenwood, D., Bennett, T. and Ryan, A. F. (1995). Identification of a short form of the P2XR1 purinoceptor produced by alternative splicing in the pituitary and cochlea, *Biochem Biophys Res Commun* **212**: 501–508.

Housley, G. D., Greenwood, D., kanjhan, R., Raybould, N. P., Thorne, P. R., Christie, D., Bennett, T., Lin, L. and Ryan, A. F. (1996). Differential expression of P2X purinoceptor isoforms in the cochlea, *Drug Dev Res* **37**: 171.

Housley, G. D., Raybould, N. P. and Thorne, P. R. (1998). Fluorescence imaging of Na^+ influx via P2X receptors in cochlear hair cells, *Hear Res* **119**: 1–13.

Howard, J. and Ashmore, J. F. (1986). Stiffness of sensory hair bundles in the sacculus of the frog, *Hear Res* **23**: 93–104.

Howard, J. and Hudspeth, A. J. (1988). Compliance of the hair bundle associated with gating of mechanoelectrical transduction channels in the bullfrog's saccular hair cell, *Neuron* **1**: 189–199.

Hu, X., Evans, B. N. and Dallos, P. (1996). Transmission of basilar membrane motion to reticular lamina motion, *Abstracts of the Nineteenth Midwinter Research Meeting*, Association for Research in Otolaryngology, St. Petersburg Beach, Florida.

Hu, X., Evans, B. N. and Dallos, P. (1999). Direct visualization of organ of Corti kinematics in a hemicochlea, *J Neurophysiol* **82**: 2798–2807.

Hu, X., Evans, B. N., Edge, R. M. and Dallos, P. (1995). Organ of Corti micromechanics studied in a hemicochlea, *Abstracts of the Eighteenth Midwinter Research Meeting*, Association for Research in Otolaryngology, St. Petersburg Beach, Florida.

Hubbard, A. E. and Mountain, D. C. (1996). Analysis and synthesis of cochlear mechanical function using models, *in* H. L. Hawkins, T. A. McMullen, A. N. Popper and R. R. Fay (eds), *Auditory Computation*, Springer-Verlag, New York.

Hudspeth, A. J. (1985). The cellular basis of hearing: the biophysics of hair cells, *Science* **230**: 745–752.

Hudspeth, A. J. and Corey, D. P. (1977). Sensitivity, polarity, and conductance change in the response of vertebrate hair cells to controlled mechanical stimuli, *Proc Natl Acad Sci USA* **74**: 2407–2411.

Inoué, S. (1986). *Video Microscopy*, Plenum Press, New York, NY.

International Team For Ear Research (ITER). (1989). Cellular vibration and motility in the organ of Corti, *Acta Otolaryngol* **467**(suppl): 1–279.

Janesick, J. R., Elliot, T., Collins, S., Blouke, M. M. and Freeman, J. (1987). Scientific charge-coupled devices, *Optical Engineering* **26**: 692–714.

Karavitaki, K. D. and Mountain, D. C. (1996). Imaging electromotility in the gerbil organ of Corti at acoustic frequencies, *Abstracts of the Nineteenth Midwinter Research Meeting*, Association for Research in Otolaryngology, St. Petersburg Beach, Florida.

Karavitaki, K. D. and Mountain, D. C. (1997). Multiple modes of vibration in the apical turn of the gerbil cochlea, *Abstracts of the Twentieth Midwinter Research Meeting*, Association for Research in Otolaryngology, St. Petersburg Beach, Florida.

Karavitaki, K. D. and Mountain, D. C. (2002). Three-dimensional reconstruction of electrically-evoked motions in the gerbil cochlea, *Abstracts of the Twenty-Fifth Midwinter Research Meeting*, Association for Research in Otolaryngology, St. Petersburg Beach, Florida.

Kiang, N. Y. S., Watanabe, T., Thomas, C. and Clark, L. F. (1965). *Discharge Patterns of Single Fibers in the Cat's Auditory Nerve*, MIT Press, Cambridge MA.

Kimitsuki, T., Nakagawa, T., Hisashi, K., Komune, S. and Komiyama, S. (1996). Gadolinium blocks mechano-electric transducer current in chick cochlear hair cells, *Hear Res* **101**: 75–80.

Kroese, A. B., Das, A. and Hudspeth, A. J. (1989). Blockage of the transduction channels of hair cells in the bullfrog's sacculus by aminoglycoside antibiotics, *Hear Res* **37**(3): 203–217.

Lambrecht, G., Friebe, T., Grimm, U., Windscheif, U., Bungardt, E., Hildebrandt, C., Bäumert, H. G., Spatz-Kümbel, G. and Mutschler, E. (1992). PPADS, a novel functionally selective antagonist of P2 purinoceptor-mediated responses, *Eur J Pharmacol* **217**: 217–219.

Liberman, M. C. (1994). Cochlear pathology. Notes for MIT course HST720.

Lin, T. and Guinan, J. (2000). Auditory-nerve-fiber responses suggest that organ of Corti vibration is a mixture of modes with different resonant properties, *Abstracts of the Twenty-Third Midwinter Research Meeting*, Association for Research in Otolaryngology, St. Petersburg Beach, Florida.

MacDonald, R. B. and Corey, D. P. (2001). Real-time confocal microscopy distinguishes two phases of FM1-43 entry into hair cells, *Abstracts of the Twenty-Fourth Midwinter Research Meeting*, Association for Research in Otolaryngology, St. Petersburg Beach, Florida.

Mammano, F. and Nobili, R. (1993). Biophysics of the cochlea: linear approximation, *J Acoust Soc Am* **93**: 3320–3332.

Manley, G. A. (2000a). Cochlear mechanisms from a phylogenetic viewpoint, *Proc Nat Acad Sci USA* **97**: 11736–11743.

Manley, G. A. (2000b). The hearing organs of lizards, *in* R. J. Dooling, A. N. Popper and R. R. Fay (eds), *Comparative Hearing: Birds and Reptiles*, Vol. 13 of *Springer Handbook of Auditory Research*, Springer-Verlag, New York.

Manley, G. A., Kirk, D. L., Köppl, C. and Yates, G. K. (2001). *In vivo* evidence for a cochlear amplifier in the hair-cell bundle of lizards, *Proc Nat Acad Sci USA* **98**: 2826–2831.

Manley, G. A. and Köppl, C. (1998). Phylogenetic development of the cochlea and its innervation, *Curr Opin Neurobiol* **8**: 468–474.

Miller, M. R. (1966). The cochlear duct of lizards, *Proc Calif Acad Sci* **33**: 255–359.

Miller, M. R. (1973). Scanning electron microscope studies of some lizard basilar papillae, *Amer J Anat* **138**: 301–330.

Money, K. E., Solkoloff, M. and Weaver, R. S. (1966). Specific gravity and viscosity of endolymph and perilymph, *Second symposium on the role of the vestibular organs in space exploration*, NASA, pp. 91–97.

Mroz, E. A. and Lechene, C. (1993). Extracellular N-methyl-D-glucamine leads to loss of hair-cell sodium, potassium, and chloride, *Hear Res* **70**: 146–150.

Muhlstein, C. L., Brown, S. B. and Ritchie, R. O. (2001). High-cycle fatigue of polycrystalline silicon thin films in laboratory air, *Materials Research Society Symposium Proceedings*, Vol. 657, Materials Research Society.

Mulroy, M. J. (1968). *Cochlear anatomy of the alligator lizard*, PhD thesis, University of California at San Francisco, San Francisco, CA.

Mulroy, M. J. (1974). Cochlear anatomy of the alligator lizard, *Brain Behav Evol* **10**: 69–87.

Mulroy, M. J. (1986). Patterns of afferent synaptic contacts in the alligator lizard's cochlea, *J Compar Neurol* **248**: 263–271.

Munson, B. R., Young, D. F. and Okiishi, T. O. (1990). *Fundamentals of Fluid Mechanics*, John Wiley and Sons, New York, NY.

Nadol, J. B., Mulroy, M. J., Goodenough, D. A. and Weiss, T. F. (1976). Tight and gap junctions in a vertebrate inner ear, *Am J Anat* **147**: 281–301.

Nakazawa, K., Liu, M., Inoue, K. and Ohno, Y. (1997). Potent inhibition by trivalent cations of ATP-gated channels, *Eur J Pharmacol* **325**: 237–243.

Nilsen, K. E. and Russell, I. J. (1999). Timing of cochlear feedback: spatial and temporal representation of a tone across the basilar membrane, *Nat Neurosci* **2**: 642–648.

Nishikawa, S. and Sasaki, F. (1996). Internalization of styryl dye FM1-43 in the hair cells of lateral line organs in Xenopus larvae, *J Histochem Cytochem* **44**: 733–741.

Page, E. L. L. and Johnstone, B. M. (1980). Nonlinear mechanical behavior of the basilar membrane in the basal turn of the guinea pig cochlea, *Hear Res* **2**: 183–189.

Paradiso, A. M., Tsien, R. Y. and Machen, T. E. (1984). Na+-H+ exchange in gastric glands as measured with a cytoplasmic-trapped, fluorescent pH indicator, *Proc Nat Acad Sci USA* **81**: 7436–7440.

Patuzzi, R. (1996). Cochlear micromechanics and macromechanics, *in* P. Dallos, A. N. Popper and R. R. Fay (eds), *The Cochlea*, Vol. 8 of *Springer Handbook of Auditory Research*, Springer-Verlag, New York.

Peake, W. T. and Ling, Jr., A. L. (1980). Basilar-membrane motion in the alligator lizard: its relation to tonotopic organization and frequency selectivity, *J Acoust Soc Am* **67**(5): 1736–45.

Peterson, S. K., Frishkopf, L. S., Lechene, C., Oman, C. M. and Weiss, T. F. (1978). Element composition of inner ear lymphs in cats, lizards, and skates determined by electron probe microanalysis of liquid samples, *J Comp Physiol* **126**: 1–14.

Pickles, J. O. (1993). The mechanical implications of variations in hair-bundle shape, *in* H. Duifhuis, J. W. Horst, P. van Dijk and S. M. van Netten (eds), *Proceedings of the international symposium on biophysics of hair cell sensory systems*, World Scientific, New Jersey, pp. 124–132.

Rauch, S. and Rauch, I. (1974). Physico-chemical properties of the inner ear especially ionic transport, *in* W. D. Keidel and W. D. Neff (eds), *Handbook of Sensory Physiology, Vol. V/1: Auditory system*, Springer, New York, pp. 647–682.

Recio, A., Rich, N. C., Narayan, S. S. and Ruggero, M. A. (1998). Basilar-membrane responses to clicks at the base of the chinchilla cochlea, *J Acoust Soc Am* **103**(4): 1972–1989.

Rhode, W. S. (1971). Observations of the vibration of the basilar membrane using the Mössbauer technique, *J Acoust Soc Am* **49**: 1218–1231.

Rhode, W. S. (1973). An investigation of post-mortem cochlear mechanics using the Mössbauer effect, *in* A. R. Møller (ed.), *Basic Mechanisms in Hearing*, Academic Press, New York, pp. 49–63.

Richter, C. P., Evans, B. N., Edge, R. and Dallos, P. (1998). Basilar membrane vibration in the gerbil hemicochlea, *J Neurophysiol* **79**: 2555–2264.

Richter, C. P., Evans, B. N., Hu, X. and Dallos, P. (1998). Basilar membrane micromechanics measured in the gerbil inner ear, *Abstracts of the Twenty-First Midwinter Research Meeting*, Association for Research in Otolaryngology, St. Petersburg Beach, Florida.

Robertson, D., Johnstone, B. M. and McGill, T. J. (1980). Effects of loud tones on the inner ear: a combined electrophysiological and ultrastructural study, *Hear Res* **2**: 39–53.

Robles, L., Ruggero, M. A. and Rich, N. C. (1991). Two-tone distortion in the basilar membrane of the cochlea, *Nature* **349**: 413–414.

Rosowski, J. J. (1996). Models of external- and middle-ear function, *in* H. L. Hawkins, T. A. McMullen, A. N. Popper and R. R. Fay (eds), *Auditory Computation*, Springer-Verlag, New York.

Rosowski, J. J., Peake, W. T., Lynch, T. J., Leong, R. and Weiss, T. F. (1985). A model for signal transmission in an ear having hair cells with free-standing stereocilia: II. Macromechanical stage, *Hear Res* **20**: 139–155.

Ruggero, M. A., Narayan, S. S., Temchin, A. N. and Recio, A. (2000). Mechanical bases of frequency tuning and neural excitation at the base of the cochlea: Comparison of basilar-membrane vibrations and auditory-nerve-fiber responses in chinchilla, *Proc Nat Acad SCI USA* **97**: 11744–11750.

Ruggero, M. A. and Rich, N. C. (1991). Furosemide alters organ of Corti mechanics: evidence for feedback of outer hair cells upon the basilar membrane, *J Neurosci* **11**: 1057–1067.

Ruggero, M. A., Rich, N. C., Recio, A., Narayan, S. S. and Robles, L. (1997). Basilar-membrane responses to tones at the base of the chinchilla cochlea, *J Acoust Soc Am* **101**: 2151–63.

Ruknudin, A., Sachs, F. and Bustamante, O. (1993). Stretch-activated ion channels in tissue-cultured chick heart, *Am J Physiol* **264**: H960–H972.

Russell, I. J., Richardson, G. P. and Kössl, M. (1986). Mechanosensitivity of mammalian auditory hair cells in vitro, *Nature* **321**: 517–519.

Saunders, J. C., Canlon, B. and Flock, Å. (1986). Growth of threshold shift in hair-cell stereocilia following overstimulation, *Hear Res* **23**: 245–255.

Saunders, J. C., Dear, S. P. and Schneider, M. E. (1985). The anatomical consequences of acoustic injury: A review and tutorial, *J Acoust Soc Am* **78**(3): 833–860.

Schmiedt, R. A. (1984). The effects of noise on the physiology of hearing: a review and tutorial, *J Acoust Soc Am* **76**: 1293–1317.

Sellick, P. M., Patuzzi, R. B. and Johnstone, B. M. (1982). Measurement of basilar membrane motion in the guinea-pig using the Mössbauer technique, *J Acoust Soc Am* **72**: 131–141.

Shatz, L. F. (1996). *Effect of hair bundle shape on hair bundle hydrodynamics of sensory cells in the inner ear*, PhD thesis, Massachusetts Institute of Technology, Cambridge, MA.

Shatz, L. F. (2000). The effect of hair bundle shape on hair bundle hydrodynamics of inner ear hair cells at low and high frequencies, *Hear Res* **141**: 39–50.

Shotwell, S. L., Jacobs, R. and Hudspeth, A. J. (1981). Directional sensitivity of individual vertebrate hair cells to controlled deflection of their hair bundles, *Ann NY Acad Sci* **374**: 1–10.

Siegel, J., Sikka, R., Zeddies, D. and Dong, Q. (2001). Intact explanted adult gerbil cochleae maintained at body temperature, *Abstracts of the Twenty-Fourth Midwinter Research Meeting*, Association for Research in Otolaryngology, St. Petersburg Beach, Florida.

Steer, R. W., Li, Y. T., Young, L. R. and Meiry, J. L. (1967). Physical properties of the labyrinthine fluids and quantification of the phenomenon of caloric stimulation, *Third symposium on the role of the vestibular organs in space exploration*, NASA, pp. 409–420.

Szymko, Y. M., Nelson-Adesokan, P. M. and Saunders, J. C. (1995). Stiffness changes in chick hair bundles following in vitro overstimulation, *J Comp Physiol* **176**: 727–735.

Thorne, P. R., Duncan, C. E. and Gavin, J. B. (1986). The pathogenesis of stereocilia abnormalities in acoustic trauma, *Hear Res* **21**: 41–49.

Tigges, M., Wittenberg, T., Mergell, P. and Eysholdt, U. (1999). Imaging of vocal fold vibration by digital multi-plane kymography, *Comp Med Imag Graph* **23**: 323–330.

Tilney, L. G., Saunders, J. C., Egelman, E. and DeRosier, D. J. (1982). Changes in the organization of actin filaments in the stereocilia of noise-damaged lizard cochleae, *Hear Res* **7**: 181–197.

Timoner, S. (1999). *Subpixel motion estimation from sequences of video images*, Master's thesis, Massachusetts Institute of Technology, Cambridge, MA.

Timoner, S. J. and Freeman, D. M. (2001). Multi-image gradient-based algorithms for motion estimation, *Optical Engineering* **40**: 2003–2016.

Ulfendahl, M., Khanna, S. M. and Heneghan, C. (1995). Shearing motion in the hearing organ measured by confocal laser heterodyne interferometry, *Neuroreport* **6**: 1157–1160.

von Békésy, G. (1960). *Experiments in Hearing*, McGraw-Hill, New York.

Weiss, T. F. (1982). Bidirectional transduction in vertebrate hair cells: A mechanism for coupling mechanical and electrical processes, *Hear Res* **7**: 353–360.

Weiss, T. F., Altmann, D. W. and Mulroy, M. J. (1978). Endolymphatic and intracellular resting potential in the alligator lizard cochlea, *Pflügers Arch* **373**: 77–84.

Weiss, T. F. and Leong, R. (1985a). A model for signal transmission in an ear having cells with free-standing stereocilia. III. Micromechanical stage, *Hear Res* **20**: 157–174.

Weiss, T. F. and Leong, R. (1985b). A model for signal transmission in an ear having cells with free-standing stereocilia. IV. Mechanoelectric transduction stage, *Hear Res* **20**: 175–195.

Weiss, T. F., Mulroy, M. J., Turner, R. G. and Pike, C. L. (1976). Tuning of single fibers in the cochlear nerve of the alligator lizard: relation to receptor morphology, *Brain Res* **115**: 71–90.

Weiss, T. F., Peake, W. T., Ling, A. and Holton, T. (1978). Which structures determine frequency selectivity and tonotopic organization of vertebrate cochlear nerve fibers? Evidence from the alligator lizard, *in* R. Naunton and C. Fernandez (eds), *Evoked Electrical Activity in the Auditory Nervous System*, Academic Press, New York, pp. 91–112.

Weiss, T. F., Peake, W. T. and Rosowski, J. J. (1985). A model for signal transmission in an ear having cells with free-standing stereocilia. I. Empirical basis for model structure, *Hear Res* **20**: 131–138.

Wever, E. G. (1965). Structure and function of the lizard ear, *J Aud Res* **5**: 331–371.

Wever, E. G. (1974). The evolution of vertebrate hearing, *in* W. D. Keidel and W. D. Neff (eds), *Handbook of Sensory Physiology. V 1. Auditory System: Anatomy, Physiology (Ear)*, Springer-Verlag, New York, pp. 423–454.

Wever, E. G. (1978). *The Reptile Ear*, Princeton University Press, Princeton, NJ.

Yamauchi, A. M., Highstein, S. M., King, C., Rabbitt, R. D. and Boyle, R. (2002). Displacement of the semicircular canal cupula for sinusoidal stimuli, *Abstracts of the Twenty-Fifth Midwinter Research Meeting*, Association for Research in Otolaryngology, St. Petersburg Beach, Florida.

Yamazaki, J., Duan, D., Janiak, R., Kuenzli, K., Horowitz, B. and Hume, J. R. (1998). Functional and molecular expression of volume-regulated chloride channels in canine vascular smooth muscle cells, *J Physiol* **507**: 729–736.

Yang, X. C. and Sachs, F. (1989). Block of stretch-activated ion channels in *Xenopus* oocytes by gadolinium and calcium ions, *Science* **243**: 1068–1071.

Zeddies, D., Dong, Q. and Siegel, J. (2000). Rapid swelling of hair cells in isolated cochleas perfused with standard culture media, *Abstracts of the Twenty-Third Midwinter Research Meeting*, Association for Research in Otolaryngology, St. Petersburg Beach, Florida.

Zenner, H. P. (1986). Motile responses in outer hair cells, *Hear Res* **22**: 83–90.

Zhou, X. L., Stampf, M. A., Hoch, H. C. and Kung, C. (1991). A mechanosensitive channel in whole cells and in membrane patches of the fungus *Uromyces*, *Science* **253**: 1415–1417.